

Electronic Theses and Dissertations, 2004-2019

2015

Meshless Direct Numerical Simulation of Turbulent Incompressible Flows

Andres Vidal Urbina
University of Central Florida

 Part of the [Mechanical Engineering Commons](#)
Find similar works at: <https://stars.library.ucf.edu/etd>
University of Central Florida Libraries <http://library.ucf.edu>

This Doctoral Dissertation (Open Access) is brought to you for free and open access by STARS. It has been accepted for inclusion in Electronic Theses and Dissertations, 2004-2019 by an authorized administrator of STARS. For more information, please contact STARS@ucf.edu.

STARS Citation

Vidal Urbina, Andres, "Meshless Direct Numerical Simulation of Turbulent Incompressible Flows" (2015). *Electronic Theses and Dissertations, 2004-2019*. 1191.
<https://stars.library.ucf.edu/etd/1191>

MESHLESS DIRECT NUMERICAL SIMULATION OF TURBULENT INCOMPRESSIBLE FLOWS

by

ANDRÉS G. VIDAL

B.S. in Mechanical Engineering, 1989

M.S. in Mechanical Engineering, 1993

M.S. in Computer Science, 1999

A dissertation submitted in partial fulfillment of the requirements
for the degree of Doctor of Philosophy
in the Department of Mechanical and Aerospace Engineering
in the College of Engineering and Computer Science
at the University of Central Florida
Orlando, Florida

Spring Term
2015

Major Professor: Alain J. Kassab

ABSTRACT

A meshless direct pressure-velocity coupling procedure is presented to perform Direct Numerical Simulations (DNS) and Large Eddy Simulations (LES) of turbulent incompressible flows in regular and irregular geometries. The proposed method is a combination of several efficient techniques found in different Computational Fluid Dynamic (CFD) procedures and it is a major improvement of the algorithm published in 2007 by this author. This new procedure has very low numerical diffusion and some preliminary calculations with 2D steady state flows show that viscous effects become negligible faster than ever predicted numerically.

The fundamental idea of this proposal lays on several important inconsistencies found in three of the most popular techniques used in CFD, segregated procedures, streamline-vorticity formulation for 2D viscous flows and the fractional-step method, very popular in DNS/LES.

The inconsistencies found become important in elliptic flows and they might lead to some wrong solutions if coarse grids are used. In all methods studied, the mathematical basement was found to be correct in most cases, but inconsistencies were found when writing the boundary conditions. In all methods analyzed, it was found that it is basically impossible to satisfy the exact set of boundary conditions and all formulations use a reduced set, valid for parabolic flows only.

For example, for segregated methods, boundary condition of normal derivative for pressure zero is valid only in parabolic flows. Additionally, the complete proposal for mass balance correction is right exclusively for parabolic flows.

In the streamline-vorticity formulation, the boundary conditions normally used for the streamline function, violates the no-slip condition for viscous flow. Finally, in the fractional-step method, the boundary condition for pseudo-velocity implies a zero normal derivative for pressure in the wall (correct in parabolic flows only) and, when the flows reaches steady state, the procedure does not guarantee mass balance.

The proposed procedure is validated in two cases of 2D flow in steady state, backward-facing step and lid-driven cavity. Comparisons are performed with experiments and excellent agreement was obtained in the solutions that were free from numerical instabilities.

A study on grid usage is done. It was found that if the discretized equations are written in terms of a *local Reynolds number*, a strong criterion can be developed to determine, in advance, the grid requirements for any fluid flow calculation.

The 2D-DNS on parallel plates is presented to study the basic features present in the simulation of any turbulent flow. Calculations were performed on a short geometry, using a uniform and very fine grid to avoid any numerical instability. Inflow conditions were white noise and high frequency oscillations. Results suggest that, if no numerical instability is present, inflow conditions alone are not enough to sustain permanently the turbulent regime.

Finally, the 2D-DNS on a backward-facing step is studied. Expansion ratios of 1.14 and 1.40 are used and calculations are performed in the transitional regime. Inflow conditions were white noise and high frequency oscillations. In general, good agreement is found on most variables when comparing with experimental data.

Dedicated to you, Trish. Thank you for your love, patient and support.

ACKNOWLEDGMENTS

I want to thank to my advisor, Dr. Alain Kassab for proposing me this interesting and challenging topic, and for being always able to help when I needed.

Thanks to Steve Dick for his help in the configuration and adjustments of the clusters I used in most of the simulations.

Thanks to the Institute of Simulation and Training IST at UCF for supplying a very important CPU time used in some simulations and in many testing runs.

Thanks to my family for their permanent support, in the good and in the bad times. Thanks to my brother, Dr. Patricio Vidal for his advising in the topic of software engineering and development.

I want to express especial thanks to all nurses, doctors, technicians and professionals of Winter Park Memorial, Florida Hospital at Sebring and Tampa General Hospital for their dedication in their effort of saving my life. Thanks particularly to doctors Anil Kumar (CFCG) and Siva Kumar (TGH) for their help during my health crisis and their continuous concern.

I want to thank particularly Dr. Kathy H Lee (Florida Hospital at Sebring) for taking the key decision that saved my life. To all of you, thank you very much.

TABLE OF CONTENTS

ABSTRACT.....	ii
ACKNOWLEDGMENTS	v
TABLE OF CONTENTS.....	vi
LIST OF FIGURES	x
LIST OF TABLES	xxiii
CHAPTER ONE INTRODUCTION.....	1
CHAPTER TWO MESHLESS APPLIED TO CFD	5
2.1 Mesh-Free Petrov-Galerkin method.....	9
2.2 Finite-Point method.....	9
2.3 Diffusive Approximation method	11
2.4 Kernel Particle Method	12
2.5 Localized RBF.....	12
2.6 Other approaches and studies.....	18
CHAPTER THREE VELOCITY PRESSURE COUPLING	21
3.1 The projection method of Harlow and Welch.....	21
3.2 The pressure equation in highly stretched grids.....	22
3.3 Boundary conditions for pressure equation.....	23
3.4 Convergence through divergence-free velocity field.....	25

3.5	SIMPLE-based procedures.....	27
3.6	Streamline-vorticity formulation.....	29
3.7	Fractional-Step method of Kim and Moin	30
3.8	The full coupled procedure	32
3.9	A local direct coupling procedure	33
CHAPTER FOUR ADDITIONAL SCHEMES/PROCEDURES		37
4.1	Convection discretization.....	37
4.2	Time integration schemes.....	42
4.3	Interpolation	44
4.4	The order of a method	49
4.5	Acceleration techniques	51
4.6	Absence of virtual points.....	53
4.7	Using a suitable grid.....	56
CHAPTER FIVE PROPOSED PROCEDURES AND VALIDATION		60
5.1	Serial procedure for 2D steady flows.....	60
5.2	Serial procedure for 2D transient flows	61
5.3	2D Steady Backward-Facing Step.....	62
5.3.1	Calculations with an expansion ratio of 1.94.....	68
5.3.1.1	Results with a coarse grid.....	69

5.3.1.2	Results with a fine grid.....	77
5.3.2	Calculations with an expansion ratio of 1.40.....	88
5.3.3	Calculations with an expansion ratio of 1.14.....	92
5.4	2D Steady Lid-Driven Cavity	98
5.5	Final comment on validation.....	112
CHAPTER SIX SIMULATION OF TURBULENT FLOW.....		113
6.1	Direct Numerical Simulation	113
6.2	Large Eddy Simulation.....	115
6.3	Generating inflow conditions.....	117
6.4	The wall roughness.....	119
6.5	Taking statistics.....	120
6.6	2D Turbulence.....	121
6.7	Transitional flow	122
6.8	Computational details on the generation of turbulence.....	123
CHAPTER SEVEN 2D-DNS ON PARALLEL PLATES		127
CHAPTER EIGHT 2D-DNS ON A BACKWARD-FACING STEP.....		144
8.1	Input data and parameters	146
8.2	Re-attachment.....	148
8.3	Backward-Facing Step with $ER=1.14$ and $Re_{D_h} = 3000$	152

8.4	Backward-Facing Step with $ER = 1.40$ and $Re_{D_h} = 2000$	166
CHAPTER NINE CONCLUSIONS.....		177
APPENDIX A BACKWARD-FACING STEP WITH $ER = 1.14$ AND $Re_{D_h} = 1000$		180
APPENDIX B BACKWARD-FACING STEP WITH $ER = 1.14$ AND $Re_{D_h} = 2000$		191
APPENDIX C BACKWARD-FACING STEP WITH $ER = 1.40$ AND $Re_{D_h} = 1000$		202
APPENDIX D COMPUTER IMPLEMENTATION		213
D.1	Computation of internal and boundary points.....	215
D.2	Search of neighboring points.....	219
D.3	Search of influence points	221
D.4	Calculation of condition number.....	221
APPENDIX E MULTICORE FLOW SOLVER		223
E.1	General multicore procedure	227
E.2	Multicore flow solver for 2D steady flows	230
E.3	Testing the multicore solver.....	232
LIST OF REFERENCES		237

LIST OF FIGURES

Figure 1: Staggered grids for u , v and p in a system of 3x3 volumes.....	33
Figure 2: Coupling schemes and volumes involved in a 4x4 volumes 2D region.....	36
Figure 3: Solutions to (32) with $Re = 5$ (classic schemes).....	39
Figure 4: Solutions to (32) with $Re = 5$ (flux limiters).....	41
Figure 5: Range of shape parameter c vs. the number of influence points.....	46
Figure 6: Condition number vs. shape parameter, for 30 influence points.....	48
Figure 7: The real grid and the virtual grid.....	54
Figure 8: Progression of details for the backward-facing step	69
Figure 9: Streamlines BFS with $ER = 1.94$, coarse grid, Reynolds 100-1000.....	71
Figure 10: Streamlines BFS with $ER = 1.94$, coarse grid, Reynolds 1100-1200.....	72
Figure 11: Streamlines BFS with $ER = 1.94$, coarse grid, Reynolds 1400-2400.....	73
Figure 12: Streamlines BFS with $ER = 1.94$, coarse grid, Reynolds 2400-4500.....	74
Figure 13: Streamlines BFS with $ER = 1.94$, coarse grid, Reynolds 5000-9000.....	75
Figure 14: Re-attachment BFS with for $ER = 1.94$, coarse grid, re-attachment	76
Figure 15: Convergence for BFS, $ER = 1.94$, fine grid, $Re=100$	80
Figure 16: Convergence for BFS, $ER = 1.94$, fine grid, $Re=200$	80
Figure 17: Convergence for BFS, $ER = 1.94$, fine grid, $Re=400$	81
Figure 18: Convergence for BFS, $ER = 1.94$, fine grid, $Re=600$	81
Figure 19: Convergence for BFS, $ER = 1.94$, fine grid, $Re=800$	82
Figure 20: Convergence for BFS, $ER = 1.94$, fine grid, $Re=1000$	82
Figure 21: Convergence for BFS, $ER = 1.94$, fine grid, $Re=1200$	83

Figure 22: Convergence for BFS, $ER = 1.94$, fine grid, $Re=1400$	83
Figure 23: Convergence for BFS, $ER = 1.94$, fine grid, $Re=1600$	84
Figure 24: Convergence for BFS, $ER = 1.94$, fine grid, $Re=1800$	84
Figure 25: Convergence for BFS, $ER = 1.94$, fine grid, $Re=2000$	85
Figure 26: Streamlines BFS with $ER = 1.94$, fine grid, Reynolds 100	85
Figure 27: Streamlines BFS with $ER = 1.94$, fine grid, Reynolds 200	85
Figure 28: Streamlines BFS with $ER = 1.94$, fine grid, Reynolds 400	86
Figure 29: Streamlines BFS with $ER = 1.94$, fine grid, Reynolds 600	86
Figure 30: Streamlines BFS with $ER = 1.94$, fine grid, Reynolds 800	86
Figure 31: Streamlines BFS with $ER = 1.94$, fine grid, Reynolds 1000	87
Figure 32: Streamlines BFS with $ER = 1.94$, fine grid, Reynolds 1200	87
Figure 33: Streamlines BFS with $ER = 1.94$, fine grid, Reynolds 1400	87
Figure 34: Streamlines BFS with $ER = 1.94$, fine grid, Reynolds 1600	88
Figure 35: Streamlines BFS with $ER = 1.94$, fine grid, Reynolds 1800	88
Figure 36: Streamlines BFS with $ER = 1.94$, fine grid, Reynolds 2000	88
Figure 37: Re-attachment BFS with $ER = 1.40$	90
Figure 38: Streamlines BFS with $ER = 1.40$, Reynolds 1000	91
Figure 39: Streamlines BFS with $ER = 1.40$, Reynolds 2000	91
Figure 40: Streamlines BFS with $ER = 1.40$, Reynolds 3000	91
Figure 41: Streamlines BFS with $ER = 1.40$, Reynolds 4000	91
Figure 42: Convergence for BFS, $ER = 1.14$, $Re=1000$	93
Figure 43: Convergence for BFS, $ER = 1.14$, $Re=2000$	93

Figure 44: Convergence for BFS, $ER = 1.14$, $Re=3000$	94
Figure 45: Convergence for BFS, $ER = 1.14$, $Re=4000$	94
Figure 46: Convergence for BFS, $ER = 1.14$, $Re=5000$	95
Figure 47: Convergence for BFS, $ER = 1.14$, $Re=6000$	95
Figure 48: Re-attachment BFS with $ER = 1.14$	96
Figure 49: Streamlines for BFS, $ER = 1.14$, $Re=1000$	96
Figure 50: Streamlines for BFS, $ER = 1.14$, $Re=2000$	97
Figure 51: Streamlines for BFS, $ER = 1.14$, $Re=3000$	97
Figure 52: Streamlines for BFS, $ER = 1.14$, $Re=4000$	97
Figure 53: Streamlines for BFS, $ER = 1.14$, $Re=5000$	97
Figure 54: Streamlines for BFS, $ER = 1.14$, $Re=6000$	98
Figure 55: Typical streamlines for different Reynolds numbers [53].....	99
Figure 56: Velocity at vertical center line for $Re = 15,000$ [53].....	100
Figure 57: Convergence LDC for Reynolds number of 5000.....	107
Figure 58: Streamlines LDC for Reynolds number of 100.....	108
Figure 59: Streamlines LDC for Reynolds number of 1000.....	108
Figure 60: Streamlines LDC for Reynolds number of 5000.....	109
Figure 61: Streamlines LDC for Reynolds number of 10000.....	109
Figure 62: Velocity at mid-plane LDC for Reynolds number of 100.....	110
Figure 63: Velocity at mid-plane LDC for Reynolds number of 1000.....	110
Figure 64: Velocity at mid-plane LDC for Reynolds number of 5000.....	111
Figure 65: Velocity at mid-plane LDC for Reynolds number of 10000.....	111
Figure 66: Number of iterations per time step, 2D-DNS PP	129

Figure 67: Streamlines, 2D-DNS PP	131
Figure 68: Contours of velocity U/\bar{V} , 2D-DNS PP	131
Figure 69: Contours of velocity V/\bar{V} , 2D-DNS PP	132
Figure 70: Contours of pressure $p/(0.5 \cdot \rho \cdot \bar{V}^2)$, 2D-DNS PP	132
Figure 71: Contours of kinetic energy k/\bar{V}^2 , 2D-DNS PP	133
Figure 72: Contours of kinetic energy k/\bar{V}^2 (zoom), 2D-DNS PP	133
Figure 73: Contours of Reynolds stress $\overline{u'u'}/\bar{V}^2$, 2D-DNS PP.....	135
Figure 74: Contours of Reynolds stress $\overline{u'v'}/\bar{V}^2$, 2D-DNS PP.....	135
Figure 75: Contours of Reynolds stress $\overline{v'v'}/\bar{V}^2$, 2D-DNS PP.....	136
Figure 76: Contours of vorticity $\omega/(0.5 \cdot \rho \cdot \bar{V}^2)$, 2D-DNS PP	136
Figure 77: Contours of u'/\bar{V} in the last time step, 2D-DNS PP.....	137
Figure 78: Contours of v'/\bar{V} at last time step, 2D-DNS PP.....	137
Figure 79: Velocity U/\bar{V} at different X-planes, 2D-DNS PP.....	138
Figure 80: Velocity V/\bar{V} at different X-planes, 2D-DNS PP.....	138
Figure 81: Pressure $p/(0.5 \cdot \rho \cdot \bar{V}^2)$ at different X-planes, 2D-DNS PP	140
Figure 82: Kinetic energy k/\bar{V}^2 at different X-planes, 2D-DNS PP	140
Figure 83: Reynolds stress $\overline{u'u'}/\bar{V}^2$ at different X-planes, 2D-DNS PP.....	141
Figure 84: Reynolds stress $\overline{u'v'}/\bar{V}^2$ at different X-planes, 2D-DNS PP.....	141
Figure 85: Reynolds stress $\overline{v'v'}/\bar{V}^2$ at different X-planes, 2D-DNS PP.....	142
Figure 86: Pressure coefficient C_p as function of position, 2D-DNS PP	142
Figure 87: Friction coefficient C_f at different X-planes, 2D-DNS PP.....	143

Figure 88: Geometry used in the 2D-DNS on a backward-facing step	146
Figure 89: Averaged re-attachment, 2D-DNS BFS, $ER = 1.14$	148
Figure 90: Averaged re-attachment, 2D-DNS BFS, $ER = 1.40$	149
Figure 91: Variation of re-attachment with time, 2D-DNS BFS, $Re = 1000$, $ER = 1.14$	150
Figure 92: Variation of re-attachment with time, 2D-DNS BFS, $Re = 2000$, $ER = 1.14$	150
Figure 93: Variation of re-attachment with time, 2D-DNS BFS, $Re = 3000$, $ER = 1.14$	150
Figure 94: Variation of re-attachment with time, 2D-DNS BFS, $Re = 1000$, $ER = 1.40$	151
Figure 95: Variation of re-attachment with time, 2D-DNS BFS, $Re = 2000$, $ER = 1.40$	152
Figure 96: Streamlines, 2D-DNS BFS, $ER = 1.14$, $Re_{D_h} = 3000$	152
Figure 97: Contours of velocity U/\bar{V} , 2D-DNS BFS, $ER = 1.14$, $Re_{D_h} = 3000$	153
Figure 98: Contours of velocity V/\bar{V} , 2D-DNS BFS, $ER = 1.14$, $Re_{D_h} = 3000$	154
Figure 99: Contours of pressure $p/(0.5 \cdot \rho \cdot \bar{V}^2)$, 2D-DNS BFS, $ER = 1.14$, $Re_{D_h} = 3000$	154
Figure 100: Contours of kinetic energy k/\bar{V}^2 , 2D-DNS BFS, $ER = 1.14$, $Re_{D_h} = 3000$	155
Figure 101: Contours of Reynolds stress $\overline{u'u'}/\bar{V}^2$, 2D-DNS BFS, $ER = 1.14$, $Re_{D_h} = 3000$..	156
Figure 102: Contours of Reynolds stress $\overline{u'v'}/\bar{V}^2$, 2D-DNS BFS, $ER = 1.14$, $Re_{D_h} = 3000$..	156
Figure 103: Contours of Reynolds stress $\overline{v'v'}/\bar{V}^2$, 2D-DNS BFS, $ER = 1.14$, $Re_{D_h} = 3000$..	157
Figure 104: Contours of vorticity $\omega/(0.5 \cdot \rho \cdot \bar{V}^2)$, 2D-DNS BFS, $ER = 1.14$, $Re_{D_h} = 3000$..	157
Figure 105: Contours of u'/\bar{V} in the last time step, 2D-DNS BFS, $ER = 1.14$, $Re_{D_h} = 3000$..	158
Figure 106: Contours of v'/\bar{V} at last time step, 2D-DNS BFS, $ER = 1.14$, $Re_{D_h} = 3000$	158

Figure 107: Velocity U/\bar{V} at different X-planes, 2D-DNS BFS, $ER=1.14$, $Re_{D_h} = 3000$;	159
Figure 108: Velocity V/\bar{V} at different X-planes, 2D-DNS BFS, $ER=1.14$, $Re_{D_h} = 3000$	160
Figure 109: Pressure $p/(0.5 \cdot \rho \cdot \bar{V}^2)$ at different X-planes, 2D-DNS BFS, $ER=1.14$, $Re_{D_h} = 3000$	160
Figure 110: Kinetic energy k/\bar{V}^2 at different X-planes, 2D-DNS BFS, $ER=1.14$, $Re_{D_h} = 3000$	162
Figure 111: Reynolds stress $\overline{u'u'}/\bar{V}^2$ at different X-planes, 2D-DNS BFS, $ER=1.14$, $Re_{D_h} = 3000$	163
Figure 112: Reynolds stress $\overline{u'v'}/\bar{V}^2$ at different X-planes, 2D-DNS BFS, $ER=1.14$, $Re_{D_h} = 3000$	163
Figure 113: Reynolds stress $\overline{v'v'}/\bar{V}^2$ at different X-planes, 2D-DNS BFS, $ER=1.14$, $Re_{D_h} = 3000$	164
Figure 114: Pressure coefficient C_p as function of position, 2D-DNS BFS, $ER=1.14$, $Re_{D_h} = 3000$	164
Figure 115: Friction coefficient C_f at different X-planes, 2D-DNS BFS, $ER=1.14$, $Re_{D_h} = 3000$; “o” [157], “-“ this work.....	165
Figure 116: Streamlines, 2D-DNS BFS, $ER=1.40$, $Re_{D_h} = 2000$	166
Figure 117: Contours of velocity U/\bar{V} , 2D-DNS BFS, $ER=1.40$, $Re_{D_h} = 2000$	167
Figure 118: Contours of velocity V/\bar{V} , 2D-DNS BFS, $ER=1.40$, $Re_{D_h} = 2000$	168

Figure 119: Contours of pressure $p/(0.5 \cdot \rho \cdot \bar{V}^2)$, 2D-DNS BFS, $ER = 1.40$, $Re_{D_h} = 2000$..	168
Figure 120: Contours of kinetic energy k/\bar{V}^2 , 2D-DNS BFS, $ER = 1.40$, $Re_{D_h} = 2000$	169
Figure 121: Contours of Reynolds stress $\overline{u'u'}/\bar{V}^2$, 2D-DNS BFS, $ER = 1.40$, $Re_{D_h} = 2000$..	169
Figure 122: Contours of Reynolds stress $\overline{u'v'}/\bar{V}^2$, 2D-DNS BFS, $ER = 1.40$, $Re_{D_h} = 2000$..	170
Figure 123: Contours of Reynolds stress $\overline{v'v'}/\bar{V}^2$, 2D-DNS BFS, $ER = 1.40$, $Re_{D_h} = 2000$..	170
Figure 124: Contours of vorticity $\omega/(0.5 \cdot \rho \cdot \bar{V}^2)$, 2D-DNS BFS, $ER = 1.40$, $Re_{D_h} = 2000$.	171
Figure 125: Contours of u'/\bar{V} in the last time step, 2D-DNS BFS, $ER = 1.40$, $Re_{D_h} = 2000$.	171
Figure 126: Contours of v'/\bar{V} at last time step, 2D-DNS BFS, $ER = 1.40$, $Re_{D_h} = 2000$	172
Figure 127: Velocity U/\bar{V} at different X-planes, 2D-DNS BFS, $ER = 1.40$, $Re_{D_h} = 2000$; “o” [202], “-“ this work.....	172
Figure 128: Velocity V/\bar{V} at different X-planes, 2D-DNS BFS, $ER = 1.40$, $Re_{D_h} = 2000$	173
Figure 129: Pressure $p/(0.5 \cdot \rho \cdot \bar{V}^2)$ at different X-planes, 2D-DNS BFS, $ER = 1.40$, $Re_{D_h} = 2000$	173
Figure 130: Kinetic energy k/\bar{V}^2 at different X-planes, 2D-DNS BFS, $ER = 1.40$, $Re_{D_h} = 2000$	174
Figure 131: Reynolds stress $\overline{u'u'}/\bar{V}^2$ at different X-planes, 2D-DNS BFS, $ER = 1.40$, $Re_{D_h} = 2000$	174

Figure 132: Reynolds stress $\overline{u'v'}/\overline{V}^2$ at different X-planes, 2D-DNS BFS, $ER = 1.40$, $Re_{D_h} = 2000$	175
Figure 133: Reynolds stress $\overline{v'v'}/\overline{V}^2$ at different X-planes, 2D-DNS BFS, $ER = 1.40$, $Re_{D_h} = 2000$	175
Figure 134: Pressure coefficient C_p as function of position, 2D-DNS BFS, $ER = 1.40$, $Re_{D_h} = 2000$	176
Figure 135: Friction coefficient C_f at different X-planes, 2D-DNS BFS, $ER = 1.40$, $Re_{D_h} = 2000$	176
Figure 136: Streamlines, 2D-DNS BFS, $ER = 1.14$, $Re_{D_h} = 1000$	181
Figure 137: Contours of velocity U/\overline{V} , 2D-DNS BFS, $ER = 1.14$, $Re_{D_h} = 1000$	181
Figure 138: Contours of velocity V/\overline{V} , 2D-DNS BFS, $ER = 1.14$, $Re_{D_h} = 1000$	182
Figure 139: Contours of pressure $p/(0.5 \cdot \rho \cdot \overline{V}^2)$, 2D-DNS BFS, $ER = 1.14$, $Re_{D_h} = 1000$	182
Figure 140: Contours of kinetic energy k/\overline{V}^2 , 2D-DNS BFS, $ER = 1.14$, $Re_{D_h} = 1000$	183
Figure 141: Contours of Reynolds stress $\overline{u'u'}/\overline{V}^2$, 2D-DNS BFS, $ER = 1.14$, $Re_{D_h} = 1000$	183
Figure 142: Contours of Reynolds stress $\overline{u'v'}/\overline{V}^2$, 2D-DNS BFS, $ER = 1.14$, $Re_{D_h} = 1000$	184
Figure 143: Contours of Reynolds stress $\overline{v'v'}/\overline{V}^2$, 2D-DNS BFS, $ER = 1.14$, $Re_{D_h} = 1000$	184
Figure 144: Contours of vorticity $\omega/(0.5 \cdot \rho \cdot \overline{V}^2)$, 2D-DNS BFS, $ER = 1.14$, $Re_{D_h} = 1000$	185
Figure 145: Contours of u'/\overline{V} in the last time step, 2D-DNS BFS, $ER = 1.14$, $Re_{D_h} = 1000$...	185

Figure 146: Contours of v'/\bar{V} at last time step, 2D-DNS BFS, $ER=1.14$, $Re_{D_h}=1000$	186
Figure 147: Velocity U/\bar{V} at different X-planes, 2D-DNS BFS, $ER=1.14$, $Re_{D_h}=1000$; “o” [202], “-“ this work.....	186
Figure 148: Velocity V/\bar{V} at different X-planes, 2D-DNS BFS, $ER=1.14$, $Re_{D_h}=1000$	187
Figure 149: Pressure $p/(0.5 \cdot \rho \cdot \bar{V}^2)$ at different X-planes, 2D-DNS BFS, $ER=1.14$, $Re_{D_h}=1000$	187
Figure 150: Kinetic energy k/\bar{V}^2 at different X-planes, 2D-DNS BFS, $ER=1.14$, $Re_{D_h}=1000$	188
Figure 151: Reynolds stress $\overline{u'u'}/\bar{V}^2$ at different X-planes, 2D-DNS BFS, $ER=1.14$, $Re_{D_h}=1000$	188
Figure 152: Reynolds stress $\overline{u'v'}/\bar{V}^2$ at different X-planes, 2D-DNS BFS, $ER=1.14$, $Re_{D_h}=1000$	189
Figure 153: Reynolds stress $\overline{v'v'}/\bar{V}^2$ at different X-planes, 2D-DNS BFS, $ER=1.14$, $Re_{D_h}=1000$	189
Figure 154: Pressure coefficient C_p as function of position, 2D-DNS BFS, $ER=1.14$, $Re_{D_h}=1000$	190
Figure 155: Friction coefficient C_f at different X-planes, 2D-DNS BFS, $ER=1.14$, $Re_{D_h}=1000$	190
Figure 156: Streamlines, 2D-DNS BFS, $ER=1.14$, $Re_{D_h}=2000$	192

Figure 157: Contours of velocity U/\bar{V} , 2D-DNS BFS, $ER=1.14$, $Re_{D_h} = 2000$	192
Figure 158: Contours of velocity V/\bar{V} , 2D-DNS BFS, $ER=1.14$, $Re_{D_h} = 2000$	193
Figure 159: Contours of pressure $p/(0.5 \cdot \rho \cdot \bar{V}^2)$, 2D-DNS BFS, $ER=1.14$, $Re_{D_h} = 2000$..	193
Figure 160: Contours of kinetic energy k/\bar{V}^2 , 2D-DNS BFS, $ER=1.14$, $Re_{D_h} = 2000$	194
Figure 161: Contours of Reynolds stress $\overline{u'u'}/\bar{V}^2$, 2D-DNS BFS, $ER=1.14$, $Re_{D_h} = 2000$..	194
Figure 162: Contours of Reynolds stress $\overline{u'v'}/\bar{V}^2$, 2D-DNS BFS, $ER=1.14$, $Re_{D_h} = 2000$..	195
Figure 163: Contours of Reynolds stress $\overline{v'v'}/\bar{V}^2$, 2D-DNS BFS, $ER=1.14$, $Re_{D_h} = 2000$..	195
Figure 164: Contours of vorticity $\omega/(0.5 \cdot \rho \cdot \bar{V}^2)$, 2D-DNS BFS, $ER=1.14$, $Re_{D_h} = 2000$.	196
Figure 165: Contours of u'/\bar{V} in the last time step, 2D-DNS BFS, $ER=1.14$, $Re_{D_h} = 2000$.	196
Figure 166: Contours of v'/\bar{V} at last time step, 2D-DNS BFS, $ER=1.14$, $Re_{D_h} = 2000$	197
Figure 167: Velocity U/\bar{V} at different X-planes, 2D-DNS BFS, $ER=1.14$, $Re_{D_h} = 2000$; “o” [202], “-“ this work.....	197
Figure 168: Velocity V/\bar{V} at different X-planes, 2D-DNS BFS, $ER=1.14$, $Re_{D_h} = 2000$	198
Figure 169: Pressure $p/(0.5 \cdot \rho \cdot \bar{V}^2)$ at different X-planes, 2D-DNS BFS, $ER=1.14$, $Re_{D_h} = 2000$	198
Figure 170: Kinetic energy k/\bar{V}^2 at different X-planes, 2D-DNS BFS, $ER=1.14$, $Re_{D_h} = 2000$	199

Figure 171: Reynolds stress $\overline{u'u'}/\overline{V}^2$ at different X-planes, 2D-DNS BFS, $ER=1.14$, $Re_{D_h} = 2000$	199
Figure 172: Reynolds stress $\overline{u'v'}/\overline{V}^2$ at different X-planes, 2D-DNS BFS, $ER=1.14$, $Re_{D_h} = 2000$	200
Figure 173: Pressure coefficient C_p as function of position, 2D-DNS BFS, $ER=1.14$, $Re_{D_h} = 2000$	200
Figure 174: Friction coefficient C_f at different X-planes, 2D-DNS BFS, $ER=1.14$, $Re_{D_h} = 2000$	201
Figure 175: Streamlines, 2D-DNS BFS, $ER=1.40$, $Re_{D_h} = 1000$	203
Figure 176: Contours of velocity U/\overline{V} , 2D-DNS BFS, $ER=1.40$, $Re_{D_h} = 1000$	203
Figure 177: Contours of velocity V/\overline{V} , 2D-DNS BFS, $ER=1.40$, $Re_{D_h} = 1000$	204
Figure 178: Contours of pressure $p/(0.5 \cdot \rho \cdot \overline{V}^2)$, 2D-DNS BFS, $ER=1.40$, $Re_{D_h} = 1000$	204
Figure 179: Contours of kinetic energy k/\overline{V}^2 , 2D-DNS BFS, $ER=1.40$, $Re_{D_h} = 1000$	205
Figure 180: Contours of Reynolds stress $\overline{u'u'}/\overline{V}^2$, 2D-DNS BFS, $ER=1.40$, $Re_{D_h} = 1000$	205
Figure 181: Contours of Reynolds stress $\overline{u'v'}/\overline{V}^2$, 2D-DNS BFS, $ER=1.40$, $Re_{D_h} = 1000$	206
Figure 182: Contours of Reynolds stress $\overline{v'v'}/\overline{V}^2$, 2D-DNS BFS, $ER=1.40$, $Re_{D_h} = 1000$	206
Figure 183: Contours of vorticity $\omega/(0.5 \cdot \rho \cdot \overline{V}^2)$, 2D-DNS BFS, $ER=1.40$, $Re_{D_h} = 1000$	207
Figure 184: Contours of u'/\overline{V} in the last time step, 2D-DNS BFS, $ER=1.40$, $Re_{D_h} = 1000$...	207

Figure 185: Contours of v'/\bar{V} at last time step, 2D-DNS BFS, $ER = 1.40$, $Re_{D_h} = 1000$	208
Figure 186: Velocity U/\bar{V} at different X-planes, 2D-DNS BFS, $ER = 1.40$, $Re_{D_h} = 1000$; “o” [1], “-“ this work.....	208
Figure 187: Velocity V/\bar{V} at different X-planes, 2D-DNS BFS, $ER = 1.40$, $Re_{D_h} = 1000$	209
Figure 188: Pressure $p/(0.5 \cdot \rho \cdot \bar{V}^2)$ at different X-planes, 2D-DNS BFS, $ER = 1.40$, $Re_{D_h} = 1000$	209
Figure 189: Kinetic energy k/\bar{V}^2 at different X-planes, 2D-DNS BFS, $ER = 1.40$, $Re_{D_h} = 1000$	210
Figure 190: Reynolds stress $\overline{u'u'}/\bar{V}^2$ at different X-planes, 2D-DNS BFS, $ER = 1.40$, $Re_{D_h} = 1000$	210
Figure 191: Reynolds stress $\overline{u'v'}/\bar{V}^2$ at different X-planes, 2D-DNS BFS, $ER = 1.40$, $Re_{D_h} = 1000$	211
Figure 192: Reynolds stress $\overline{v'v'}/\bar{V}^2$ at different X-planes, 2D-DNS BFS, $ER = 1.40$, $Re_{D_h} = 1000$	211
Figure 193: Pressure coefficient C_p as function of position, 2D-DNS BFS, $ER = 1.40$, $Re_{D_h} = 1000$	212
Figure 194: Friction coefficient C_f at different X-planes, 2D-DNS BFS, $ER = 1.40$, $Re_{D_h} = 1000$	212
Figure 195: Application of Green’s theorem to check if a point is internal	216
Figure 196: Application of Jordan’s curve theorem	217

Figure 197: Intersection between a direction and a straight boundary	218
Figure 198: Speedup of multicore solver, parallel plates, 11 cores	234
Figure 199: Speedup of multicore solver, BFS, $ER = 1.14$, 11 cores	236

LIST OF TABLES

Table 1: Simplified boundary conditions for Equation (3).....	25
Table 2: Sequence of sweeps for a 2D calculation	35
Table 3: Data used in BFS with $ER = 1.94$, fine grid.....	79
Table 4: Data used in BFS with $ER = 1.40$	90
Table 5: Data used in BFS with $ER = 1.14$	92
Table 6: Data used in Lid-driven cavity	105
Table 7: Parameters, 2D-DNS PP	129
Table 8: Geometric parameters, 2D-DNS BFS.....	147
Table 9: Time-dependent parameters, 2D-DNS BFS	147
Table 10: Data used in parallel plates (multicore runs)	233
Table 11: Range of iterations, multicore solver, parallel plates	234
Table 12: Range of iterations, multicore solver, BFS, $ER = 1.14$	235

CHAPTER ONE

INTRODUCTION

In recent years, with the incredible evolution of computer architectures, Direct Numerical Simulation (DNS) has become a very important research tool to analyze the phenomena of turbulence. Those results are frequently used to develop simpler models or procedures to solve practical engineering problems. Unfortunately, the high cost of solving all the scales (to get all the information of the flow) makes this tool limited to simple geometries and low speed flows.

With very few exceptions, most problems in DNS are solved in cartesian or cylindrical coordinate systems, due mainly that the transformation of the full Navier-Stokes equations to a general non-orthogonal curvilinear coordinate system, makes prohibitive the solution of turbulent flow in irregular geometries due to the huge amount of metrics that must be computed in every single derivative. Moreover, not all problems of turbulent flow in irregular geometries can be solved with a general curvilinear system at an affordable cost.

A cheaper alternative is the Large Eddy Simulation (LES), which solves the large scales directly and simulates the behavior of the small scales with a mathematical model. With LES, computer memory and CPU time is reduced significantly and problems in irregular geometries can be solved at a reasonable cost. Of course, the quality of any LES simulation depends on the numerical scheme, the filter used (implicit/explicit) to simplify the equations of motion and the subgrid model chosen to simulate the small eddies. The choice of a subgrid model is the most important aspect in a good LES simulation.

Independent of the method used (DNS or LES) the phenomena of turbulent flow is then solved with the full Navier-Stokes equations (including the transient term). This means that the

numerical procedure must reproduce all necessary physical conditions for the turbulence to appear. The most accepted hypotheses are the permanent inflow fluctuations and the wall roughness.

The generation of inflow fluctuations is conceptually very simple, and a lot of research has been done to find a suitable way to accomplish that task. Some groups of researchers are working in a way to find convenient analytic functions of the velocity inflow, while others are working on numerical procedures to compute perturbations to the main velocity field. Unfortunately, very little numerical research has been published, specifically, how fluctuations should be created as well as the degree of intensity needed.

The study of the effect of the wall roughness in the creation of turbulence has been limited to very simple cases due mainly to the limitations that a general curvilinear coordinate system has to reproduce absolutely any surface with a coarse grid. In general, most research is done with smooth surfaces and permanent inflow fluctuations.

In the numerical point of view, one common problem that DNS and LES have is in flow problems with highly stretched grids, used to save computing resources. Almost 90% of the computation is spent in the solution of the pressure equation (a Poisson-like equation) due basically that a grid with very high aspect ratio produce an important structural problem in the corresponding linear system.

Additionally, transient Navier-Stokes equations are discretized with the same traditional methods, Finite Elements, Finite Differences and Finite Volumes, as well as other hybrid approaches. If DNS and LES simulations are desired to be done in complex geometries, these techniques require the transformation of flow equations in a general non-orthogonal curvilinear coordinate system.

An alternative is the *Meshless* approach, which has no need of a specific coordinate system to solve the equations of motion (equations are solved always in the cartesian coordinate system). This makes the meshless idea very attractive for DNS and LES computations in irregular geometries.

Another important issue is the numerical diffusion. If any numerical procedure is intended to reproduce all the details of the flow, this computational error must be kept at a very low level. One example can be found in the segregated procedure SIMPLE and its variants, where the pressure and mass-enforcement equations have a considerable amount of numerical diffusion because some coefficients of momentum equations appear inside the derivatives. This numerical diffusion is normally observed in the results, showing a fluid considerable more viscous than the real one. For many practical situations, this error is not important. Unfortunately, under some flow problems, if both viscous and inertia forces are present and they are similar in magnitude, this numerical error may lead to nonphysical solutions.

In general, it can be shown that the mass-enforcement equation in all segregated procedures is accurate only in parabolic flows. If DNS or LES are desired in a complex flow problem, the accurate boundary conditions for this mass equation lead to a discrete system of more equations than unknowns. Of course, this issue can be solved with a coordinate transformation in order to obtain a parabolic flow problem in the new coordinate system.

The proposed numerical procedure is a major modification to the method proposed in [340], where the discretization of momentum and continuity equations will be performed in a staggered grid arrangement. In this scheme derivatives in the diffusion term will be substituted with standard second order finite differences. On the other hand, convection terms will be

discretized with flux limiters. Additionally, all interpolations, needed in the convection terms, are performed with Radial-Based Functions (RBF).

Another goal of this work is to develop an in-house code in C++, paying special attention on performance, especially in the calculation of all geometric information, where classical programming procedures are too slow for large calculations. The choice of C++ was done because this programming language allows the efficient usage of all computer resources. In order to achieve this goal, two areas were explored: algorithm implementation and communication patterns.

Two different codes were built, serial and parallel. The serial procedure was done to validate all the numerical procedures developed in this work. On the other hand, a novel parallel flow solver, using the concept of *concurrency* was developed in order to obtain the best performance on multicore processors. The idea of concurrency uses non trivial concepts for non expert programmers but it needs no communication protocols.

Finally some DNS simulations are presented. First a 2D-DNS on parallel plates in order to study the basic features that are present in any DNS calculation as well as to determine some basic parameters for further calculations. The case of 2D-DNS on a backward-facing step is computed and studied in detail.

CHAPTER TWO MESHLESS APPLIED TO CFD

The first attempt to solve the Navier-Stokes and Euler equations with a meshless technique can be found in [28] and [29]. The technique consists in the use of a bi-linear polynomial to compute all derivatives, using least-squares fitting to approximate the coefficients. The idea of *clouds of points* is introduced so the number of points used for the approximation of the coefficients is limited to a certain pre-defined number.

Later, Kansa in [162] and [163] introduced the idea of multiquadrics, using Radial-Based Functions (RBF), in order to enhance the calculation of spatial derivatives as well as for interpolation. The observed properties of this scheme are mainly monotonicity and convexity as a result of the high accuracy of that procedure. The proposed procedure is then applied in the solution of parabolic, elliptic and hyperbolic equations. The main disadvantage is this proposal is that the calculation of the coefficients for derivatives and interpolations is done globally, with a high computational cost for large problems. The same author, years later explored a series of alternatives [164] to improve the ill-conditioning problem of the collocation matrix:

- Replacement of global solvers by block-partitioning and LU decomposition schemes.
- Matrix preconditioners.
- Variable multiquadrics shape parameters, based upon the local radius of curvature.
- A truncated multiquadrics basis function.
- Multizone methods for large problems.

- Knot adaptivity that minimizes the total number of knots.

Their conclusion is that there are no magic answers, with all alternatives with pros and cons. Their recommendation is that any procedure should implement the ideas developed in the well-known Finite Element Method (FEM).

Another precursor of the meshless technique is Belytschko [30, [31, [94] and [224] with his very important contributions to the field of structural computations through the so-called Element-Free Galerkin (EFG) method. In [30], with a similar idea of [28] and [29], the moving least-squares interpolants is used to construct the trial and test functions for the variational principle in its weak form.

In [224], the EFG procedure is improved and tested, where the Lagrange multipliers are used to enforce the essential boundary conditions. One of the main ideas explored in this paper is the reduction of the computational cost of Lagrange multipliers, a modified variational principle is used, in which the Lagrange multipliers are replaced at the outset by their physical meaning.

Additionally in [31], ideas like kernels and partitions of unity are explored, as well as methods for constructing discontinuous approximations and approximations with discontinuous derivatives, quite frequent in compressible flows. In spite of the accuracy obtained in all cases tested, the computational of the techniques proposed is still high in comparison with the most used techniques.

Another contribution of Belytschko to CFD can be found in [94], where an explicit-explicit/implicit-explicit/second-order staggered time-integration algorithms are proposed for the solution of nonlinear transient fluid-structure interaction problems, one of the most difficult practical problems. The problem of the collapse of a cylindrical shell is solved, their scheme proved to be stable and robust.

A mesh-free and time-free approach is proposed in [50] using the dual reciprocity method (DRM) for the modified Helmholtz operator and the Laplace transform are developed to solve diffusion and diffusion-reactions problems, and using the recent discovery of closed forms of approximate particular solutions of Helmholtz operator.

Similarly, a Finite-Point Method (FPM), based on the combination of weighted least-squares interpolants on a cloud of points is proposed in [256]. Additionally, a procedure for stabilizing the numerical solution for advective-diffusive transport is also explained. Calculations done with some typical NACA profiles show the utility of this procedure for compressible/incompressible flow problems.

Finally, an important contributor to the meshless technique is the group of Šarler. For example, in [288], the dual reciprocity boundary element method is used to solve transient incompressible flow problems in terms of a structured by the fundamental solution of the Laplace equation.

In [285] and [286], a meshless variation using the Trefftz method is explained to solve nonlinear transport phenomena, such as coupled, nonlinear, inhomogenous, anisotropic, multiphase, and multifield heat and mass transfer problems. This procedure has been found to be quite applicable in DC casting of aluminum alloy billets.

The idea of mesh-free RBF collocation method in heat and fluid flow problems is explored in [287] and [289], reformulating the entire problem with a Poisson general transport equation, using the primitive variables. In [287], a comparison of different collocation strategies is performed based on the two dimensional De Vahl Davis steady natural convection problems in cavities. Similarly, in [289] different shape parameters and different order of polynomial augmentation is explored. The study is validated with several calculation of convection heat

transfer in rectangular cavities. As expected, the solution of the full system of algebraic equations represents the main drawback in the computational cost. This is the most important issue to be solved in order for the meshless technique to be competitive with other alternatives.

Another application of the meshless technique can be found in [267], [290] and [291], where the Darcy-Brinkman steady state natural convection problem in a porous media is solved by the dual reciprocity boundary element method. Results performed with coarse a mesh show excellent agreement with available data. This numerical procedure has proven to be almost insensitive to the increased order of boundary field shape functions.

References [292] and [293] formulate a simple explicit local version of the classical RBF collocation method. Instead of global, the collocation is made locally over a set of overlapping domains of influence and the time-stepping is performed in an explicit way. Only small systems of linear equations with the dimension of the number of nodes included in the domain of influence have to be solved for each node. The computational effort thus grows roughly linearly with the number of the nodes. The developed approach thus overcomes the principal large scale problem bottleneck of the original Kansa method.

Since then, many other groups and researchers have made important contributions in the meshless scheme applied to fluid flow problems. In the literature, there are basically four mayor techniques, the Mesh-Free Petrov-Galerkin approach, the Finite-Point Method, the Diffusive Approximation Method, Kernel Particle Method and the localized RBF scheme.

2.1 Mesh-Free Petrov-Galerkin method

The idea is basically the same as in the finite element method but using trial functions with global scope. This idea has been applied extensively in structural calculations but not very often in CFD. One application of the meshless Petrov-Galerkin procedure is found in [10] and [11], where a comparison study of the efficiency and accuracy of a variety of meshless trial and test functions is presented.

Reference [354] is a typical application of meshless approach for the stress analysis of two-dimensional solids. This specific technique is based on a local weighted residual method with the Heaviside step function as the weighting function over a local sub-domain. Trial functions are constructed using radial basis functions (RBF). The present method is a truly meshless method based only on a number of randomly located nodes. Effects of the sizes of local sub-domain and interpolation domain on the performance of the present method are investigated with different shape parameters of RBF.

One application of the Mesh-Free Petrov-Galerkin method to CFD is found in [352] where the flow equations are solved in the weak form using the moving least-squares approximation. The simulation of natural convection in concentric annuli with different geometries is studied.

2.2 Finite-Point method

Here, a multidimensional Taylor series expansion is done and a linear system is build to find the value of the unknown scalar and its derivatives in term of the neighboring points.

In [52], the Finite Point Method is used where the approximation of the derivatives is through interpolations based on the properties of Taylor series expansion. The method is validated with the cavity flow and flow around cylinders. In [215] for example, a variation of the above scheme is evaluated. The local weak form is modified in a very careful way to overcome the so-called Babuska-Brezzi conditions.

In general, procedures are quite similar. In [257], a stabilized finite point method (FPM) for the meshless analysis of incompressible fluid flow problems is presented. The stabilization approach is based in the finite calculus (FIC) procedure. An enhanced fractional step procedure allowing the semi-implicit numerical solution of incompressible fluids using the FPM is described.

One more application of the finite point method is shown in [351] to simulate the two-dimensional natural convection problems within enclosed domain of different geometries. The vorticity-stream function form of N-S equations is taken as the governing equations. It was observed that the obtained results agreed very well with others available in the literatures, and with the same nodal density, the accuracy achieved by the LRPIM method is much higher than that of the finite difference (FD) method. In general, the following advantages are found. Their conclusions is that the nodal distribution in the problem domain can be arbitrary and that accurate results can be achieved by using less number of nodes than that required by the FD method.

Other similar approaches found in the literature are [217], [218] and [219], in which a meshfree weak-strong formulation is reformulated to solve the incompressible Navier-Stokes equations. In this method, the meshfree collocation method based on strong form equations is

applied to the interior nodes and the nodes on the essential boundaries; the local Petrov-Galerkin weak form is applied only to the nodes on the natural boundaries of the problem domain.

2.3 Diffusive Approximation method

There are several researchers working with this idea. The scalar function φ to be solved gets its estimates and its derivatives using Taylor expansions by a weighted least-square method which uses the values of φ at the vicinity of the corresponding point only.

For example, in [283], a Diffusive Approximation Method (DAO) is presented for the calculation of 2D laminar flows. The problem of natural convection in square cavity and eccentric annulus are solved for high Rayleigh numbers.

Reference [359] is another case in which the elements are locally created at each node in an autonomous manner, so that only nodal information is necessary without global meshing. The method has been tested with various applications such as heat conduction, fluid and fracture analyses, as well as techniques for parallelization.

In [316], a diffuse approximation method (DAM) for three-dimensional, incompressible, viscous fluid flow is presented. The method works directly with primitive variables. The discretized equations are solved using a first-order-in-time, implicit projection algorithm.

A comparative study of between the weak form local Petrov-Galerkin method and the strong form meshless diffusive approximation method is found in [332]. In both cases, the shape functions are obtained by moving least-squares approximation. The advantage of DAM is in simpler numerical implementation and lower computational cost.

2.4 Kernel Particle Method

The kernel estimate was first introduced in the smooth hydrodynamics method, in which the kernel estimate of a function is an integral similar to the band-pass filters used in LES but integrated in the solution domain. For the kernel function, several approximations such as splines, Gaussian or any canonical function.

Particularly, in [367], the kernel particle method (RKPM) is used for 3-D implicit CFD analysis. A novel procedure for implementing the essential boundary condition using the hierarchical enrichment method is presented. Using this enrichment along the essential boundaries produces results that more closely match experimental and analytical results for a flow past a cylinder problem than does either the finite-element method or other meshfree methods that require matrix inversion for the application of essential boundary conditions.

The study of micro channel flow using a meshfree particle approach is given in [222]. The scheme is based on smoothed particle hydrodynamics (SPH) and its variant, adaptive smoothed particle hydrodynamics (ASPH). The incompressible flow in the micro channels is modeled as an artificially compressible flow. The surface tension is incorporated into the equations of motion. The classic Poiseuille flow and a practical micro channel flow problem of flip-chip under-fill encapsulation process are investigated.

2.5 Localized RBF

This is probably the most popular technique in meshless. The main idea is to use RBF interpolation technique with a limited scope, so that the computation costs of the calculation of

the coefficients is reduced significantly. This scheme is the approach used at the *Computational Mechanics Lab* at University of Central Florida.

In [76] and [77], a localized RBF meshless method is developed for coupled viscous fluid flow and convective heat transfer problems. Here, an efficient set of formulae are derived to compute the RBF interpolation in terms of vector products thus providing a substantial computational savings over traditional meshless methods. Moreover, the approach presented is applicable to explicit or implicit time marching schemes as well as steady-state iterative methods. The flow equations are solved using a time-marching scheme with the Helmholtz decomposition.

Additionally, the computation is accelerated by distributing the load over several processors via domain decomposition along with an interface interpolation tailored to pass information through each of the domain interfaces to ensure conservation of field variables and derivatives. Numerical results are presented for several cases including channel flow, flow in a channel with a square step obstruction, and a jet flow into a square cavity. Under the same ideas, in [75] and [78], the same procedure is tested in natural-convection heat transfer problems in fully viscous fluid flows.

The meshless procedure developed at UCF has been applied successfully in blood flow problems. In [84], the problem of the improvement of the blood flow or hemodynamic in the synthetic bypass graft end to-side distal anastomosis (ETSDA) is solved. Similarly in [85], the procedure called *Localized Collocation Meshless Method* (LCMM) is improved using a high order upwinding scheme to dampen the numerical oscillation in convection dominated flows. The proposed procedure is validated in the decaying vortex problem and compared with some commercial CFD packages. The validated procedure is used to solve blood flow situations in the

inter-connection between bypass graft and artery. Additionally, in [86], a study is performed to compute the wall shear stress, the spatial and temporal gradients. These two hemodynamic parameters are correlated with endothelial damage.

Other applications of the meshless procedure developed at UCF can be found in [88], in which the problem for determining the rate of heat generation in living tissue is studied. The generation rates of the tissue are then computed by using genetic algorithm optimization. These calculations allow the determination of tumors, infections and other conditions. Moreover, the same procedure has been adapted to compressible flow calculation in turbulent regime ([89] and [90]).

Finally, in [104], [105], [106] and [107], a Model Integrated Meshless Solver (MIMS) is presented, which establishes the method as a generalized solution technique capable of competing with more traditional PDE methodologies (such as the finite element and finite volume methods). This was accomplished by developing a robust meshless technique as well as a comprehensive model generation procedure. Specifically, MIMS implements a blended meshless solution approach which utilizes a variety of shape functions to obtain a stable and accurate iteration process. This solution approach is then integrated with a newly developed, highly adaptive model generation process which employs a quaternary triangular surface discretization for the boundary, a binary-subdivision discretization for the interior, and a unique shadow layer discretization for near-boundary regions.

The same previous procedure has been extended to adaptive grid calculations as for example [108]. As Meshless method solutions require only an underlying nodal distribution, this approach works well even for complex flow geometries with non-aligned domain boundaries. Through the addition of a so-called shadow layer of body-fitted nodes, application of boundary

conditions is simplified considerably, eliminating the stair-casing issues of typical Cartesian-based techniques. A similar idea of RBF with domain decomposition is presented in [233].

In [51], a local radial basis function-based differential quadrature (RBF-DQ) method is developed. In this paper, the weighting coefficients in the spatial derivative approximation of the Euler equation are determined by using a weighted least-square procedure in the frame of RBFs, which enhances the flexibility of distributing points in the computational domain. An upwind method is further introduced to cope with discontinuities by using Roe's approximate Riemann solver for estimation of the inviscid flux on the virtual mid-point between the reference knot and its surrounding knot.

Similarly, in [57] and [58] a symmetric and un-symmetric meshless with RBF is presented with application to unsteady convection equations. For Navier-Stokes, the ghost node strategy is used for the no-slip condition. For large scale problems, the method proposes the creation of clouds of nodes in the local region of the node by means of statistical estimators.

Reference [145] examines the numerical solution of the transient nonlinear coupled Burgers' equations by a Local Radial Basis Functions Collocation Method (LRBFCM) for large values of Reynolds number (Re) up to 103. The time discretization is performed in an explicit way and collocation with the multiquadrics radial basis functions (RBFs) are used to interpolate diffusion-convection variable and its spatial derivatives on decomposed domains.

Under the same ideas, [181] explore the application of the RBF method in the solution of coupled heat transfer and fluid flow problems. Here, derivatives are computed directly by differentiating the RBF functions. The performance of the method is assessed on the classical two dimensional de Vahl Davis steady natural convection benchmark for Rayleigh

numbers from 103 to 108 and Prandtl number 0.71. The results show good agreement with other methods at a given range.

Another application of this RBFCM procedure is found in [183] where, for the first time, the meshless procedure is used for solving the freezing process with convection in the liquid phase for a metals-like material in a closed rectangular cavity.

A variation of the local RBF approach is presented in [309] which discretizes any derivative at a knot by a weighted linear sum of functional values at its neighboring knots, which may be distributed randomly. The proposed method is validated by its application to the simulation of natural convection in a square cavity. Excellent numerical results are obtained on an irregular knot distribution.

The local RBF functions has been also applied to the problem of coupled heat and fluid flow in Darcy porous media [180], where the overlapping sub-domain through multiquadrics RBF collocation. All needed derivatives are computed from those RBF functions. The energy and momentum equations are solved through explicit time stepping. The pressure-velocity coupling is calculated iteratively, with pressure correction, predicted from the local continuity equation violation. The solution procedure is represented for a steady natural convection problem in a rectangular cavity, filled with Darcy porous media.

Another variant of the local RBF idea is given in [310], in which an upwind local RBF differential quadrature scheme is presented for the simulation of inviscid compressible flows with shock wave. The scheme consists of two parts. The first part is to use the local RBF-DQ method to discretize the Euler equation in conservative, differential form on a set of scattered nodes. The second part is to apply the upwind method to evaluate the flux at the mid-point between the reference knot and its supporting knots. The proposed scheme is validated by its

application to simulate the supersonic flow in a symmetric, convergent channel and the shock tube problem.

In [184], the local RBF function collocation scheme is used to solve the case of macrosegregation as a consequence of solidification of a binary Al-4.5%Cu alloy in a two dimensional rectangular enclosure. The phase properties are resolved from the Lever solidification rule, the mushy zone is modeled by the Darcy law and the liquid phase is assumed to behave like an incompressible Newtonian fluid. Double diffusive effects in the melt are modeled by the thermal and solutal Boussinesq hypothesis.

References [179], [182] and [185] show the application of the local RBF approach in the solution of multi-phase thermo-fluid problems. The volume averaged governing equations for mass, energy, momentum and species transfer on the macroscopic level, together with the species transfer on the microscopic level are considered.

As it can be observed, local RBF collocation has many different approaches. An Integrated RBF Network method is developed in [199], [200] and [201]. In [199] and [200], the procedure is explained through the solution of strain localization due to strain softening in quasi-brittle materials. On the other hand, in [201], a numerical collocation procedure, based on Cartesian grids and one-dimensional integrated radial-basis-function networks (1D-IRBFNs) is devised for the simulation of natural convection defined in two-dimensional, multiply connected domains and governed by the stream function-vorticity-temperature formulation. Special emphasis is placed on the handling of vorticity values at boundary points that do not coincide with grid nodes. This technique has been tested for cavity flows [234]. In the case of moving interface problems, the IRBFN method is combined with the level set method to capture the evolution of the interface. The accuracy of the method is investigated by considering several

benchmark test problems, including the classical lid-driven cavity flow. Very accurate results are achieved using relatively low numbers of data points.

A full study of the IRBFN procedure is presented in [229] where this procedure is explained through the solution from linear problems to nonlinear flow situations and unsteady fluid flow calculations.

The problem of energy transport in solid-liquid phase change systems is solved in [337], [338] with an one-domain solving of the non-linear convection-diffusion equation. The collocation is made locally over a set of overlapping domains of influence and the time stepping is performed in an explicit way.

Similarly as in [89], the mesh-free local RBF technique is applied in the simulation of turbulent flow using the low-Re Jones and Launder model. The involved velocity, pressure, turbulent kinetic energy and dissipation fields are represented on overlapping 5-noded sub-domains through collocation by using multiquadrics RBF functions. The pressure-velocity coupling is calculated iteratively, based on the Chorin's fractional step method.

2.6 Other approaches and studies

As expected, there are several additional studies with the meshless technique. In [14], [15], [16], [17], [18] and [19], a novel grid-free upwind relaxation scheme for simulating inviscid compressible flows is presented. The non-linear conservation equations are converted to linear convection equations with nonlinear source terms by using a relaxation system and its interpretation as a discrete Boltzmann equation. A splitting method is used to separate the convection and relaxation parts. Least squares upwinding is used for discretizing the convection

equations, thus developing a grid-free scheme which can operate on any arbitrary distribution of points.

In [122], the stability problem in the analysis of the convection dominated problems using meshfree methods is first discussed through an example problem of steady state convection-diffusion.

A meshless volume approach is presented in [166], [167] and [168] using the Taylor least-squared method. For the stabilization of this meshless procedure, a convective upwind split pressure scheme is proposed. Additionally, the multigrid algorithm is implemented under the idea of multi-cloud scheme.

References [175] and [176] develop a *gridless* approach for boundary condition treatment on a patched and embedded Cartesian field mesh. The gridless boundary treatment is implemented by means of a least squares fitting of the conserved flux variables using a cloud of nodes in the vicinity of the body. The method allows for accurate treatment of the surface boundary conditions without the need for excessive refinement of the Cartesian mesh.

In [230], [231] and [232] the problem of moving interface problems is presented. This situation is known as the passive transport where an ambient flow characterized by its velocity field causes the interfaces to move and deform without any influences back on the flow.

A meshless projection-based technique is presented in [249] using the primitive variables. The number of points required to obtain comparable accuracy is much less than mesh-based methods.

The case of upwinding finite differencing for meshless procedures has been also studied. In [319] a scheme, capable of working on any type of grid (structure, unstructured or even a

random distribution of points) produces superior results. Numerical computations for different types of flow over a wide range of Mach numbers are presented.

Other similar approaches are the development of the upwind least squares finite difference method [320] with implicit time-stepping. The idea of matrix-free implicit procedure in the framework of finite volume solver has been exploited in the present work to obtain a cheap and robust implicit time integration procedure.

A comparison between global RBF and local RBF is done in [361] for three-dimensional parabolic partial differential equations. The local methods show superior efficiency and accuracy, especially for the problems with Dirichlet boundary conditions. Global methods are efficient and accurate only in cases with small amount of nodes. For large amount of nodes, they become inefficient and run into ill-conditioning problems. Local explicit method is very accurate, however, sensitive to the node position distribution, and becomes sensitive to the shape parameter of the RBF function when the mixed boundary conditions are used.

In [368], a least-squares meshfree method (LSMFM) based on the first-order velocity-pressure-vorticity formulation for two-dimensional steady incompressible viscous flow is presented. The discretization of all governing equations is implemented by the least-squares method. The equal-order moving least-squares (MLS) approximation is employed. Gauss quadrature is used in the background cells constructed by the quadtree algorithm and the boundary conditions are enforced by the penalty method. The matrix-free element-by-element Jacobi preconditioned conjugate method is applied to solve the discretized linear systems.

Finally, as usual, there are several other studies in the meshless approach to CFD problems, and some of them are [7], [80], [81], [148], [220], [225], [294] and [295].

CHAPTER THREE

VELOCITY PRESSURE COUPLING

The main objective of any CFD procedure, in the solution of any incompressible flow problem, is to compute velocity and pressure from momentum and continuity equations. This set of equations is quite simple, but unfortunately, there is no explicit equation for pressure. The development of a robust procedure able to compute velocity and pressure from those incompressible flow equations, is called *velocity-pressure coupling problem*.

The so-called segregated procedure, initially devised in 1965 by Harlow and Welch [128], has played a fundamental role in the development of the Computational Fluid Dynamics science as it is known today. Basically, the segregated procedure manipulates momentum and continuity equation to obtain an explicit equation for pressure. Additionally, mass balance is enforced via the Helmholtz decomposition.

Since the velocity-pressure coupling is the fundamental procedure in the solution of any incompressible flow problem, it is convenient to review it in order to identify the possible sources of numerical error.

3.1 The projection method of Harlow and Welch

This coupling procedure [128] solves velocity and pressure in a segregated way:

a) Solve velocity with momentum equation:

$$\mu \nabla^2 \vec{v} - \rho (\vec{v} \cdot \nabla) \vec{v} - \frac{\partial \vec{v}}{\partial t} = \nabla p + \rho \vec{g} \quad (1)$$

Compute pressure by taking the divergence of (1):

$$\nabla^2 p = -\rho \nabla \cdot [(\vec{v} \cdot \nabla) \vec{v}] \quad (2)$$

b) Enforce mass continuity through Helmholtz decomposition:

$$\vec{v} = \vec{v}^* + \vec{v}' \quad \vec{v}' = \nabla \varphi \quad \nabla^2 \varphi = -\nabla \cdot \vec{v}^* \quad (3)$$

This segregated method of coupling velocity and pressure is easy to implement and to parallelize. It is very important to remember that almost all segregated procedures, in differential form or integral form, are based on this idea.

3.2 The pressure equation in highly stretched grids

Let's assume that we have a uniform grid in the problem of 2D flow in parallel plates (laminar or turbulent). In order to save computing resources, points in the direction of the flow are very stretched with respect to the points in the vertical direction.

Using the projection method of Harlow and Welch, if x is the direction of the flow, and the spacing in both directions is related to a constant C , the discretized equation (2) becomes:

$$\frac{1}{C^2 \Delta^2} (p_W - 2p_P + p_E) + \frac{1}{\Delta^2} (p_S - 2p_P + p_N) = b(\vec{v}) \quad (4)$$

For DNS and LES simulations, the constant C can reach values from 100 to 250. This issue makes the first term of Eq. (4) negligible, and the equation becomes equivalent to:

$$\frac{\partial^2 p}{\partial y^2} = -\rho \nabla \cdot [(\vec{v} \cdot \nabla) \vec{v}] \quad (5)$$

which is wrong since, for parabolic flows: $\partial^2 p / \partial x^2 \gg \partial^2 p / \partial y^2$. Even more, boundary conditions for pressure at the wall or at the line of symmetry imply that Eq. (5) has to be solved with $\partial p / \partial y = 0$ at both boundaries (or a normal derivative very closed to zero at the wall). This resulting linear system of equations is singular (or nearly singular).

This huge unbalance of coefficients explains why pressure equation takes usually 90% of computing time in DNS or LES calculations when the problem is the solution of a simple linear equation. For example, in [151] and in many publications, it is outlined that a good tri-diagonal solver is required to solve efficiently Eq. (4). The problem is not the solver, which is just one well known procedure. The problem is that the system of equations (4) has a severe structural problem.

Paradoxically, in the momentum equations, the large aspect ratio favors the terms in the opposite direction of the main flow (i.e. diffusion terms, which produce pressure drop) with the immediate counterpart in the pressure gradient in the direction of the flow. This feature explains why the solution of the momentum equation is not a problem.

3.3 Boundary conditions for pressure equation

When solving pressure equation on a collocated grid arrangement, boundary conditions must be supplied. The straightforward approach is to extract information from the same momentum equation by projecting it in a given direction:

$$\frac{dp}{dn} = \hat{n} \cdot [\mu \nabla^2 \vec{v} - \rho (\vec{v} \cdot \nabla) \vec{v} + \rho \vec{g}] \quad (6)$$

$$\frac{dp}{ds} = \hat{s} \cdot [\mu \nabla^2 \vec{v} - \rho (\vec{v} \cdot \nabla) \vec{v} + \rho \vec{g}] \quad (7)$$

with \hat{n} and \hat{s} the normal and tangent unit vector to any specific boundary. At walls, velocity field is zero, and the pressure derivative is described by the diffusion term.

This condition may produce problems at inflows in the case, for example, that any inflow velocity profile is supplied and the velocity is zero everywhere else (typical condition to start an iteration). If the inflow is in the x-direction, the convective term $u \partial u / \partial x$ is negative, the diffusion term is negative but it is not large enough for the total result to be negative (the expected pressure gradient).

This issue produces a positive pressure gradient, forcing (numerically) the fluid to flow in negative x-direction. On the other hand, boundary conditions for velocity force the fluid to flow in the positive direction, resulting in no convergence.

One way to remedy this problem is by using the continuity equation to modify the convection terms. For a 2D flow, this means:

$$\frac{dp}{dn} = \hat{n} \cdot \left[\mu \nabla^2 \vec{v} - \rho \left(-u \frac{\partial v}{\partial y} + v \frac{\partial u}{\partial y} \right) + \rho \vec{g} \right] \quad (8)$$

$$\frac{dp}{ds} = \hat{s} \cdot \left[\mu \nabla^2 \vec{v} - \rho \left(-u \frac{\partial v}{\partial x} + v \frac{\partial u}{\partial x} \right) + \rho \vec{g} \right] \quad (9)$$

Now, all convection terms are expressed in products of main velocity and tangent velocity components. Since most frequent inflow conditions specify the main velocity with a zero tangent velocity, pressure gradient in the boundary will be governed by the diffusion term only and the right value will be obtained immediately.

3.4 Convergence through divergence-free velocity field

The main idea behind the projection method is that mass continuity, or divergence-free velocity field, is enforced with successive corrections, based on the Helmholtz decomposition as described in Equation (3).

Since velocity correction is expressed in terms of a velocity potential, boundary conditions are necessary to solve the Poisson equation (3):

$$\text{Inflows and walls: } \vec{v}' = \vec{0} \Rightarrow \nabla \varphi = \vec{0} \quad (10)$$

$$\text{Outflows: } (\hat{n} \cdot \nabla) \vec{v}' = 0 \Rightarrow (\hat{n} \cdot \nabla) \nabla \varphi = 0 \quad (11)$$

Clearly, since for walls and inflows, there are more equations than unknowns, solution of Equation (3) with boundary conditions (10)-(11) has no solution, unless a minimization procedure is used. It is convenient to remember that most minimization methods are linearly convergent, making this approach too slow and expensive for DNS/LES simulations. Because of this problem, typical simplifications are used, as explained in Table 1.

Table 1: Simplified boundary conditions for Equation (3)

Boundary Condition	Projection [128]
Inflow	$\frac{d\phi}{dn} = 0$
Wall	$\frac{d\phi}{dn} = 0$
Outflow	$\phi = 0$

The condition $d\phi/dn=0$ in the wall means $\vec{v}' \cdot \hat{n} = 0$, that is, do not correct the tangent component of the velocity field; correct only the main velocity component. Enforcing mass continuity by correcting only the component of the direction of the flow is correct in parabolic flows, where the tangent component of the velocity field is just a small percentage of the main velocity.

For elliptic flows, boundary conditions in Table 1 are incorrect because, in the most general case, there is no way to know in advance the fraction that each component must be corrected. For complex flows, if a grid fine enough is used, the first nodes (in the tangent direction from the wall) are going to be located in the boundary layer, so that the parabolic flow assumption is valid.

In order to understand the effect of the boundary conditions in Table 1, let's take a look at a horizontal wall. The condition $\partial\phi/\partial n = 0$ means $\partial\phi/\partial y = 0$, and that implies $v' = 0$ and $u' \neq 0$. Substituting in momentum equation, the perturbation produced in the pressure gradient at the wall is:

$$\begin{aligned} \frac{1}{\rho} \frac{\partial p'}{\partial x} &= \nu \nabla^2 u' - \frac{\partial u'}{\partial t} - u' \frac{\partial u'}{\partial x} \\ \frac{1}{\rho} \frac{\partial p'}{\partial y} &= \nu \nabla^2 v' \end{aligned} \quad (12)$$

which is correct except for the term $\partial u'/\partial t + u' \cdot \partial u'/\partial x$. If the flow is not parabolic, the additional term may produce a wrong pressure gradient in the direction of the wall.

The problem of boundary conditions for the mass-enforcement equation explains why all Finite-Volume based procedures have problems when the velocity is not normal to the faces of every control volume or when the flow is not absolutely parabolic.

3.5 SIMPLE-based procedures

The finite volume method proposed by Patankar [264], with SIMPLE and SIMPLER techniques as velocity-pressure coupling procedures, is the most popular method in CFD. These coupling schemes are used in most commercial and noncommercial CFD packages, using finite volume, finite difference or finite element method as the main discretization procedures.

However, these coupling procedures are known to produce significant numerical diffusion. The most general procedure (SIMPLER) can be resumed as:

- a) Discretize momentum equation:

$$\hat{p} = \frac{p}{\rho} - \vec{r} \cdot \vec{g} \quad \vec{\tilde{v}}_p = \frac{1}{a_p} \sum a_{nb} \vec{v}_{nb} \quad \vec{v}_p = -\vec{\tilde{v}}_p + \frac{1}{a_p} \nabla \hat{p} \quad (13)$$

- b) Compute pressure by introducing (13) into continuity equation:

$$\nabla \cdot \left(\frac{1}{a_p} \nabla \hat{p} \right) = \nabla \cdot \vec{\tilde{v}}_p \quad (14)$$

- c) Update pressure in Eq. (13) and solve for velocity.

- d) Correct velocity to enforce mass continuity:

$$\vec{v} = \vec{v}^* + \vec{v}' \quad \hat{p} = \hat{p}^* + \hat{p}' \quad (15)$$

$$\vec{v}' = -\vec{\tilde{v}}' + \frac{1}{a_p} \nabla \hat{p}' \quad \nabla \cdot \left(\frac{1}{a_p} \nabla \hat{p}' \right) = -\nabla \cdot \vec{v}^* + \nabla \cdot \vec{\tilde{v}}' \quad (16)$$

where the term $\nabla \cdot \vec{\tilde{v}}'$ is frequently neglected.

The first comment that it is convenient to make to this procedure is that, the main coefficient a_p is inside all partial derivatives in pressure and mass-enforcement equations. The structure of this coefficient is:

$$a_p = \nu C_L - u_p C_{DX} - v_p C_{DY} \quad (17)$$

with C_L , C_{DX} and C_{DY} the coefficients of finite-differencing schemes. For a non uniform mesh, the coefficient a_p is a function of the position. This coefficient will produce clearly numerical diffusion in equations (14) and (16).

The only way that equations (14) and (16) will not produce numerical diffusion is with a mesh of constant spacing and using central differencing in convection terms. Since a_p gathers the diffusion and convection terms, central differencing for convection derivative will not have any coefficient. With a uniform mesh, the diffusion term of \vec{v} is zero and the Eq. (16) becomes exactly the same equation (3). Similarly, with a mesh of uniform spacing, Eq. (14) becomes the same equation (2).

By updating velocity in SIMPLER, the procedure becomes the same algorithm of Harlow and Welch, but in SIMPLE, updating pressure with p' is updating pressure with the velocity potential. This explains why SIMPLE takes so many iterations to converge and why this procedure works only when velocity is corrected and not pressure (as initially inferred).

Another problem that SIMPLE and SIMPLER have is, in pressure equation (14), boundary conditions (pressure coefficient zero in all boundaries) imply that the viscosity of the fluid is infinite at the wall, inflows and outflows.

The condition of viscosity infinite is correct at the wall but, at inflows and outflows is evidently incorrect. At inflows, this numerical change in the viscosity of the fluid produces a force that helps the motion of the fluid but, at outflows, this change in viscosity produces a force that decelerates the fluid. This is one reason why pressure equation (14) converges usually very

slowly, unless a block-correction or multigrid algorithm is used. One way to correct this problem is by changing the outflow condition to normal derivative zero of pressure coefficient, but of course, numerical diffusion will be present anyway.

3.6 Streamline-vorticity formulation

A popular technique used in 2D flows is the streamline-vorticity formulation. The advantage is that no pressure has to be computed and the streamline function satisfies automatically the continuity equation. The streamline and vorticity are related to velocity by:

$$u = \frac{\partial \phi}{\partial y} \quad v = -\frac{\partial \phi}{\partial x} \quad \omega = \frac{\partial v}{\partial x} - \frac{\partial u}{\partial y} \quad (18)$$

Taking the curl to the momentum equation and expressing the definition of vorticity in terms of the streamlines, the flow equations to be solved is now:

$$\begin{aligned} \nabla^2 \phi &= -\omega \\ \frac{\partial \omega}{\partial t} + \frac{\partial \phi}{\partial y} \frac{\partial \omega}{\partial x} - \frac{\partial \phi}{\partial x} \frac{\partial \omega}{\partial y} &= \nu \nabla^2 \omega \end{aligned} \quad (19)$$

The system of equation (19) does not look complicated to solve. The problem arises when trying to set boundary conditions for both, streamline and vorticity. For the case of the wall, the exact boundary conditions are:

$$\frac{\partial \phi}{\partial x} = \frac{\partial \phi}{\partial y} = 0 \quad (20)$$

which makes the problem over-determined again. Studying the implementations of [6], [22], [65], [91], [92], [118], [213], [274], [301], [318] and [347], the boundary condition at the wall for the streamlines is frequently $\varphi_{WALL} = 0$, which implies that the normal velocity (to the wall)

is zero but the tangent velocity is not. This simplification violates the no-slip condition. For the vorticity, a series expansion is developed assuming $\partial\phi/\partial n = 0$, and it is equivalent to say:

$$\nu \nabla^2 \omega = \frac{\partial \omega}{\partial t} - \frac{\partial \phi}{\partial x} \frac{\partial \omega}{\partial y} \quad (21)$$

at the wall. The expression (21) is correct except for the last term, that it is not necessarily imposed to be zero in the series expansion. This additional term may produce an incorrect motion very closed to the wall if the flow is not parabolic.

3.7 Fractional-Step method of Kim and Moin

The fractional-step method of Kim and Moin [173] is very popular in DNS and LES since provides a simple procedure for time integration without using any explicit ODE method. Basically, the method consists of several steps:

$$\begin{aligned} \frac{\bar{v}^* - \bar{v}^n}{\Delta t} &= \frac{1}{2} [3\bar{C}^n - \bar{C}^{n-1}] + \frac{1}{2} [\bar{D}^* + \bar{D}^n] \\ \nabla^2 p^{n+1} &= \frac{\rho}{\Delta t} \nabla \cdot \bar{v}^* \\ \frac{\bar{v}^{n+1} - \bar{v}^n}{\Delta t} &= -\frac{1}{\rho} \nabla p^{n+1} \end{aligned} \quad (22)$$

where \bar{C}^n and \bar{D}^n are the corresponding convection and diffusion terms of the Navier-Stokes equations, evaluated at the current time step n . By combining the equations in (22), the following expression is obtained:

$$\frac{1}{\rho} \nabla^2 p^{n+1} - \frac{2\Delta t}{\rho} \nabla^4 p^{n+1} = \frac{1}{2} \nabla \cdot [3(\bar{v}^n \cdot \nabla) \bar{v}^n - (\bar{v}^{n-1} \cdot \nabla) \bar{v}^{n-1}] \quad (23)$$

The first consideration in equation (23) is that the second term of the left-hand-side is negligible only if the pressure gradient is small, usually in parabolic flows. The second aspect is that, from the analysis performed in the projection method, equation (23) does not guarantee mass balance since is basically the derivative of the momentum equation.

Of course, the system (23) can be complemented with the same mass-correction procedure as in the projection method, but the scheme will have the same inconvenient as all SIMPLE-based methods. Additionally, the boundary condition $\vec{v}^* = \vec{v}^n$ means that:

$$4(\dot{v}^n \cdot \nabla)\dot{v}^n - (\dot{v}^{n-1} \cdot \nabla)\dot{v}^{n-1} + \frac{\partial \dot{v}^n}{\partial t} + \frac{1}{\rho} \nabla p^n = 0 \quad (24)$$

which is not true. Moreover, at the wall, expression (24) implies that $\nabla p|_{WALL} = 0$, exactly the same boundary condition of all SIMPLE-based methods. Finally, writing the equation for pressure in terms of the coefficients we have:

$$\begin{aligned} \frac{\Delta t}{\rho} \nabla^2 p^{n+1} = \nabla \cdot \left\{ \frac{2}{a_p^D - 2} \left[-\frac{1}{2} \sum a_{nb}^D \vec{v}_{nb}^* + \frac{3}{2} \left(a_p^{Cn} \vec{v}_p^n + \sum a_{nb}^{Cn} \vec{v}_{nb}^n \right) \right. \right. \\ \left. \left. - \frac{1}{2} \left(a_p^{Cn-1} \vec{v}_p^{n-1} + \sum a_{nb}^{Cn-1} \vec{v}_{nb}^{n-1} \right) + \frac{1}{2} \left(a_p^D \vec{v}_p^n + \sum a_{nb}^D \vec{v}_{nb}^n \right) \right] \right\} \end{aligned} \quad (25)$$

which has a lot of numerical diffusion. The only way to reduce the numerical errors is using a uniform grid and discretizing the convection terms with a central finite-differencing scheme.

3.8 The full coupled procedure

The most straightforward way to solve the equations of motion, on a collocated grid, is by solving the discrete linear system, say momentum and continuity, with a sparse matrix solver. The fact that there is no pressure term in the continuity equation makes the condition number of that full system closed to infinity.

Additionally, the amount of resources needed to solve a sparse linear system of several millions of equations is prohibitive in 3D simulations. One way to reduce the huge computational resources needed in this problem is dividing the entire region in small blocks or sub-domains.

In a given block, the linear system of equations to be solved can be written as, in 2D (\bar{p} is a vector containing the pressure in all grid points):

$$\mathbf{A}\bar{u} + \mathbf{B}\bar{p} = \mathbf{b}^u \quad \mathbf{A}\bar{v} + \mathbf{C}\bar{p} = \mathbf{b}^v \quad \mathbf{D}\bar{u} + \mathbf{E}\bar{v} = 0 \quad (26)$$

If boundary conditions are excluded, in every sub-domain, a pressure equation can be obtained by simple matrix manipulation:

$$(\mathbf{D}\mathbf{A}^{-1}\mathbf{B} + \mathbf{E}\mathbf{A}^{-1}\mathbf{C})\bar{p} = \mathbf{D}\mathbf{A}^{-1}\mathbf{b}^u + \mathbf{E}\mathbf{A}^{-1}\mathbf{b}^v \quad (27)$$

where it is necessary to invert one diagonal dominant matrix with all main diagonal coefficients non zero and consequently, a very low condition number.

3.9 A local direct coupling procedure

A useful alternative that solves the problems associated to both segregated and direct full coupling procedures can be found in [340]. This scheme uses the segregated grid arrangement in the same way as finite volume method as seen in Figure 1.

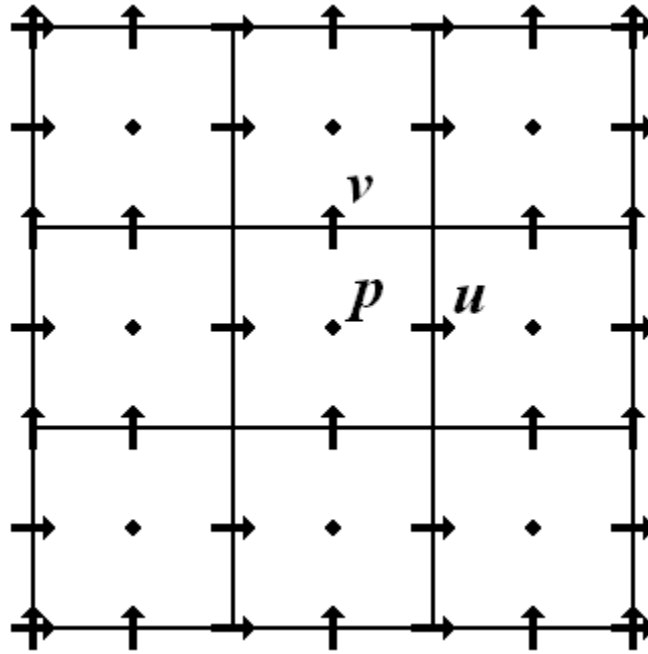


Figure 1: Staggered grids for u , v and p in a system of 3x3 volumes

The fundamental aspect of this scheme is that the velocity - pressure coupling procedure, done with the momentum and continuity equations in the original form, for example in 2D steady state this means:

$$\begin{aligned}
 u \frac{\partial u}{\partial x} + v \frac{\partial u}{\partial y} &= -\frac{\partial p}{\partial x} + \frac{1}{Re} \left(\frac{\partial^2 u}{\partial x^2} + \frac{\partial^2 u}{\partial y^2} \right) \\
 u \frac{\partial v}{\partial x} + v \frac{\partial v}{\partial y} &= -\frac{\partial p}{\partial y} + \frac{1}{Re} \left(\frac{\partial^2 v}{\partial x^2} + \frac{\partial^2 v}{\partial y^2} \right) \\
 \frac{\partial u}{\partial x} + \frac{\partial v}{\partial y} &= 0
 \end{aligned} \tag{28}$$

After substituting expressions of finite differences in the staggered grid arrangement shown in Figure 1, the system of equation (28) can be expressed as:

$$\begin{aligned}
 a_p^u u_p + C_p^u (p_p - p_E) &= b_p^u \\
 a_p^v v_p + C_p^v (p_p - p_N) &= b_p^v \\
 D_p^u (u_p - u_W) + D_p^v (v_p - v_S) &= 0
 \end{aligned} \tag{29}$$

With the system (29), the coupling of u , v and p is performed by writing, in all possible ways, a linear system of 3 equations of the kind:

$$\begin{pmatrix} a_{11} & 0 & a_{13} \\ 0 & a_{22} & a_{23} \\ a_{31} & a_{32} & 0 \end{pmatrix} \begin{pmatrix} u \\ v \\ p \end{pmatrix} = \begin{pmatrix} b_1 \\ b_2 \\ b_3 \end{pmatrix} \tag{30}$$

whose solution is:

$$\begin{pmatrix} u \\ v \\ p \end{pmatrix} = \begin{pmatrix} \frac{a_{23}a_{32}b_1 - a_{13}a_{32}b_2 + a_{13}a_{22}b_3}{a_{11}a_{23}a_{32} + a_{31}a_{13}a_{22}} \\ \frac{-a_{23}a_{31}b_1 + a_{13}a_{31}b_2 + a_{11}a_{23}b_3}{a_{11}a_{23}a_{32} + a_{31}a_{13}a_{22}} \\ \frac{a_{22}a_{31}b_1 + a_{11}a_{32}b_2 - a_{11}a_{22}b_3}{a_{11}a_{23}a_{32} + a_{31}a_{13}a_{22}} \end{pmatrix} \tag{31}$$

Having in mind the linear system (30) and its solution (31), the discretized system (29) may be rearranged in many different ways, as shown in Table 2 and Figure 2.

Table 2: Sequence of sweeps for a 2D calculation

Case	X direction	Y direction
1	Positive	Positive
2	Positive	Negative
3	Negative	Negative
4	Negative	Positive

This scheme was successfully tested in 3D turbulent flows using the $k - \varepsilon$ model of Launder-Sharma (see [340] for more details).

Another advantage of this procedure is the memory required to solve the linear system that arises after discretization of the hydrodynamic system.

For example, in 3D flows, using SIMPLER method [264], it is necessary to store all coefficients of all momentum equations including the pressure coefficients. Furthermore, coefficients for pressure equation are needed and 3 more matrices are necessary to store all pseudo-velocities. Pressure correction equation uses the same coefficients that the pressure equation, so no additional space is needed. All this makes that SIMPLER method needs 38 arrays to perform any iteration.

This approach needs the same 9 arrays per momentum equation plus another 3 to store the coefficients of the continuity equation, making a total of 30 arrays, representing always about 27% less computer memory than SIMPLER. In 2D flows, the comparison gives 24 arrays for SIMPLER versus 16 arrays needed for this method.

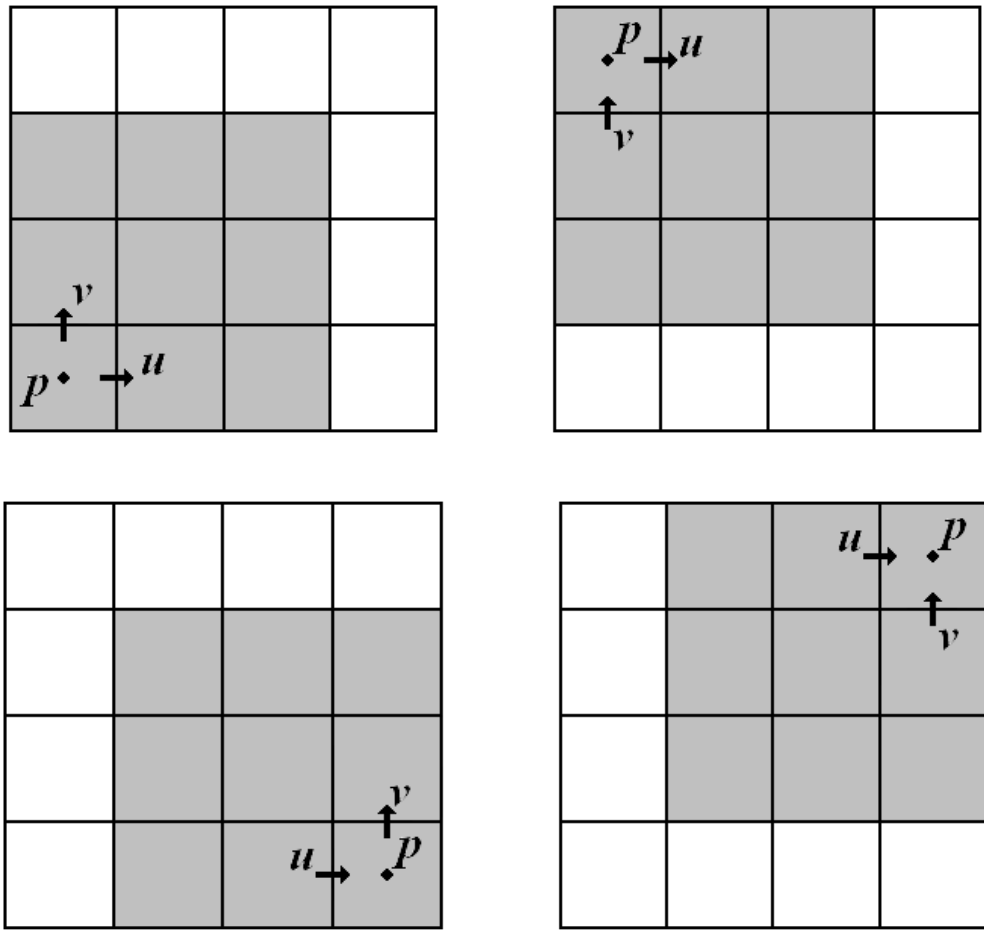


Figure 2: Coupling schemes and volumes involved in a 4x4 volumes 2D region

CHAPTER FOUR

ADDITIONAL SCHEMES/PROCEDURES

The velocity-pressure coupling alone is obviously not the only numerical issue to be solved in DNS or LES. There are some other aspects where a lot of care must be taken in order to have a robust numerical procedure.

4.1 Convection discretization

From the computational point of view, DNS and LES simulations are quite challenging problems due to the huge amount of calculations involved as a result of a long term integration process, where a lot of detail is necessary in order to have a good description of the phenomena. The choice of a suitable convection scheme is crucial to keep numerical errors in a reasonable level. These numerical errors come mainly from two sources: numerical dissipation and order of accuracy.

Numerical dissipation can be kept very low by using central differences, as in [101], [196], [251], and [339] for DNS and [113], [126], [170], [221], [330], [335], [363] for LES. However, if the grid has a very large aspect ratio (i.e. 100-250), central differencing schemes become unstable. Upwind schemes are stable for any aspect ratio, but they induce numerical dissipation in large gradients [96]. Although, a successful example of DNS over a flat plate, where a 5th order upwind scheme is used, can be found in [360]. On the other hand, LES calculations with central differencing can be seen in [113], [126], [221], [353], [360], and [363].

As an exception, in [170] a 3rd order upwind method was successfully used to solve DNS with heat transfer over a backward-facing step.

One intermediate alternative to the inconvenient of upwinding and centered procedures can be a biased-scheme, but the resulting discrete equation has the same stability problems than the central differencing procedure.

With respect to the order of the differencing scheme, in [151] is outlined that, at least 4th order is acceptable for DNS calculations, while 2nd order is acceptable for LES. The use of a 4th order centered scheme is more time-consuming and it is frequently unstable since the discretized equations have some complex eigenvalues, the main source of instabilities. One solution can be found with 4th order compact schemes. Compact schemes reduce calculation time with respect to non compact ones, but they are not easy to implement due to the implicit nature of the procedure, and that they are limited to structured grids and explicit evaluation of the derivative.

One way to solve the problem of the order of discretization is using a very accurate procedure, like spectral or pseudo-spectral methods, as in [135], [154], [161], [211], [241], [248], [259], [276], and [331]. These methods are limited to simple geometries with periodic boundaries. The typical benchmark problem to evaluate the ability of any convection scheme is [96]:

$$\nu \frac{\partial^2 \varphi}{\partial x^2} - U \frac{\partial \varphi}{\partial x} = 0 \quad \varphi(0) = 0 \quad \varphi(1) = 1 \quad (32)$$

whose analytical solution is:

$$\varphi(x) = \frac{e^{Bx} - 1}{e^B - 1} \quad B = \frac{U}{\nu} \quad (33)$$

With $B = 100$, writing the discretized equations in terms of a local Reynolds number, $Re = U\Delta x/\nu$, and using second order central differences for the diffusion term, in Figure 3 there

is a comparison of three typical convection schemes with a local Reynolds number equal to 5. As expected, upwind scheme is dissipative, second order centered scheme is unstable but, 4th order compact scheme (described in [151]) is unstable too. This issue could explain why compact schemes are not frequently used in parabolic flows, where stretched grids are necessary to save computing resources.

Unfortunately, there is not enough information in the literature to make a full diagnosis of the best choice between upwind/central/compact differencing scheme and order of the method, since most papers never give details of the convection discretization scheme that they used.

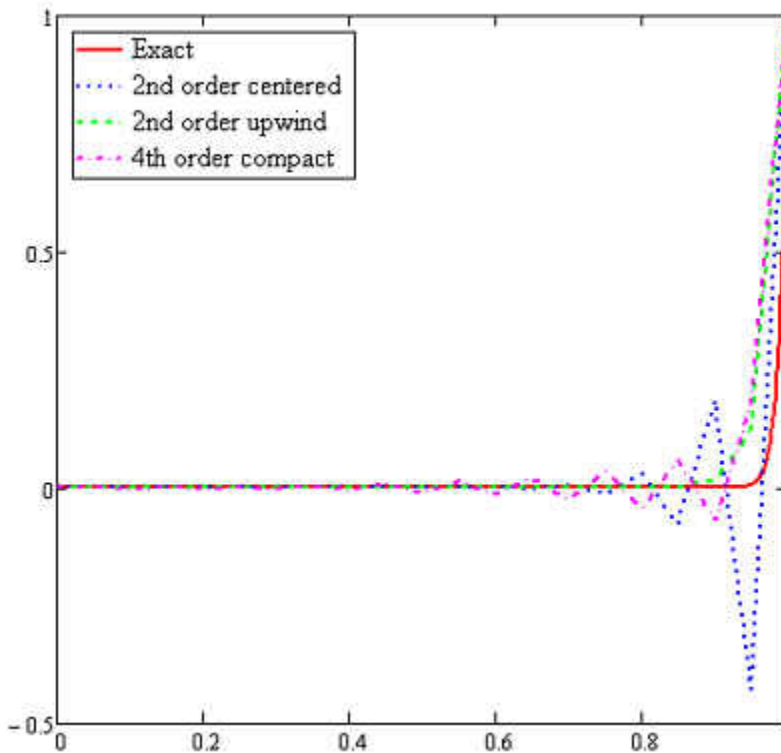


Figure 3: Solutions to (32) with $Re = 5$ (classic schemes)

Another alternative, quite popular in the solution of the Euler equations and in the simulation of compressible flows is the technique of flux limiters.

The main idea behind the construction of flux limiters is to limit the convection derivative to realistic values [369] using a combination of low resolution and high resolution schemes. Consider the scalar advection equation:

$$\frac{d\varphi}{dt} + \frac{d(U\varphi)}{dx} = 0 \quad (34)$$

The core idea is to discretize the x-derivative in (34) in the form of the subtraction of the fluxes in the two adjacent faces or mid-points:

$$\frac{d\varphi}{dt} + \frac{1}{\Delta x} [U_e \varphi_e - U_w \varphi_w] = 0 \quad (35)$$

The value of the field variable in any face f will be computed depending on the sign of the velocity:

$$\begin{aligned} U_f > 0 &\Rightarrow r = \frac{\varphi_E - \varphi_W}{\varphi_W - \varphi_{WW}} \Rightarrow \varphi_f = \varphi_W + \frac{1}{2} \phi(r) (\varphi_W - \varphi_{WW}) \\ U_f < 0 &\Rightarrow r = \frac{\varphi_W - \varphi_E}{\varphi_E - \varphi_{EE}} \Rightarrow \varphi_f = \varphi_E + \frac{1}{2} \phi(r) (\varphi_E - \varphi_{EE}) \end{aligned} \quad (36)$$

where the sub-indices WW, W, E and EE are relative to the corresponding faces, not the nodes in the grid.

Here, $\phi(r)$ is the flux limiting function (or flux limiter) and it depends on the ratio of consecutive values in the mesh (downwards or upwards). There are many proposals with different characteristics but, unfortunately, no particular limiter has been found to work for all cases. Some limiters can be found in [59], [60], [205], [206], [282] and [326]. For example, two popular limiters are the Superbee and Osher limiters [282]:

$$\phi_{Osher(r)} = \max[0, \min(r, \beta)] \quad 1 \leq \beta \leq 2 \quad (37)$$

$$\phi_{Superbee}(r) = \max[0, \min(2r, 1), \min(r, 2)] \quad (38)$$

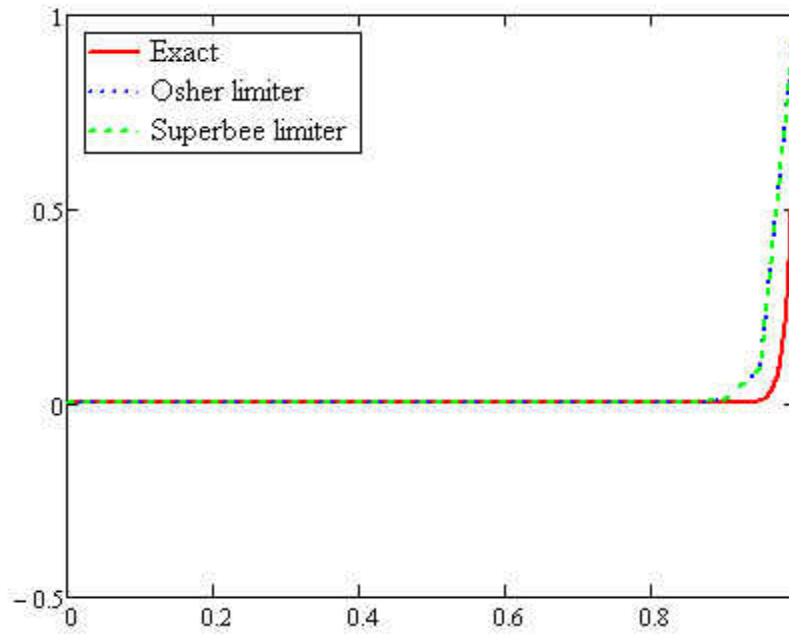


Figure 4: Solutions to (32) with $Re = 5$ (flux limiters)

As observed in Figure 4, there is a considerable improvement in the results for a local Reynolds of 5 and the same amount of points. These results imply a low numerical diffusion and this is the recommended approach for LES simulations in some software packages as Fluent and Open Foam.

4.2 Time integration schemes

As expected, if a simulation of turbulent flow is desired, the momentum equation must be integrated in time (additional to space). In the numerical point of view, time integration is a typical Initial Value Problem (IVP). In DNS and LES, time integration is performed with the same methods for ordinary differential equations.

First of all, time integration algorithms depend on the coupling scheme used. For example, in the segregated approach, all variables have an independent equation, and the procedure can be seen as a system of Ordinary Differential Equations (ODE) of first order. On the other hand, the direct coupled approach, that is, by solving the momentum and continuity equation is a typical Differential Algebraic Equation (DAE) since continuity equation ($\nabla \cdot \vec{v} = 0$) does not have time derivative.

Now, time integration schemes can be divided in implicit and explicit. Explicit schemes, such as Runge-Kutta and Adams-Bashford, are very fast for long term integration, but they have stability conditions that must be met in order to give a physical solution. On the other hand, implicit methods, such as Implicit-Runge-Kutta, Adams-Moulton or BDF, are much more stable, but they are very expensive since the solution of a non linear system is required in every time step.

At the same time, explicit schemes are divided in one step methods and multistep methods. One step methods, such as Runge-Kutta of 2nd, 3rd and 4th order, are very popular in DNS and LES because they are stable, easy to parallelize and they represent a good compromise of accuracy and computing time. Runge-Kutta methods of order greater than 5 are rarely used because they require more function evaluations than the order of the method, and this issue is

expensive for long term integration. Navier-Stokes equations are considered [151] expensive in the scope of IVP. For direct simulation of compressible flows, Runge-Kutta is a good choice to describe correctly shock waves. A cheaper alternative to long term integration with an explicit scheme are the multistep methods, such as Adams-Bashford, has usually half of the function evaluations than a typical Runge-Kutta.

Implicit methods are used normally in stiff differential equations and in DAE. They imply the solution of a nonlinear system (in the general case), they are more robust but at a higher computing cost. Typical approaches are the multistep methods Adams-Moulton and Backward-Differentiation Formulas (BDF).

A very important issue is that explicit time integration schemes have a limited stability region, forcing the delta time (used in the integration) be limited to a certain maximum value. In some cases, the time increment may be severely small. On the other hand, stability region of implicit methods is considerable larger.

For the specific case of DNS and LES simulations the time integration scheme depends on the velocity-pressure coupling procedure chosen.

If the segregated approach is used, a good alternative can be the explicit methods as Runge-Kutta. Multistep methods such as the predictor/corrector Adams Bashford/Adams Moulton can be used separately for convection and diffusion terms respectively.

Finally, if the direct approach is chosen, the only alternative is the implicit approach. Here, perhaps the best choice is the BDF method since it has a larger stability region than its counterpart Adams-Moulton.

4.3 Interpolation

Independent of the location of the variables in the grid, interpolation is a mandatory procedure. For example, collocated grid arrangement (all variables located at the same place) needs interpolation for the mass balance equation. Here the bilinear interpolation produces nonphysical oscillations and some nonlinear interpolation schemes have been proposed with great success, as for example [279].

On the other hand, the segregated approach, where velocity components and pressure are located at different positions, needs interpolation for the convection terms. In this case, bilinear interpolation has been widely used since is much more stable and provides faster convergence.

For many practical situations in engineering, the quality of the interpolation is not fundamental for the validity of the results. Unfortunately, for DNS/LES simulations, is convenient to pay more attention in the accuracy of the interpolation scheme.

For example, in [77] and [104] a Radial-Based Function (RBF) procedure is chosen to perform all interpolations. In this procedure, RBF is used basically to compute the coefficients of all derivatives without the use of a connectivity mesh. It is convenient to underline that RBF interpolation has a spectral error.

For all collocation methods, the underlying nodal influence can be expressed in the form of a set of weights multiplied by a set of nodal values. For any variable, this means that any derivative will be expressed in the form:

$$\frac{\partial \varphi}{\partial x_j} = \sum_{i=1}^{NF} a_{i,j} \varphi_i \quad (39)$$

with NF the number of neighboring points or influence points. Localized Radial Basis Function (RBF) begins with the principle that any arbitrary domain Ω can be interpolated over by collocating a number of points with some basis function χ . The field ϕ is then represented by multiplying the basis functions by a set of expansion coefficients where, for stability reasons, a series of NF polynomial functions $P_k(\vec{x})$ are added to the interpolation scheme:

$$\varphi(\dot{x}) = \sum_{j=1}^{NF} \alpha_j \chi_j(\dot{x}) + \sum_{k=1}^{NP} \alpha_{k+NF} P_k(\dot{x}) \quad (40)$$

With respect to the basis function, the most accurate and stable one belongs to the group of Inverse Hardy Multiquadrics, which is of the form:

$$\chi_j(\vec{x}) = \frac{1}{\sqrt{r_j(\vec{x})^2 + c^2}} \quad (41)$$

where $r_j(\vec{x})$ is the Euclidean distance. At this moment, there is no unique way to determine the parameter c so different formulations are employed. The expansion coefficients are then computed by writing Eq. (40) in every neighboring point and solving the corresponding linear system:

$$[G] \vec{\alpha} = \vec{\varphi} \quad (42)$$

By substituting (42) in (40), a general interpolation scheme is obtained:

$$\varphi(\dot{x}) = \sum_{i=1}^{NF} \left[\chi_i(\dot{x}) \left(\sum_{j=1}^{NF} G_{i,j} \varphi_j \right) \right] \quad (43)$$

expression that can be written as:

$$\varphi = \sum_{i=1}^{NF} b_i \varphi_i \quad (44)$$

The calculation procedure (40)-(43) must be preceded by a proper selection of the free parameter c . Practice has showed that the best results are obtained when the condition number of the matrix G in equation (42) is between 10^0 and 10^2 .

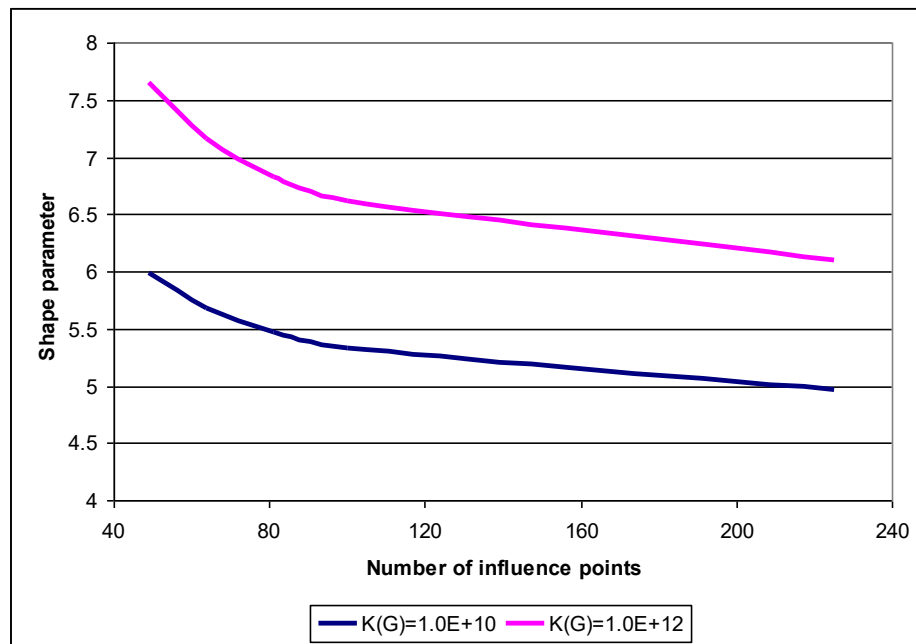
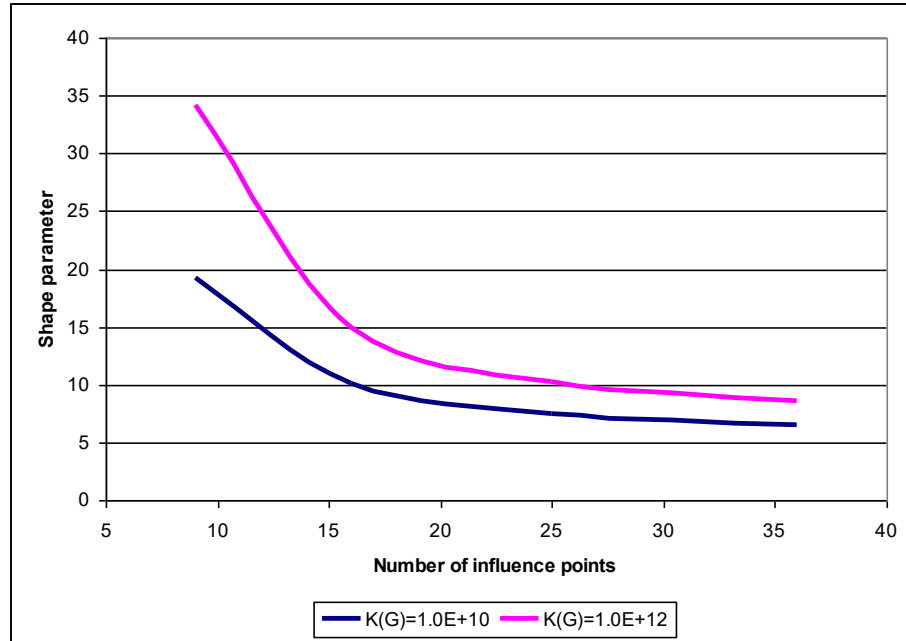


Figure 5: Range of shape parameter c vs. the number of influence points

Figure 5 shows the range of the shape parameter as a function of the number of influence points for a 2D uniform distribution with the interpolation point located exactly in the geometric center. The blue line is the condition number of 10^{10} while the violet line represents the condition number of 10^{12} . For a number of influence points larger than 30, the variation of the shape parameter is very small. This feature is convenient in the design of a searching strategy of the optimum value without an excessive computational cost.

It is important to underline that the calculation of the optimum shape parameter can be very expensive if we don't take a look to some details. First, the way the polynomial expansion is written may affect the final condition number. After some experiments, it was found that the following scheme works correctly on most cases, even on very large grids. For 1D-RBF interpolation, this means:

$$\begin{aligned}
 P_1(x) &= 1 \\
 P_2(x) &= \frac{x - x_{REF}}{c} \\
 P_3(x) &= \left(\frac{x - x_{REF}}{c} \right)^2
 \end{aligned} \tag{45}$$

where x_{REF} is a local reference coordinate, chosen to be the smallest coordinate of all influence points used for any particular interpolation point.

A naïve algorithm to find the optimum shape parameter is by performing a single force brute search until a suitable parameter is found. This approach may take too much time considering that the calculation of the condition number of a matrix is an expensive operation. In this work, a different approach is used, by doing a search of the optimum shape parameter in terms of the logarithm of the condition number. For 30 points and 1D-RBF interpolation, Figure

6 shows the results when plotting the logarithm of the condition number versus the shape parameter with 30 influence points uniformly distributed.

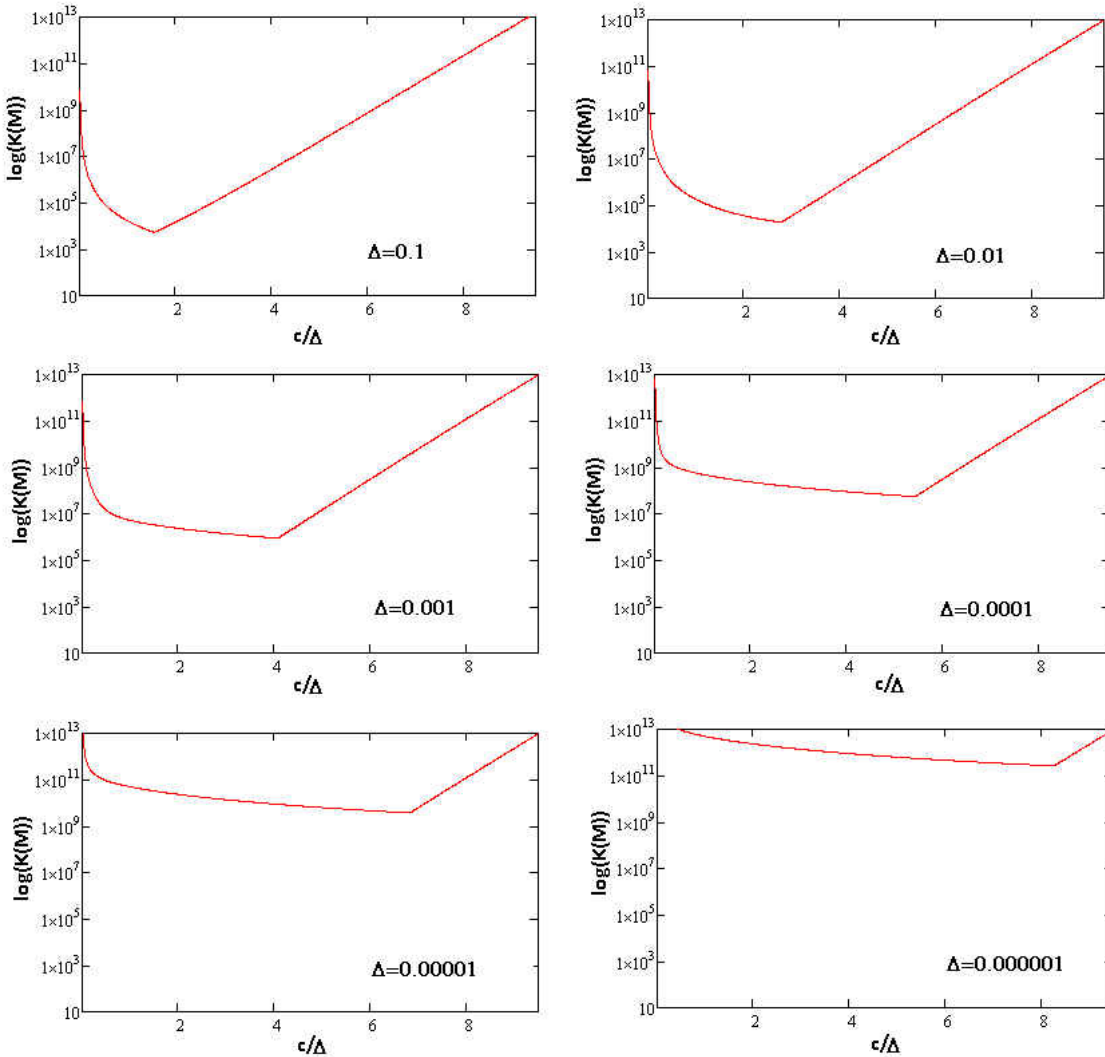


Figure 6: Condition number vs. shape parameter, for 30 influence points

As it can be observed in Figure 6, the distance between influence points is ranged from 0.1 to 10^{-6} and there are two solutions, one easy to find (between 2 and 8) and the second one hard to find since they are values very close to zero and quite different in order of magnitude. Using the logarithm of the condition number, the right part of each plot is a single straight line.

Additionally, the point c/Δ , where the condition number is 10^{13} , is basically the same in all cases ($c/\Delta \approx 9$). Using this point and a set of pre-computed optimum values, a very simple procedure can be developed where the optimum shape parameter will be calculated with no more than 3 computations of condition number.

Moreover, for deltas (between influence points) of 10^{-5} and 10^{-6} , there is basically no space to compute the optimum shape parameter because the condition number is basically in the upper limit of the acceptable range. For this reason, all calculations in this dissertation are performed with a delta of 10^{-3} . It is important to mention that the variation of the number of points produced no significant modification of the plots presented in Figure 6.

4.4 The order of a method

A very important issue in DNS and LES is the accuracy of the procedure. It is clear that high order methods report better results than low order methods. As it was mentioned earlier, in [151], it is always outlined that at least 4th order is acceptable for DNS, and that 2nd order is enough for LES. However, 4th order schemes (or higher) are more difficult to implement because they are unstable and they take more computing time. On the other hand, low order methods are easier to code and they require less computing time and resources with the same grid.

When discretizing Navier-Stokes equations in space and time, the resulting vector equation is of the form:

$$\mathbf{F}(\mathbf{V}^{n+1}) + \mathbf{G}(\mathbf{V}^n) + \mathbf{H}(P^{n+1}) = \mathbf{C}_x \Delta x^p + \mathbf{C}_y \Delta y^q + \mathbf{C}_z \Delta z^r + \mathbf{C}_t \Delta t^s \quad (46)$$

with n the time step. It is clear that the order of the method is the minimum order of all different discretizations because it will have the largest error. A method of order 4 must have all

discretizations of order 4, or the grids in the other directions, or the time step must be adjusted to have the same error in all terms. On the other hand, the lack of accuracy of a low order method can be resolved with a finer grid.

It is not clear what is best:

- a) A high order method in a coarse mesh, more difficult to implement.
- b) A low order scheme in a fine grid, easier to implement efficiently.

In a survey made to 124 papers with DNS calculations, 85% (105) used second order in time, while for LES, out of 132 papers, 95% (125) used second order for time integration. There is no publication that used a time scheme of order greater than 4.

Most publications use 2nd order in space and time, and there are no important differences with results with low order in time and high order in space.

For example, in [211], [241], [260] and [331] the pseudo-spectral method is used for spatial derivatives, but the classical Runge-Kutta scheme of order 2, 2, 3 and 4 respectively is used for time integration. In other studies, such as [335], a pseudo-spectral method is used in tangent direction but low order spatial discretization is used in the main direction of the flow.

In one study [101], where second order was used for pressure equation and Crank-Nicholson method for time integration (a 2nd order method), comparisons were made with schemes of 2nd and 6th order for momentum equations. Their conclusion is that second order was enough to reach spectral accuracy.

4.5 Acceleration techniques

The typical procedure in the solution of the nonlinear system of equation momentum-continuity is by solving a series of linear systems and updating the coefficients iteratively.

In this area, two major approaches have been widely used, the *block-correction* scheme as proposed in [140] which is useful in structured grids. For 2D problems, the basic idea is to perform corrections in lines, solving a simple tri-diagonal linear system. Unfortunately, this procedure has not been popular.

In fact, the most popular acceleration method for CFD, usable in structured and unstructured grids is the *multigrid* algorithm as explained in [240]. This method performs corrections by solving an equivalent system in a coarse grid. The general technique involves several coarser grids intended to accelerate the convergence of the previous finer grid.

The efficiency of the multigrid algorithm depends strongly on the problem, because if a given flow pattern has different resolution scales, the solution in the coarser grid acts as a filter and the corrections do not necessarily lower residuals. For a good convergence of the multigrid scheme is highly convenient to have a priori knowledge of the phenomena in order to specify in what parts of the problem is necessary the technique. The multigrid technique is useful in the segregated approach because every equation is treated separately and the corrections can be performed without perturbing the others.

In the case of the direct coupled procedure, an effective block correction procedure can be constructed.

Let's begin with the discretized equations (29) but with more detail:

$$\begin{aligned}
a_p^u u_p + \sum_{nb} a_{nb}^u u_{nb} + C_p^u (p_p - p_E) &= b_p^u \\
a_p^v v_p + \sum_{nb} a_{nb}^v v_{nb} + C_p^v (p_p - p_N) &= b_p^v \\
D_p^u (u_p - u_W) + D_p^v (v_p - v_S) &= 0
\end{aligned} \tag{47}$$

Using a tentative solution u^* , v^* and p^* , the residual of momentum and continuity equations can be written as:

$$\begin{aligned}
r^u &= b_p^u - a_p^u u_p^* - \sum_{nb} a_{nb}^u u_{nb}^* + C_p^u (p_E^* - p_p^*) \\
r^v &= b_p^v - a_p^v v_p^* - \sum_{nb} a_{nb}^v v_{nb}^* + C_p^v (p_N^* - p_p^*) \\
r^c &= -D_p^u (u_p^* - u_W^*) - D_p^v (v_p^* - v_S^*)
\end{aligned} \tag{48}$$

Expressing the exact value of velocity and pressure in terms of the previous tentative solution in terms of the corrections u' , v' , p' we obtain:

$$\begin{aligned}
a_p^u u_p' + \sum_{nb} a_{nb}^u u_{nb}' + C_p^u (p_p' - p_E') &= r^u \\
a_p^v v_p' + \sum_{nb} a_{nb}^v v_{nb}' + C_p^v (p_p' - p_N') &= r^v \\
D_p^u (u_p' - u_W') + D_p^v (v_p' - v_S') &= r^c
\end{aligned} \tag{49}$$

Performing the summation in horizontal and vertical lines, and forcing the same correction in every line, the following equations are obtained:

$$\sum_X (a_p^u + a_E^u + a_W^u) u_p' + \sum_X a_N^u u_N' + \sum_X a_S^u u_S' = \sum_X r^u \tag{50}$$

$$\sum_Y (a_p^u + a_N^u + a_S^u) u_p' + \sum_Y a_E^u u_E' + \sum_Y a_W^u u_W' = \sum_Y r^u$$

$$\sum_X (a_p^v + a_E^v + a_W^v) v_p' + \sum_X a_N^v v_N' + \sum_X a_S^v v_S' = \sum_X r^v \tag{51}$$

$$\sum_Y (a_p^v + a_N^v + a_S^v) v_p' + \sum_Y a_E^v v_E' + \sum_Y a_W^v v_W' = \sum_Y r^v$$

$$\sum_X D_p^v (v_p' - v_S') = \sum_X r^c \tag{52}$$

$$\sum_Y D_p^u (u_p' - u_W') = \sum_Y r^c$$

Now, considering that any acceleration algorithm is effective when the time involved in the correction part is small compared to the time of the iterative solver, a suitable approach seems to be a partial implementation of equations (49)-(52):

$$u'_P = u'_W + \frac{\sum_Y r^c}{\sum_Y D_P^u} \quad (53)$$

$$p'_E = p'_P - \frac{\sum_Y r^u}{\sum_Y C_P^u} \quad (54)$$

$$v'_P = v'_S + \frac{\sum_X r^c}{\sum_X D_P^v} \quad (55)$$

$$p'_N = p'_P - \frac{\sum_X r^v}{\sum_X C_P^v} \quad (56)$$

The great advantage of this scheme is that the corrections are calculated directly, with the summations of coefficients constant, so they can be computed and their inverse stored at the beginning of the computation.

4.6 Absence of virtual points

Perhaps the most characteristic feature of any meshless approach is the use of virtual points. Figure 7 shows the typical configuration used in meshless methods, the real grid and the virtual grid.

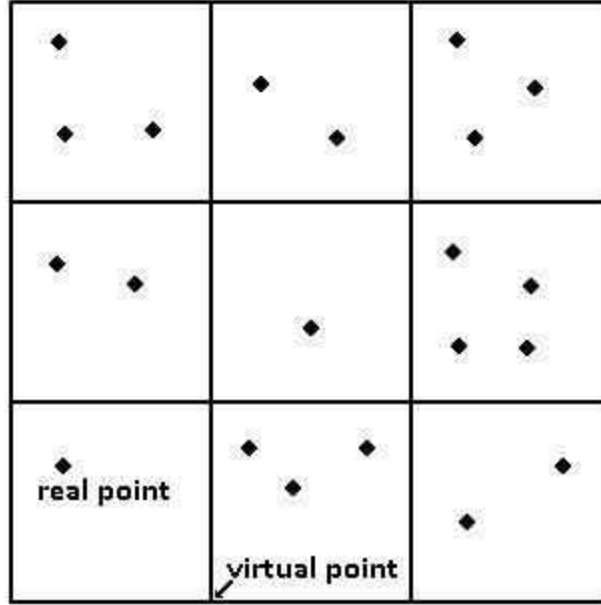


Figure 7: The real grid and the virtual grid

The main idea of any meshless procedure is to store the solution in the real grid, which can have a random distribution of points. On the other hand, the virtual grid, normally a perfect aligned grid, is used to discretize all governing equations, using finite differences for the calculation of the derivatives and RBF to perform any necessary interpolation between the real grid and the virtual grid.

The proposed procedure does not utilize any virtual points, but just a single perfectly aligned grid for each variable. The reason for not using virtual points can be observed by taking a look at the calculation of a single derivative. Consider the calculation of the first derivative using central differencing:

$$\frac{\partial \varphi}{\partial x} = \frac{\varphi_{VPE} - \varphi_{VPW}}{\Delta x} + O(\Delta x^2) \quad (57)$$

The calculation of ϕ at virtual points E and W is done using RBF interpolation. By substituting the interpolation relation (44) for both virtual points we obtain the interpolation vector plus the error term:

$$\frac{\partial \phi}{\partial x} = \frac{1}{\Delta x} \left(\sum_{i=1}^{NF} \alpha_i^{VPE} \cdot \varphi_i \right) - \frac{1}{\Delta x} \left(\sum_{i=1}^{NF} \alpha_i^{VPW} \cdot \varphi_i \right) + O(\Delta x^2) + IE_{VPE} + IE_{VPW} \quad (58)$$

Considering that the RBF interpolation has an error term considered pseudo-spectral, the interpolation error at both virtual points must be smaller than the error of the finite difference scheme.

$$\begin{aligned} O(\Delta x^2) &>> IE_{VPE}, IE_{VPW} \\ &\Downarrow \\ \frac{\partial \phi}{\partial x} &\approx \frac{1}{\Delta x} \left(\sum_{i=1}^{NF} \alpha_i^{VPE} \cdot \varphi_i \right) - \frac{1}{\Delta x} \left(\sum_{i=1}^{NF} \alpha_i^{VPW} \cdot \varphi_i \right) + O(\Delta x^2) \end{aligned} \quad (59)$$

Since the error of the derivative is the leading term, calculating and storing the interpolation vectors for any single derivative will consume a more time and memory than the classical finite differencing scheme. In conclusion, using a perfectly aligned grid for each variable and RBF for any necessary interpolation will be faster and it will consume less computer memory. The error in the calculation of the derivative will be the same order than using virtual points. This issue can be very important if a meshless approach is desired to be used for DNS/LES simulations.

4.7 Using a suitable grid

One non trivial task is to find a suitable grid for any fluid flow calculation. In parabolic flows, where convection terms are negligible compared to the the diffusion terms, basically any coarse grid can be used to find an acceptable solution. But, in elliptic flows, as in the backward-facing step problem, the situation changes drastically since both, diffusion terms and convection terms coexist at the same time.

Due to memory costs and computing time, the idea in any numerical simulation is to use the coarsest possible grid that can help describing the flow phenomena correctly. The classical approach is to perform a coupled of computations (with different grid sizes) and check later both solutions. For simple cases, that is a good approach, but in DNS or LES simulations, that idea is too expensive in time and resources. In the literature, a lot of information can be found about the appropriate number of nodes (per direction) that are necessary to solve any DNS/LES problem.

Another objective of this work is to provide some guidelines and ideas about how a suitable grid can be determined without the need of performing several simulations.

The key idea is found in the first lessons of any undergraduate course on numerical methods, but unfortunately ignored most of the time. Let's begin taking a look at the momentum equation in x-direction:

$$\left(v \frac{\partial^2 \varphi}{\partial x^2} - u \frac{\partial \varphi}{\partial x} \right) + \left(v \frac{\partial^2 \varphi}{\partial y^2} - v \frac{\partial \varphi}{\partial y} \right) - \frac{\partial \varphi}{\partial t} = \frac{1}{\rho} \frac{\partial p}{\partial x} \quad (60)$$

Substituting the finite difference expressions for both, diffusion and convection terms, the above equation (60) can be written as, assuming a uniform grid on both directions x and y:

$$\begin{aligned}
& \frac{v}{\Delta^2} \left(a_P^{DX} \varphi_P + \sum_{nb} a_{nb}^{DX} \varphi_{nb} \right) - \frac{u}{\Delta} \left(a_P^{CX} \varphi_P + \sum_{nb} a_{nb}^{CX} \varphi_{nb} \right) \\
& + \frac{v}{\Delta^2} \left(a_P^{DY} \varphi_P + \sum_{nb} a_{nb}^{DY} \varphi_{nb} \right) - \frac{v}{\Delta} \left(a_P^{CY} \varphi_P + \sum_{nb} a_{nb}^{CY} \varphi_{nb} \right) \\
& - \frac{1}{\Delta t} (\varphi_P - \varphi_P^*) = \frac{1}{\rho} \frac{\partial p}{\partial x}
\end{aligned} \tag{61}$$

where the DX , DY refers to diffusion in x , y , as well as CX and CY . Additionally, all coefficients a^D , a^C are intended to be of order $O(1)$. What is important here is the balance of magnitudes between both, diffusion and convection terms at the moment of being summed to build the discretized equation. The discretized equation (61) can be re-written in terms of a *local Reynolds number* as well as the CFL number:

$$\text{Re}_x = \frac{u\Delta}{\nu} \qquad \text{Re}_y = \frac{v\Delta}{\nu} \qquad \text{CFL} = \frac{u\Delta t}{\Delta} \tag{62}$$

$$\begin{aligned}
& \left(a_P^{DX} \varphi_P + \sum_{nb} a_{nb}^{DX} \varphi_{nb} \right) - \text{Re}_x \left(a_P^{CX} \varphi_P + \sum_{nb} a_{nb}^{CX} \varphi_{nb} \right) \\
& + \left(a_P^{DY} \varphi_P + \sum_{nb} a_{nb}^{DY} \varphi_{nb} \right) - \text{Re}_y \left(a_P^{CY} \varphi_P + \sum_{nb} a_{nb}^{CY} \varphi_{nb} \right) \\
& - \frac{\text{Re}_x}{\text{CFL}} (\varphi_P - \varphi_P^*) = b^u
\end{aligned} \tag{63}$$

In order to understand the purpose of equation (63), let's begin with a simple example. One fundamental rule in computer programming is that if we want to add or subtract two numbers, they must have roughly the same order of magnitude, otherwise, the result will be a similar number to the largest. For example, adding 2 and 3 will produce 5, which is different to 2 and 3. If we now add 10 and 1, the result will be 11, which is no more different than 10 (just 10% more). One extreme case, add 100 and 1, the result 101 is basically the same than 100 (1% more).

When adding the coefficient of diffusion and convection terms in x-direction (for example), the local Reynolds number Re_x will determine the proportion between these two terms. If the mesh used is very coarse, the local Reynolds Re_x will be very large, and the summation of the coefficients will be similar in magnitude to the convection terms. This misbalance of terms will make the equation very similar (numerically speaking, to the machine) to the Euler equation at the moment of the iteration. This issue may produce clearly numerical instability. It is convenient to recall that in most DNS calculations, the local Reynolds number has a value of the order of 100.

On the other hand, in an elliptic problem, if the mesh is extremely fine and the local Reynolds Re_x gets very close to zero, the equation will be basically a diffusion equation (like heat conduction). This misbalance will hide all nonlinear effects that must be present in any elliptic flow problem.

Performing test on different grids with the present method, a local Reynolds number greater than 10 is enough to produce numerical instabilities. In order to keep a balance between both, diffusion and convection terms, it seems that they should not be 10 times larger than the other. If we set the limiting misbalance of magnitudes to be 10, the local Reynolds numbers will be bounded by:

$$\frac{1}{10} \leq \text{Re}_x \leq 10 \quad (64)$$

Additionally, for the y-direction, if the delta used in one direction is too different than in the other, Re_y will be too different from Re_x , and the coefficients of the resulting equation will

have a magnitude similar to the coefficients of the largest delta. This misbalance imposes a restriction on how stretched a grid can be.

It is clear that the worst case will be with the maximum velocity at a given point. If we want to develop a criterion to set the grid before the calculation, the idea of local Reynolds number can be changed using the velocity of reference \bar{V} :

$$\begin{aligned}\overline{\text{Re}}_x &= \frac{\bar{V}\Delta x}{\nu} \Rightarrow \frac{1}{10} \leq \overline{\text{Re}}_x \leq 10 \\ \overline{\text{Re}}_y &= \frac{\bar{V}\Delta y}{\nu} \Rightarrow \frac{1}{10} \leq \overline{\text{Re}}_y \leq 10\end{aligned}\tag{65}$$

Finally, for the transient term the situation is similar. If the courant number CFL is too large, the equation will be, numerically speaking, a quasi steady state equation. On the other hand, if CFL is too small, the coefficients of the resulting equation will be, in magnitude, similar to the transient term, or the original equation with excessive numerical diffusion.

Once again, the delta time that can be used is also bounded for stability reasons. With $CFL \approx 1$, the magnitude of the transient term will be similar to the magnitude of the convection term, and the criterion of the local Reynolds number will again prevail. What is interesting is that the criteria of a bounded local Reynolds number is that it is possible to develop a strong criteria to know, in advance, the necessary grid for any problem, steady state or transient, laminar flow or DNS/LES simulations.

CHAPTER FIVE PROPOSED PROCEDURES AND VALIDATION

5.1 Serial procedure for 2D steady flows

As mentioned earlier, the method proposed here is a major modification of the procedure published in [340]. The method used second order upwinding for the convection terms and bilinear interpolation. This procedure was previously validated [339] and [340] by solving the case of turbulent flow in a squared duct with the $k - \varepsilon$ model of Launder-Sharma. The main features are:

- Use a segregated grid arrangement for velocity components and pressure
- Discretize the diffusion term with second order finite differences
- Discretize the convection term with the Osher flux limiting scheme
- Use RBF to interpolate velocity components (needed in the flux limiting scheme)
- Use second order central differencing for pressure gradient
- Use second order central differencing for continuity equation
- Solve the resulting system (29) with the procedure explained in chapter 3, part 3.9
- Use the block-correction scheme (53)-(56) to speed-up convergence

For the case of 2D steady flows, the main solution sequence used is:

1. Set an initial guess for velocity and pressure
2. Set inflow and wall boundary conditions
3. Compute diffusion coefficients in momentum equation and store them
4. Compute pressure gradient coefficients and store them

5. Compute coefficients in continuity equation and store them
6. Iterate until convergence:
 - 6.1 Store current velocity components
 - 6.2 Update velocity in outflow (original and interpolated grids)
 - 6.3 Compute momentum equation
 - 6.4 Perform block-corrections
 - 6.5 Interpolate velocity to the other grids
 - 6.6 Do some sub-iterations:
 - 6.6.1 Update main variables from flow equations
 - 6.6.2 Adjust pressure of reference (to reduce numerical errors)
 - 6.6.3 Find maximum increment
 - 6.7 Check convergence

5.2 Serial procedure for 2D transient flows

For the transient procedure, and with the analysis done in previous chapters, the calculation at each time step is an implicit procedure:

1. Set an initial condition for velocity and pressure
2. Compute diffusion coefficients in momentum equation and store them
3. Compute pressure gradient coefficients and store them
4. Compute coefficients in continuity equation and store them
5. For each time step:
 - 5.1 Iterate until convergence:

- 5.1.1 Store current velocity components
- 5.1.2 Update velocity in outflow (original and interpolated grids)
- 5.1.3 Compute momentum equation
- 5.1.4 Perform block-corrections
- 5.1.5 Interpolate velocity to the other grids
- 5.1.6 Do some sub-iterations:
 - 5.1.6.1 Update main variables from flow equations
 - 5.1.6.2 Adjust pressure of reference (to reduce numerical errors)
 - 5.1.6.3 Find maximum increment
- 5.1.7 Check convergence
- 5.2 Take statistics if a DNS/LES calculation

5.3 2D Steady Backward-Facing Step

The backward-facing step is one of the hardest validation cases since the structure of the flow is highly elliptic and it is excellent to show the robustness of any numerical procedure. It is convenient to remember that most fluid flow calculation procedures are designed for parabolic flows.

This flow is characterized by a straight entry length, where the flow may or may not reach a fully developed state. Later the fluid enters in a sudden expansion and a big vortex is formed. In this zone, the structure is completely elliptic.

Finally, the flow re-attaches and the parabolic regime is back again. In general, at low Reynolds numbers, the re-attachment increases and, when the flow enters in the transition stage, the re-circulation zone reduces to increase in size later as the speed of the flow increases.

In general, there is a very important disagreement between experiments and numerical predictions when the fluid enters in the transitional regime. Under very few exceptions, almost all numerical calculations fail to predict transition.

Reviewing the literature, two different numerical approaches are used, the segregated SIMPLE procedure and the streamline-vortex formulation, in transient or steady state. There is no clear difference in the quality of the results.

In [26] a time-dependent SIMPLE scheme is used and different transient procedures are testes. Calculations with Reynolds number of 800 are performed with an inflow length of 40. Re-attachment occurs at 9.55 after 50 seconds. A similar case can be seen in [37] where calculations are done with Reynolds of 800 and an inlet of 5. A study is done by modifying the expansion ratio but no differences are reported with the entry length.

A different approach is used in [121], where the boundary element method is used with primitive variables and an entry length of 0.02 is set. Validations are presented at Reynolds number of 500 but no comparisons are presented. Similarly in [172], a spectral method with primitive variables is used and calculations with Reynolds number of 800 are performed. Re-attachment is consistent with other references but no info of the location of the inlet.

References [308] and [344] are similar cases where only one Reynolds number is used, 800. A study of outflow length is performed and the re-attachment is found to be consistent with previous works.

Some incomplete works can be found in [24] and [252]. In the first case, calculations with open and enclosed facing-step are performed but no comparisons are done on the re-attachment. In [252], SIMPLE scheme is used to perform 3D calculations with heat transfer but no info of inflow location is supplied. Here, some patterns are shown but no info on the re-attachment.

In the literature, very few experiments have been published. The classical reference [8] is a complete study of the behavior of the flow in the whole laminar regime. The expansion rate used is 1.94 and the entrance length equal to 40, claimed to be enough to obtain fully developed flow at all Reynolds. Measurements show clearly a 3D pattern. The re-attachment shows a permanent increment up to Reynolds number to 1,200, but then the size of the vortex decreases. Additionally, numerical calculations are performed using the measured inflow velocity profile and SIMPLE procedure. These calculations show an increment up to Reynolds of 450-500 and then decreases. This is the only numerical prediction that shows a decrement in the size of the vortex.

Another series of experiments can be found in [204]. The geometry and conditions are the same as [8] and the results are in good agreement. Here, transition is measured at Reynolds number of 1,200 when the re-attachment decreases.

Several other works have been published where the Reynolds number used ranges up to 1,000. For example, in [21] an expansion ratio of 2 is used and the entrance length is set to 1 and the Reynolds number ranges from 150 up to 1050. Re-attachment increases permanently. Stability analyses show that for Re from 750 and over, the flow becomes unstable to any 3D instability. Their results suggest that the flow is stable up to 1050 but they have not been able to compute for larger Reynolds.

In [25], different entrance locations are tested. SIMPLE method with QUICK convection scheme is proposed and extrapolation for outflow boundary conditions is used. Calculations are done up to Reynolds of 800 and the re-attachment increases always. If no entrance, re-attachment increases tremendously.

Similarly, in [35], computations are performed up to Reynolds of 800 with an expansion ratio of 1.94. In this paper, different convection schemes are tested, including TVD. All re-attachments increase as Reynolds except for the hybrid central-upwind that shows a decrement after Reynolds of 500. When refining the grid, all methods get an increasing Re-attach.

Using an expansion ratio of 1.94 and Reynolds from 100 to 1,000 [56], two different entry lengths are used, 0 and 10. In all cases re-attachment always increases. In [65], and expansion ratio of 1.94 is used with an entrance length of 2. Streamline vorticity formulation is proposed and they consider that for $Re > 1200$ the flow is transitional. For Reynolds 800 results agree with one reference but there is no detail for calculation with Reynolds larger than 1000, only graphics at different scales.

Reference [91] is perhaps the most complete calculation using the streamline-vorticity formulation. Some validations are presented with an expansion ratio of 1.94. It presents full results with expansion ratio of 2 and an inflow length of 20. Reynolds number is varied from 100 to 3000. Re-attachment always grows. No mention of transition and claims very accurate results. After Re 500, results differ from experiments. No mention that for higher Re, re-attachment decreases. Claim that re-attachment increases linearly as Re increases.

A study using primitive variables and Reynolds from 800 to 1,600 can be seen in [97]. Validation is presented for Reynolds of 800 and Hopf bifurcations are searched. Critical Reynolds is close to 1,200. In [275], a streamline-vorticity Boundary Element Method is

presented. No entrance region is set and Reynolds numbers are computed from 100 to 50,000. Mesh used is too coarse for the results to be correct. For Reynolds equal to 100, re-attachment is very low compared to other calculations. For $Re=800$ good agreement is found but, for $Re=1000$, no comparison is done.

On the other hand, in [328], primitive variables and SIMPLE is used. Study effect of step height is done. Expansion ratio from 1.25 to 1.75 is analyzed and Reynolds number computed from 50-900. Good agreement with available data. In [366], a curvilinear coordinate system with QUICK scheme is proposed, with primitive variables and fractional step method. No entry length is used and the inflow profile is parabolic. Calculations are done with Reynolds up to 800 and re-attachment always increases.

A different work can be found in [202], where a 3D simulation is done. The expansion ratio is 1.94 and the entrance region is equal to 1. Numerical predictions are performed for Reynolds from 100 to 800. Re-attachment increases always. One stability analysis through 2D DNS simulations can be seen in [362], where calculations are done for Reynolds number of 500 and 800 with different grid sizes.

A very interesting study can be found in [6], where a streamline-vorticity formulation is used. The geometry is a sudden expansion, which can be seen as a double backward-facing step. For Reynolds number of 550, an asymmetric solution is obtained and for Reynolds of 786, three different solutions are found, two of them asymmetric.

There are some other references related to the backward-facing step, as for example [61] where a streamline-vorticity method is used, or [67] where a SIMPLE-based method is used. A transient study can be found in [82], where at the beginning, two separate vortices are formed, but after some time, they unify into one large vortex.

In other works, as for example [83], several calculations with a Reynolds number from 10 to 610 are done, obtaining good agreement with experimental data. In a similar study [103], a calculation with a Reynolds number of 800 is done and good agreement is presented with available data.

An old reference but very interesting is [114], being one of the first to report that the re-attachment is a function of the Reynolds number for laminar, but constant in turbulent regime.

In [119], a stability study is performed for a Reynolds of 800. Their conclusion is that the flow is completely stable. Similarly in [123], a streamline-velocity procedure is proposed and a validation is performed for a Reynolds of 800.

In other ideas, a 3D backward-facing step analysis is done in [159]. Additionally, a 2D DNS backward facing step simulation is done in [160] and two different types of perturbations are studied, obtaining quite different responses. In [177], a study with heat transfer is done, obtaining different results for the Nusselt number with respect to the available data.

Similar publications can be found with alternative procedures, the streamline-vorticity in [247] and the vorticity-velocity in [258], with good agreement. In [266], a comparative study is done with a collocated procedure and the classical staggered grid. Their conclusion is that both procedures produce the same results. In other references, the well-known FIDAP package is used for validation of the results on this problem. In [329] a numerical procedure with a general curvilinear coordinate system is developed, where the backward-facing step is used for validation issues.

Finally, there are some other references with many interesting studies of the flow in this geometry, as for example, [12], [48], [62], [195], [210] [214], [246], [281] and [317], or one 3D simulation as in [348].

In the next sections, three different expansion ratios were computed, with different Reynolds numbers in the transition region basically. The way they are presented is the way they were computed. The order in which results are shown will help the reader understand the issues present and the conclusions reached.

5.3.1 Calculations with an expansion ratio of 1.94

Due to the big variations of inflow conditions in all numerical calculations reviewed, and in order to have a good comparison basis, it was decided to perform calculations with exactly the same geometry, expansion ratio and inflow conditions as the experiments of Armali [8].

Figure 8 shows the progression of the details in all calculations. Being h the separation of the plates before the expansion, the inlet length is $38.4h$, while the outlet length is $96.2h$. The expansion ratio used is 1.94, exactly the same as in the experiments. A potential inlet profile, with a realistic boundary layer was used to match the uniform velocity at inflows in the experiments:

$$\frac{u}{\bar{u}} = [1 - |s|]^{1/100} \quad -1 \leq s \leq +1 \quad (66)$$

Two series of calculations were performed. The first series was done with a mesh of ratio 2:1, while the second mesh was with a ratio 1:1 and DNS resolution for many cases. At the outflow, the non reflecting boundary condition $\partial u / \partial x = \partial v / \partial x = 0$ was set.

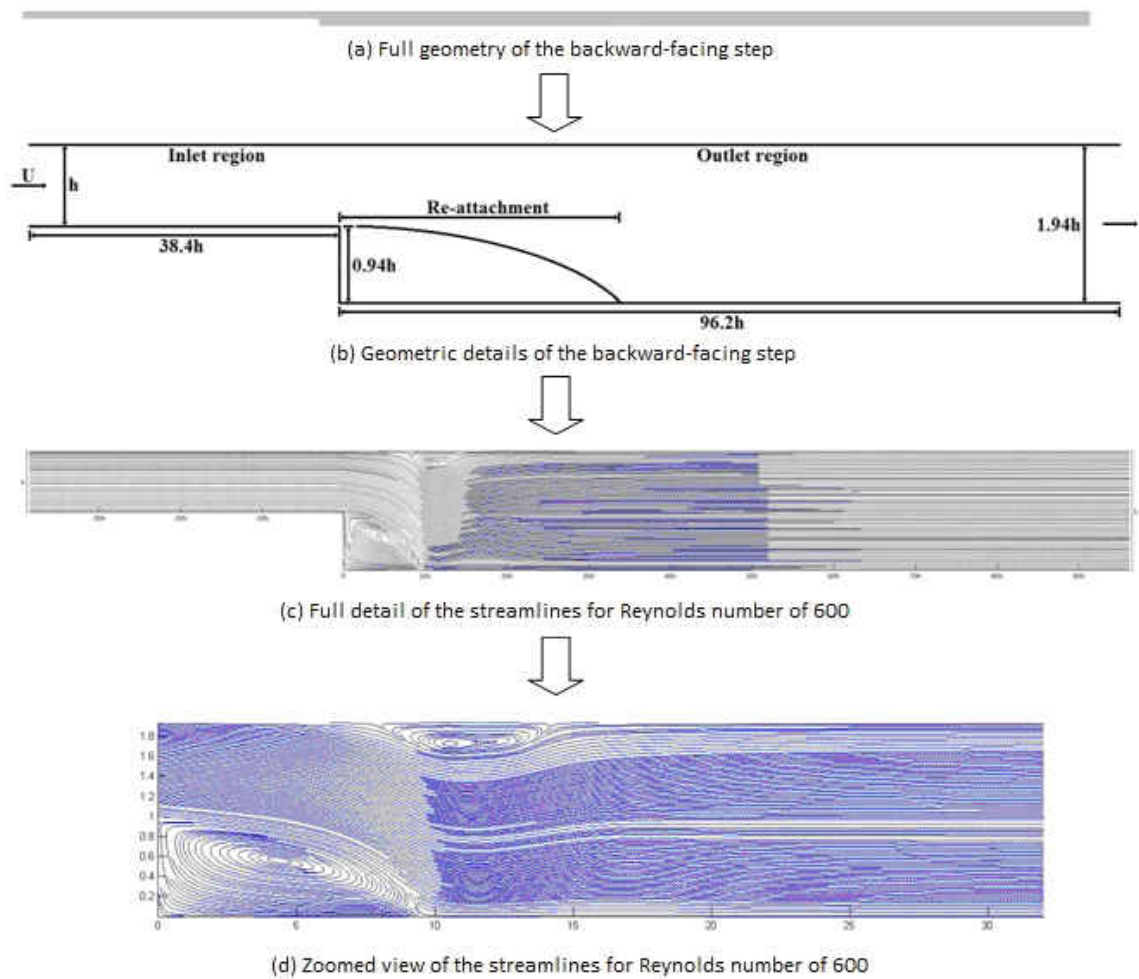


Figure 8: Progression of details for the backward-facing step

5.3.1.1 Results with a coarse grid

The mesh used in this first series has 50×960 internal pressure points while the expansion has $97 \times 2,405$ pressure points. This gives a total of 281,285 points for pressure, with a similar but slightly smaller number of points for both velocity components.

Calculations were performed for Reynolds numbers from laminar to turbulent. The Reynolds number was calculated as $Re_L = UD_H/\nu$, with the hydraulic diameter as $D_H = 2h$, and U the bulk velocity.

The procedure was to use as initial guess the solution with first order upwinding. The first aspect that called our attention in these series of calculations was the good description of the phenomena. The streamlines obtained from the calculation can be seen from Figure 9- Figure 13. Looking at Figure 9, from Reynolds 100 to 600 the results are in perfect agreement with the classic theory, in the sense that the size of the big vortex increases almost linearly with the Reynolds number. For Reynolds number of 600, a second vortex appears in the upper wall.

For Reynolds of 800, the small upper vortex breaks into several consecutive vortices, called Taylor-Görtler longitudinal vortices are oscillations due to instability of the flow. For Reynolds 1,000, the structure is similar but the size of the big vortex does not increase much.

Figure 10 shows the change in the streamlines pattern present when transition occurs at this expansion ratio, somewhere between 1,180 and 1,200. It is very interesting to note that the experiments of Armali [8] show a similar behavior. The difference is the size of the re-attachment which in our calculation is smaller than in the experiments.

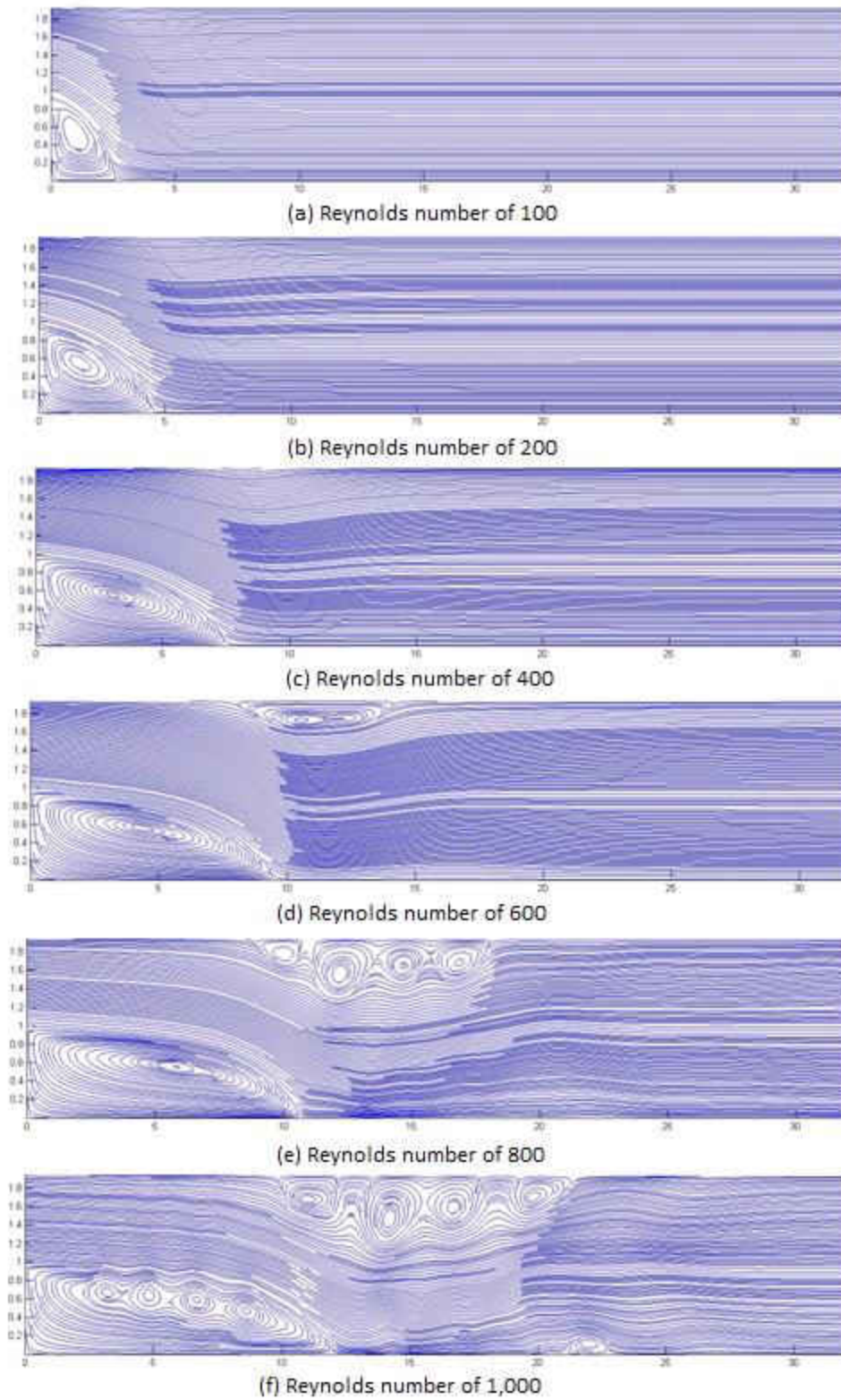


Figure 9: Streamlines BFS with $ER = 1.94$, coarse grid, Reynolds 100-1000

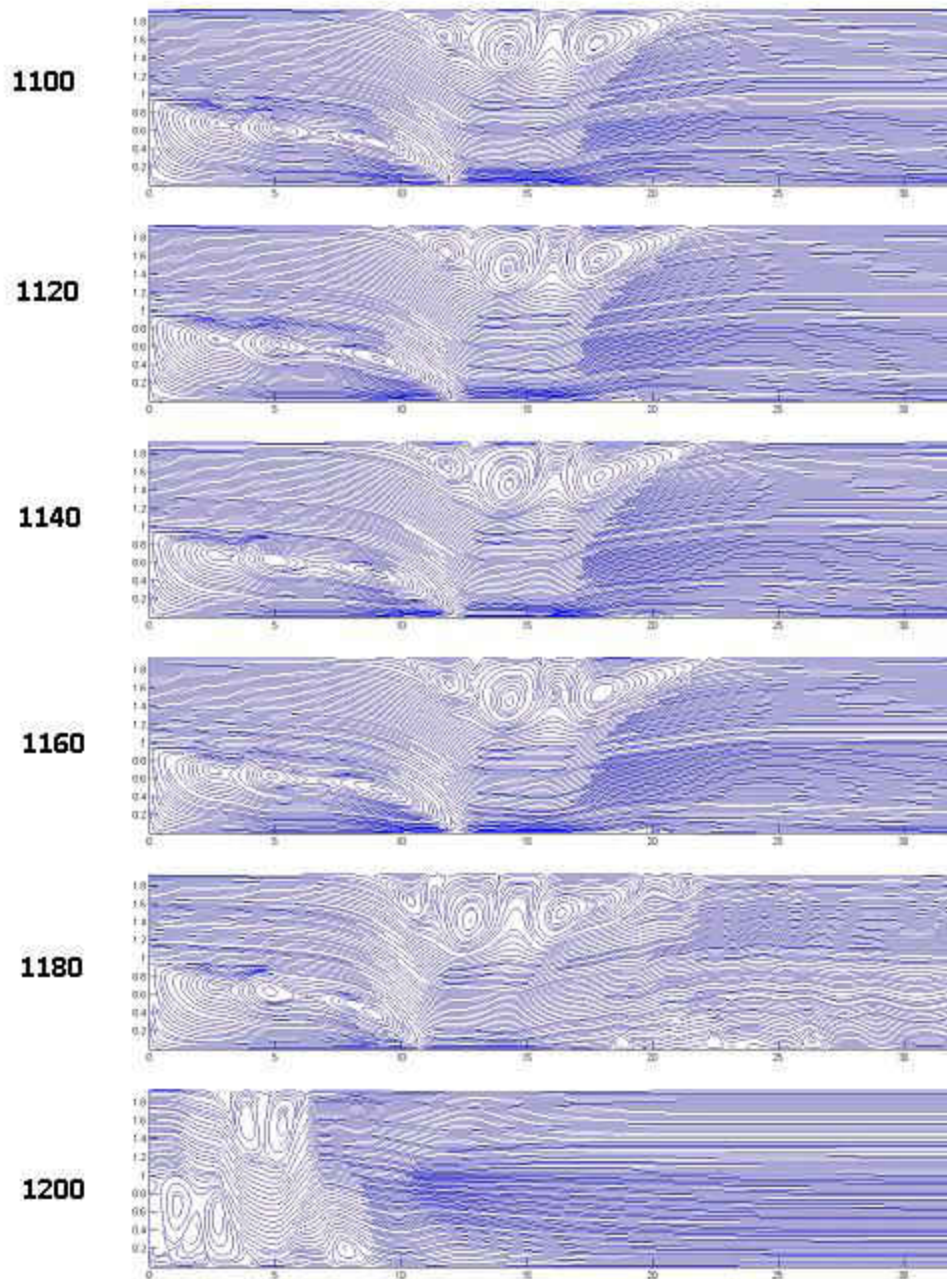


Figure 10: Streamlines BFS with $ER = 1.94$, coarse grid, Reynolds 1100-1200

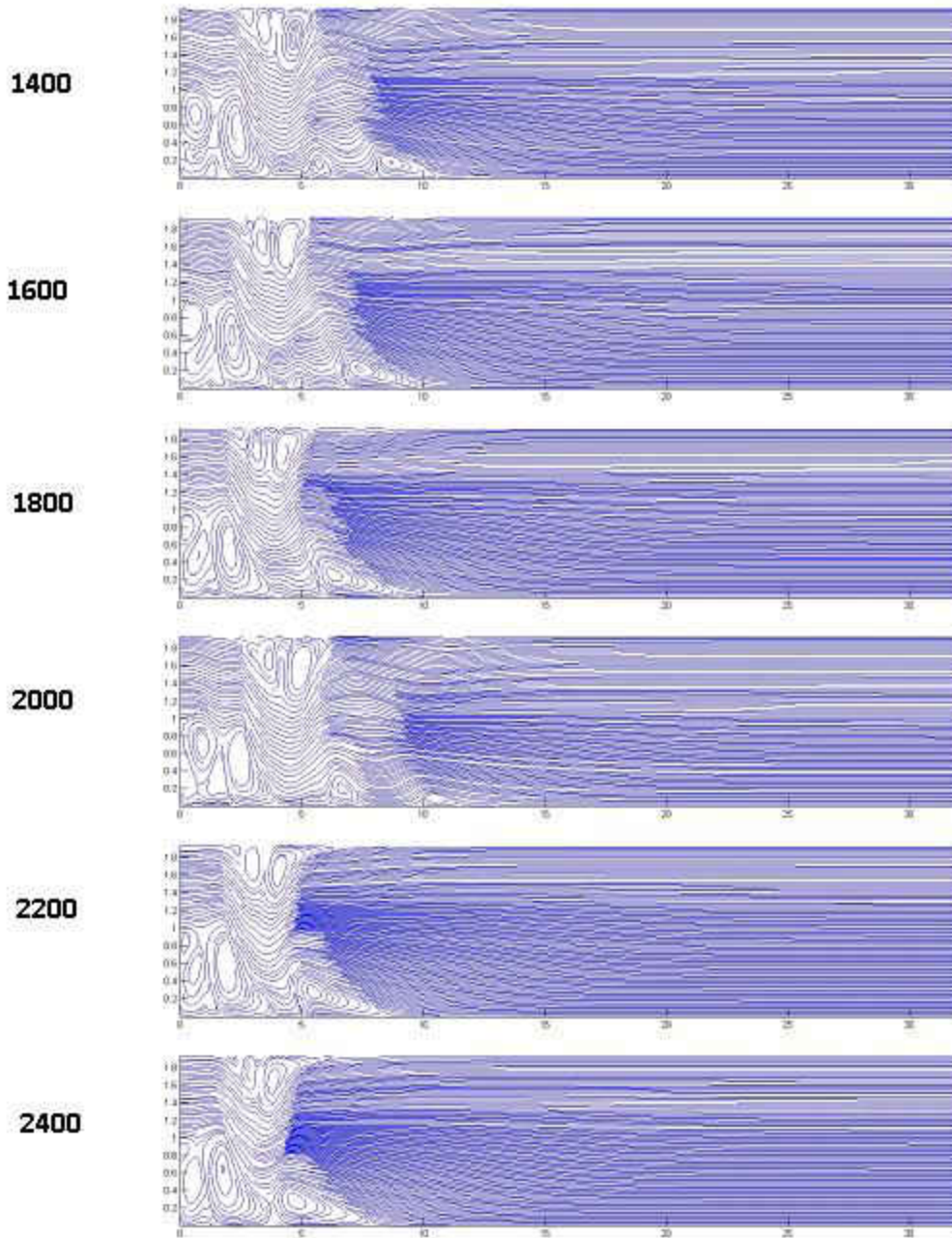


Figure 11: Streamlines BFS with $ER = 1.94$, coarse grid, Reynolds 1400-2400

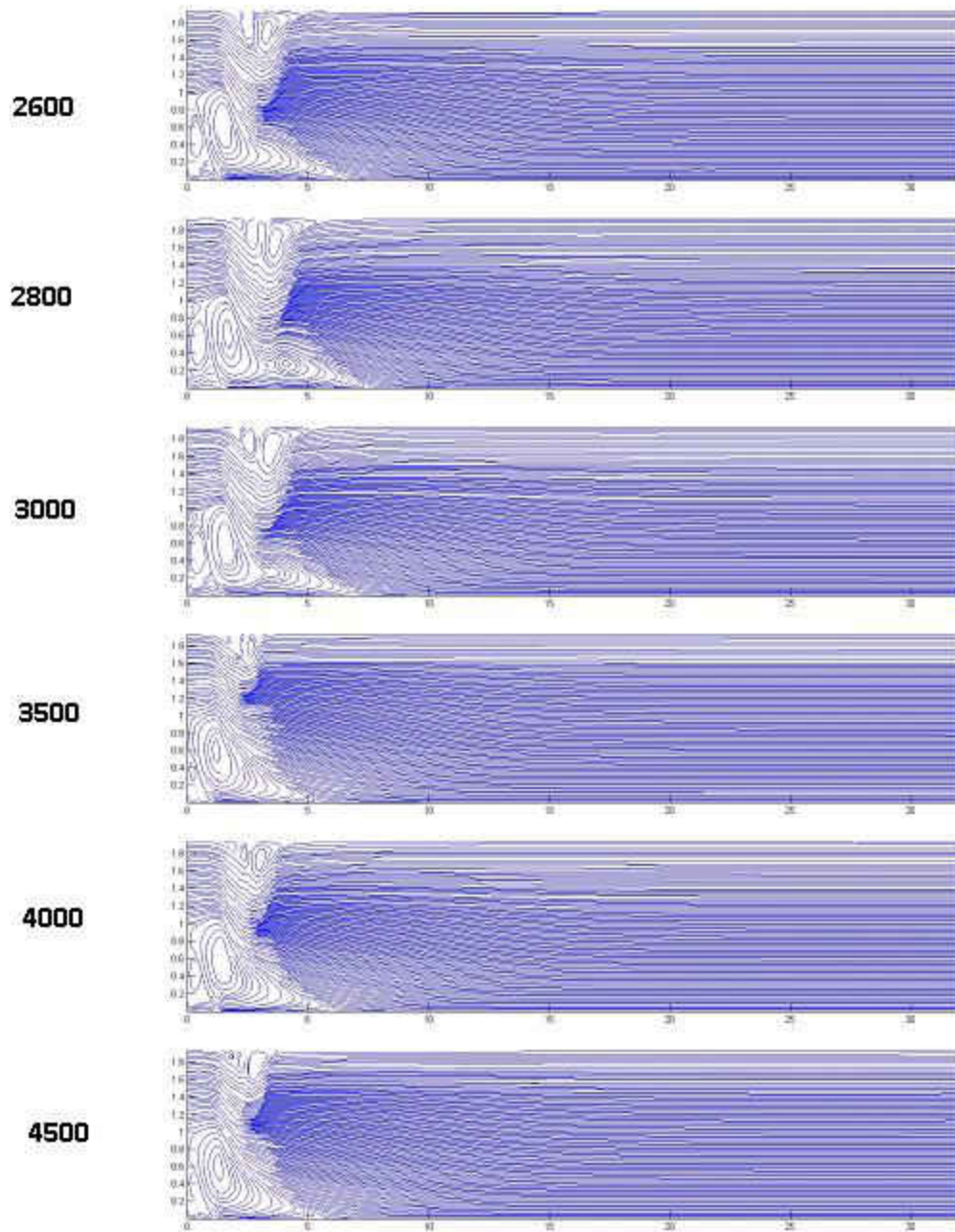


Figure 12: Streamlines BFS with $ER = 1.94$, coarse grid, Reynolds 2400-4500

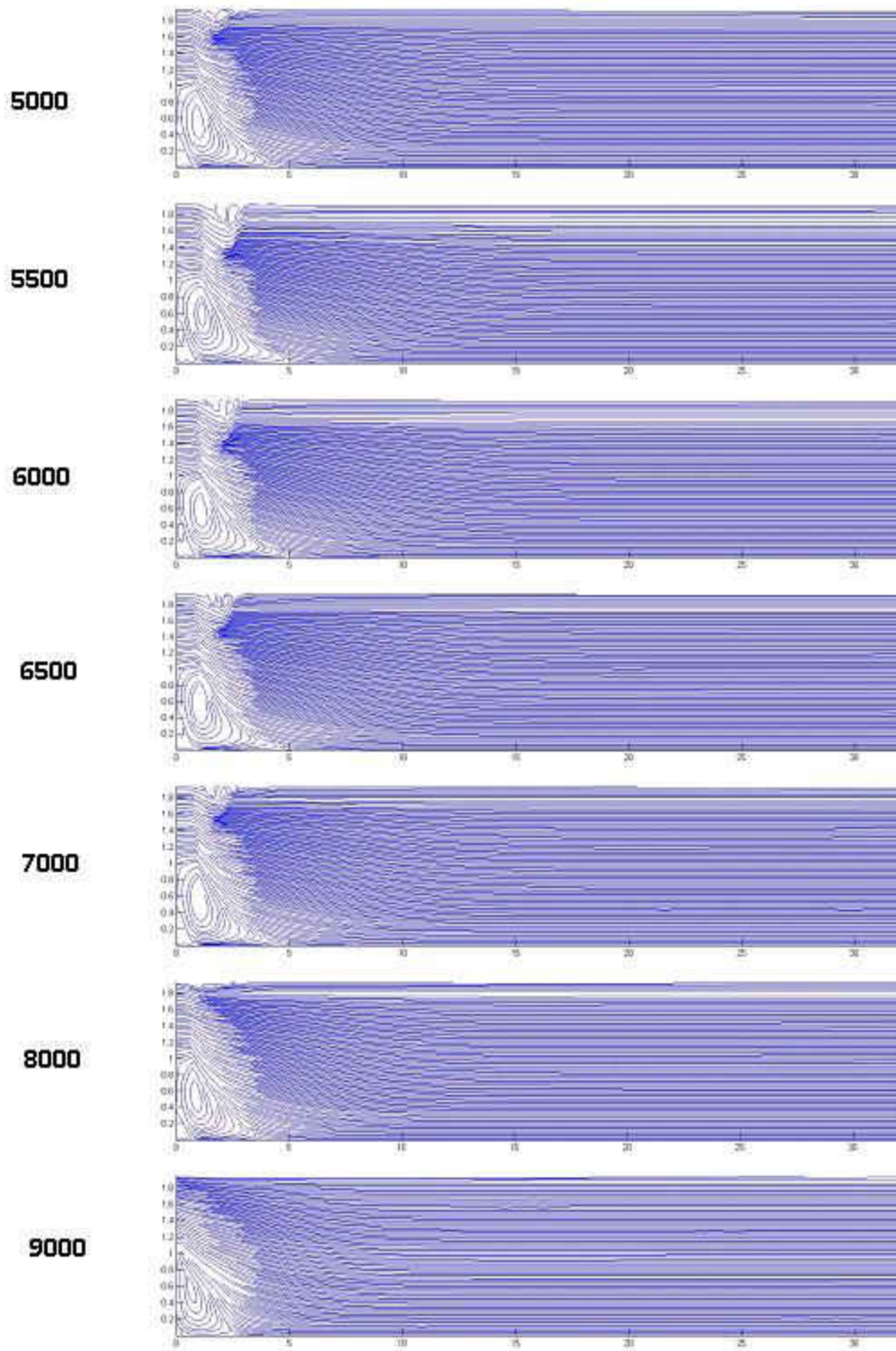


Figure 13: Streamlines BFS with $ER = 1.94$, coarse grid, Reynolds 5000-9000

Figure 11 and Figure 12 show the change in the pattern from a series of unstable vortices, similar to the results published by Rani [276] and the clear Kelvin-Helmholtz oscillations present after the first re-attachment.

From Reynolds number 3,500 and up, the upper Taylor-Görtler longitudinal vortices disappear due to the increasing kinetic energy of the fluid. Figure 13 show the streamlines for Reynolds number from 5,000 to 9,000, where the structure of the flow becomes stable and most previous instabilities disappear.

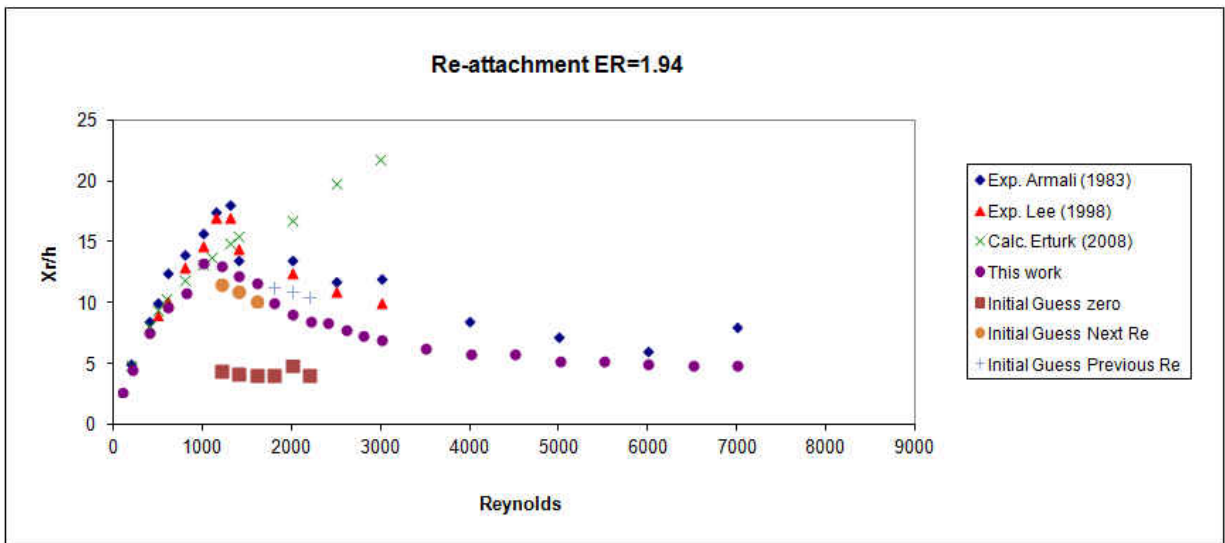


Figure 14: Re-attachment BFS with for $ER = 1.94$, coarse grid, re-attachment

Figure 14 shows the re-attachment and the comparison with experimental data. The agreement is reasonable good except in the range 1,200-2,400, where the solution convergence was very unstable and too sensitive to the initial guess. In general, the description of the phenomena is consistent with those of the experiments.

Since these results have not been published before, an analysis on convergence and on grid size, done on chapter three, forced the decision to use a fine grid with DNS resolution for the smallest Reynolds numbers.

5.3.1.2 Results with a fine grid

After the results observed with the previous grid, an analysis of the grid was performed. A uniform grid was chosen with the same geometry of the experiments of Armali [8] but the exit was reduced to $40h$ in order to save some computer memory. At the entrance, a mesh of 100×3840 pressure points was used and at the expansion, a grid of 194×4000 points was used, for a total of 1.16 million pressure points. Additionally, the grid has DNS resolution for almost all cases computed.

Table 3 shows the data used in all simulations, with the relaxation factor to be decreased considerably as the Reynolds number exceeded 600. The convergence history in all simulations performed can be seen from Figure 15 to Figure 25. It calls the attention that the convergence is complete up to Reynolds of 400. For Reynolds number of 600 and up, the convergence history shows an unstable behavior, very unusual considering that the mesh has DNS resolution and the number of iterations done was 1 million.

Analyzing the streamlines, shown from Figure 26 to Figure 36, it can be seen that the pattern is totally unstable at Reynolds number were the solution must be stable. Considering that these calculations are performed with a very fine grid, three ideas were considered:

- There is an anomaly that may appear in 2D calculations but never in 3D (as one reviewer suggested)

- The finite difference scheme becomes unstable
- The RBF interpolation scheme may become unstable

In general, the finite difference scheme is second order and it is the most popular method in CFD. Even that there are very few publications with a complete study of the 2D-BFS in the transition region; the anomaly is not a choice to be ignored. The instability of the interpolation procedure is known to happen with high order polynomials and functions that are of the type *step*. The procedure described before to determine the optimum shape parameter is suitable for most cases but not for *step* functions. These step functions may appear in the viscous sub-layer for the axial velocity component.

Table 3: Data used in BFS with $ER = 1.94$, fine grid

Re	Re_{Local}	Relax. Factor	Δ / Δ_K
100	0.5	0.50	0.32
200	1	0.25	0.53
400	2	0.20	0.89
600	3	0.10	1.21
800	4	0.01	1.50
1,000	5	0.001	1.78
1,200	6	0.001	2.04
1,400	7	0.001	2.29
1,600	8	0.001	2.53
1,800	9	0.001	2.76
2,000	10	0.001	2.99

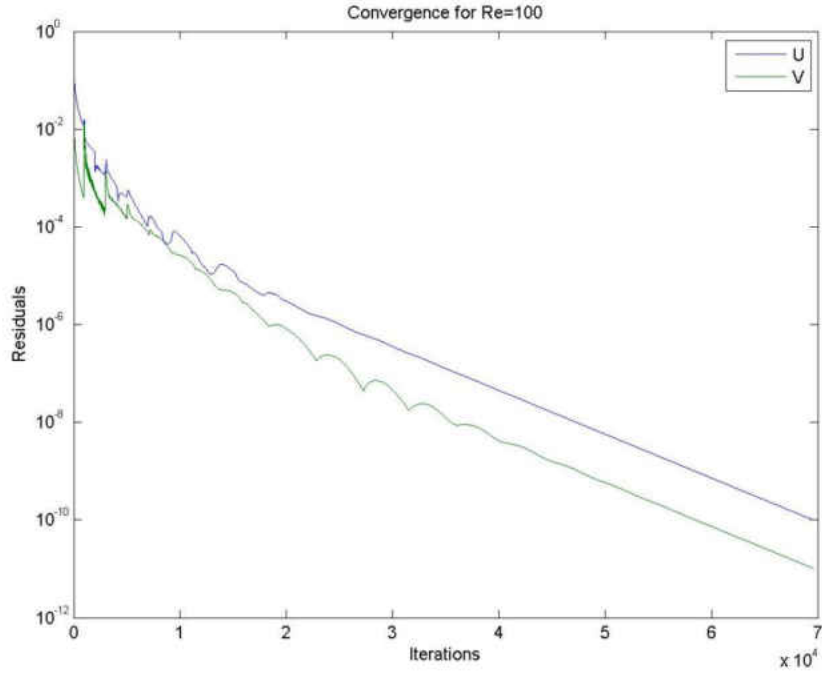


Figure 15: Convergence for BFS, $ER = 1.94$, fine grid, $Re=100$

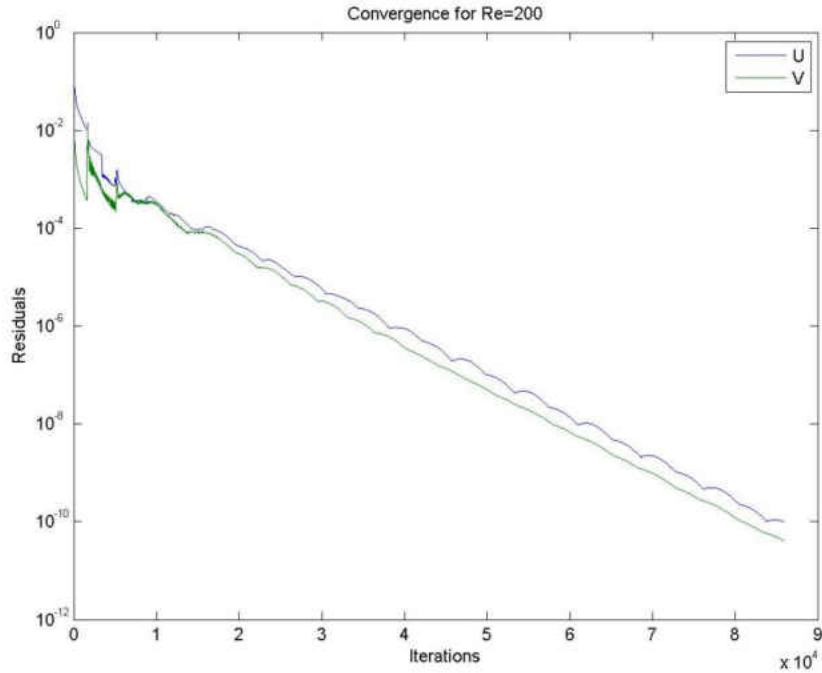


Figure 16: Convergence for BFS, $ER = 1.94$, fine grid, $Re=200$

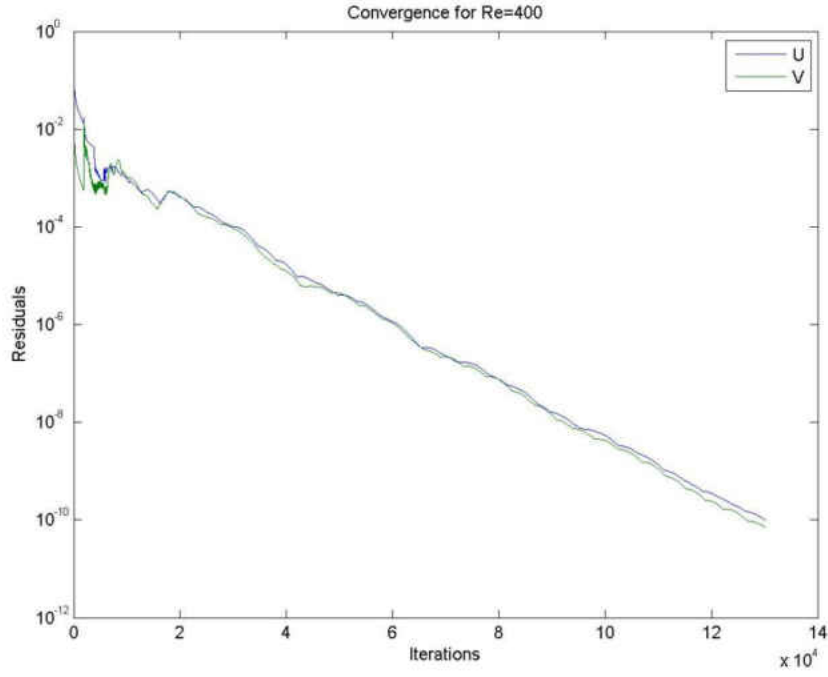


Figure 17: Convergence for BFS, $ER = 1.94$, fine grid, $Re=400$

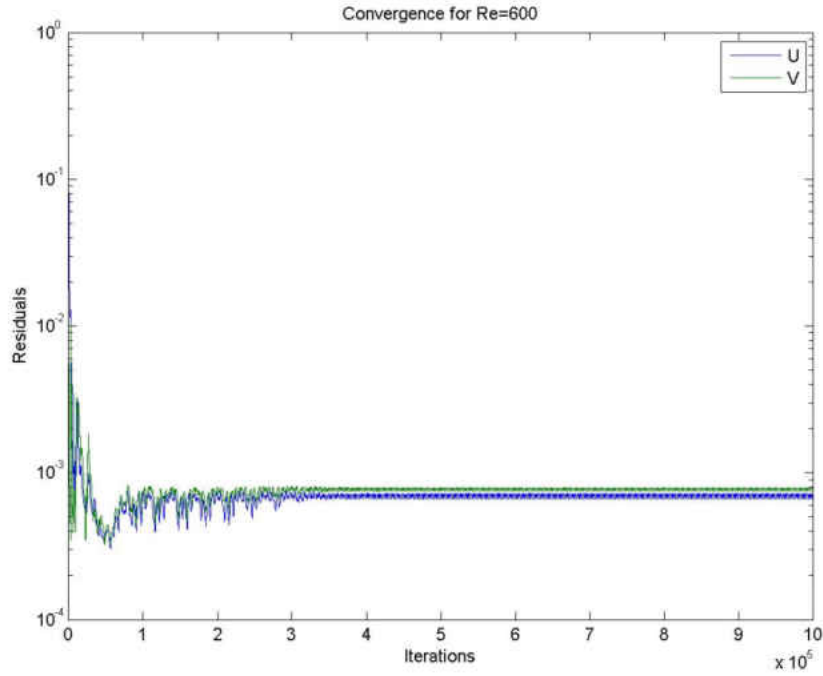


Figure 18: Convergence for BFS, $ER = 1.94$, fine grid, $Re=600$

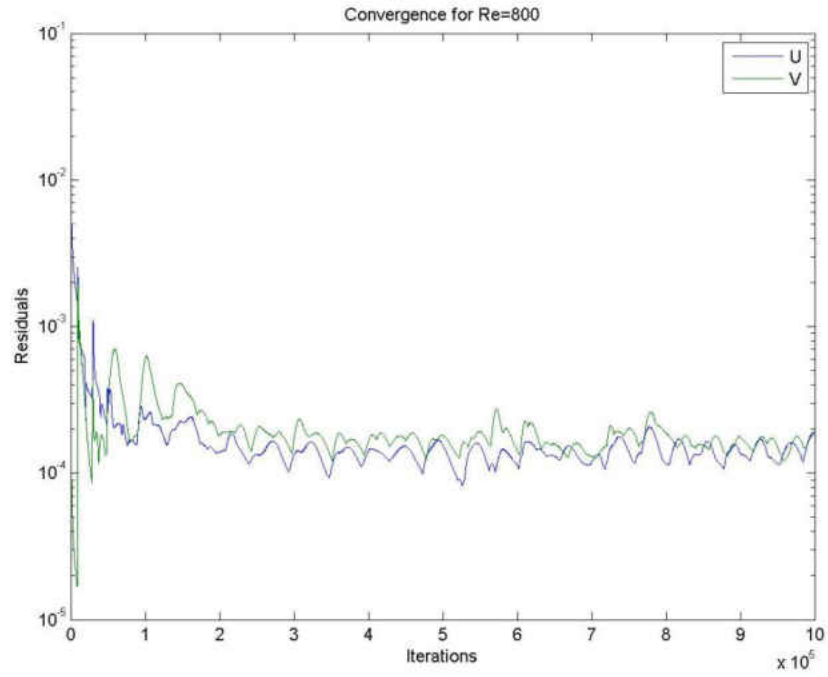


Figure 19: Convergence for BFS, $ER = 1.94$, fine grid, $Re=800$

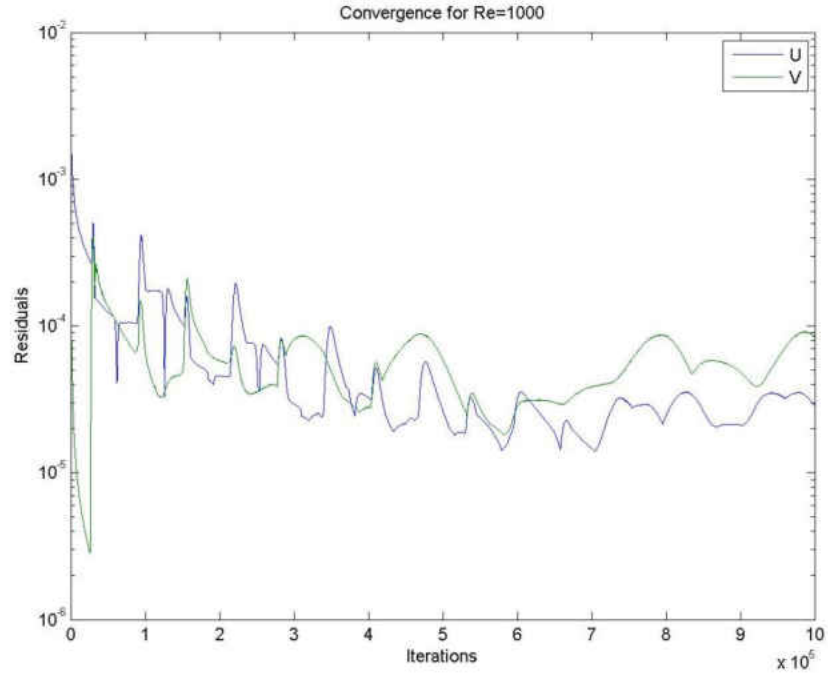


Figure 20: Convergence for BFS, $ER = 1.94$, fine grid, $Re=1000$

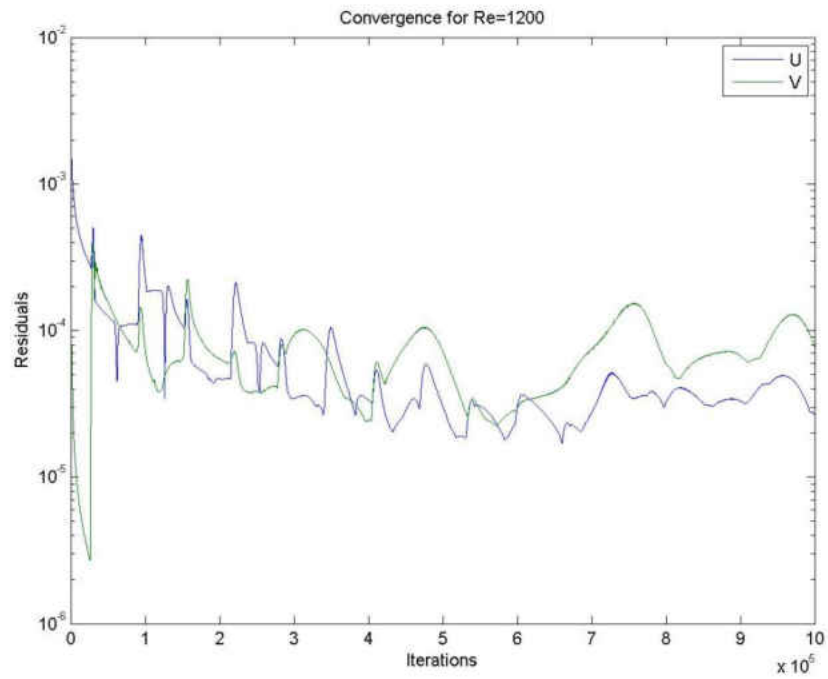


Figure 21: Convergence for BFS, $ER = 1.94$, fine grid, $Re=1200$

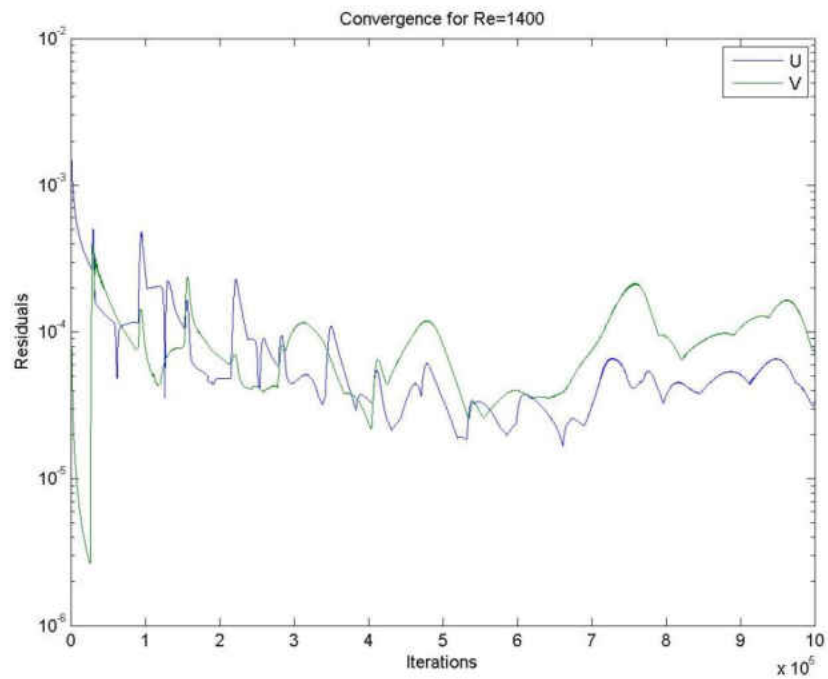


Figure 22: Convergence for BFS, $ER = 1.94$, fine grid, $Re=1400$

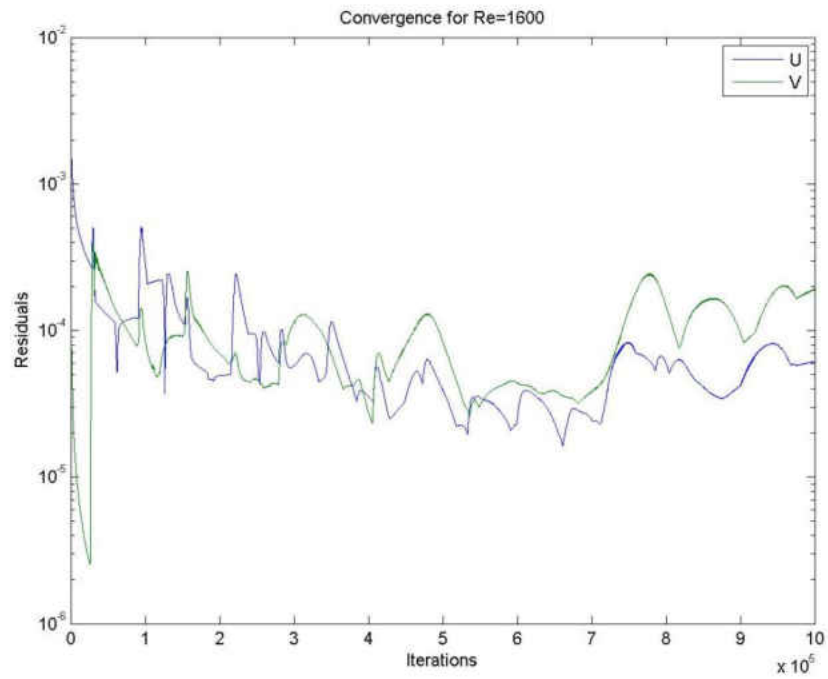


Figure 23: Convergence for BFS, $ER = 1.94$, fine grid, $Re=1600$

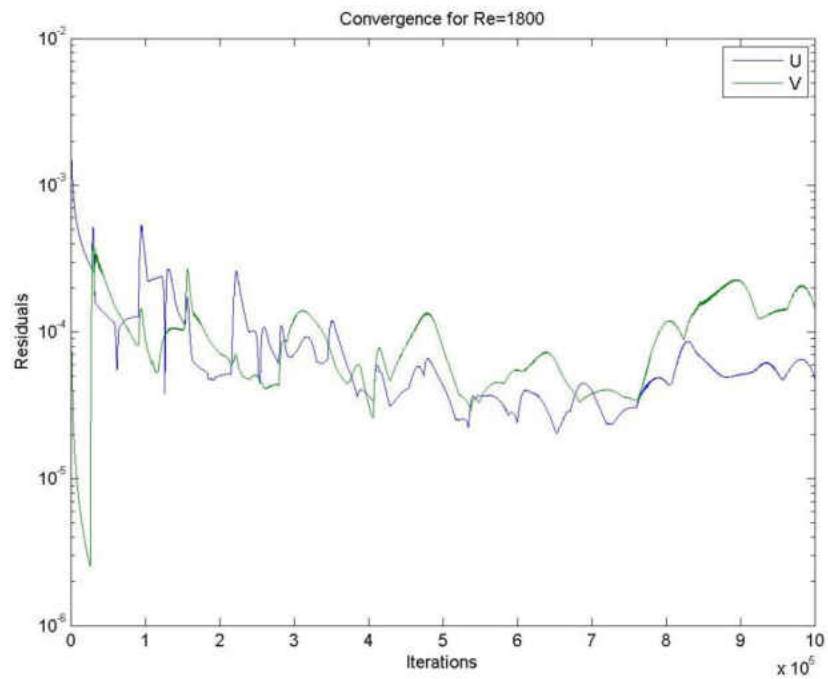


Figure 24: Convergence for BFS, $ER = 1.94$, fine grid, $Re=1800$

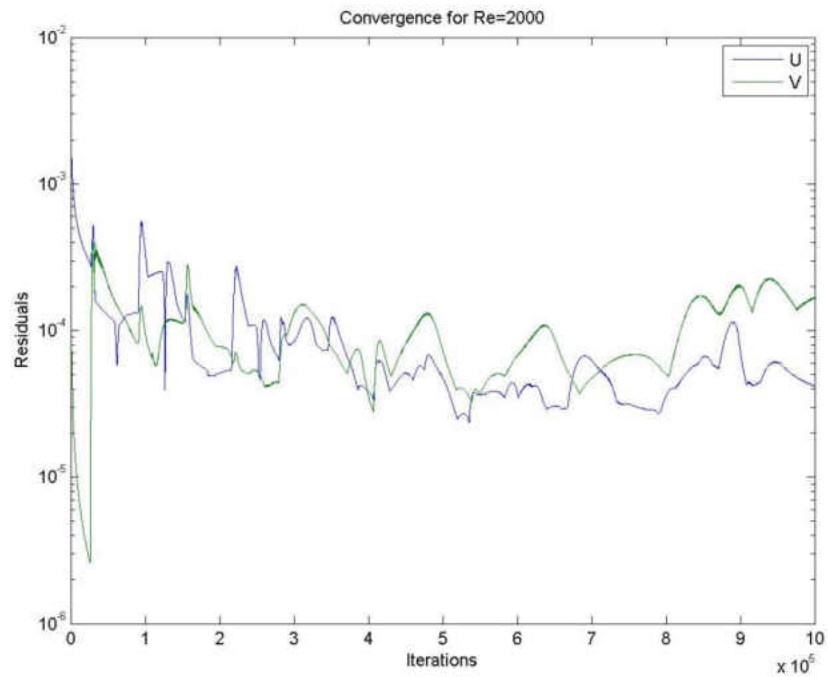


Figure 25: Convergence for BFS, $ER = 1.94$, fine grid, $Re=2000$

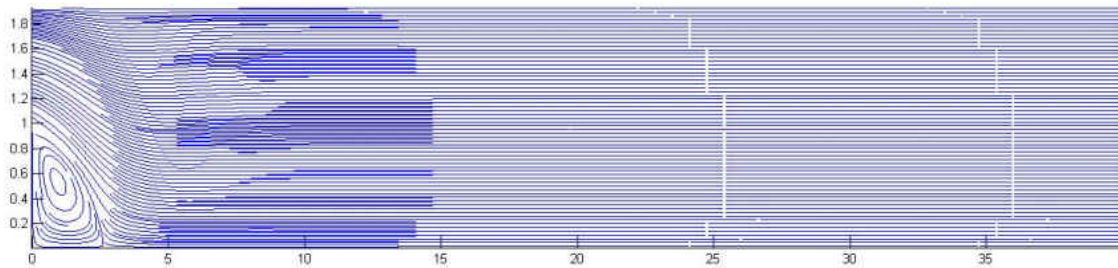


Figure 26: Streamlines BFS with $ER = 1.94$, fine grid, Reynolds 100

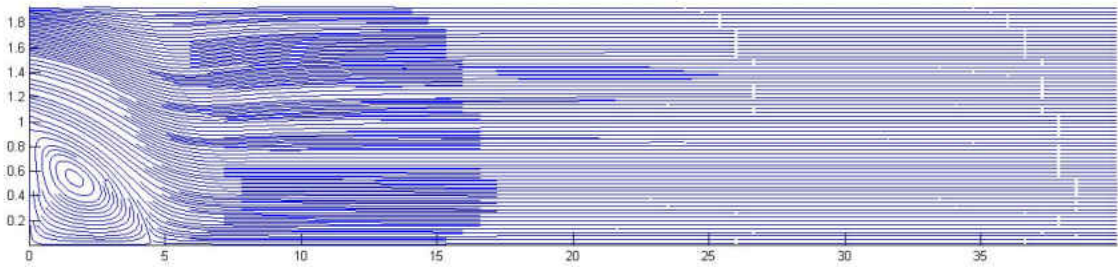


Figure 27: Streamlines BFS with $ER = 1.94$, fine grid, Reynolds 200

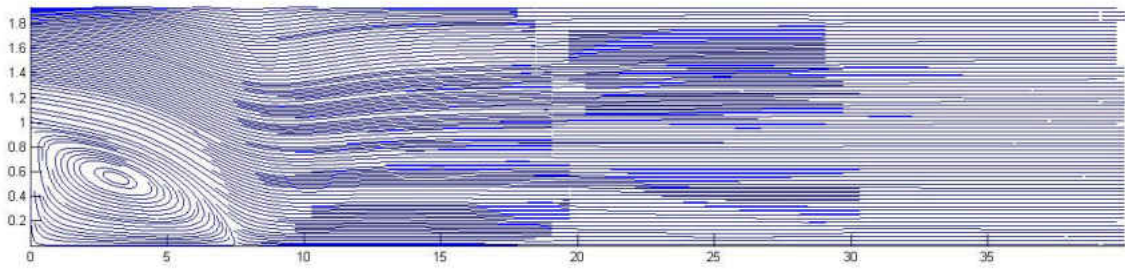


Figure 28: Streamlines BFS with $ER = 1.94$, fine grid, Reynolds 400

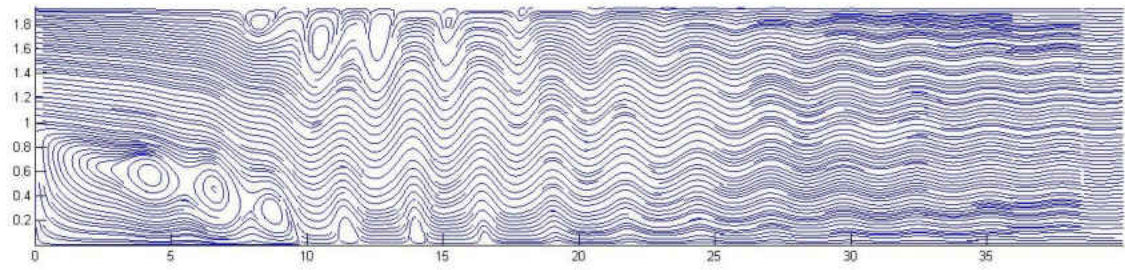


Figure 29: Streamlines BFS with $ER = 1.94$, fine grid, Reynolds 600

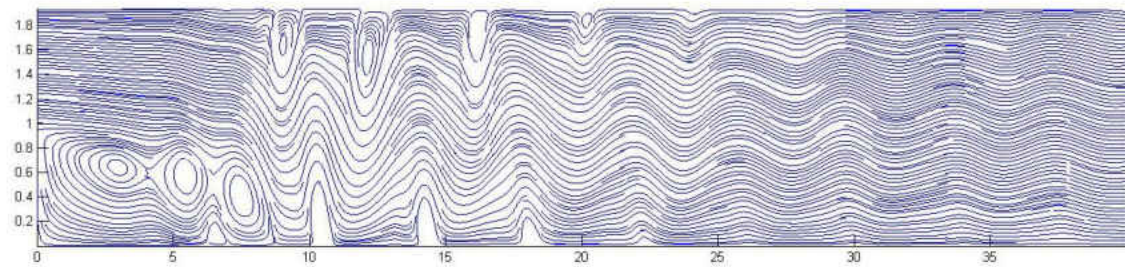


Figure 30: Streamlines BFS with $ER = 1.94$, fine grid, Reynolds 800

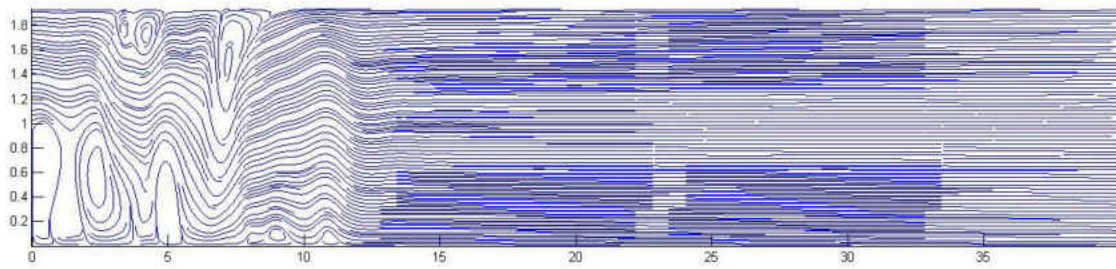


Figure 31: Streamlines BFS with $ER = 1.94$, fine grid, Reynolds 1000

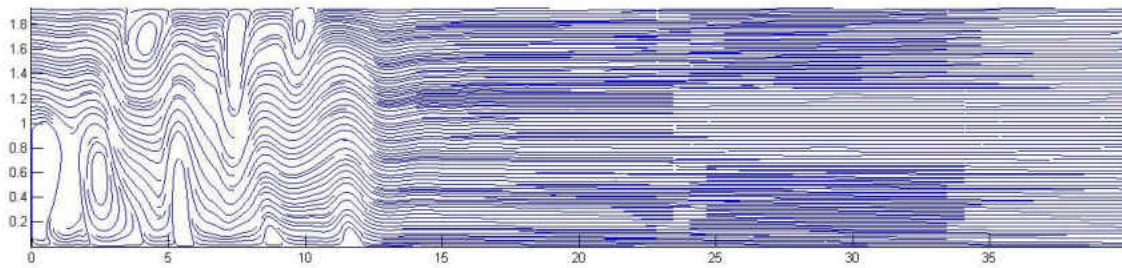


Figure 32: Streamlines BFS with $ER = 1.94$, fine grid, Reynolds 1200

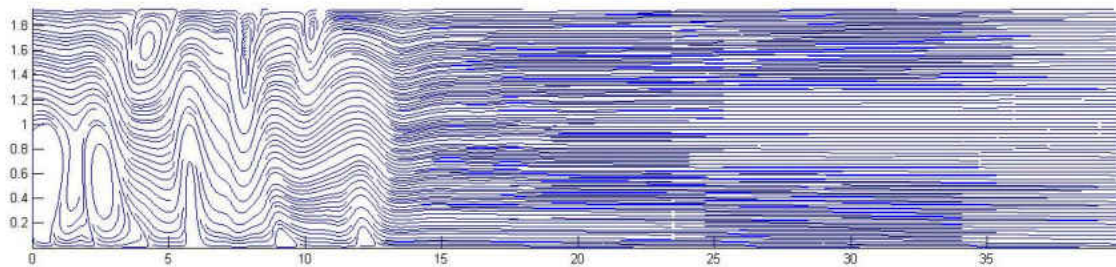


Figure 33: Streamlines BFS with $ER = 1.94$, fine grid, Reynolds 1400

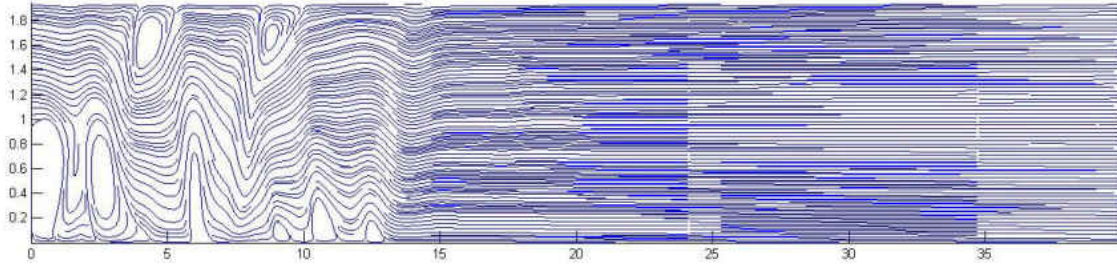


Figure 34: Streamlines BFS with $ER = 1.94$, fine grid, Reynolds 1600

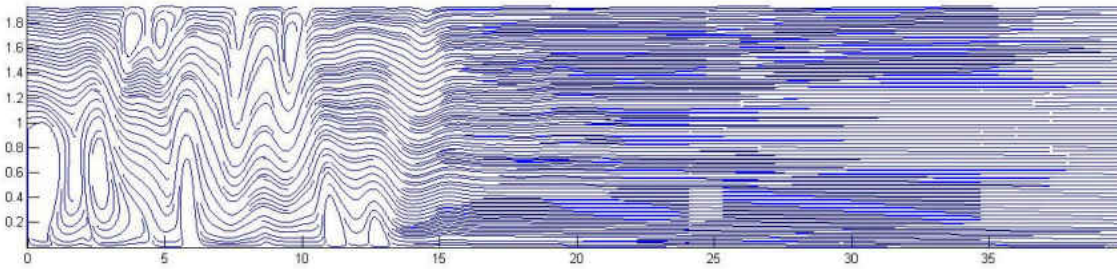


Figure 35: Streamlines BFS with $ER = 1.94$, fine grid, Reynolds 1800

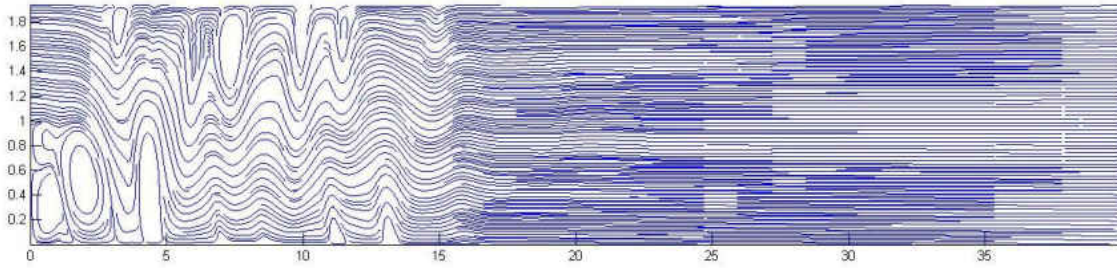


Figure 36: Streamlines BFS with $ER = 1.94$, fine grid, Reynolds 2000

5.3.2 Calculations with an expansion ratio of 1.40

Considering that a backward-facing step of an expansion ratio of almost 2 is highly elliptic, it was decided to perform calculations with a smaller expansion ratio. Results will be

compared with the experiments of Tropea [334] who made an important experimental work with several expansion ratios.

The mesh built has full DNS resolution with $\Delta x = \Delta y$ and no inlet region. The velocity profile was the same Equation 66. The expansion length was chosen to be $10h$ to save memory space and to cover the main vortex.

Table 4 shows the data used in these simulations. As it can be observed, a lot of care was taken in order to keep the local Reynolds number below the maximum recommended values.

Figure 37 shows the re-attachment for the expansion ratio of 1.40 and the Reynolds numbers from 1000 to 4000. The agreement with the experimental results of Tropea [334] is excellent. However, a closer look is necessary to take. Looking at the streamlines shown from Figure 38 to Figure 41, it can be observed that for Reynolds 1000 and 2000, the streamline pattern matches the classical solution.

However, for Reynolds numbers of 3000 and 4000, even that the re-attachment matches the experiments, these two solutions cannot be accepted since they present too much instability. It is clear that the convection level here is smaller than for the case of expansion ratio of 1.94.

Table 4: Data used in BFS with $ER = 1.40$

Re	Nodes X	Nodes Y	Re_{Local}	Δ / Δ_K
1000	800	280	2.5	0.89
2000	1200	420	3.33	1.00
3000	1600	560	3.75	1.01
4000	2000	700	4	1.00

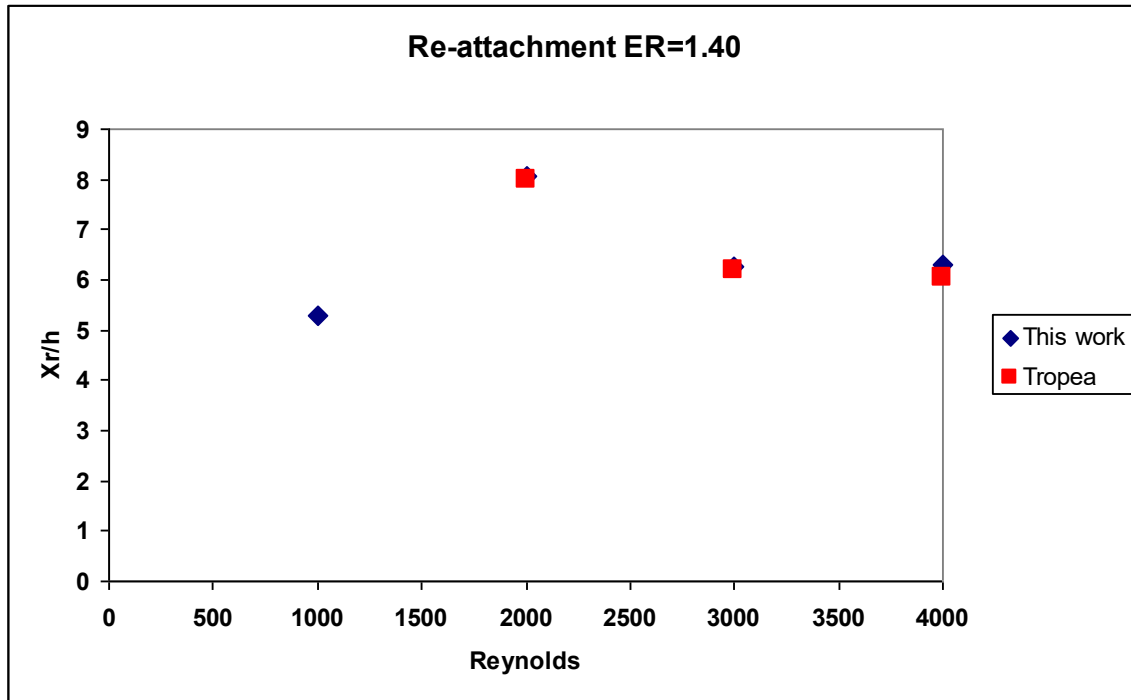


Figure 37: Re-attachment BFS with $ER = 1.40$

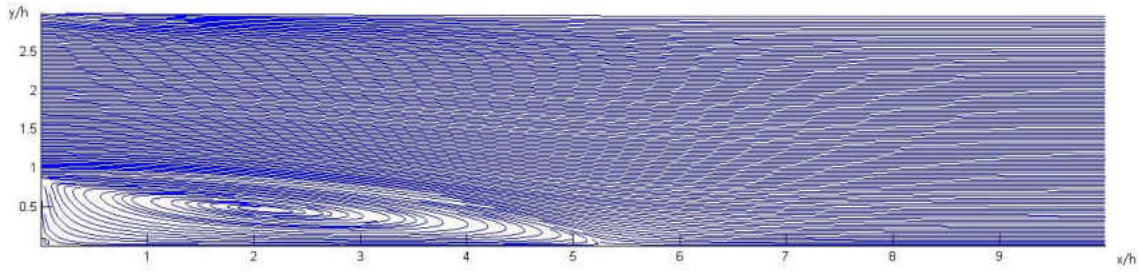


Figure 38: Streamlines BFS with $ER = 1.40$, Reynolds 1000

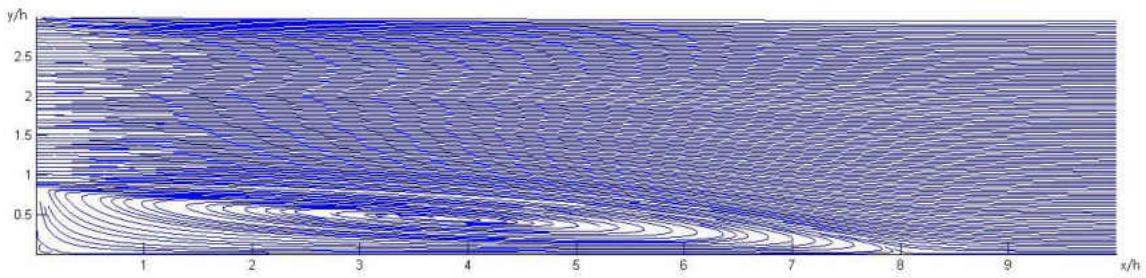


Figure 39: Streamlines BFS with $ER = 1.40$, Reynolds 2000

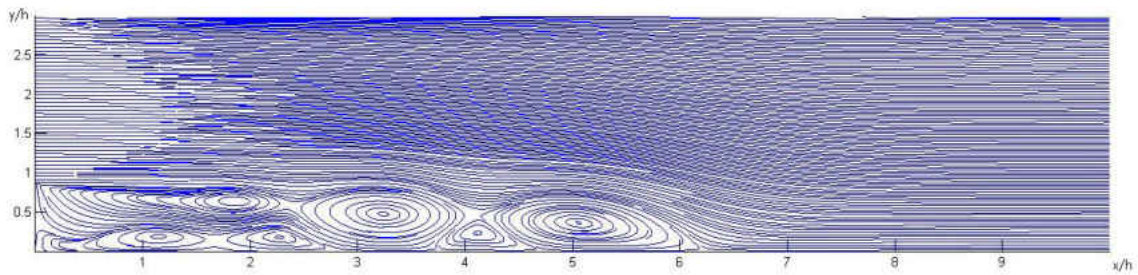


Figure 40: Streamlines BFS with $ER = 1.40$, Reynolds 3000

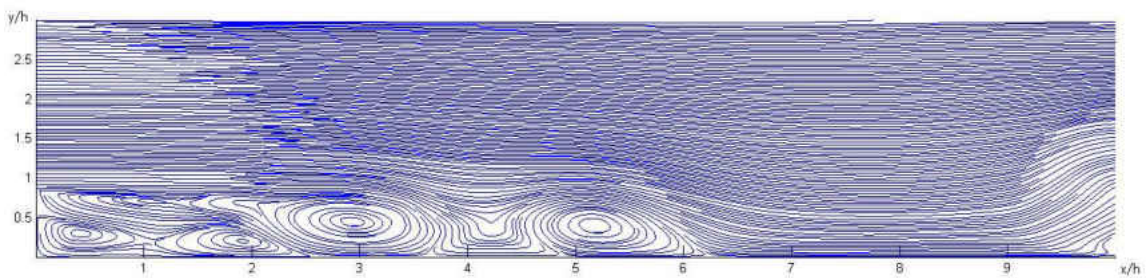


Figure 41: Streamlines BFS with $ER = 1.40$, Reynolds 4000

5.3.3 Calculations with an expansion ratio of 1.14

With the same idea in mind than in the previous section, the calculations with the expansion ratio of 1.14 were performed using a grid with DNS resolution and taking a lot of care with the local Reynolds number.

Table 5 shows the number of nodes used, local Reynolds number as well as the proportion between the delta used and the *Kolmogorov* delta, fundamental parameter in DNS/LES simulations (to be explained in next chapter).

Table 5: Data used in BFS with $ER = 1.14$

Re	Nodes X	Nodes Y	Re_{Local}	Δ / Δ_{κ}
1000	280	228	2.5	0.89
2000	420	342	3.33	1.00
3000	560	456	3.75	1.01
4000	700	570	4	1.01
5000	840	684	4.17	0.99
6000	980	798	4.29	0.97

The convergence history for all computed cases is shown from Figure 42 to Figure 47. The tolerance was set to 10^{-6} since, for flow with small convection intensity, this procedure report excellent and consistent results with high tolerances. However, for this type of flows, this procedure becomes too slow to lower residuals to almost machine level. Figure 48 shows the re-attachment for this expansion ratio and a comparison with the experiments of Tropea [334].

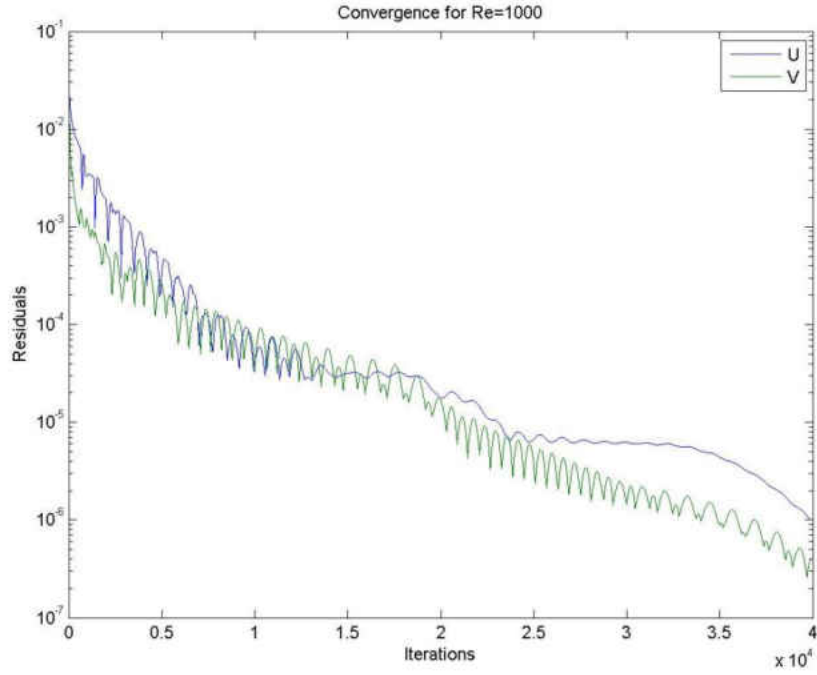


Figure 42: Convergence for BFS, $ER = 1.14$, $Re=1000$

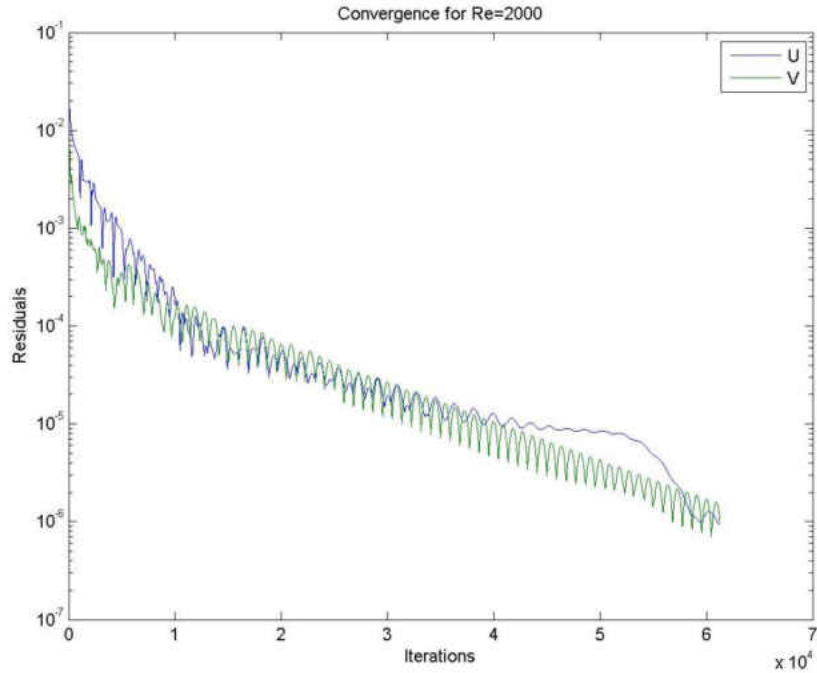


Figure 43: Convergence for BFS, $ER = 1.14$, $Re=2000$

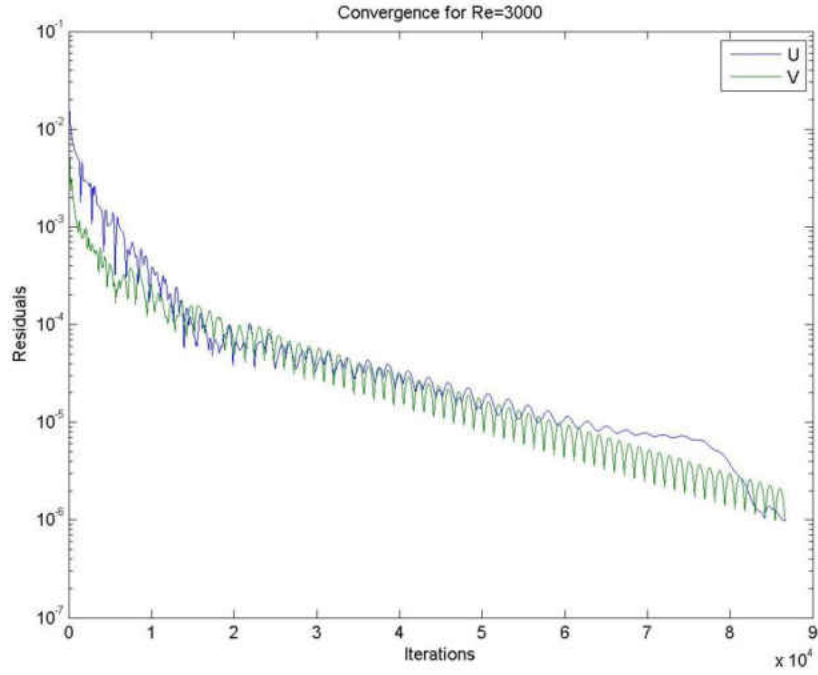


Figure 44: Convergence for BFS, $ER = 1.14$, $Re=3000$

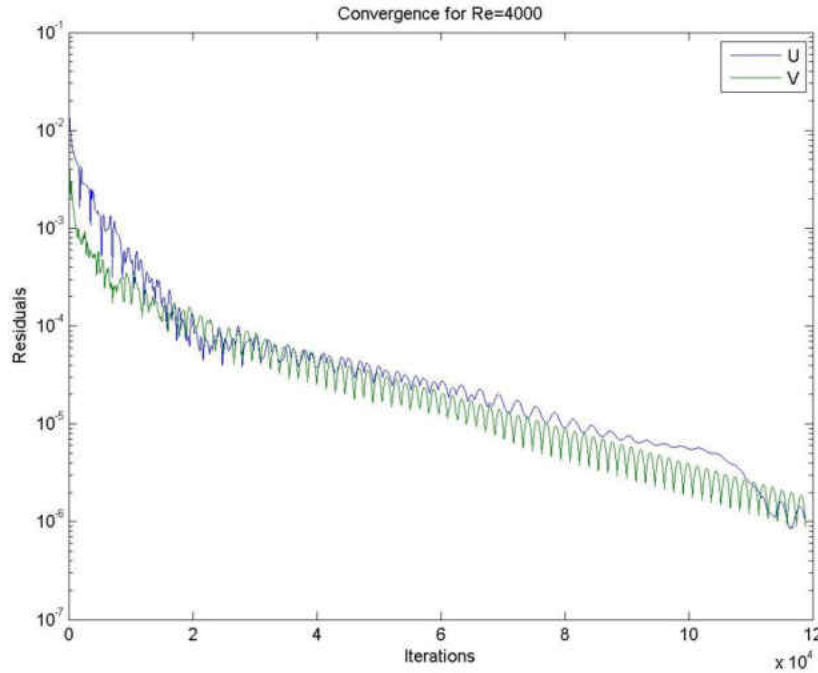


Figure 45: Convergence for BFS, $ER = 1.14$, $Re=4000$

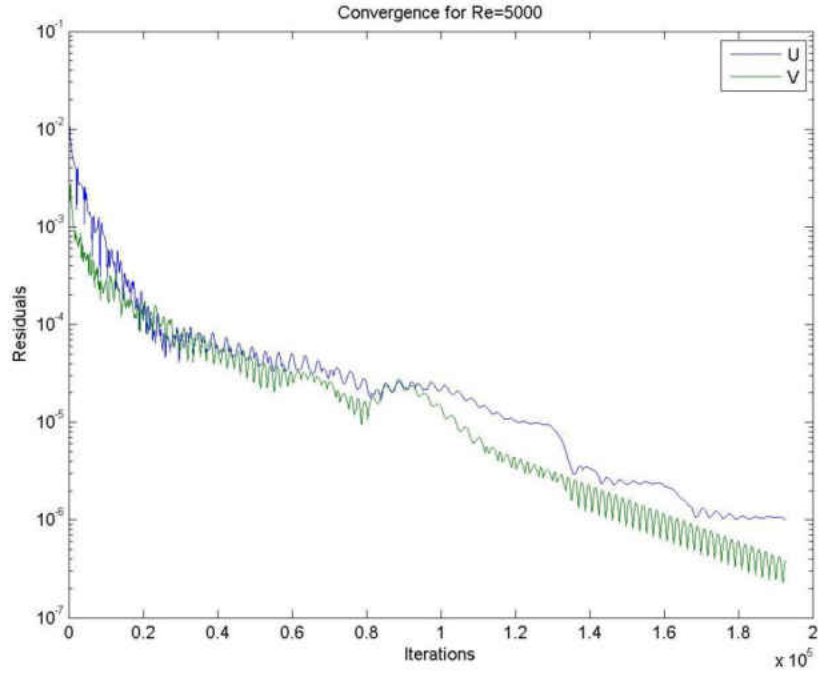


Figure 46: Convergence for BFS, $ER = 1.14$, $Re=5000$

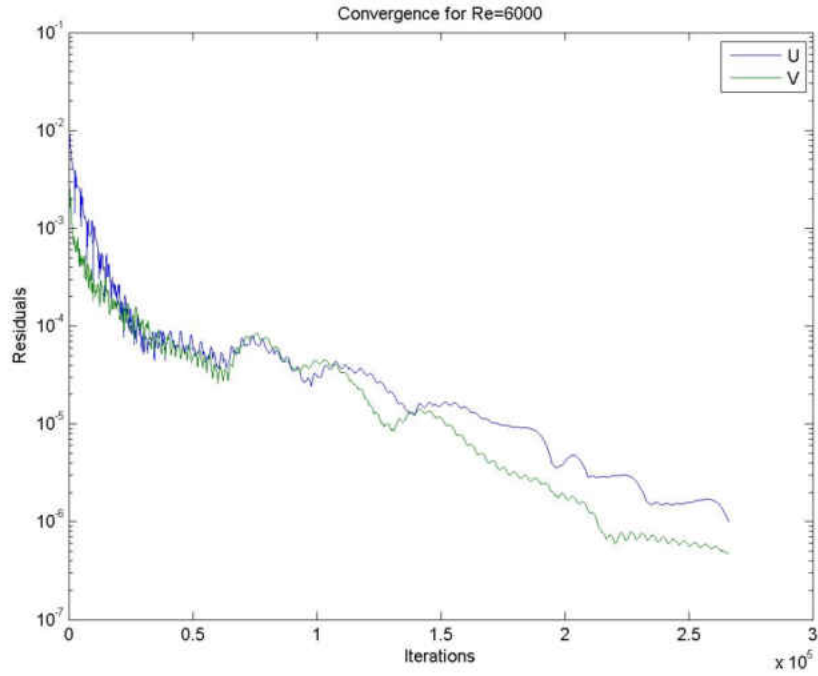


Figure 47: Convergence for BFS, $ER = 1.14$, $Re=6000$

As it can be observed, the re-attachment increases linearly in almost the entire range of Reynolds numbers, and it keeps the same behavior even in the transitional region, where experiments show a constant re-attachment. The behavior reported by this procedure is consistent with previous calculations using the segregated procedure. The streamlines for all cases and the expected behavior can be observed from Figure 49 to Figure 54.

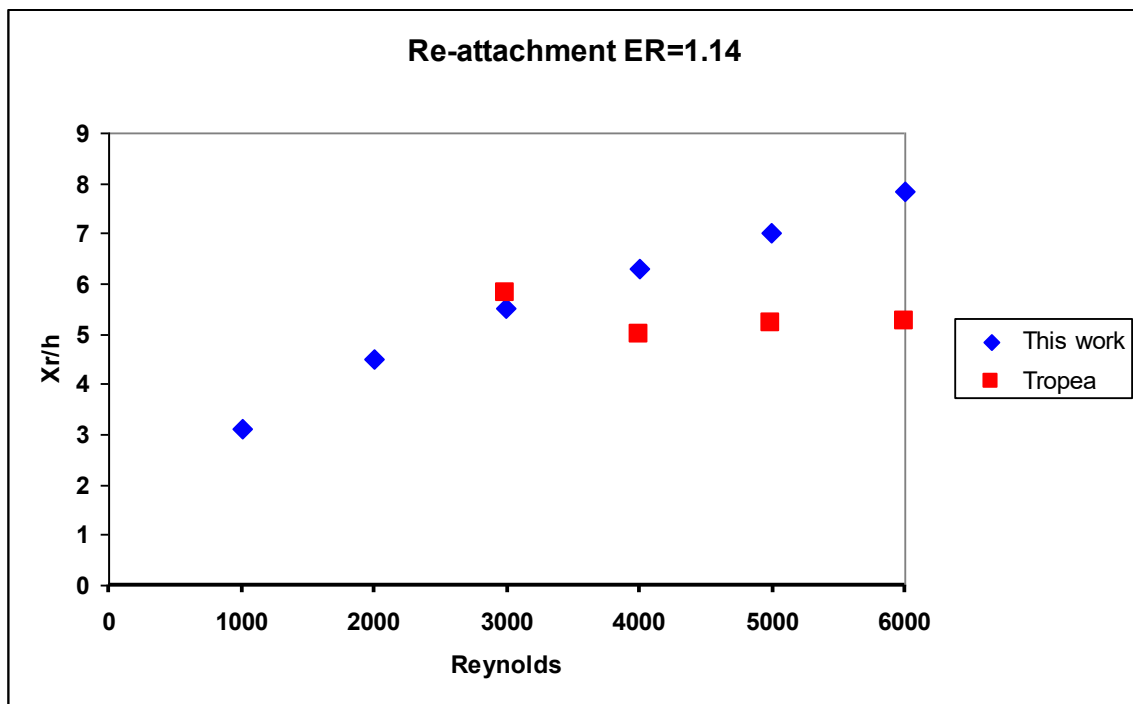


Figure 48: Re-attachment BFS with $ER = 1.14$

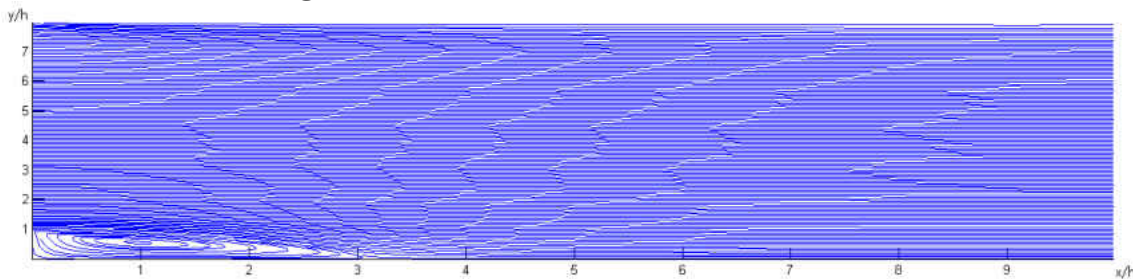


Figure 49: Streamlines for BFS, $ER = 1.14$, $Re=1000$

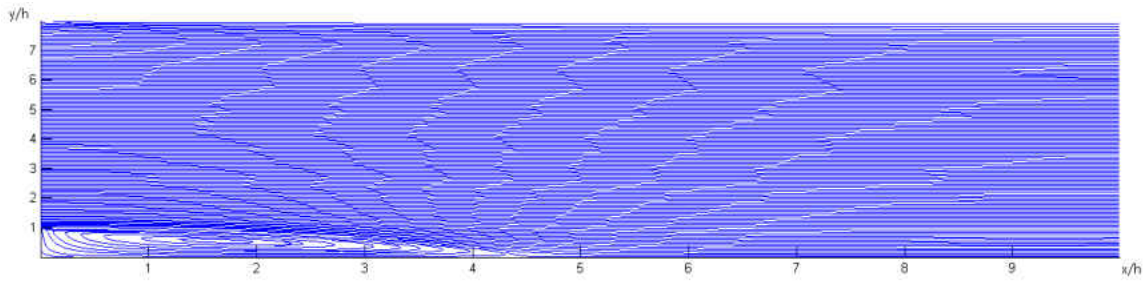


Figure 50: Streamlines for BFS, $ER = 1.14$, $Re=2000$

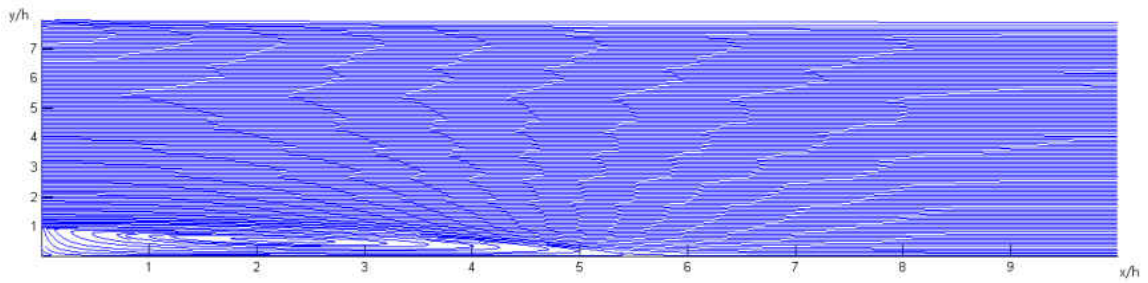


Figure 51: Streamlines for BFS, $ER = 1.14$, $Re=3000$

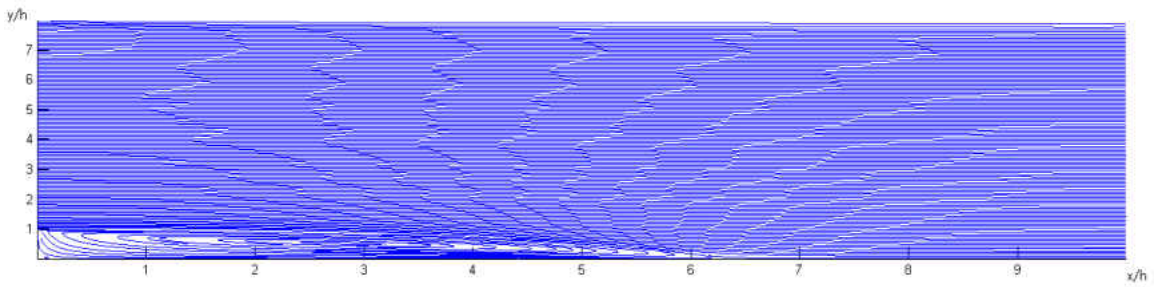


Figure 52: Streamlines for BFS, $ER = 1.14$, $Re=4000$

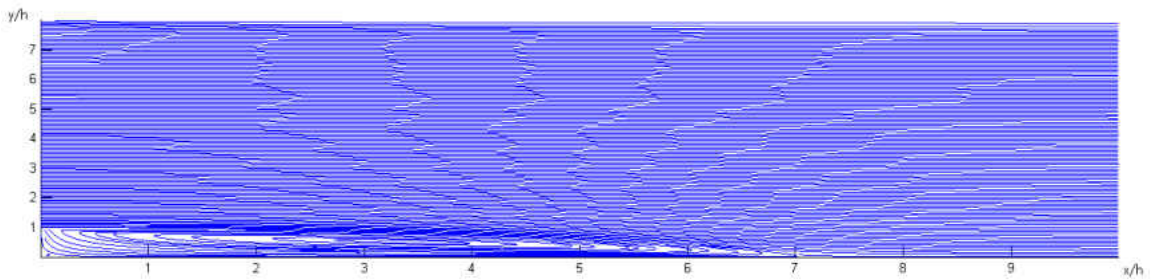


Figure 53: Streamlines for BFS, $ER = 1.14$, $Re=5000$

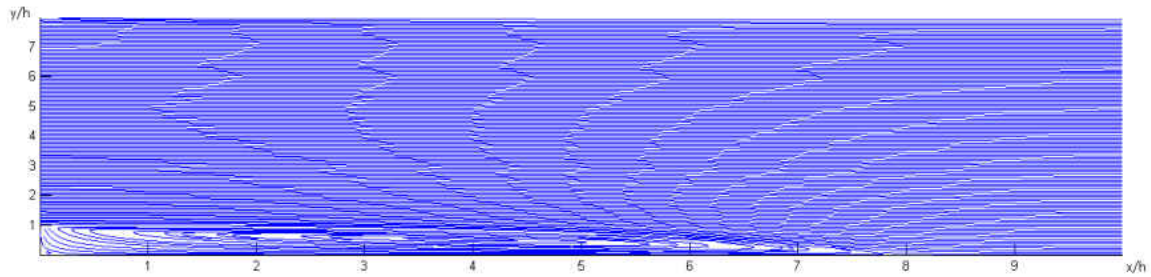


Figure 54: Streamlines for BFS, $ER = 1.14$, $Re=6000$

5.4 2D Steady Lid-Driven Cavity

This problem is one of the most popular cases used for validation of any velocity-pressure coupling scheme. In general, and with some exceptions, a three to five vortex structure is found depending on the method and/or the Reynolds number used.

Figure 55 shows the streamlines for several Reynolds numbers for reference [53]. In the latest calculations published, the pattern of the flow changes from three-vortex structure at low speeds to five-vortex structure at high speeds, as shown in [22], [53], [92], [118], [213] and [347]. For example, in [22], calculations are performed for Reynolds of 10,000, 12,500 and 16,000. A three and four-vortex structure is analyzed and good results are claimed.

A SIMPLE-based procedure is proposed in [53], with calculations for Reynolds number from 5,000 and 15,000 as well as calculation with skewed cavities.

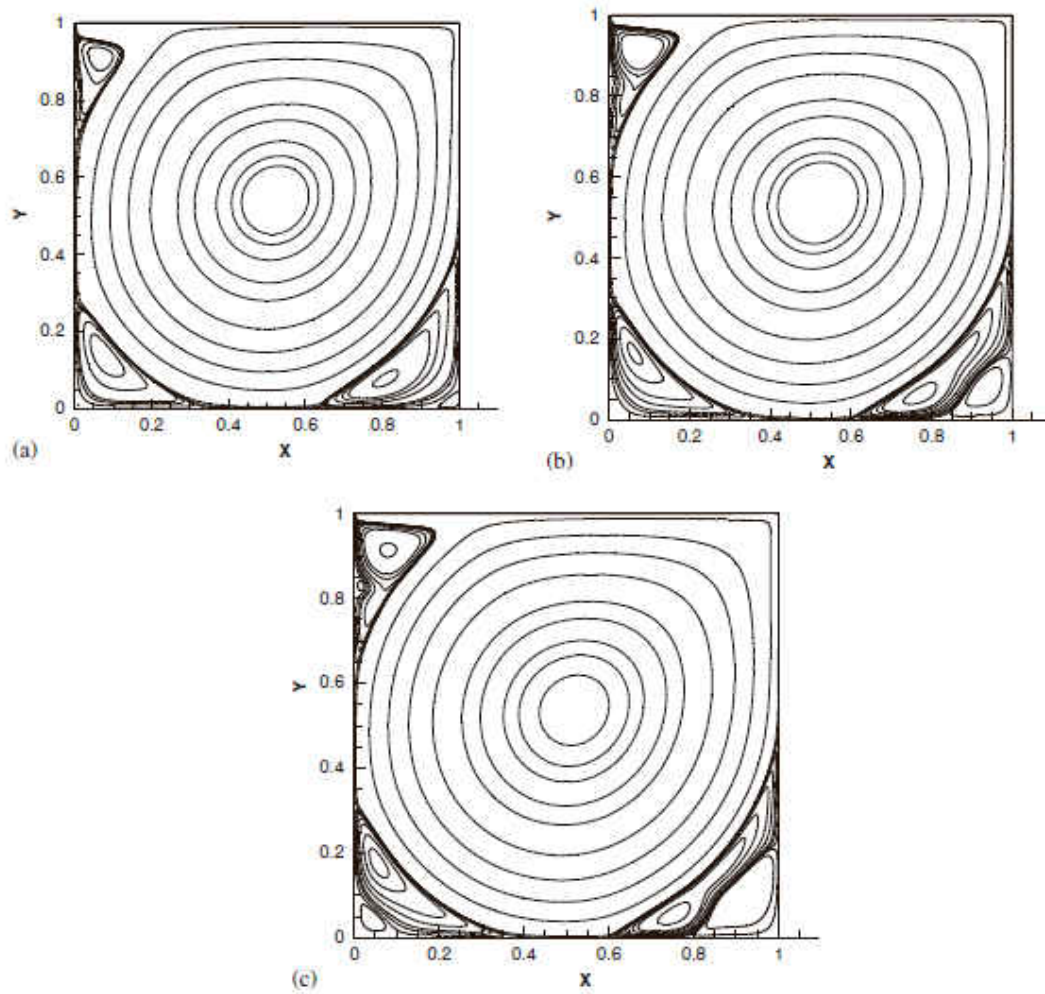


Figure 55: Typical streamlines for different Reynolds numbers [53]
 (a) $Re = 5,000$; (b) $Re = 10,000$; (c) $Re = 15,000$

Similar calculations can be found, as for example [92], in which a five-vortex pattern is obtained and accurate results are claimed. Another interesting case is in [118], with coarse grids and periodic solutions are shown. Calculation with moderate grids can be found in [213] and another transient study using a MAC scheme is presented in [347].

In other cases, a simple three-vortex pattern is computed, as it can be seen in [13], [27], [40], [54], [55],[121], [133], [149], [158], [212], [263], [265], [274], [301], [305], [312], [318], [350] and [364].

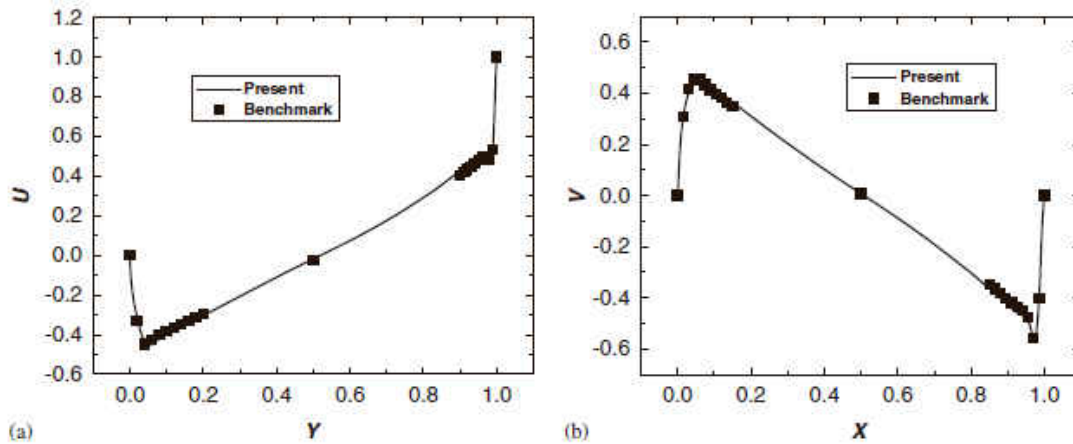


Figure 56: Velocity at vertical center line for $Re = 15,000$ [53]

In [13], a Boundary-Element method is used and accurate calculations are claimed for Reynolds number up to 1,000. A similar work with the same method is in [121] with calculations for Reynolds up to 5,000 but with no convergence for Reynolds number of 7,500.

A couple of transient calculations can be found in [54], [55] and [265] with simulations with Reynolds up to 5,000. A pair of papers with calculations using the finite-element method can be found in [149] and [158], but for low speed flows. A different approach is found in [318], where the streamline-vorticity scheme is used with the Jensen's formula for the boundary conditions. Only the case for Reynolds of 1,000 is presented.

There are some other different procedures presented, as for example, the Chebyshev collocation method in [40] with accurate results claimed for Reynolds up to 1,000. Additionally, the Lattice-Boltzmann method is used to simulate the flow in a cavity with Reynolds numbers up to 10,000. The classical three to four-vortex structure is reported.

In [263], the QMIM method is proposed and compared with SIMPLE with momentum interpolation. Important differences are found when comparing the results with other references.

An interesting study is shown in [274], with calculation for Reynolds up to 1,000. At 600, only one main vortex is present and no secondary eddies are reported.

Similarly, in [301], the flow pattern is studied near the corners but no Reynolds number is specified. A good review of present results (up to year 2,000) can be found in [305], with a full study of the flow in rectangular cavities and the study of the eddy structure near the corners.

References [27], [212], [350] and [364] are different implementations of the SIMPLE method with good agreement in the results for Reynolds up to 1,000, but in [364], important differences are found for greater flow speeds.

With some few exceptions, the most complex structure is normally found with the streamline-vorticity formulation, while the simplest pattern is usually computed with the SIMPLE-based methods. These differences in the results may be product of the inconsistencies found in the boundary conditions for both streamline-vorticity and SIMPLE-based formulations.

Reviewing the literature for more previous works, some very interesting studies are found. The study presented in [46] is one of the first to show that, for low Reynolds, the flow in the cavity show a unique vortex.

For example, in [5], experiments are done where, for large Reynolds, multiple steady states are reported. Additionally, their conclusion is that the cavity flow is locally stable but globally unstable.

A couple of more experiments can be found in [187] and [188]. In the first work, experiments with a rectangular cavity are done. When the span of the cavity is reduced, the size of the downstream sec. eddy becomes smaller (Reynolds less than 2,000). In [188], a review of several experiments is reported. They study the formation of Taylor-Görtler vortices. For

turbulent regime (Reynolds of 10,000), the flow is unsteady in the downstream region of the secondary eddies.

Other similar experiments can be found in [186], where the flow exhibits regions with Taylor instabilities for Reynolds from 1,000 to 10,000. It is curious that they report that turbulent flow begins at Reynolds between 6,000 and 8,000.

In [193], an experimental and numerical study is performed of steady flow in a two-sided cavity. The different instability mechanisms are reported and studied. A pair of natural convection in a cavity can be found in [13], [61], [255] and [268], where excellent agreement is reported.

Another experiment study in rectangular cavities experiment different work can be found in [262]. For Reynolds numbers up to 4,000, they suggest a full inviscid flow pattern.

Finally, another series of experiments are found in [270], for Reynolds number of 3,200 and 10,000. At low Reynolds, structures account for most of the energy contained in the flow, irrespective of aspect ratio. As Reynolds increases, the energy is contained mainly in the high frequency fluctuations.

Some transient calculations with interesting conclusions are found in [124] and [139]. In [122], for Reynolds of 10,000, and after 70 seconds, transient bifurcations appear (2, 3 and 4 vortex pattern). On the other hand, in [139], for Reynolds number up to 30,000, the flow is continuously developing but, for larger Reynolds, the unsteady regime appears, most likely a transition state. In [44], computations are done for Reynolds number up to 15,000. When Reynolds is larger than 5,000, the solution becomes unstable. In [115], a cavity with an aspect ratio of 2 is solved with a time dependent stream function formulation. For Reynolds number of

5,000, a periodic solution is reported and, for Reynolds of 10,000, an asymptotic solution is presented.

Other works use the cavity just to evaluate different numerical schemes. For example, in [32], comparisons are done with Reynolds of 10 and important differences are encountered. Similarly, in [42], different discretization schemes are tested and the strongly implicit scheme produces the best results. In [311], different convection schemes are evaluated. Their conclusion is that second order or higher gives the most satisfactory results. In the same way, [98] use a modified QUICK scheme with good agreement. The work [43] is quite old but is one of the first to report the effect of numerical dissipation in the results.

Different numerical approaches are found in the literature when trying to solve the flow in the cavity. In [47], a streamline-vorticity scheme is presented and the solutions show good agreement with available data.

In [49], a proper orthogonal decomposition is done with DNS data for Reynolds number of 22,000. Different flow phenomena are studied. Additionally, in [63], a method that extends the Jacobi collocation method is presented and validated.

In [69] a reduced DNS simulation is done for Reynolds of 3,200 and 10,000. Even that the results show good agreement with experimental data, the grid is not enough to resolve all the scales.

Reference [110] is a classic benchmark, extensively used for comparison. The streamline-vorticity scheme is used and calculations for Reynolds number up to 10,000 are computed, showing good agreement with available data.

In [171], an integral equation method is used. In spite that no Reynolds number is indicated, the dynamics of the two lower corners is explored, showing how they combine to form

two small eddies and later three, to mix in only one long vortex as the speed of the moving lid is increased.

A pseudo-spectral method is used in [307], where the flow is stable up to Reynolds of 10,000. A first critical value appears before Reynolds of 10,500 and a second critical value is reported at a Reynolds of about 15,000. Then the flow becomes periodic in time, indicating a Hopf bifurcation.

In other references, [146] use a modified MAC method with Reynolds up to 2,000. A full 3D pattern is shown at high speeds as result of Görtler-like vortices and the corner vortices. In [250], a finite-difference scheme is used for Reynolds numbers up to 50,000. For Reynolds larger than 30,000, the flow responds to the Batchelor's model for separated flows. Secondary vortices decay as Reynolds increases. Another study of the 3D cavity can be found in [68].

A different calculation is shown in [302] and [303], where the flow in a cylindrical container is computed. An eigenfunctions expansion method is presented to compute the Stokes flow. The method show some special features in the 3D flow.

In [130] a method for integral flow equations is presented and validated. In [165], the GSMAC finite-element method is shown with good agreement for Reynolds up to 1,000. The 3D unsteady motion is investigated. Another 3D flow is computed in [192], using a Chebyshev pseudo-spectral approach, validated for Reynolds of 1,000.

In [203] a grid adaption method is used to validate results up to Reynolds of 1,000. A high order method is presented in [256], where better results are claimed with respect to [110]. Similarly, in [297] uses another high order method for Reynolds up to 10,000. Finally, in [306] a second order scheme is shown with flow effects claimed not to be reported before. A couple of

DNS/LES simulations can be found in [155] and [365], for Reynolds numbers from 3,200 to 10,000. Excellent agreement is reported with respect to experimental data.

As expected, there are many other references in the area, as for example [3], [20], [38], [70], [71], [72], [99], [132], [144], [147], [150], [169], [189], [190], [239], [254], [296], [304], [315] and [321].

For these series of calculations, only four characteristic Reynolds numbers were computed: 100, 1000, 5000, 10000. The mesh used was the same for all calculations was 800x800, enough considering the criteria of the local Reynolds number. For higher Reynolds number, no full convergence was obtained.

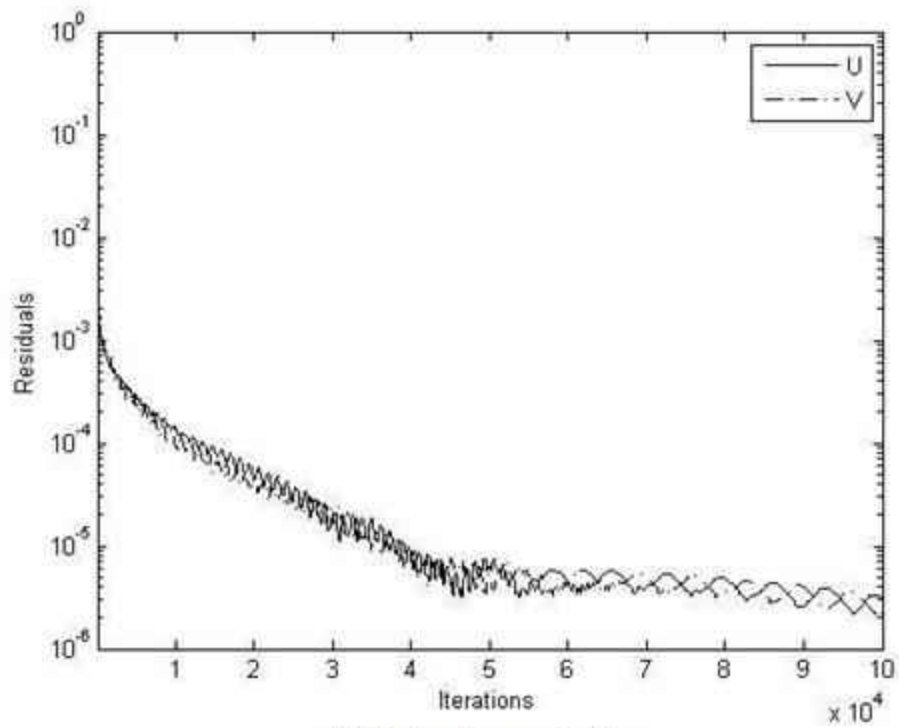
Table 6: Data used in Lid-driven cavity

Re	Nodes X	Nodes Y	Re_{Local}	Δ / Δ_{κ}
100	800	800	0.1	0.1
1000	800	800	1	1
5000	800	800	5	5
10000	800	800	10	10

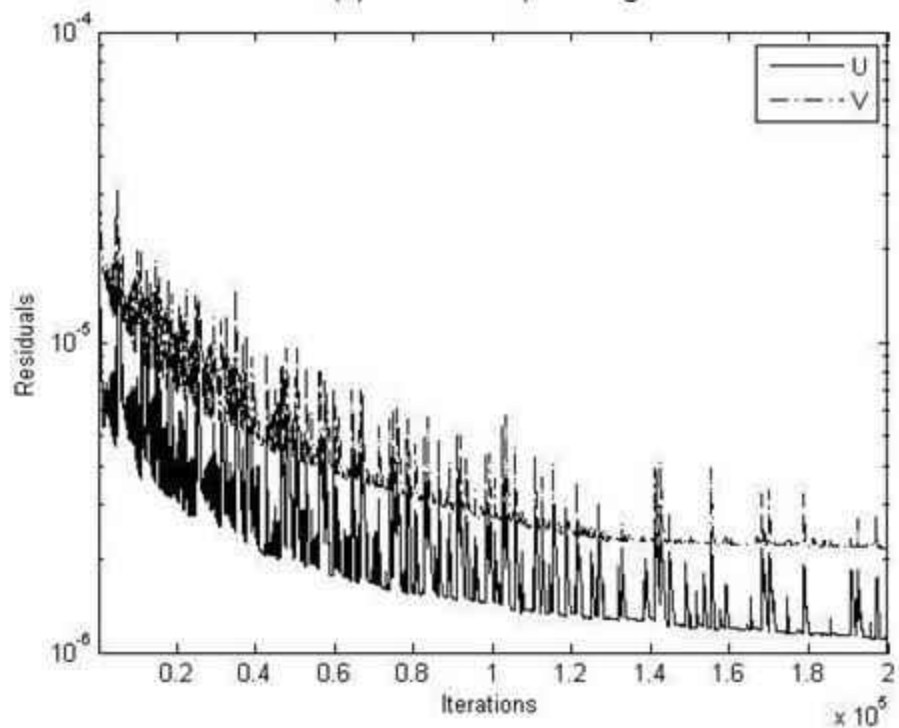
Table 6 shows the grid details used in these calculations. The strategy in this geometry was to use first-order upwinding to get the initial guess of the calculation with second-order upwinding. Figure 57 shows the convergence history for the case of Reynolds 5000. From Figure 58 to Figure 61, the streamlines for all cases computed is shown, with the expected behavior. The only difference is that for the case of Reynolds number of 10000, shown in Figure 61, the

size of the two smallest vortices (adjacent to the lower corners) are a bit smaller than other references. These two vortices were larger in the solution with first-order upwinding.

From Figure 62 to Figure 65, both velocity components and their comparison with the classical results of Ghia [110] are shown. For Reynolds numbers of 100, 1000 and 5000, the agreement is excellent. For the case of Reynolds number of 10000, this procedure under-predicts both components. This difference may be produced by the large value of the local Reynolds number, in the limit of the recommended value of 10.



(a) First order upwinding



(b) Second order upwinding with RBF interpolation

Figure 57: Convergence LDC for Reynolds number of 5000

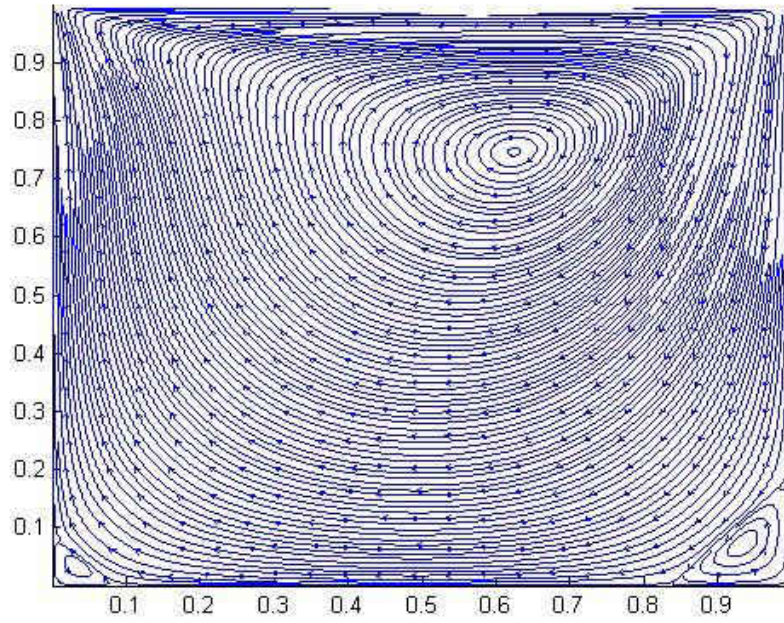


Figure 58: Streamlines LDC for Reynolds number of 100

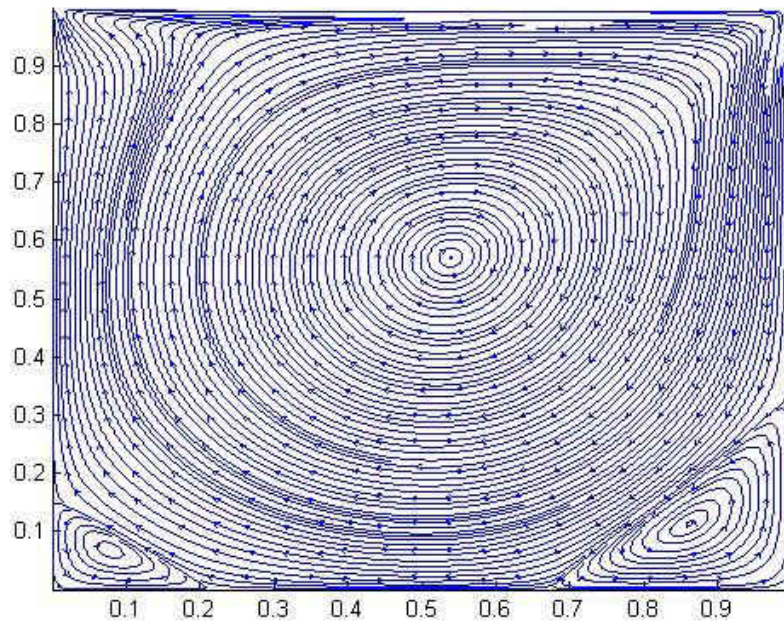


Figure 59: Streamlines LDC for Reynolds number of 1000

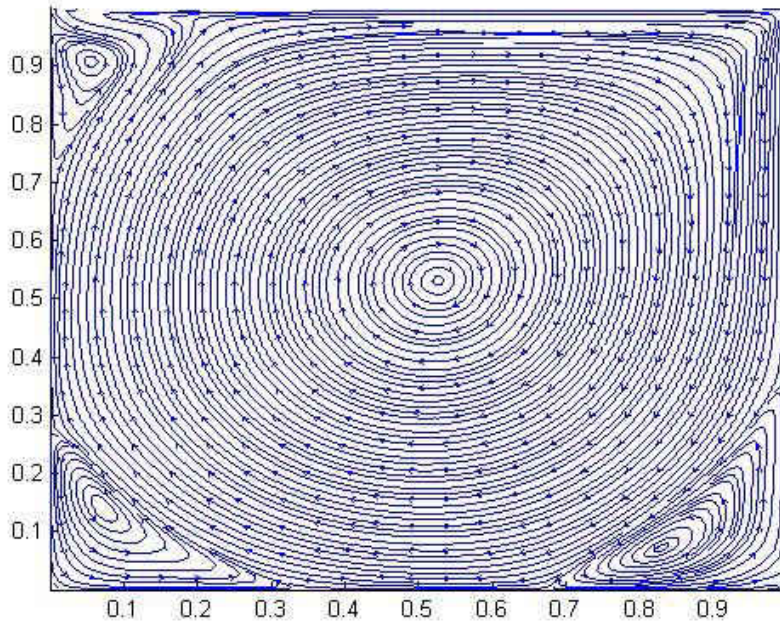


Figure 60: Streamlines LDC for Reynolds number of 5000

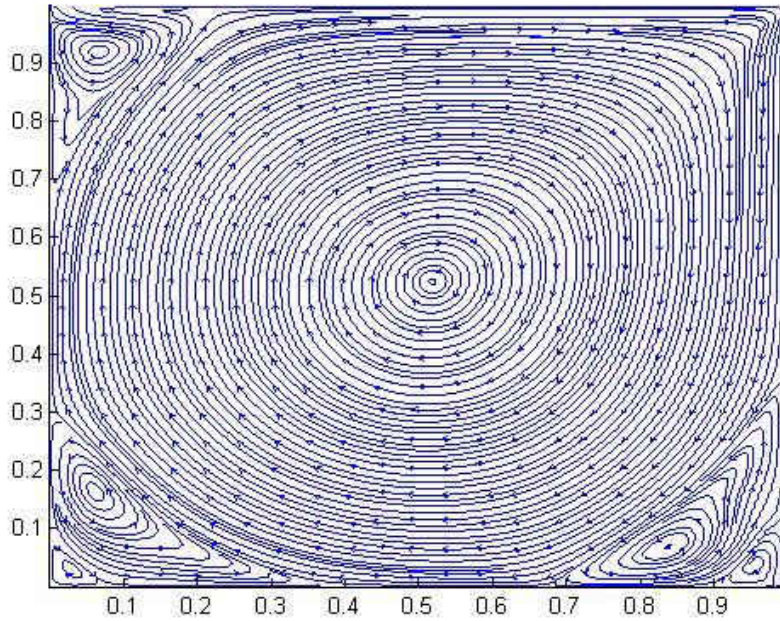


Figure 61: Streamlines LDC for Reynolds number of 10000

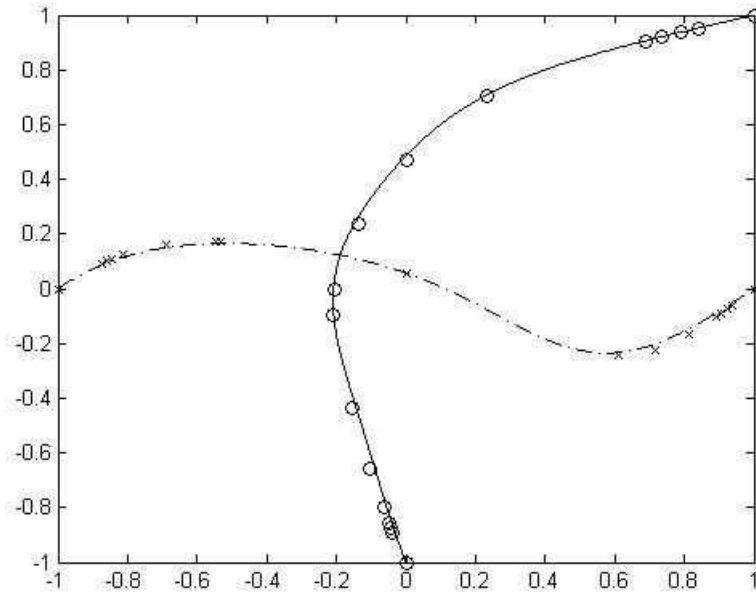


Figure 62: Velocity at mid-plane LDC for Reynolds number of 100
 (“x”, “o”...[110]; “-”, “.-”...this work)

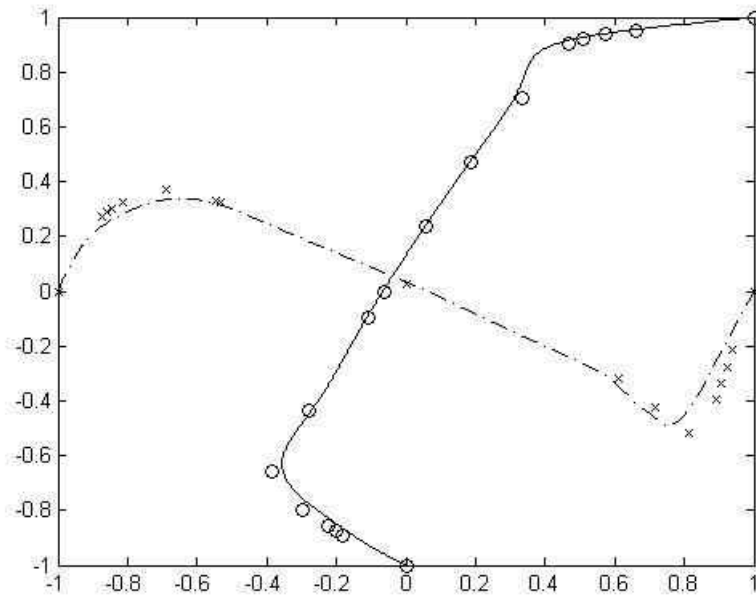


Figure 63: Velocity at mid-plane LDC for Reynolds number of 1000
 (“x”, “o”...[110]; “-”, “.-”...this work)

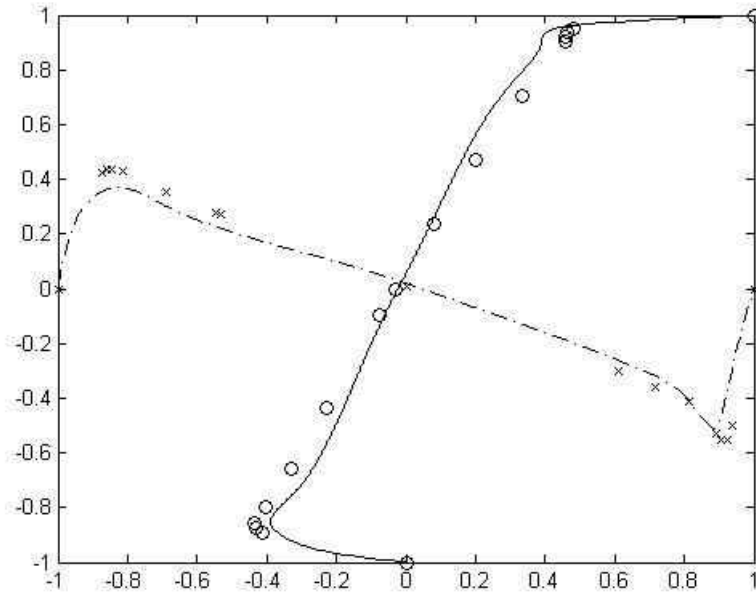


Figure 64: Velocity at mid-plane LDC for Reynolds number of 5000
 (“x”, “o”...[110]; “-”, “.-”...this work)

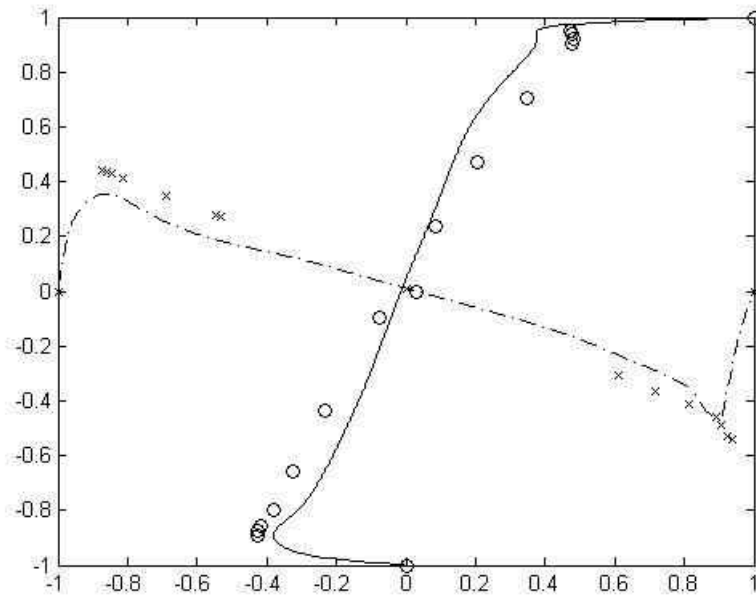


Figure 65: Velocity at mid-plane LDC for Reynolds number of 10000
 (“x”, “o”...[110]; “-”, “.-”...this work)

5.5 Final comment on validation

In this chapter the intention was to show all calculations done for the validation of the present procedure. Comparing which results are correct and which are not in the backward-facing step, it is possible to conclude that low aspect ratios are directly related to low convection intensity.

For the case of expansion ratio of 1.94, the good agreement between calculations with the coarse grid and the experiments was just a mere coincidence. Calculations with a DNS resolution grid show that, when convection is high, this meshless procedure shows some instability.

The fact that, in the expansion ratio of 1.40, the results are correct for Reynolds 1000 and 2000 and incorrect for 3000 and up (where transition begins) is again another coincidence. As soon as the convection level increases, the proposed procedure shows signs of instability.

The good agreement obtained for the expansion ratio of 1.14 is particular since the flow pattern is basically parabolic, with low convection intensity. This issue is consistent with the good agreement obtained in all cases solved in the lid-driven cavity. It is convenient to underline that there are not many publications of meshless procedures solving highly convective flows.

In general it is possible to say that the proposed meshless procedure provides good predictions if the convection intensity is low or moderate.

CHAPTER SIX SIMULATION OF TURBULENT FLOW

6.1 Direct Numerical Simulation

The basic idea of Direct Numerical Simulation is to solve the full Navier-Stokes equations with a grid fine enough to describe all the details involved. The size of the grid spacing is directly associated to the smallest scales that describe the flow.

The large scales are usually associated to the geometry of the flow, while the small scales are related to the flow itself. Estimates of the size of the smallest scales are available from simple dimensional reasoning. The Kolmogorov microscale η is defined if we assume that it only depends on the fluid viscosity ν and the rate of dissipation of energy ε [197]:

$$\eta = \left(\frac{\nu^3}{\varepsilon} \right)^{1/4} \quad (67)$$

A connection with flow Reynolds number can be made if we make some further assumptions. For a flow in equilibrium we may take production equal to dissipation. The production can be assumed to scale as U^3/L where U is a reference of bulk velocity and L is a length scale of the problem, usually fixed by the geometry. Both U and L are characteristic of the largest scales of the turbulence. Thus we can write:

$$\frac{\eta}{L} \approx Re^{-3/4} \quad (68)$$

The number of grid points required for a given simulation will be proportional to L/η and hence to $Re^{3/4}$. From practical simulations of flows away from solid boundaries, it appears that the actual resolution required is approximately 5η .

For flows near the wall, some recommended references are $\Delta x^+ < 15$ (streamwise), $\Delta z^+ < 8$ (spanwise) and $\Delta y^+ < 10$ (normal).

As expected, the time step must be small enough to solve the smallest scales. For the majority of algorithms (fully explicit and mixed explicit/implicit), the time step required for stability reasons is already significantly smaller than this time scale [197].

Despite restrictions of the Reynolds number and the variety of flows available, the use of DNS data is changing the way turbulence models are built and tested. In particular the completeness of information available from simulation, including terms such as pressure-velocity correlation, that have not been available from experiments, is enabling the use of DNS data to test closure models at several levels.

At this moment, the variety of problems solved with DNS with internal flows is restricted mainly to geometries described by simple known coordinate systems.

Examples of annular duct [357] or backward-facing step [197], [251] are not frequently solved since they require a very fine grid. The most computed problems are DNS in channels [2], [135], [141], [161], [174], [235], [248], and [333], DNS in ducts and pipes [253], [272], [278], [327], [344], and [353] and direct simulation of Couette flow [154], [216], and [335].

Another interesting study can be found in [300], where transitional flow in a channel is analyzed, with Reynolds numbers ranging from 1,800 to 4,000.

In general, mesh sizes range from roughly 128^3 for low Reynolds numbers to 256^3 for higher Reynolds numbers. In the case of [235], where a long duct is solved, a mesh of $1,536 \times 257 \times 384$ is used. For Couette flows, meshes of the order of $1024 \times 512 \times 96$ are found in the literature.

An exception of flow in generalized coordinate system can be found in [137], [197], where the serpentine channel flow and the rotating serpentine duct flow are solved with grids from $192 \times 32 \times 64$ to $1,536 \times 125 \times 256$ and $Re \approx 5,000$.

6.2 Large Eddy Simulation

When computing resources are not enough to solve a given problem, a coarser grid is used. This coarser grid is able to resolve the larger eddies in the flow but not the ones which are smaller than one or two cells. From a physical point of view, there is an interaction between the motions on all scales so that the result for the large scales would generally be wrong without taking into account the influence of the fine scales on the larger ones [197].

There are several common ways of reducing the number of degrees of freedom in the numerical solution [284]:

- a) By calculating the statistical average of the solution directly (RANS), which is used mostly in engineering calculations.
- b) By calculating directly only certain low-frequency modes in time and the average field (URANS, Semi-Deterministic Simulation SCS, Very Large Eddy Simulation VLES and Coherent-Structure Capturing CSC).

- c) By projecting the solution on the ad hoc function basis and retaining only a minimum number of modes, to get a dynamical system with fewer degrees of freedom (Proper-Orthogonal Decomposition POD).
- d) By calculating only the low-frequency modes in space directly. This is what is done in Large Eddy Simulation.

The scale selection that the Large Eddy Simulation technique is based on is a separation between large and small scales. In order to define these two categories, a reference or cutoff length first has to be determined.

The scales that are of a characteristic size greater than the cutoff length are called large or resolved scales, and others are called small or subgrid scales. The latter are included by way of a statistical model called a subgrid model. An example of a sub-grid model can be found in [109].

On the mathematical model, the theoretical scale separation is formalized in the form of a frequency low-pass filter. The application of this filter to the Navier-Stokes equations yields the constitutive mathematical model for the Large Eddy Simulation:

$$\frac{\partial \bar{u}_i}{\partial t} + \frac{\partial}{\partial x_j} (\bar{u}_i \bar{u}_j) = -\frac{\partial \bar{p}}{\partial x_i} + \nu \left(\frac{\partial \bar{u}_i}{\partial x_j} + \frac{\partial \bar{u}_j}{\partial x_i} \right) - \frac{\partial \tau_{ij}}{\partial x_j} \quad (69)$$

$$\tau_{ij} = \overline{u_i u_j} - \bar{u}_i \bar{u}_j$$

where two modeling approaches are mostly used to simulate the term τ_{ij} : functional modeling, based on the representation of kinetic energy transfers, and structural modeling, which aims to reproduce the eigenvectors of the statistical correlation tensors of the subgrid modes. With respect to the stresses τ_{ij} , the model of Smagorinsky [313] have been widely used since keeps the concept of the turbulent viscosity.

For internal flows, and in general, LES allows the solution of more complex problems. Examples of LES in annular duct and pipes can be found in [223], [357], while for the backward-facing step, some studies can be found in [4], [113], [120], [143] and [170].

As expected, the most solved problem is turbulent flow in a channel [9], [39], [66], [87], [113], [120], [125], [126], [129], [131], [143], [153], [211], [241], [280], [299], [323], [330], [355], and [363]. However, other interesting studies are the lid-driven cubic cavity [113], [127], flow in ducts and pipes [138], [227], [325], and [363], Taylor-Couette flow [66], turbulent mixing layers [238], and flow in an annular duct [356].

Due to the amount of computing resources, LES allows the solution of turbulent flow in complex geometries, as the repeating constricting channel [336] and flow over a staggered cube array [355].

Finally, two very complex cases of LES in a nuclear power plant and flow in a mixed-flow pump can be found in [284]. In this reference, there are two interesting cases of external flow: flow around a landing gear configuration and flow around a full scale car.

6.3 Generating inflow conditions

The first fundamental hypothesis of turbulence is that permanent fluctuations must exist at inflow in order for the turbulence to appear. When the speed of the flow is slow, viscous forces damp those fluctuations and turbulence will never occur. At higher speeds, the flow is dominated by convection forces and the non linear phenomena will govern the fluid motion.

Of course, there is an intermediate stage call transitional flow, where the behavior of the flow is highly unstable and there is not a well defined fluid structure. From experiments, it is

well known that at least 1% percent of fluctuation is necessary to produce a permanent turbulent regime [245].

For the generation of inflow conditions, there are a variety of techniques that can be used [73], [151], [221], [238], and [355]:

a) *Random number or white noise*: This method is very simple but it is the worst of all possible techniques. Computer-generated random data is normally of a very high frequency, changing rapidly and randomly between time steps. However, the velocity field in a real turbulent flow does have certain correlations.

b) *Stochastic fluctuations with a prescribed energy spectrum*: Inflow conditions of this type try to provide a more realistic turbulent inflow by taking low wave numbers or low frequencies in the velocity field. However, individual flows encountered in practical applications may not always follow a prescribed energy spectrum.

c) *Synthetic eddy method and proper orthogonal decomposition*: The idea is to focus directly on prescribing coherent structures in the inflow. It tries to reproduce prescribed first- and second-order one-point statistics, characteristic length and time scales, and the shape of the coherent structures. Unfortunately, this technique cannot be applied systematically for general flows as it requires a previous realization of the flow.

d) *Perturbed laminar inflow*: It is based on a simple perturbation added to a mean velocity profile. There are situations where the inflow is laminar and the transition to turbulence takes place downstream. In general, the rms of the perturbations does not affect the flow too much if it is not too large. When the perturbation is very large, the flow will be of a pulsating nature.

e) *Inflow from an auxiliary simulation*: Obtaining data from an auxiliary computation or *precursor simulation* is an accurate technique to provide inflow conditions. On the other hand, it is costly because it requires reproducing the entire history of the flow. If the precursor simulation is not run in parallel with the main one, the results can become problematic if a signal (acoustic wave, for example) is emitted by the main simulation [284].

f) *Other inflow conditions*: The use of periodic boundary conditions or inflow conditions without perturbations will avoid inflow and outflow completely. However, the applicability of this type of inflow conditions is restricted to flow configurations that are indeed periodic owing to their geometry.

One common issue that all these methods have is that they never report the percentage of those fluctuations. For inflow conditions, experiments report typical values from 4% to 6%, with a minimum of 1%, but usually no paper reports what was the percentage of fluctuation used to generate all inflow conditions.

6.4 The wall roughness

The second fundamental hypothesis of turbulence is the roughness of a solid surface near the fluid [298]. The well known experiments of Nikuradse, with controlled wall roughness, are the most complete set of experimental data available.

The difficulty to reproduce the general random behavior of wall roughness of any kind with a coordinate system has limited the numerical study of this hypothesis. Usually, most DNS and LES calculations are limited to smooth surfaces.

In DNS for example, there are many groups that work permanently with rough walls. The first group [33], [34] uses the Immersed Boundary Method to set a virtual no-slip surface that reproduces a given rough wall (usually an “egg-carton” wall).

Other major group that works with rough surfaces can be found in [45], [207], [208], [209], [259], [260], [261], where a wide variety of techniques are used to simulate the roughness of any wall, driblets, array of staggered cubes, wall velocity disturbances and the immersed boundary method. Another group can be found in [142], [322], where a rough wall is simulated using the idea of rib lets. This idea is very simple to implement in a cartesian coordinate system code.

A more economical way to reproduce the roughness of a wall can be found in [284], [330], where the perturbation of any wall is modeled through known values for velocity field very close to the real wall [284], [330], where eddies have a behavior close related to RANS simulations. For irregular geometries, this approach lacks of generality.

6.5 Taking statistics

Direct Numerical Simulation and Large Eddy Simulation compute basically the instantaneous velocity profile and pressure field. As it is done in lab experiments, a reasonable time is necessary to wait before statistics can be taken and then the result can be analyzed.

The *characteristic time* or reference time is estimated as the ratio of a characteristic length (defined by the geometry) and the characteristic velocity (usually the bulk velocity).

If DNS or LES computations are started from rest, up to 10 characteristic times are needed before statistics can be taken. On the other hand, if direct simulation is started from a

quasi-steady-state solution (computed as laminar flow or with a RANS simulation), only 2 or 3 characteristic times will be necessary before statistics can be reliable [6], [151].

6.6 2D Turbulence

One way to check the validity of any in-house code is by performing 2D-DNS or 2D-LES. Some interesting studies of this phenomenon can be found in [41], [74], [95], [152], [191], [198], [314], and [349].

The dynamics of high Reynolds number turbulent flow couples a large range from the characteristic size of the domain to the dissipative scales. This range is usually too large to be fully resolved by DNS. This is the case for many applications in aeronautics, geophysics or astrophysics where the typical Reynolds numbers are of the order of $10^6 - 10^8$. The largest Reynolds numbers which can be achieved by DNS are of the order of $10^4 - 10^5$ [198].

Two-dimensional flow around bluff obstacles is interesting because the results obtained in studying vortex-shedding phenomena are applicable to the construction of buildings (large rectangular boxes), cars, etc. Particularly, in 2D flow around circular cylinders, the transition process in the wake of a circular cylinder can only be described by 2D numerical simulations [349].

While 3D turbulence is governed by a direct cascade of energy from the scale of injection to the small scales, 2D turbulence admits two different ranges. The first one is governed by an inverse energy cascade from the scale of injection to the large scales. The second one is governed by a cascade of enstrophy from the scale of injection to the small scales [95].

In the case of MHD turbulence, the underlying physics is related to the predominant electromagnetic dissipation mechanism, which enforces strong flow anisotropy, until the limit of quasi-two-dimensional turbulence is achieved. In contrast to ordinary fluid flows, modeling turbulence in MHD flows, especially in a strong magnetic field, has not obtained full consideration yet [314].

In the simulation of the atmosphere or the ocean, there are several physical reasons why the large-scale flow dynamics is behaving quasi-two dimensionally. Such geophysical flows have horizontal scales of hundreds of kilometers in the ocean and of an order of thousands of kilometers in the atmosphere, while their vertical extension measures a few kilometers only [191].

6.7 Transitional flow

More than a century ago O. Reynolds suggested that the instability of stationary pipe flows may be the reason for transition to turbulence and since then numerous attempts have been undertaken to verify this hypothesis. Continuing interest in the problem is based on the desire to gain an insight into laminar-turbulent transition phenomena and its control [271].

Recent years have seen a resurgence of interest in the topic, spurred by new developments in linear and nonlinear stability theories. As is now well known, classical small-perturbation theory is not able to provide an explanation for the onset of transition in ducts and pipes. A yet unresolved issue concerns the initial conditions that are most suited to yield such unstable states. Current understanding ascribes the failure of classical theory to its focus on the asymptotic behavior of individual modes; when a small disturbance composed of a weighted

combination of linear eigenfunctions is considered, there is the potential for very large short-time amplification of perturbation energy, even in nominally stable flow conditions. Traditional emphasis on so-called optimal perturbations may be misplaced. In fact, there is but a weak connection between the flow structures that grow most during the linear transient phase and the chaotic flows found at large times [36].

Additionally, the phenomenon of flow separation in a backward-facing step channel has received considerable attention owing to its geometric simplicity, physical abundance and its close relevance to some fundamental engineering flows. For instance, this phenomenon often corresponds to drastic losses in the aerodynamic performance of airfoils and in automotive vehicles. Although some of the fundamental flow phenomena have become clear through the two-dimensional solutions, many of the subtleties of third dimensionality are yet to be learned. Whereas for transient flows, it is well known that the transitional and turbulent regimes are susceptible to oscillations; in the case of incompressible flows, the oscillations due to the Kelvin-Helmholtz (KH) instability are caused by the interaction between the shear layer and the recirculating flow near the step wall. Due to the KH instability in the shear layer, unsteady vortical structures are generated and convected downstream to produce fluctuations in the velocity and pressure, thus leading to the destabilization of the flow field [64], [276].

6.8 Computational details on the generation of turbulence

There are several important aspects that must be mentioned in order for the DNS/LES technique to work properly. The idea that the inflow conditions alone are enough to produce

turbulence, independent of the grid size, might not be completely correct. It seems that some numerical tricks may be needed for the current DNS/LES techniques to work properly.

The most popular technique used in almost all DNS/LES calculations, the pseudo-spectral method transforms the equations of motion in the Fourier domain. When applying the Fourier transform to the flow equations in one specific direction, the boundary condition at both limits must be the same. This case is known as periodic boundary condition.

Normally, in parabolic flows, the Fourier transform is applied to the direction of the flow, with the boundary condition in that direction to be periodic. With the inflow and outflow conditions to be exactly the same, there are only two possibilities of calculating a DNS/LES procedure:

- Set a predefined velocity profile (with its fluctuations): In this case there are two possibilities. First, if the mesh is fine enough in the direction of the flow, the fluid will develop until, very close to the outflow, both velocity components will adjust to the exit conditions. The second possibility is to use a highly stretched grid (high local Reynolds number), producing instabilities that will impede the development of the flow.
- Set a constant pressure gradient: Here, the pressure gradient is adjusted permanently to keep it constant. At any moment, the existing outflow/inflow conditions have to be perturbed to produce the desired turbulence level. Keeping the pressure gradient constant will force both inflow and outflow conditions to be the fully developed flow (the only solution here). The problem with this idea is that, in parabolic flows, pressure is not constant in the entire cross-section area. In [340] it is shown that the pressure gradient in

the viscous sub-layer is several times larger than the averaged pressure gradient of the whole cross-section.

Using a predefined velocity profile, only a few problems in DNS/LES will be able to be solved. With the constant pressure gradient, the solution at the viscous sub-layer will have some error. This issue can explain why it is common to find an error of about 10% in similar problems solved by different authors.

With the LES technique there is another numerical issue. Basically most of the LES simulation is done using a model for the filtered turbulent stresses. A very popular technique is the so-called turbulent viscosity, with the dynamic models being widely used. If the total numerical viscosity of the fluid is going to be variable, point by point, that variation will produce additional effects in the solution that may not be absolutely physical.

The utilization of a highly stretched grid in the direction of the flow seems fundamental for the DNS/LES technique to work. For example in [357], DNS and LES simulations are performed in an annular duct. The local Reynolds number for DNS is 150 while for LES is 300. These huge values will produce numerical instabilities.

In the case of DNS on pipes/ducts, as shown in references [196], [253], [271], [327], [344] and [355] the local Reynolds number used, in the direction of the flow, in the simulations ranges from 110 to 400 typically, reaching values of more than 1000 in some cases.

For DNS on a backward-facing step, in [23] and in [251], the local Reynolds numbers used in the direction of the flow is in about 270-285, high enough for the equations to be, numerically, the Reynolds equations.

Perhaps one classical reference, [202], uses a local Reynolds number of 2000 in the direction of the flow. In this work, a pseudo-spectral procedure is used, forcing the inflow and the outflow to be the same. Since there are more nodes in the output than in the input, some re-scaling it is necessary.

For Couette flows, references [154], [216] and [335] use an average local Reynolds number ranging from 281 to 695. In DNS with heat transfer, in [278] a local Reynolds number of 334 is used.

For the case of LES, the situation is not so straight forward. Since most of sub-grid models use the idea of turbulent viscosity, being very popular the ones that adjust dynamically the turbulent viscosity, the total diffusion term will be higher than for DNS. However, LES use coarser grids so the local Reynolds number is not so large, but it is not small to fit in the free-instability region.

In all references studied, the common feature is the use of highly stretched grids. Using the analysis done in chapter 3, it seems that it is necessary to have a grid that produces numerical instability in order for the technique to work. Additionally, most works use a random velocity profile as initial guess to compute the initial condition.

CHAPTER SEVEN

2D-DNS ON PARALLEL PLATES

The 2D-DNS on parallel plates (or 3D-DNS on ducts/pipes) is the most popular DNS/LES problem for the evaluation and fine tuning of any numerical procedure. The main objective of these preliminary series is to obtain the parameters that will allow the calculation of the main problem.

Using the relations developed by A. Kolmogorov, the necessary delta to solve all the scales is given by, with h the separation of the plates:

$$D_h = 2h \Rightarrow \frac{\Delta_{Kolmogorov}}{h} = Re_{D_h}^{-3/4} \quad (70)$$

Additionally, the time-scale, necessary to perform the integration is given by:

$$\frac{\Delta t_{Kolmogorov} \cdot \bar{V}}{h} = Re_{D_h}^{-1/2} \quad (71)$$

In order to explore the behavior of the proposed procedure, free from numerical instabilities, and using Equation (70), the grid was built using $\Delta x = \Delta y = 2\Delta_{KOLMOGOROV}$.

In order to study the creation of turbulence without any pre-defined condition or assumption, the white noise condition was used. Due to the nature of random numbers, and in order to keep a strict control on the fluctuation level, the algorithm used for the inflow condition is:

- a) Select a set of random numbers (between -1 and +1) for every point in the inflow region. Here, the Mersenne-Twister algorithm was selected [236].
- b) Compute a *correction factor* f_x so the average of the fluctuations in absolute value is 1 (one):

$$f_x = \frac{A}{\int_A |x| dA} \quad (72)$$

- c) With p_f the *percentage of fluctuation* (set by the user), compute the velocity fluctuation of each point:

$$v' = f_x p_f x v_{Inflow} \quad (73)$$

- d) Compute velocity correction δv to enforce mass continuity:

$$\delta v = V_{Bulk} - \frac{1}{A} \int_A (1 + f_x p_f x) v_{Inflow} dA \quad (74)$$

Several tests were performed, varying the Reynolds number from 5000 to 10000 and using length ratios from $L_x = h$ to $L_x = 10h$, and the characteristic time, given by $t_c = \frac{D_h}{\bar{V}}$ was modified from 2 to 20. Additionally, a big number of experiments were made using high frequency oscillations and varying the percentage of fluctuation from 0.5% to 50%. In all cases there was no significant difference in the results.

The boundary condition imposed at the outflow is the so-called Sommerfeld outflow condition, which is the one dimensional equation $\partial\phi/\partial t + V_c \cdot \partial\phi/\partial x$, where V_c is the average velocity of the corresponding outflow section.

Table 7 shows the parameters used for the simulation, where a lot of care was taken to keep all parameters in the stability zone. Figure 66 shows the number of iterations per time step. Here, the first 1200 time steps are necessary for the turbulent regime to stabilize and the last 600 time steps were used for the statistics. As it can be observed, the most frequent range is between 300 and 500 iterations per time step. Additionally, it is possible to observe a low frequency oscillation from the high order oscillation on the number of iterations per time step.

Table 7: Parameters, 2D-DNS PP

Parameter	Value
Re	5000
L_x, L_y	h, h
N_x, N_y	300,300
Local Reynolds	8.33
$\Delta/\Delta_{KOLMOGOROV}$	1.98
CFL	1
Fluctuation Intensity	10%

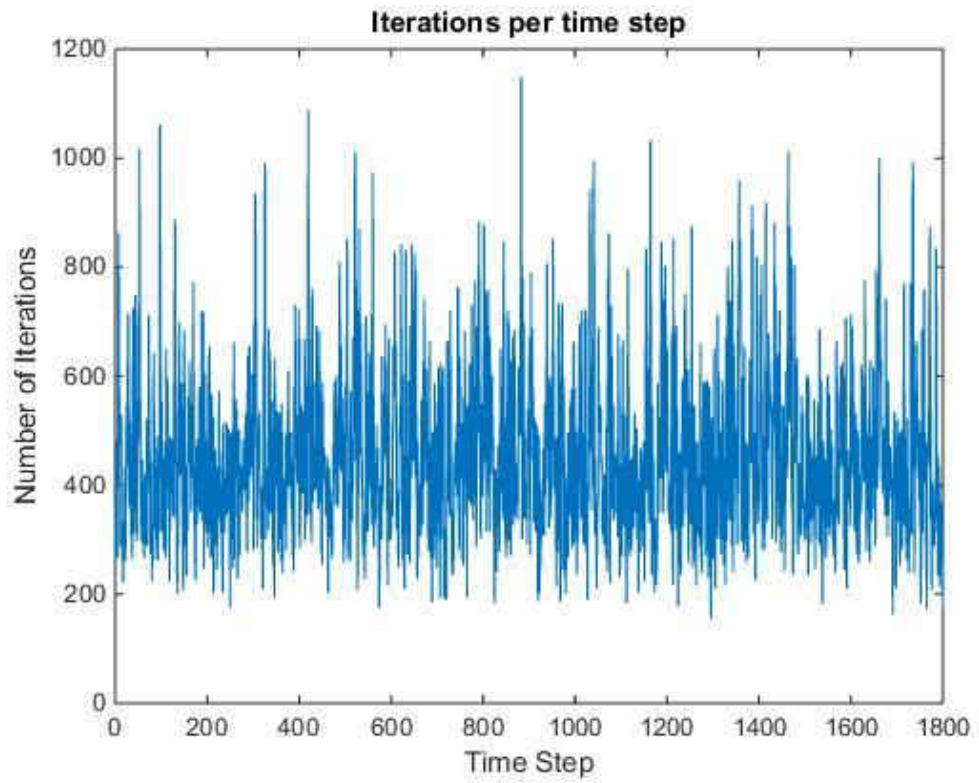


Figure 66: Number of iterations per time step, 2D-DNS PP

Figure 67 show the averaged streamlines where the pattern of the flow is clearly steady. Figure 68 and Figure 69 show the contour lines for both velocity components. For velocity component V , there is some intensity in both left corners of the plates but the value goes to zero very quickly.

Figure 70 shows the pressure contours where there are two singularities at both lefty corners. At $x=0.35h$ the pressure is basically constant but outside from the boundary layer. At $x=0.50h$, the pressure at the cross-section is not constant but consistent with the development of the flow.

Figure 71 shows the contours of kinetic energy. The main characteristic here is that the turbulent intensity decays very quickly. Looking at the zoomed view in Figure 72, for $x \leq 0.005h$, the intensity of kinetic energy is very high as expected by the fluctuation of 10% set at the inflow. However, it decays very fast as $x \approx 0.01$. This phenomenon was observed for all fluctuations tested (from 0.5% to 50%) and all Reynolds numbers evaluated (from 5000 to 10000).

More than disappointing, this issue is very interesting since it may suggest that, in order for any DNS/LES technique to work, the system of equations must be numerically unstable. The physical instabilities that are shown in those results may be produced from numerical instabilities and no by the physical phenomenon itself.

The common factor that most published papers on DNS/LES have is that a highly stretched grid is used in at least one direction.

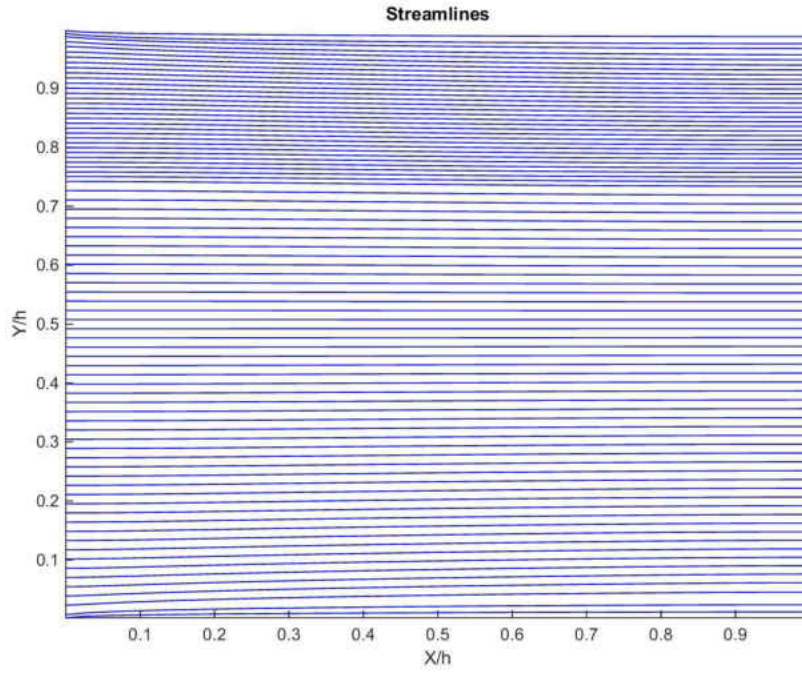


Figure 67: Streamlines, 2D-DNS PP

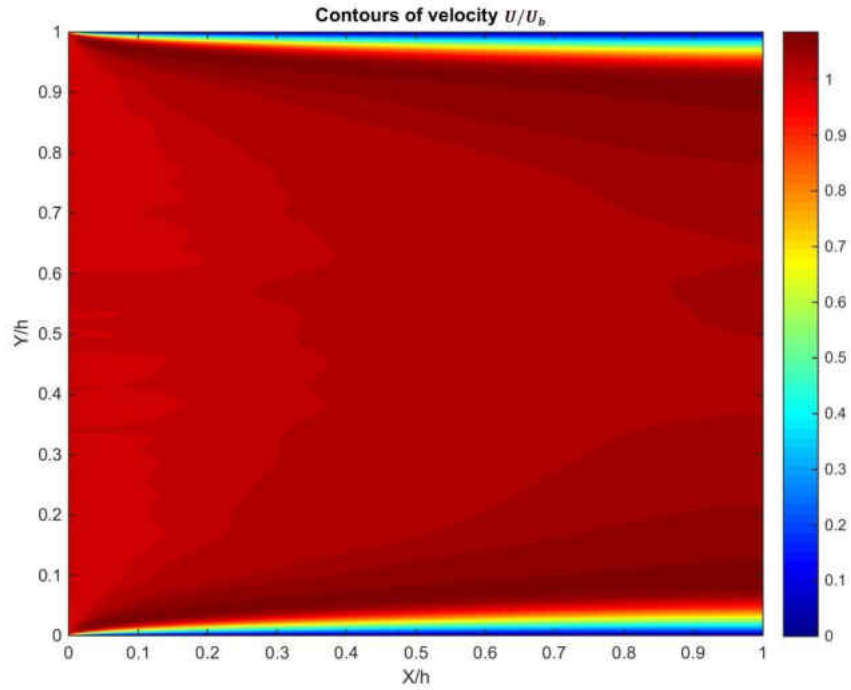


Figure 68: Contours of velocity U/\bar{V} , 2D-DNS PP

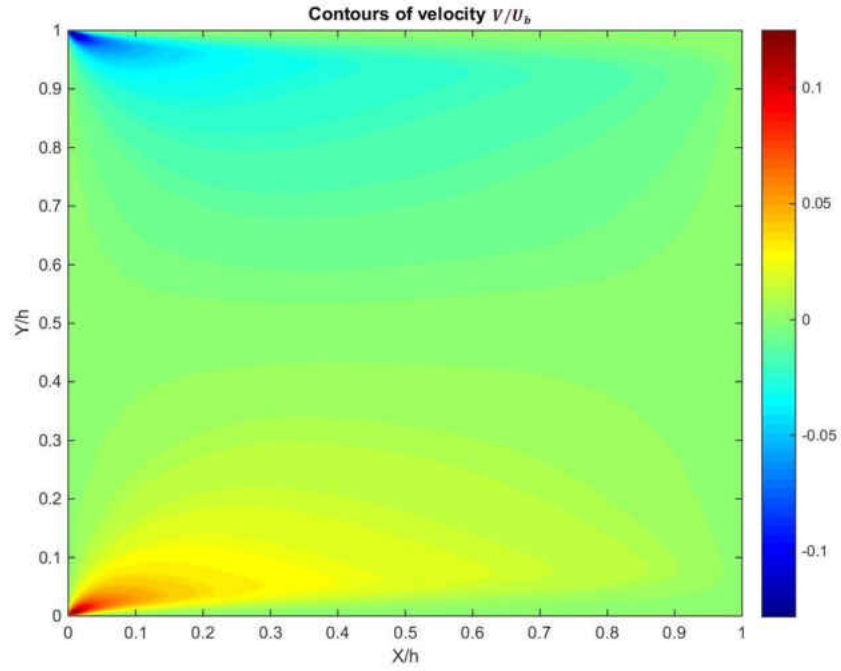


Figure 69: Contours of velocity V/\bar{V} , 2D-DNS PP

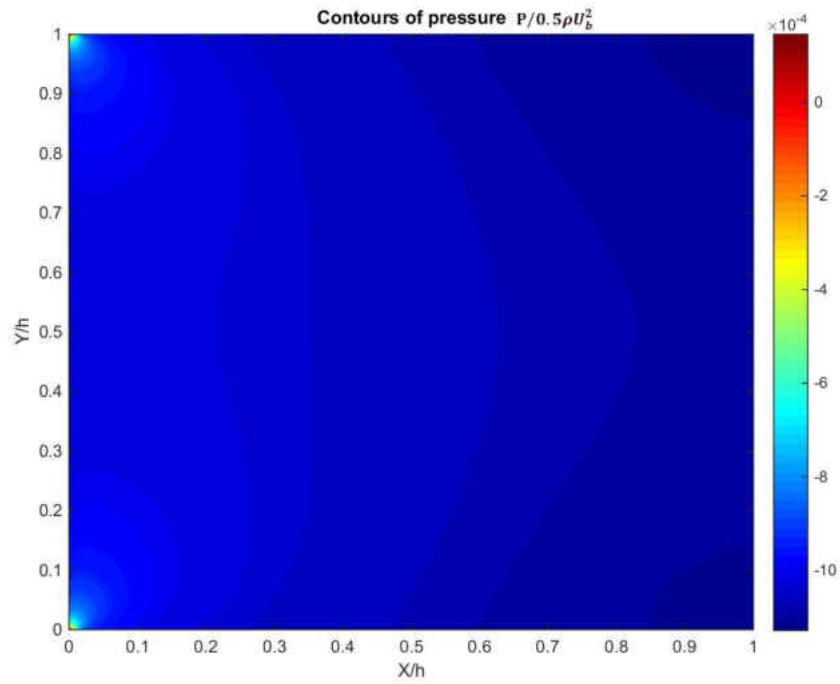


Figure 70: Contours of pressure $p/(0.5 \cdot \rho \cdot \bar{V}^2)$, 2D-DNS PP

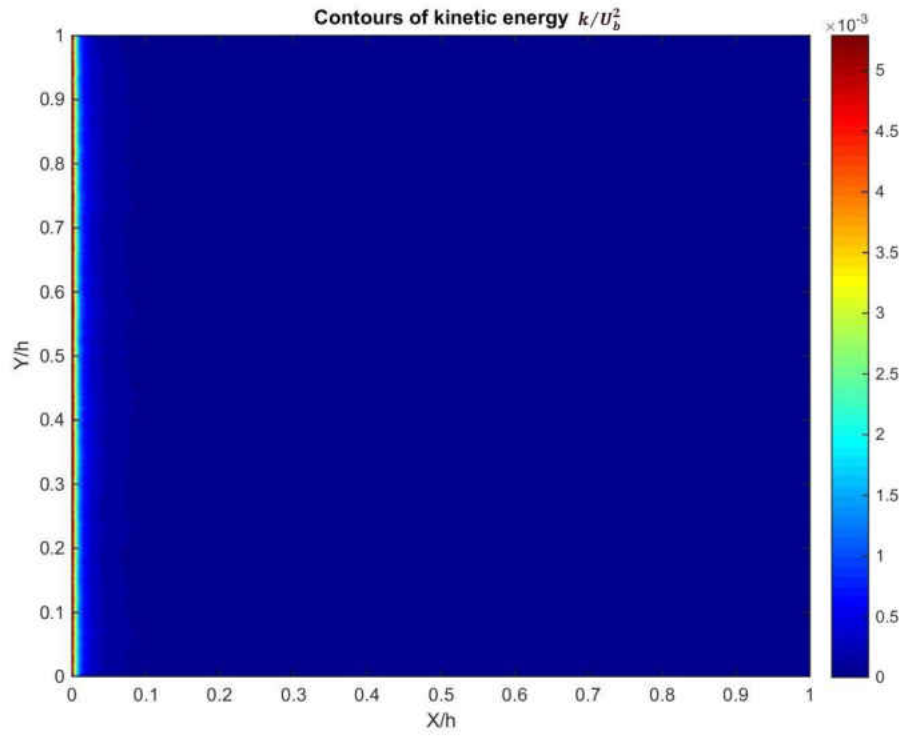


Figure 71: Contours of kinetic energy k/\bar{V}^2 , 2D-DNS PP

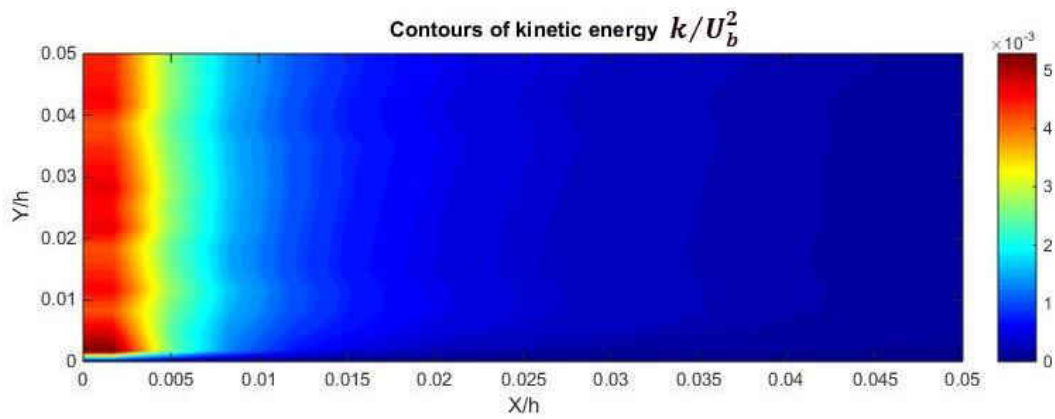


Figure 72: Contours of kinetic energy k/\bar{V}^2 (zoom), 2D-DNS PP

By observing Figure 72, the zone of high kinetic energy is just a bit larger than the viscous sub-layer. In this layer, viscous and inertia forces are in quasi-equilibrium. If the discretized equations are assumed to reproduce the physical phenomena of turbulence, the results present here may indicate that the inflow fluctuations alone might not be enough to keep consistently the turbulent regime.

If instead of the inflow fluctuations, the flow is perturbed from the wall, the magnitude of the kinetic energy in the viscous sub-layer should keep permanently the disequilibrium between viscous and inertia forces, as it happens with real rough walls/surfaces.

It is convenient to remember that from experiments, the wall roughness is one of the key hypotheses for generation of turbulence. The effect of inflow fluctuations has not been extensively studied due to the great difficulty of keeping all conditions under control.

Figure 73, Figure 74 and Figure 75 show the contours for the Reynolds stresses, with the stress $\overline{v'v'}$ taking more time to vanish. The contours of vorticity are shown in Figure 76, with a typical laminarization behavior. The contours of the fluctuations u' and v' at the last time step are shown in Figure 77 and in Figure 78. For the case of u' , a high intensity is observed mainly near the wall and low intensity at the core of the fluid, as expected from the laminarization.

Figure 79 and Figure 80 show the progress of both velocity components at selected X-positions, confirming the laminarization process after the inflow fluctuations are being damped.

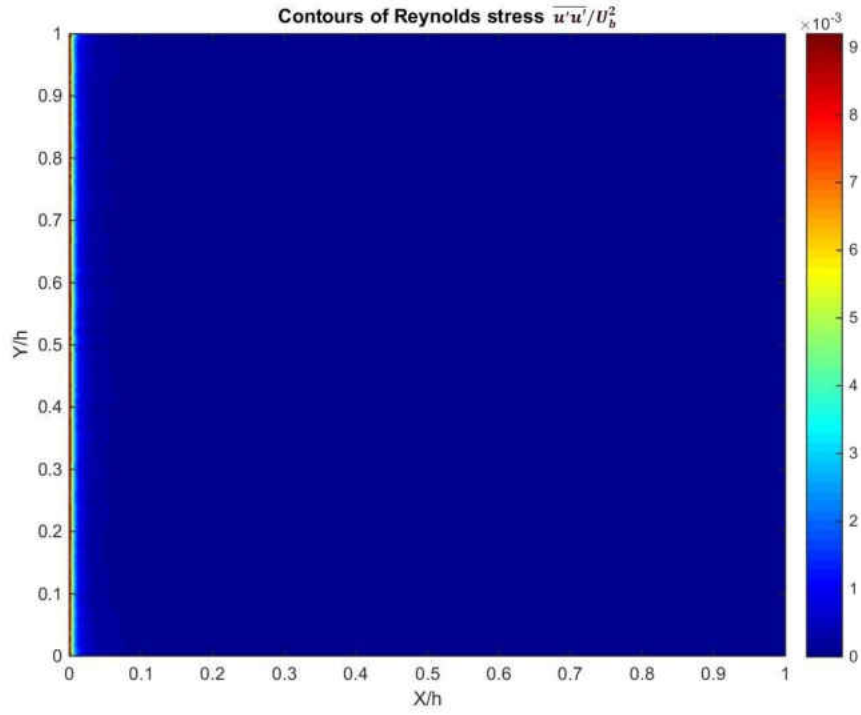


Figure 73: Contours of Reynolds stress $\overline{u'u'} / \overline{V}^2$, 2D-DNS PP

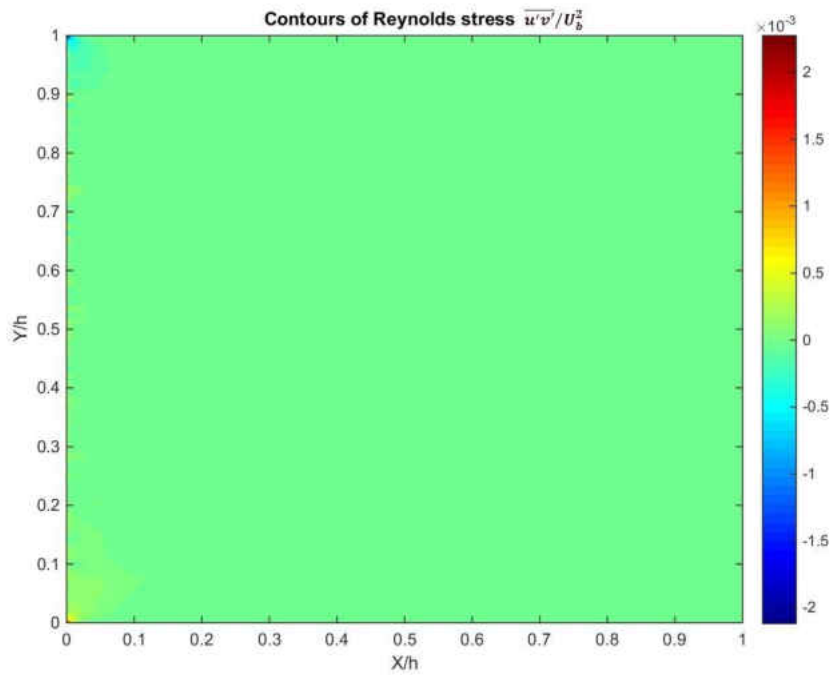


Figure 74: Contours of Reynolds stress $\overline{u'v'} / \overline{V}^2$, 2D-DNS PP

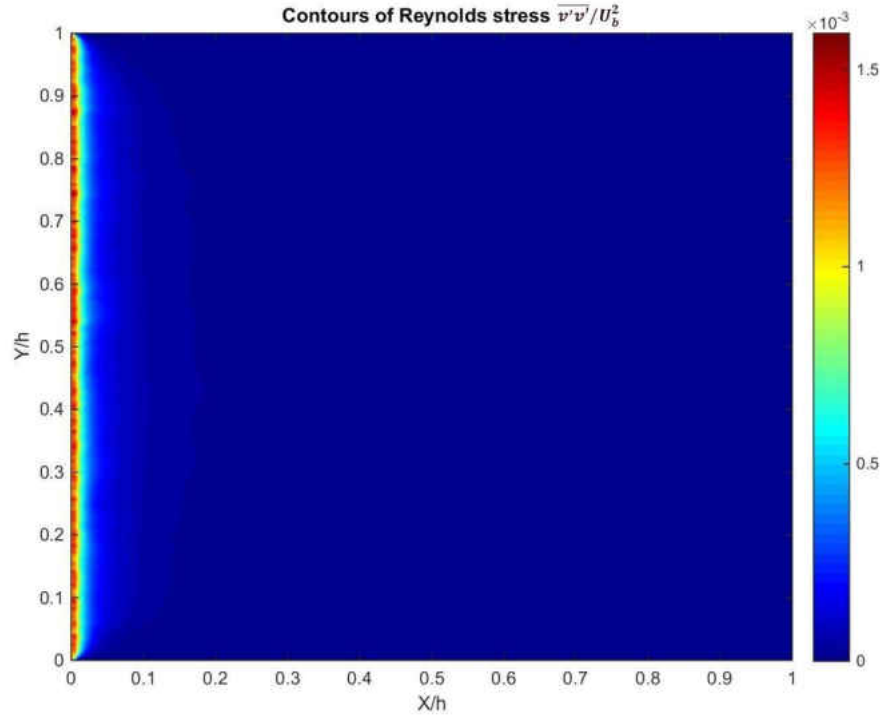


Figure 75: Contours of Reynolds stress $\overline{v'v'}/\bar{V}^2$, 2D-DNS PP

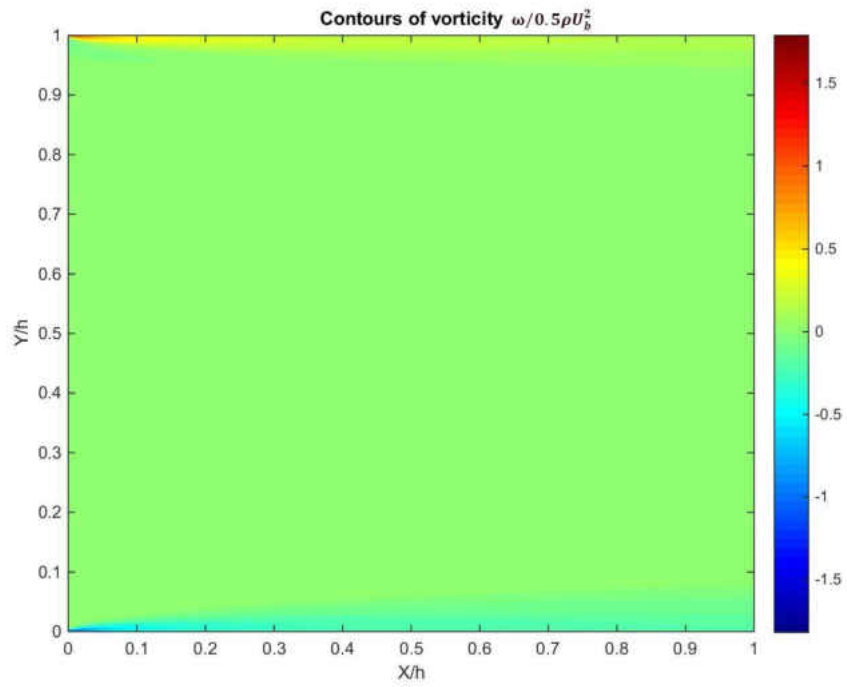


Figure 76: Contours of vorticity $\omega/(0.5 \cdot \rho \cdot \bar{V}^2)$, 2D-DNS PP

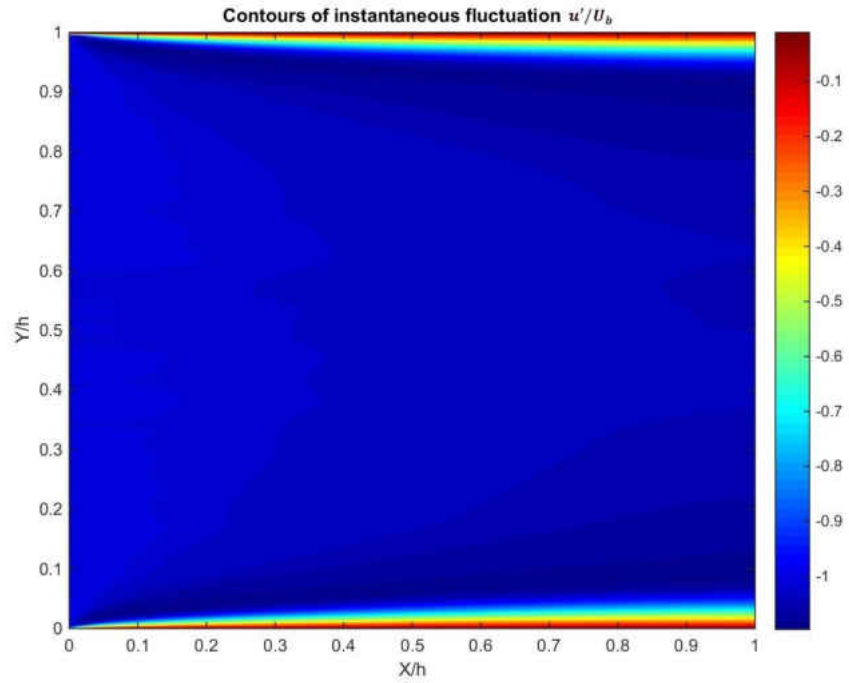


Figure 77: Contours of u'/\bar{V} in the last time step, 2D-DNS PP

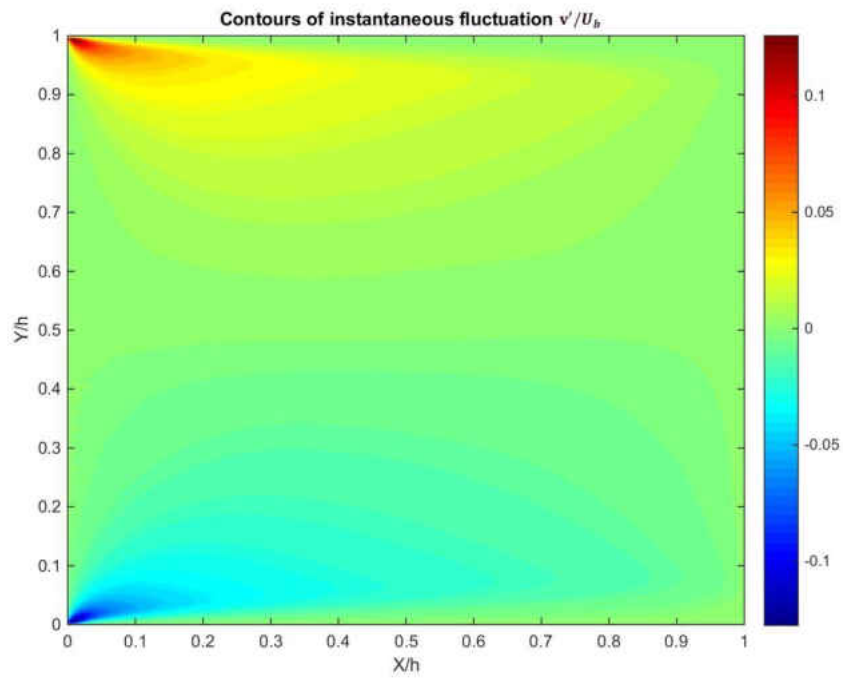


Figure 78: Contours of v'/\bar{V} at last time step, 2D-DNS PP

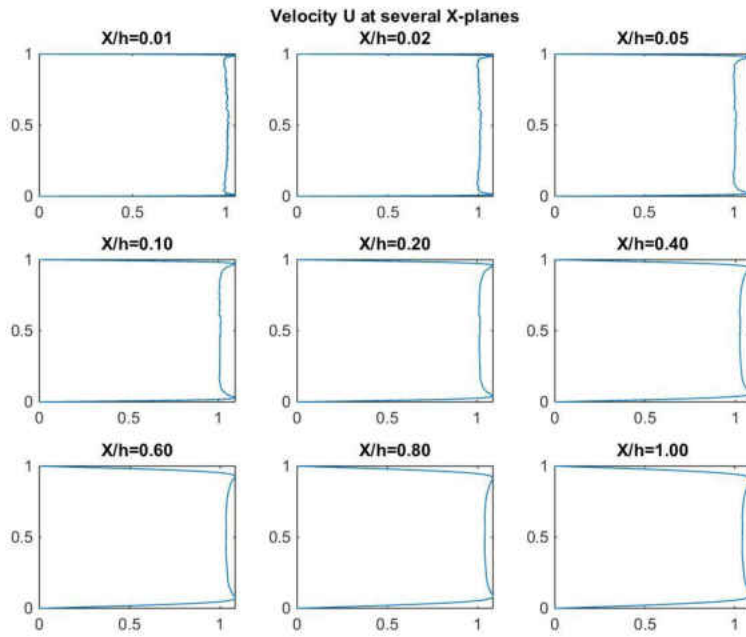


Figure 79: Velocity U/\bar{V} at different X-planes, 2D-DNS PP

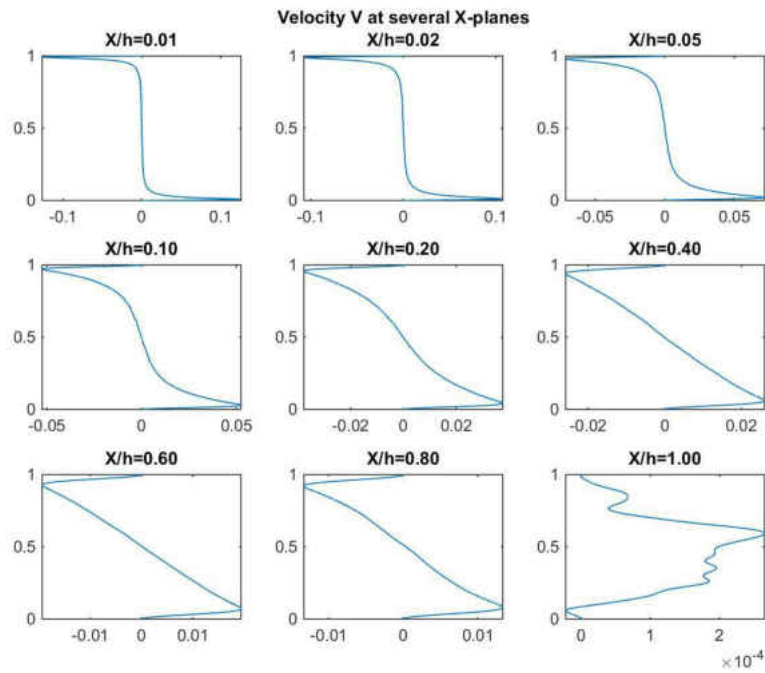


Figure 80: Velocity V/\bar{V} at different X-planes, 2D-DNS PP

The evolution of pressure field can be observed in Figure 81, where the pressure gradient in the viscous sub-layer is huge in comparison with the gradient in the core of the fluid. This effect has been confirmed with in [340] with simulations of turbulent flow in ducts using the $k - \varepsilon$ model of Launder-Sharma.

From Figure 82 to Figure 85, the evolution of turbulent kinetic energy and the Reynolds stresses trough the plates are shown. Here, big oscillations are observed, due probably that the averaging time was not enough.

However, some interesting aspects can be observed. First, in Figure 82, the turbulent kinetic energy decays fast through the plates, being more important close to the walls. A similar behavior can be seen in Figure 84 with the Reynolds stress $\overline{v'v'}$. This decay may reinforce the idea that fluctuations from the wall may look necessary in order to keep the turbulence level in the viscous sub-layer.

Figure 86 shows the pressure coefficient $(p - p_{REF}) / (0.5 \cdot \rho \cdot \bar{V}^2)$ at both top and bottom walls. As expected, they are exactly the same and the value become linear very fast, at $x \approx 0.1h$. A similar behavior is observed in Figure 87 with the friction coefficient $C_f = \tau_w / (0.5 \cdot \rho \cdot \bar{V}^2)$ that reaches a constant value.

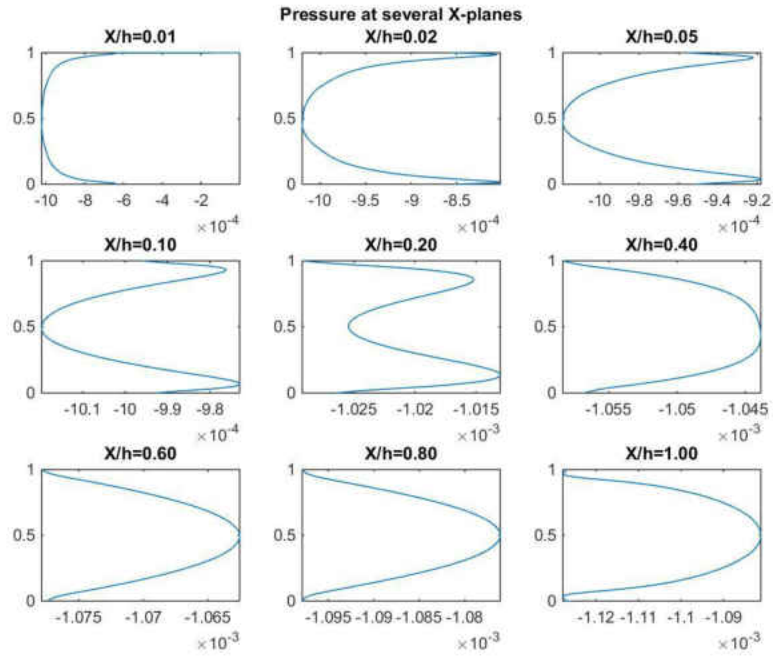


Figure 81: Pressure $p/(0.5 \cdot \rho \cdot \bar{V}^2)$ at different X-planes, 2D-DNS PP

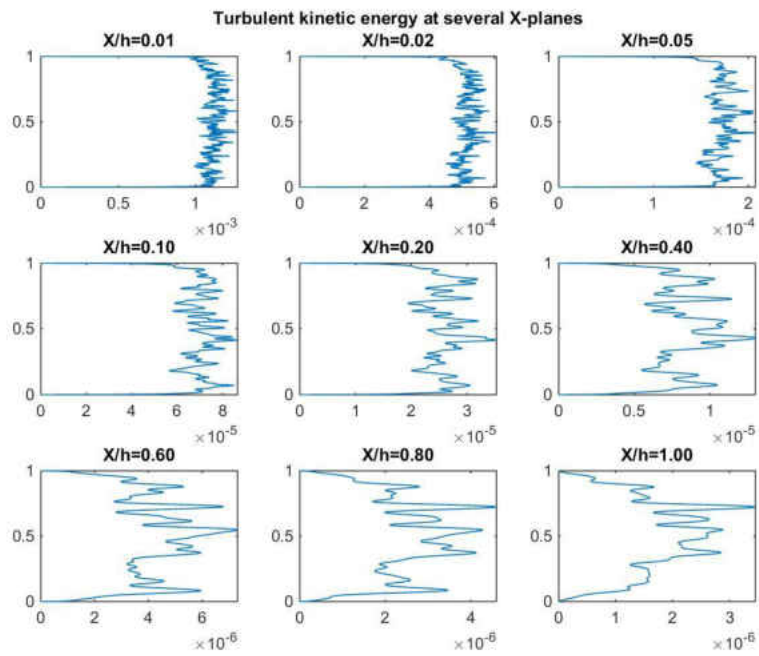


Figure 82: Kinetic energy k/\bar{V}^2 at different X-planes, 2D-DNS PP

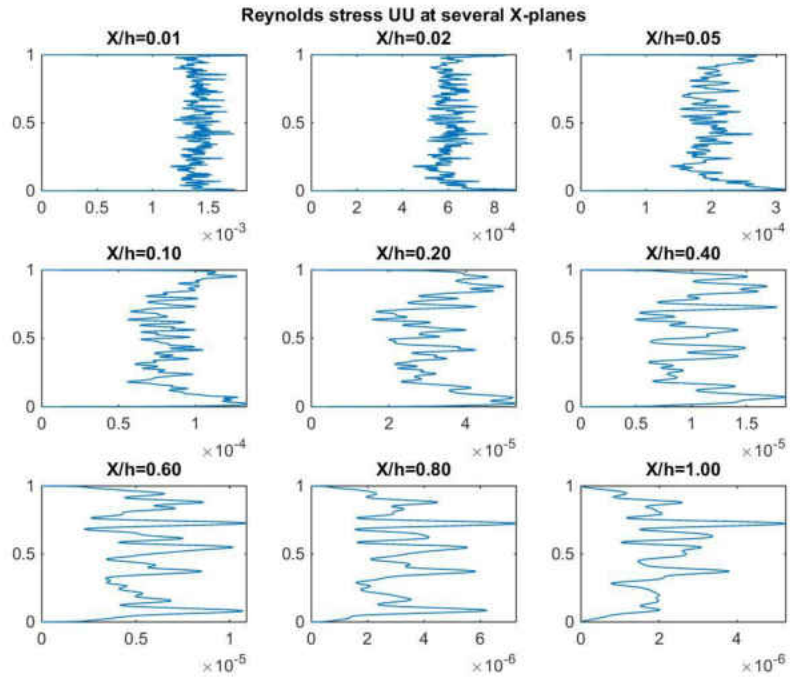


Figure 83: Reynolds stress $\overline{u'u'}/\bar{V}^2$ at different X-planes, 2D-DNS PP

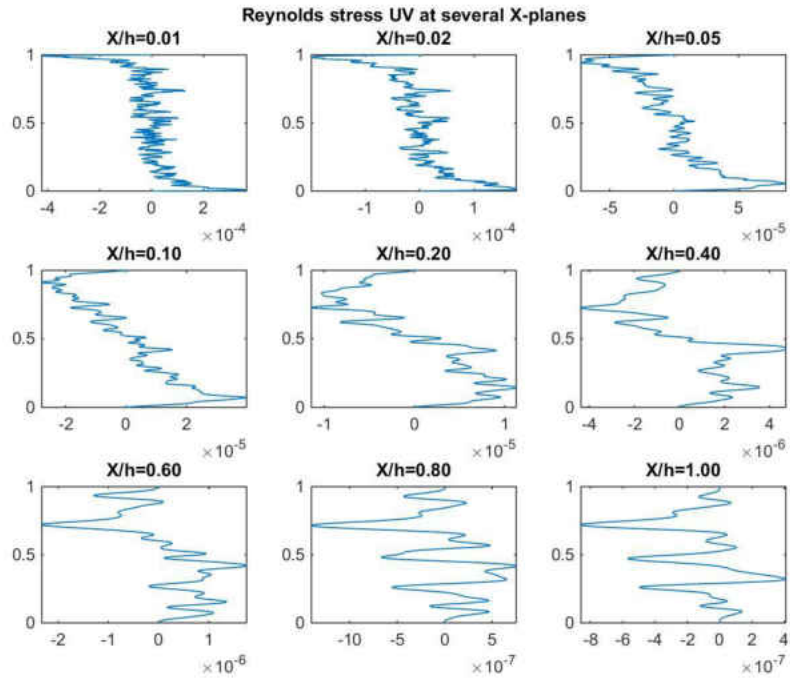


Figure 84: Reynolds stress $\overline{u'v'}/\bar{V}^2$ at different X-planes, 2D-DNS PP

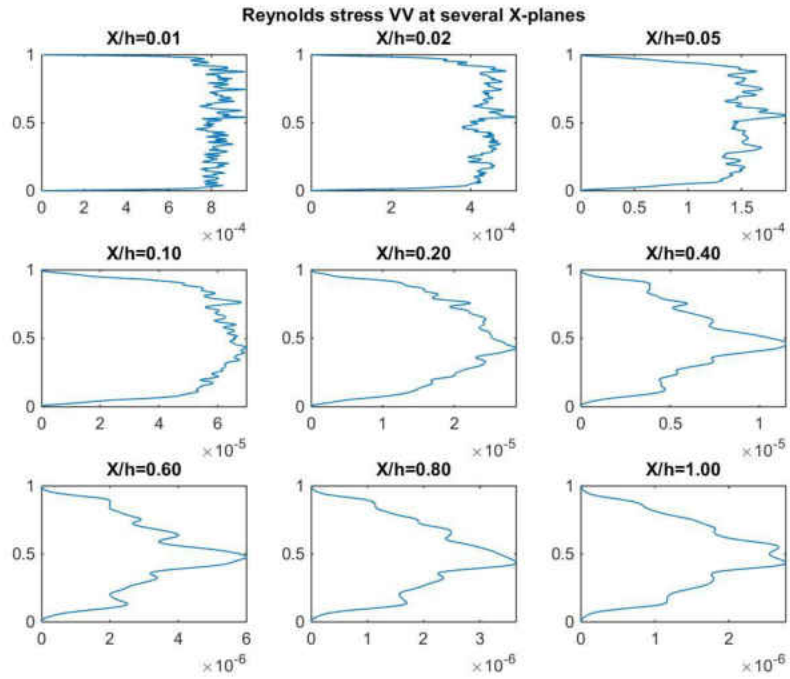


Figure 85: Reynolds stress $\overline{v'v'}/\overline{V}^2$ at different X-planes, 2D-DNS PP

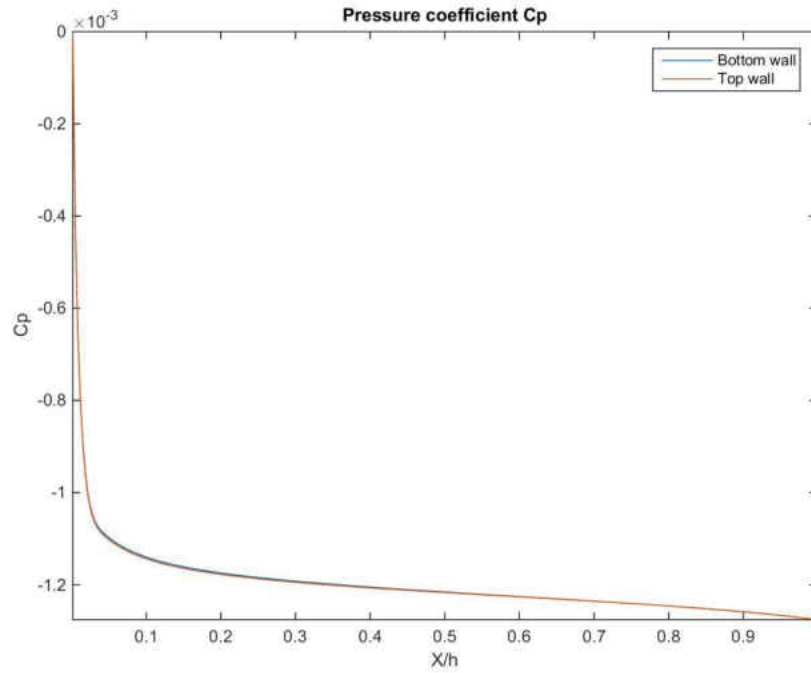


Figure 86: Pressure coefficient C_p as function of position, 2D-DNS PP

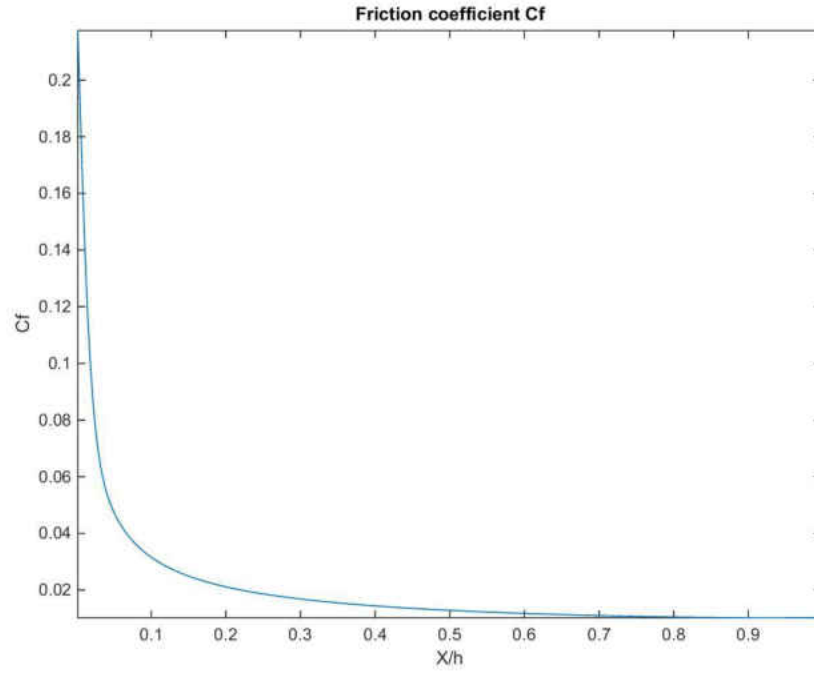


Figure 87: Friction coefficient C_f at different X-planes, 2D-DNS PP

CHAPTER EIGHT

2D-DNS ON A BACKWARD-FACING STEP

The first direct simulations on a backward-facing step seem to be performed by the early 1990's. The dissertation of Kopera [178] has a very good review of the history of experiments performed as well as simulations computed. Only some paragraphs will be extracted here.

The first LES simulation of turbulent flow in a backward-facing step was performed by Friedrich and Arnal [100] in an open channel with a Reynolds number of $1.65 \cdot 10^5$. The re-attachment reported was 7.0 which differ from the value of 8.5 from the experiments of Durst and Tropea [178].

Kaitktis et al [159] applied a high order mixed spectral/spectral element method to a transitional flow over a backward-facing step. Their interest was to study the early transition to turbulence in a 2D geometry. The re-attachment was consistently under-predicted for Reynolds number above 600, in the same way as the calculations done previously in this work. The authors concluded that the difference is due to the 2D simplification for the calculations and the three-dimensionality of the real flow [178].

The first DNS simulation on a backward-facing step was the work of Le et al [202] in 1997, with the calculation on an open channel and a Reynolds number of 5,100 based on the height of the step (Reynolds of 60,000 considering the hydraulic diameter at the inflow) and an expansion ratio of 1.20. The time-advancement is performed by using a semi-implicit, pseudo-spectral method and the fractional-step method of Kim and Moin [173]. The inflow conditions are generated assuming a prescribed energy spectrum arguing that the white noise technique produces too much small scale oscillations. The results obtained were validated with the

experiments of Jovic and Driver [156] and [157]. The computed averaged re-attachment ($6.28h$) agrees well with the experiments but the peaks of the friction coefficient C_f are over-predicted in 2.5 times. In spite of these differences, this work has become a reference for the rest of the DNS performed on this geometry.

Recently, the work of Barri et al [23] performed a DNS simulation on an open channel with an expansion ratio of 2.0 and a Reynolds number of 5,600 based on the height of the step. The equations of motion were discretized with finite volume method and the Adams-Bashford method for the time integration, obtaining a second order method. The inflow conditions were created by a precursor simulation. The comparison of the turbulent quantities agreed very well with the work of Matsunaga [228]

With respect to LES on a backward-facing step, the work of Aider [4] makes experiments on an open channel, using a dynamic turbulent eddy viscosity model. The expansion ratio is 1.2 and the Reynolds number is 5,100 based on the step height. Two different inflow conditions are used, precursor simulation and white noise. The averaged re-attachment obtained with white noise is 5.8, versus 5.29 obtained with the precursor simulation. Unfortunately no information is provided about the generation of the white noise. The results with both inflow conditions are basically the same and the agreement with the works of Le [202] and Jovic and Driver [157] and [157] is excellent, except for the vertical velocity component where the difference is somewhat important.

Studies in the transitional region have also been studied, as in the work of Rani et al [276], with an aspect ratio of 2.02 and two Reynolds numbers, 1000 and 2000. The Taylor-Görtler-Like oscillations as well as the Kelvin-Helmholtz fluctuations are correctly described.

One interesting detail is that, in these transitional simulations, the main vortex does not have a well described structure, at least in the results presented.

8.1 Input data and parameters

Based on the laminarization phenomena observed in the 2D-DNS on parallel plates, a very short region was selected.



Figure 88: Geometry used in the 2D-DNS on a backward-facing step

Figure 88 shows the details of the problem, where no inlet region was used in order to avoid the laminarization of the fluid. The expansion length was set to $10H$ which is enough to describe correctly the re-attachment.

After the re-attachment, in the so-called recovery zone, the laminarization of the fluid is unavoidable (due to the fine grid used here) and no relevant information can be provided to be compared with other publications.

Table 8 shows all the relevant geometric information. In all cases the size of the grid was chosen to have full DNS resolution without making any assumption of any kind. Additionally the local Reynolds number Re_{δ} is significantly below the critical value.

Table 8: Geometric parameters, 2D-DNS BFS

Re_{D_h}	ER	N_x	N_y	Re_Δ	$\Delta/\Delta_{KOLMOGOROV}$
1000	1.14	280	228	2.5	0.889
2000	1.14	420	342	3.33	0.997
3000	1.14	560	456	3.75	1.013
1000	1.40	800	280	2.5	0.889
2000	1.40	1200	420	3.33	0.997

Table 9 shows the time dependent parameters with the CFL chosen to be roughly 1 so that the transient derivative has the same order of magnitude than the convection terms.

Table 9: Time-dependent parameters, 2D-DNS BFS

Re_{D_h}	ER	CFL	Time Steps (before stats.)	Time Steps (for stats.)
1000	1.14	0.999	40	400
2000	1.14	0.998	60	600
3000	1.14	0.997	80	800
1000	1.40	0.999	40	400
2000	1.40	0.998	60	600

Additionally, since in the transitional region, both laminar and turbulent solutions are roughly the same, the number of time steps selected for statistics is enough for a particle to cross

the main vortex one time. This short time was enough to have good results on the main variables but not enough for the turbulent quantities which still have an important amount of noise. The intensity of fluctuations was set to 10% in all cases with high frequency oscillations.

8.2 Re-attachment

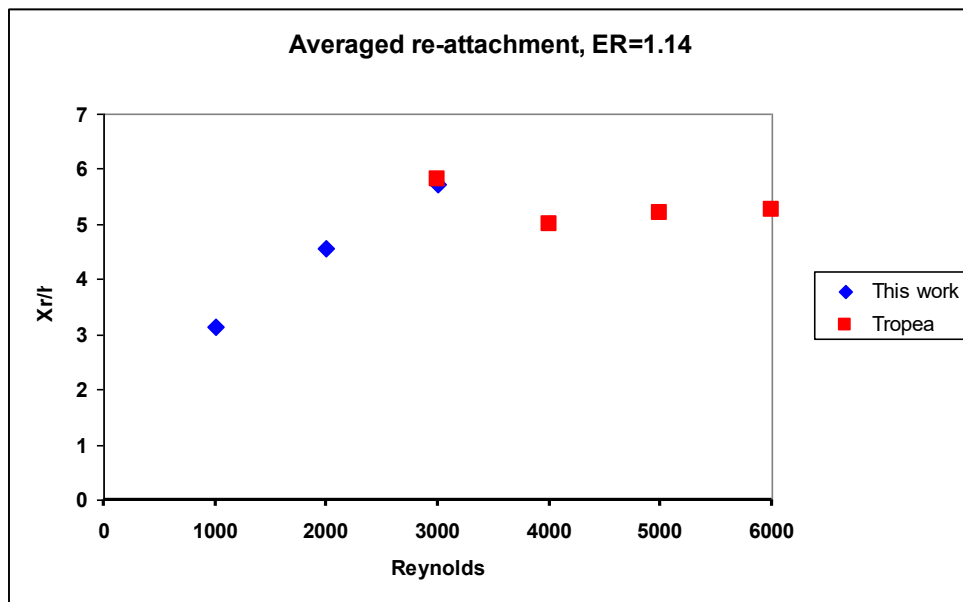


Figure 89: Averaged re-attachment, 2D-DNS BFS, $ER = 1.14$

Figure 89 and Figure 90 show the averaged re-attachment obtained in all simulations. The behavior is almost linear, expected in this region of Reynolds numbers. Additionally, the agreement at the beginning of the transitional region is excellent.

From Figure 91 to Figure 95, the variation of the re-attachment with time in all cases simulated can be observed. The behavior of both expansion ratios is different but consistent with that observed in other publications.

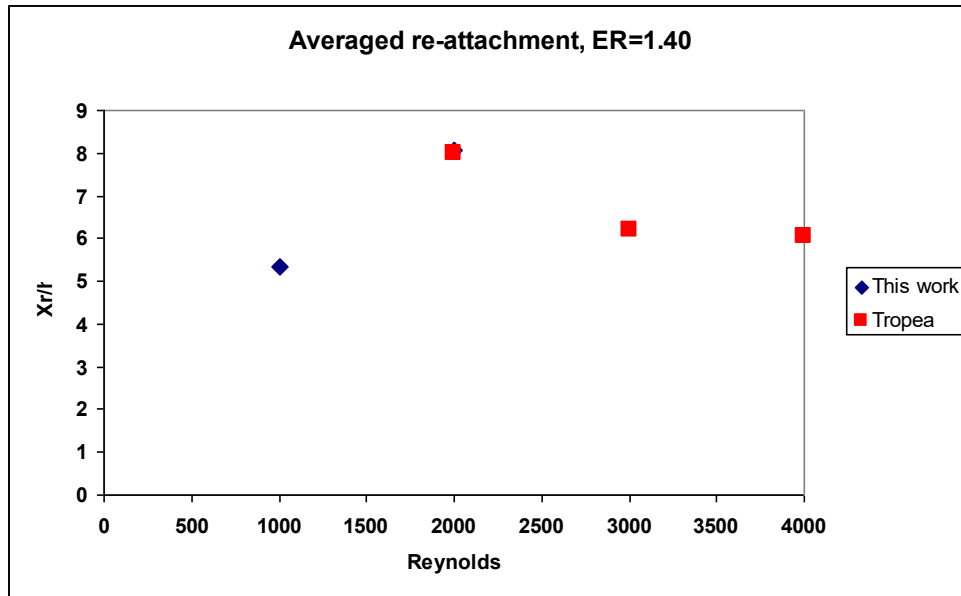


Figure 90: Averaged re-attachment, 2D-DNS BFS, $ER = 1.40$

The first aspect to observe is the percentage of fluctuation of the re-attachment. For the expansion ratio of 1.14, the oscillations are in the range from $\pm 5\%$ to $\pm 10\%$, consistent with the high percentage observed in the calculations of Le [202] with an oscillation of $\pm 15\%$ for an equivalent Reynolds number of 60,000.

These high oscillations are explained because with this small expansion ratio (1.14), most of the flow is parabolic and the size of the main vortex is very small with respect to the size of the rest of the region.

Additionally, it can be observed that there are two types of oscillations, high frequency and low frequency. The first one occurs from time step to time step while the other is a variation of the averaged re-attachment.

From Figure 91 to Figure 93, some local and very high variations of the re-attachment can be observed.

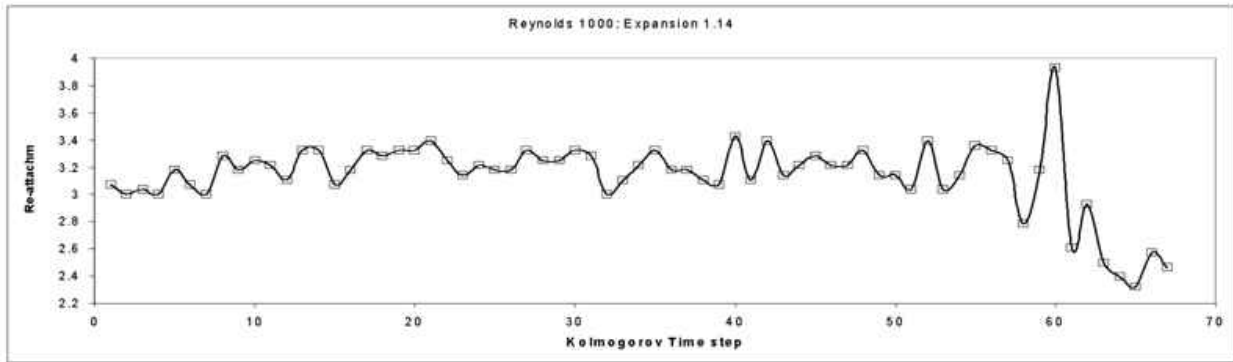


Figure 91: Variation of re-attachment with time, 2D-DNS BFS, $Re = 1000$, $ER = 1.14$

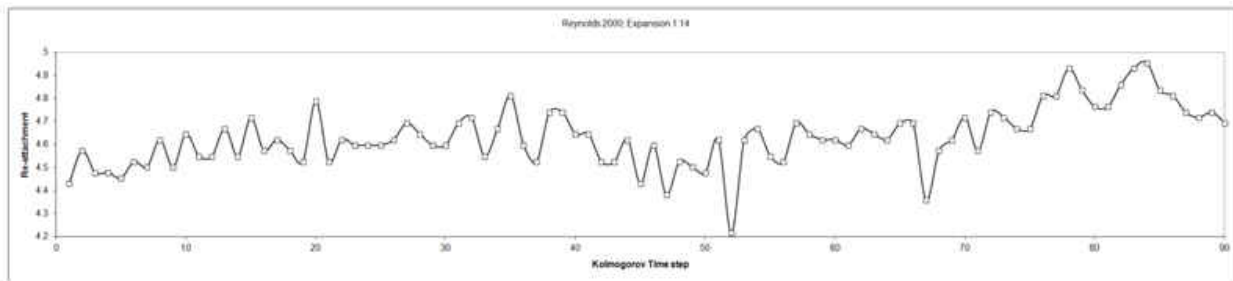


Figure 92: Variation of re-attachment with time, 2D-DNS BFS, $Re = 2000$, $ER = 1.14$

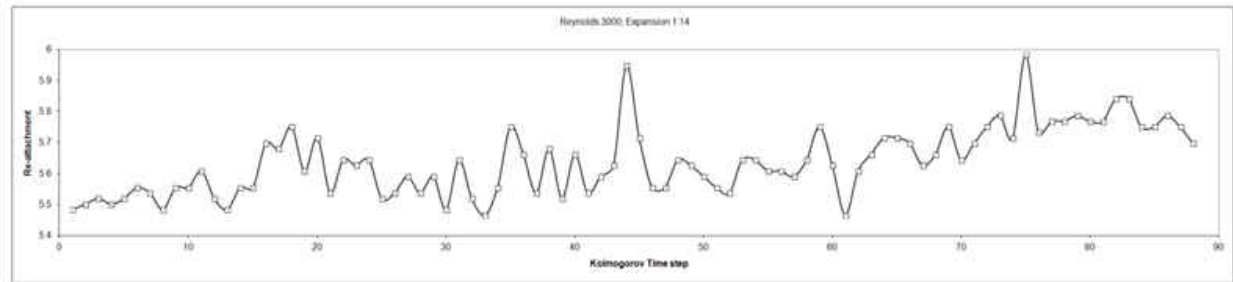


Figure 93: Variation of re-attachment with time, 2D-DNS BFS, $Re = 3000$, $ER = 1.14$

This issue, also reported with similar simulations using the package Open Foam, can be due to some white noise effects of the inflow but it can be also due to some transitional effects observed experimentally, with huge variations of the flow pattern and then a return to the

average behavior. Obviously, it cannot be ignored some other instability of the numerical procedure.

The behavior of the re-attachment with time becomes interesting for the expansion ratio of 1.40. Figure 94 shows the variation of the re-attachment for a Reynolds number of 1000, in which very small variations in spite of the high percentage of fluctuations introduced at the inflow profile. This behavior is fully consistent with the expected variations of laminar flow, in which the viscosity forces are still big enough to damp the effects of any perturbation of the flow.

For the case of Reynolds of 2000, seen in Figure 95, the maximum fluctuation is in the order of roughly 3%, consistent with the DNS performed by Kopera [178], with an aspect ratio of 2.0 and a Reynolds number of 9000, in which a damped fluctuation in the re-attachment of less than 1% was observed.

In spite of the expected differences observed with previous DNS/LES calculations, present results are consistent with that observed in other publications.

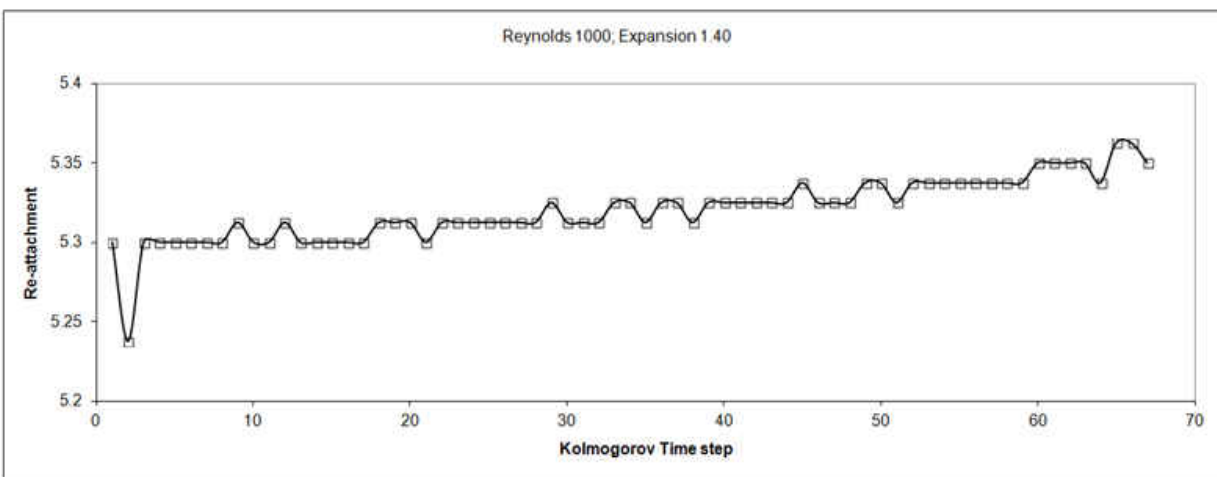


Figure 94: Variation of re-attachment with time, 2D-DNS BFS, $Re = 1000$, $ER = 1.40$

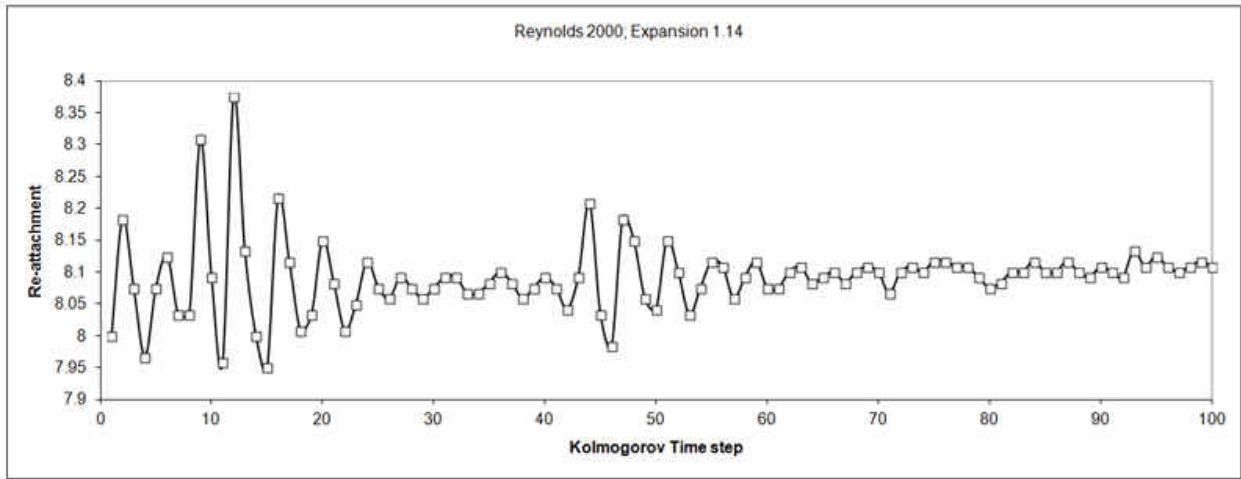


Figure 95: Variation of re-attachment with time, 2D-DNS BFS, $Re = 2000$, $ER = 1.40$

8.3 Backward-Facing Step with $ER = 1.14$ and $Re_{D_h} = 3000$

For the simulations with an expansion ratio of 1.14, only the one corresponding to a Reynolds number of 3000 is presented here since the analysis is similar for the other cases.

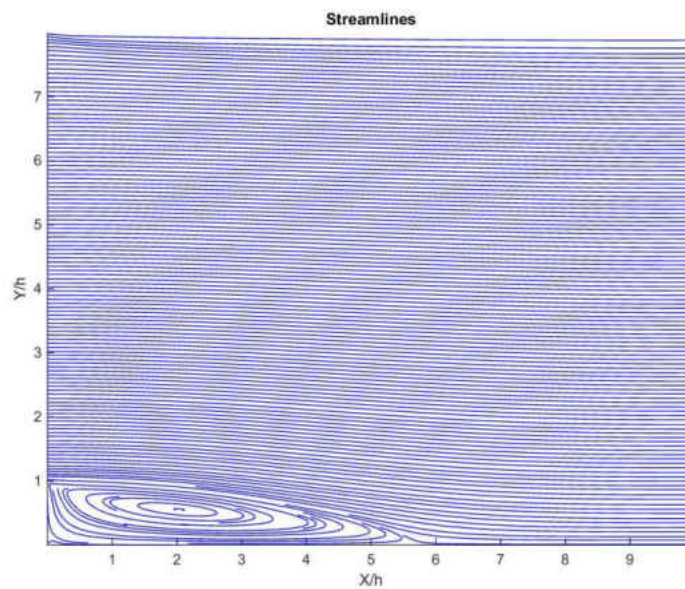


Figure 96: Streamlines, 2D-DNS BFS, $ER = 1.14$, $Re_{D_h} = 3000$

Figure 96 shows the averaged streamlines, with basically one main vortex and a very small one in the left corner, the so-called Moffatt vortex. Figure 97 and Figure 98 show the velocity contours where a clear laminarization phenomenon is observed. In spite of this issue, the averaged pattern of the flow is correctly described for this expansion ratio as observed in the experimental measurements of Tropea [334].

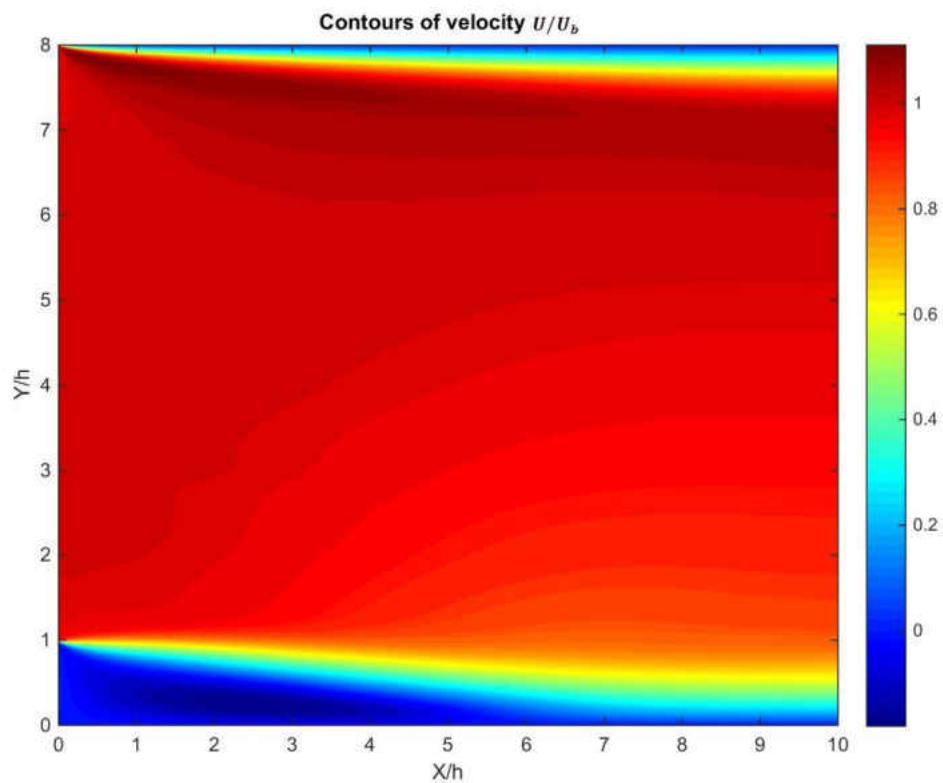


Figure 97: Contours of velocity U/\bar{V} , 2D-DNS BFS, $ER = 1.14$, $Re_{D_h} = 3000$

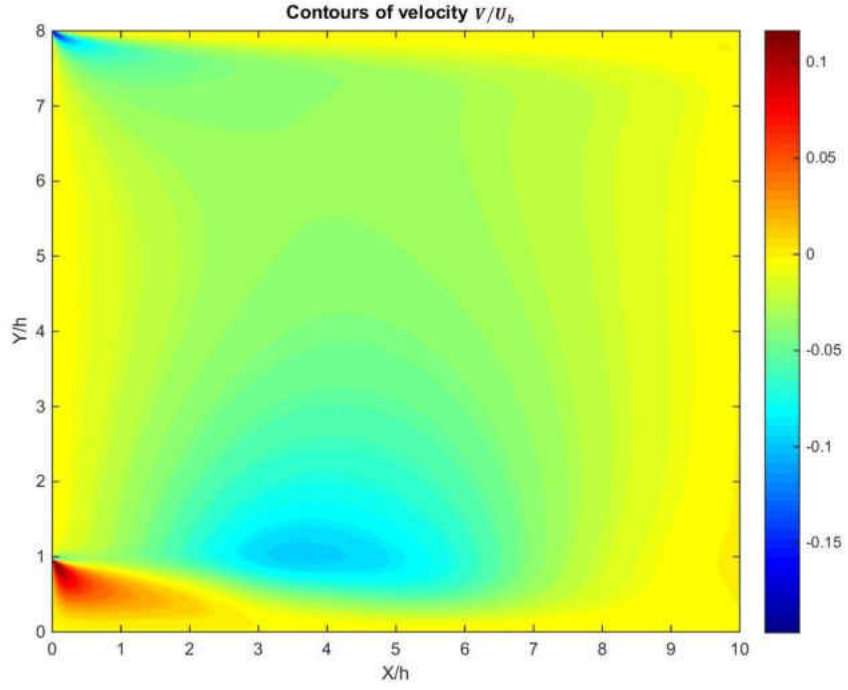


Figure 98: Contours of velocity v/\bar{v} , 2D-DNS BFS, $ER=1.14$, $Re_{D_h} = 3000$

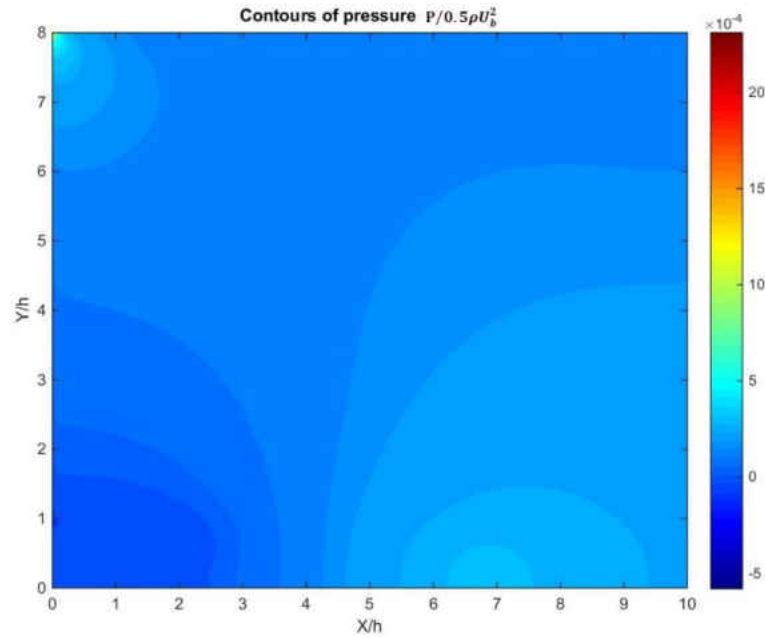


Figure 99: Contours of pressure $p/(0.5 \cdot \rho \cdot \bar{v}^2)$, 2D-DNS BFS, $ER=1.14$, $Re_{D_h} = 3000$

Figure 99 shows the pressure contours with the corresponding singularities in both left corners. From Figure 100 to Figure 103, the contours of the turbulent quantities are shown, with high level activity in the entrance of the step but the high activity is clearly damped as observed in Figure 100. An interesting aspect is observed from Figure 101 to Figure 103, where the stress $\overline{v'v'}$, even of smaller magnitude than the stress $\overline{u'u'}$, takes a longer distance to disappear. The same phenomenon was observed in the 2D-DNS on parallel plates.

In part disappointing but this issue may suggest that the turbulence might be produced from the wall and not from the inflow. The contours of vorticity, seen in Figure 104 do not provide much information, just the development of the boundary layer in the upper wall.

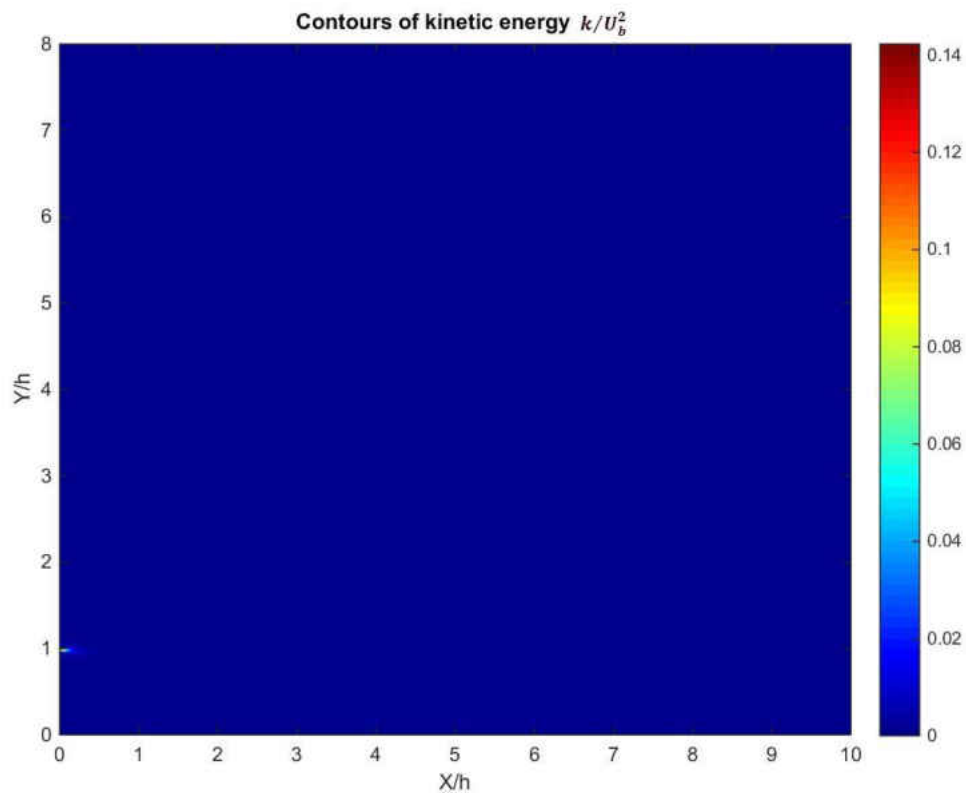


Figure 100: Contours of kinetic energy k/\bar{V}^2 , 2D-DNS BFS, $ER=1.14$, $Re_{D_h} = 3000$

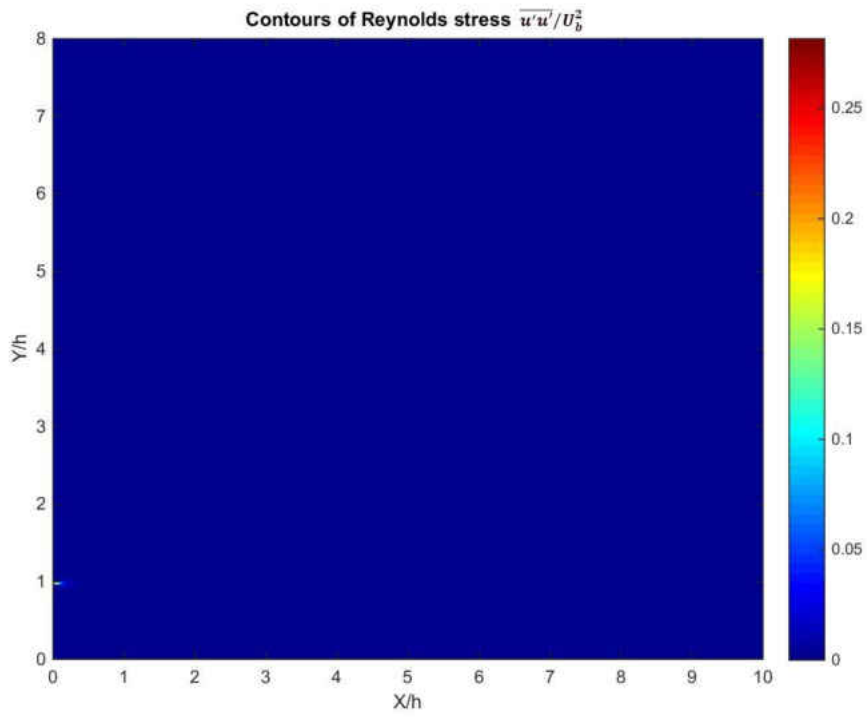


Figure 101: Contours of Reynolds stress $\overline{u'u'}/\bar{V}^2$, 2D-DNS BFS, $ER = 1.14$, $Re_{D_h} = 3000$

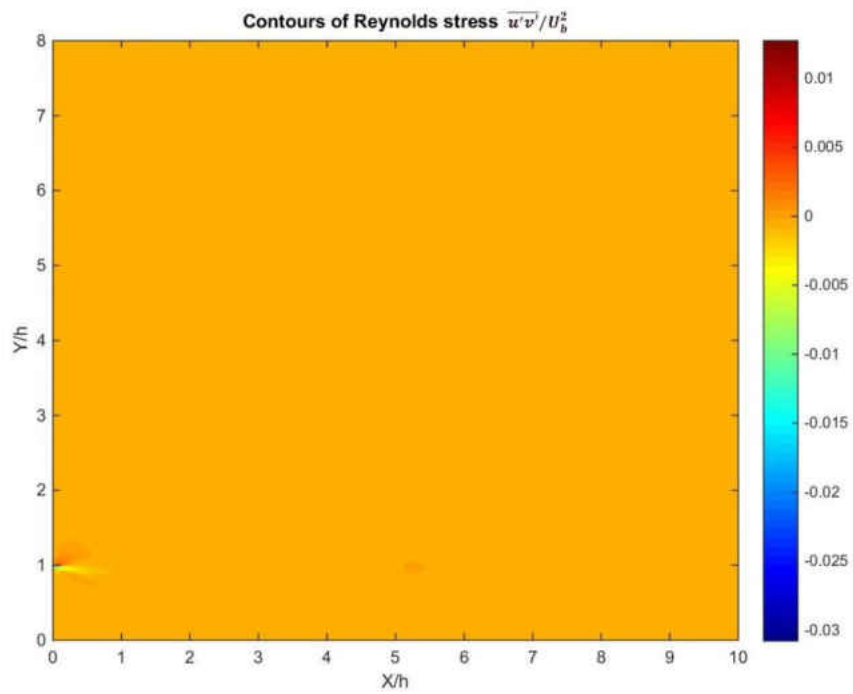


Figure 102: Contours of Reynolds stress $\overline{u'v'}/\bar{V}^2$, 2D-DNS BFS, $ER = 1.14$, $Re_{D_h} = 3000$

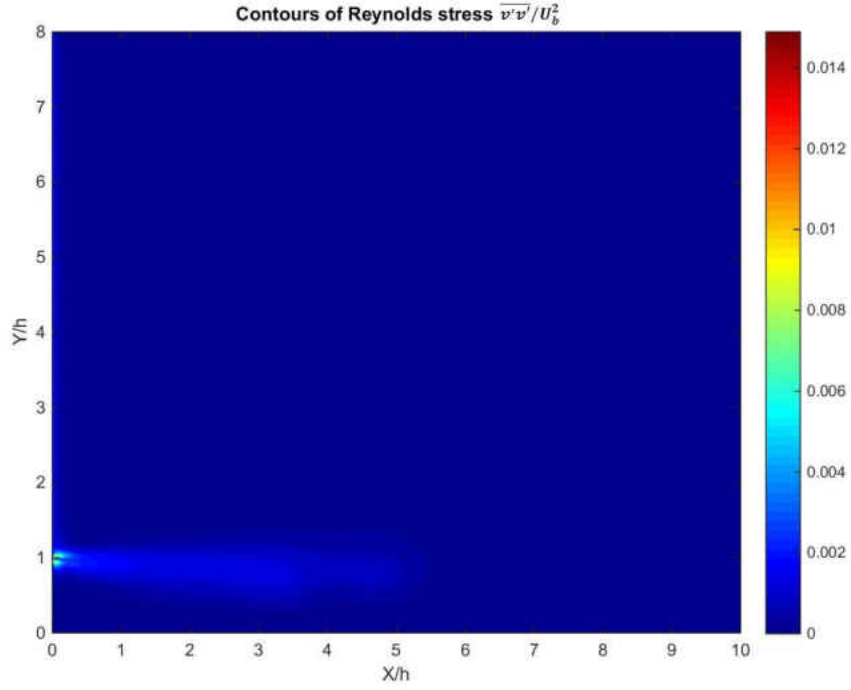


Figure 103: Contours of Reynolds stress $\overline{v'v'}/\overline{V}^2$, 2D-DNS BFS, $ER=1.14$, $Re_{D_h} = 3000$

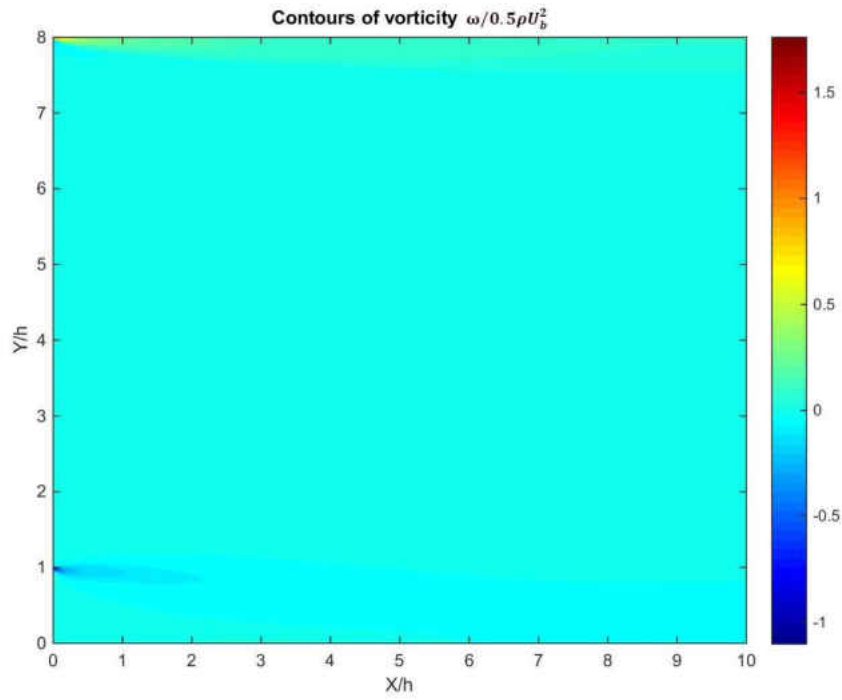


Figure 104: Contours of vorticity $\omega/(0.5 \cdot \rho \cdot \overline{V}^2)$, 2D-DNS BFS, $ER=1.14$, $Re_{D_h} = 3000$

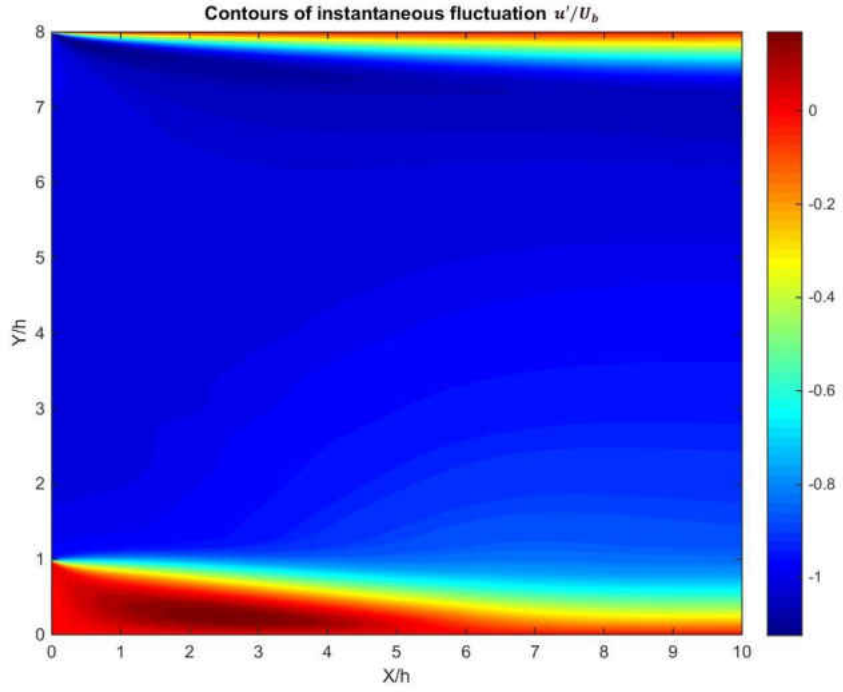


Figure 105: Contours of u'/\bar{V} in the last time step, 2D-DNS BFS, $ER = 1.14$, $Re_{D_h} = 3000$

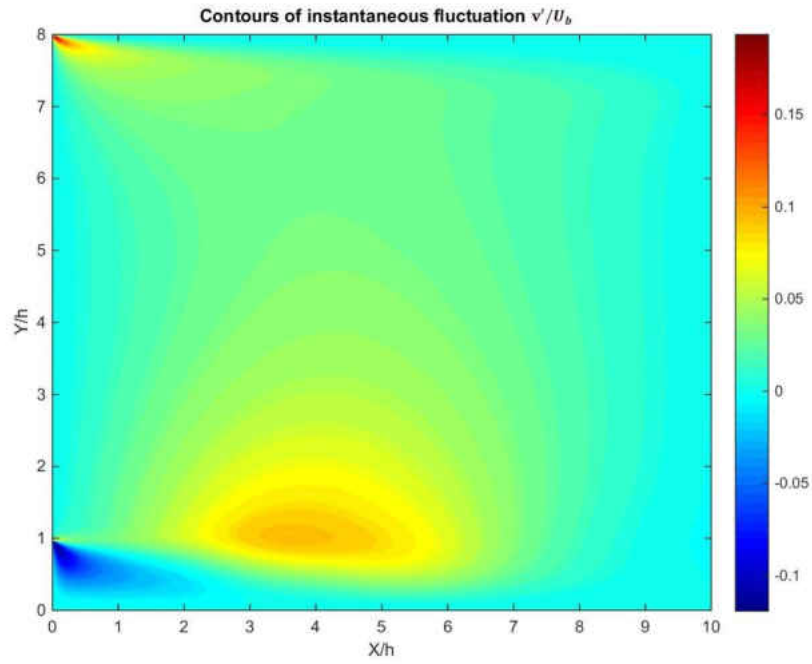


Figure 106: Contours of v'/\bar{V} at last time step, 2D-DNS BFS, $ER = 1.14$, $Re_{D_h} = 3000$

Figure 105 and Figure 106 show the instantaneous fluctuations u' and v' , in the last time step of the simulation, where the averaged quantities was computed. Hot colors show positive values while cold colors show negative ones. In the case of fluctuations u' , shown in Figure 105, the positive variations are in the vicinity of the wall while the negative ones are in the core of the fluid. A small activity recovery zone can be observed in the core of the fluid just over the boundary layer at the exit of the main vortex.

The decay of the activity in the core of the fluid is consistent with the constant decrement in the re-attachment observed in the last 3 time steps (Figure 93). In the same way, in Figure 106 can be observed that the negative instantaneous fluctuations of v' are negative in the back wall of the step and positive exactly over the main vortex.

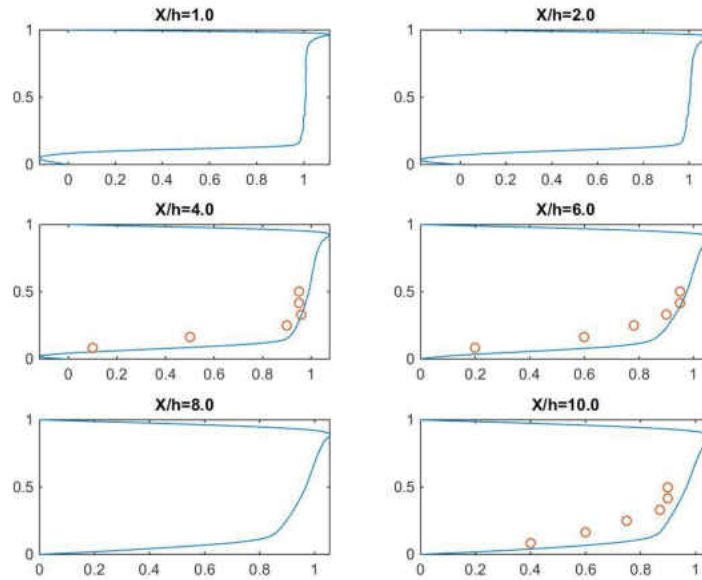


Figure 107: Velocity U/\bar{V} at different X-planes, 2D-DNS BFS, $ER = 1.14$, $Re_{D_h} = 3000$; “o” [202], “-“this work

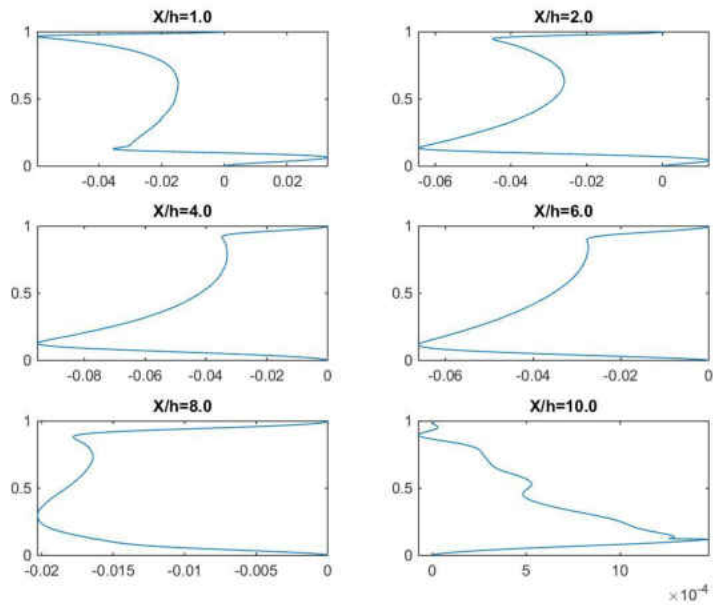


Figure 108: Velocity V/\bar{V} at different X-planes, 2D-DNS BFS, $ER = 1.14$, $Re_{D_h} = 3000$

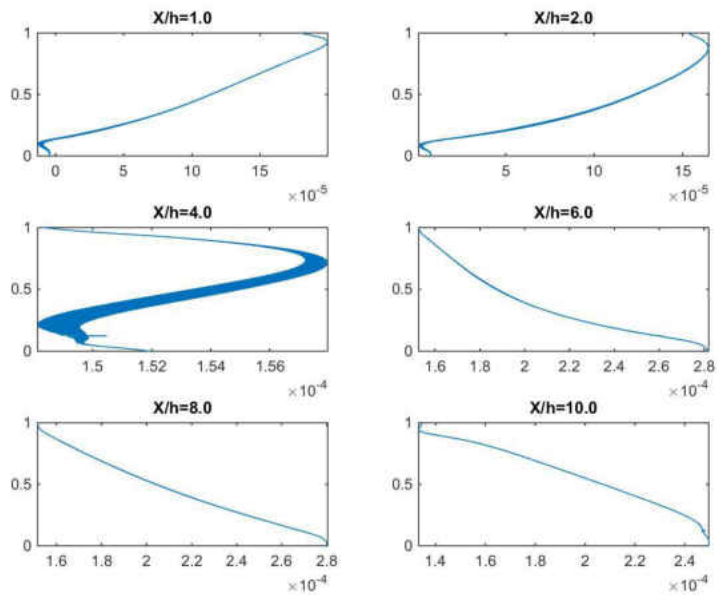


Figure 109: Pressure $p/(0.5 \cdot \rho \cdot \bar{V}^2)$ at different X-planes, 2D-DNS BFS, $ER = 1.14$, $Re_{D_h} = 3000$

Although not shown here, the increment of the turbulent activity in the boundary layer and in the main vortex might explain the later increment in the re-attachment. This behavior is consistent with the cyclic nature of turbulence.

Figure 107 shows the velocity U profile at several X-planes. The comparison with the results of Le [202] shows a reasonable agreement considering that in [202] an open channel was used, with an equivalent Reynolds number of 60,000 and an aspect ratio of 1.2. It is convenient to remember that the higher the Reynolds number is, the faster the boundary layer grows, due mainly to a decrement in the viscous forces.

The profiles of the vertical velocity V , shown in Figure 108 shows some numerical errors at the exit due to the tolerance set to reduce a bit the computing time at each time step.

Figure 109 shows the variation of pressure at several X-planes. First, there is a minimum of pressure in the line of the main vortex and the core of the flow. This effect can also be observed in the DNS performed by Koperka [178]. Additionally, there is a maximum of pressure very close to the upper wall but in the area of the main vortex, produced mainly to the sudden expansion and the corresponding acceleration of the fluid.

As soon as the re-attachment of the core of the fluid happens, there is an abrupt reduction of the pressure of the core is observed, consistent with the increment of the velocity of the fluid.

From Figure 110 to Figure 113, the turbulent quantities at several X-planes are shown. As expected, there is a high activity in the viscous sub-layer but the turbulent intensity decreases suddenly in the core, and rapidly as the fluid enters into the expansion.

The behavior of the stress $\overline{v'v'}$ is once again consistent with the one observed in Figure 103, in the meaning that the magnitude of $\overline{v'v'}$ is smaller than the magnitude of $\overline{u'u'}$, but it takes more time for this stress to diminish in the fluid.

In all, from Figure 110-Figure 113 an important fluctuation is observed, due probably to the short period of time spent for the statistics and/or for the effects of the white noise, useful to create turbulence but not absolutely correct statistically.

Figure 114 shows the pressure coefficient C_p at both, upper and lower walls. Here there is a considerable disagreement with the results of Kopera [178], where the pressure coefficient is roughly the same at both walls.

This difference can be due to the different numerical method used here, which can compute correctly the variations of pressure very close to the wall, as it is shown in [340].

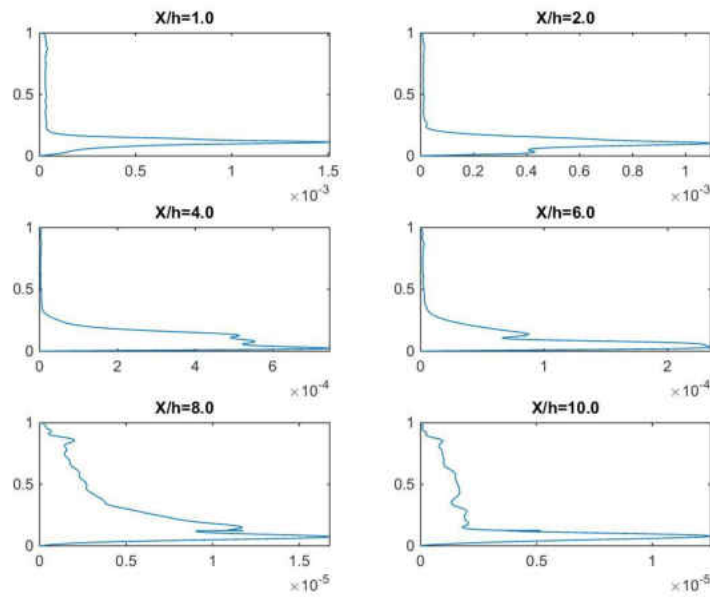


Figure 110: Kinetic energy k/\bar{V}^2 at different X-planes, 2D-DNS BFS, $ER = 1.14$, $Re_{D_h} = 3000$

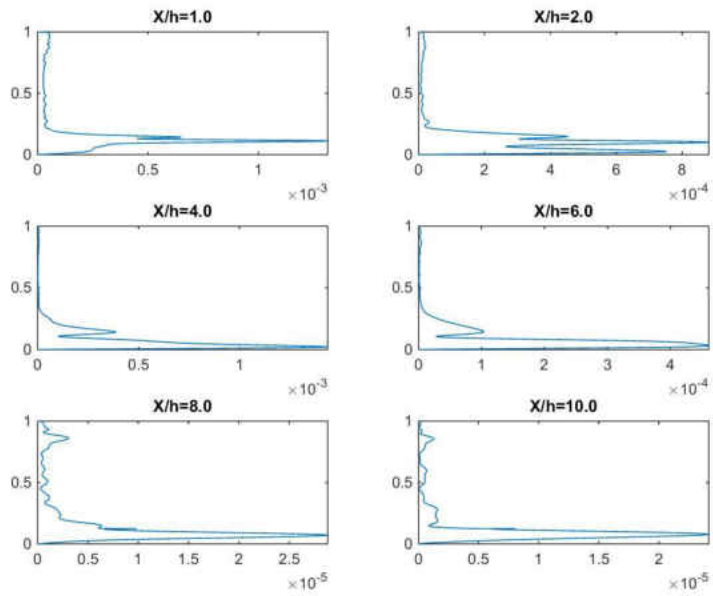


Figure 111: Reynolds stress $\overline{u'u'}/\bar{V}^2$ at different X-planes, 2D-DNS BFS, $ER = 1.14$, $Re_{D_h} = 3000$

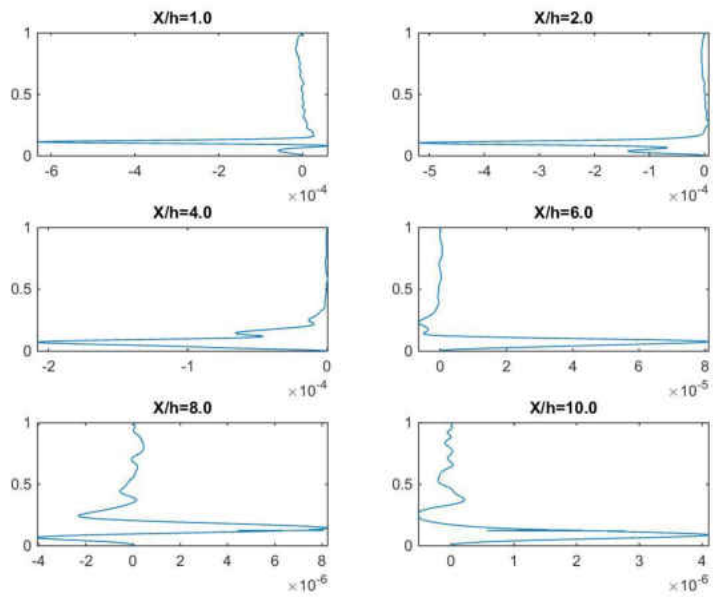


Figure 112: Reynolds stress $\overline{u'v'}/\bar{V}^2$ at different X-planes, 2D-DNS BFS, $ER = 1.14$, $Re_{D_h} = 3000$

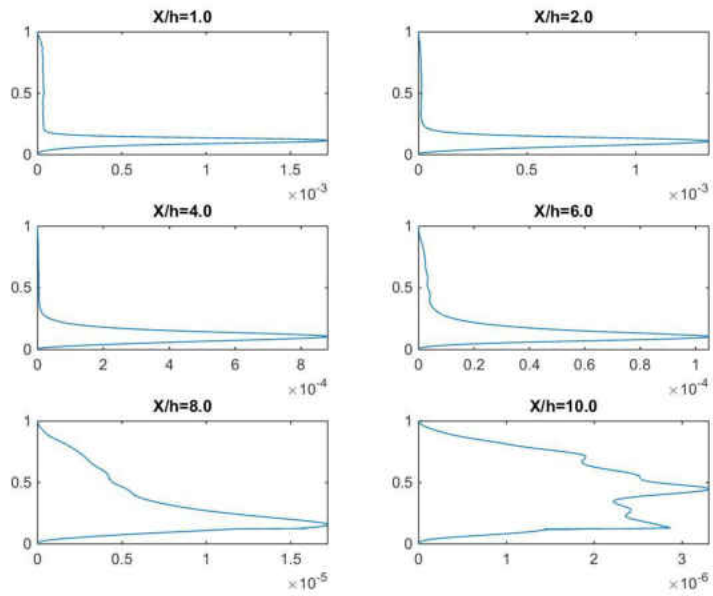


Figure 113: Reynolds stress $\overline{v'v'}/\overline{V}^2$ at different X-planes, 2D-DNS BFS, $ER = 1.14$, $Re_{D_h} = 3000$

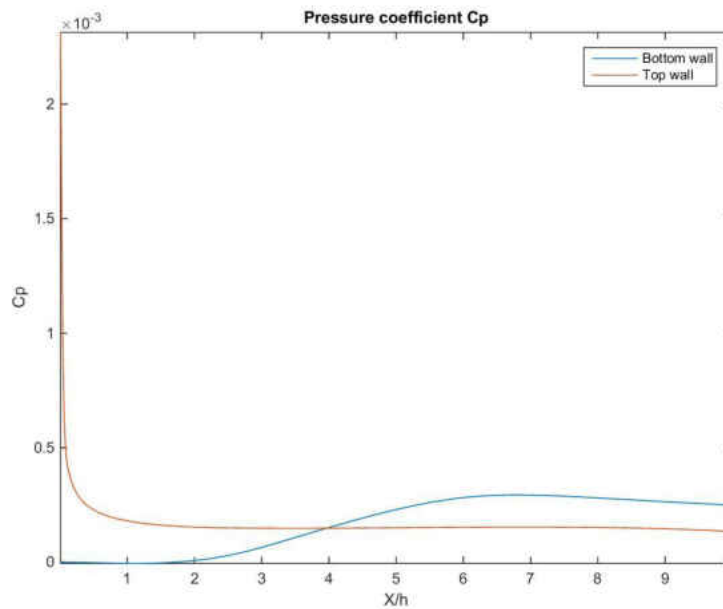


Figure 114: Pressure coefficient C_p as function of position, 2D-DNS BFS, $ER = 1.14$, $Re_{D_h} = 3000$

For a distance $x/h \leq 4$, the pressure coefficient at the lower wall is smaller than in the upper wall, due to the sudden acceleration of the fluid. As soon as the re-attachment occurs, at $x/h \geq 6$, the pressure coefficient of the lower wall increases due to the re-attachment.

Finally, friction coefficient, seen in Figure 115, shows good qualitative agreement, in the sense that, as reported in the simulation of Le [202], the peak of $|C_f|$ decreases as the Reynolds number increases.

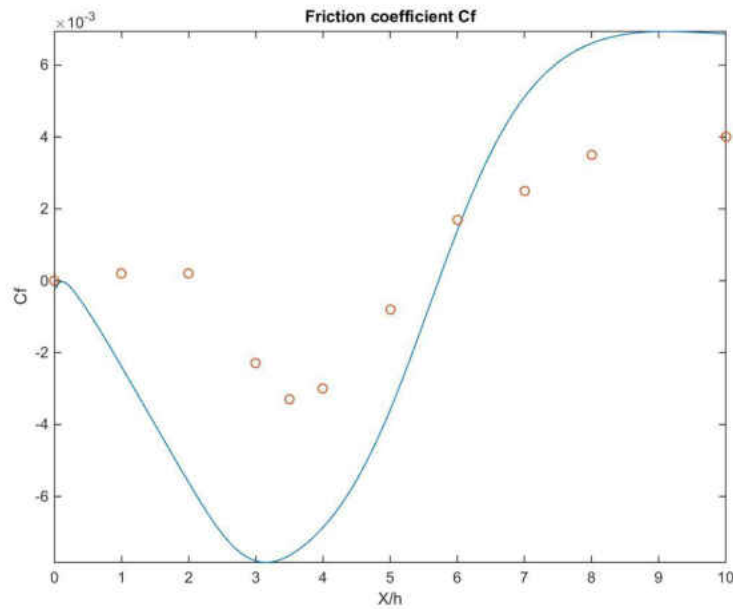


Figure 115: Friction coefficient C_f at different X-planes, 2D-DNS BFS, $ER=1.14$, $Re_{D_h} = 3000$; “o” [157], “-“ this work

8.4 Backward-Facing Step with $ER = 1.40$ and $Re_{D_h} = 2000$

For the simulations with an expansion ratio of 1.40 the situation is similar, only the one corresponding to a Reynolds number of 2000 is presented here since the analysis is similar for case of Reynolds number of 1000.

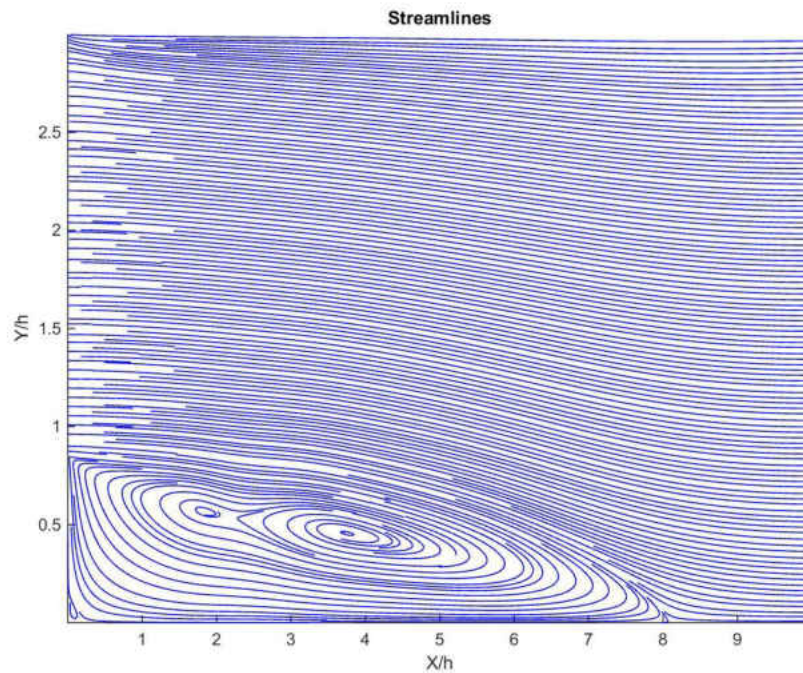


Figure 116: Streamlines, 2D-DNS BFS, $ER = 1.40$, $Re_{D_h} = 2000$

Since the flow conditions are similar to the previous section, the analysis is similar. In Figure 116 the streamline shows a very small vortex, closed to the center of the main vortex. This effect can be due to the beginning of transition. Additionally, the corresponding Moffatt vortex is observed in the left-lower corner.

When observing the contours of the Reynolds stress $\overline{v'v'}$, a large area of high activity is appreciated. This issue is consistent with the observed previously and in the results presented in

the appendix, and it may confirm that the turbulence has to be produced from the wall and not from the inflow.

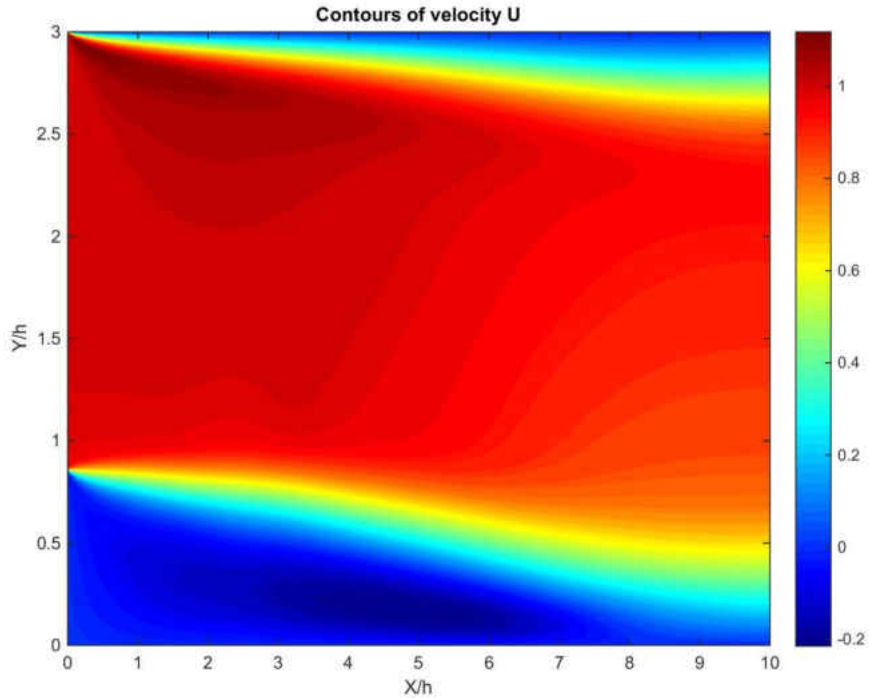


Figure 117: Contours of velocity U/\bar{V} , 2D-DNS BFS, $ER = 1.40$, $Re_{D_h} = 2000$

Figure 127 shows the development of the horizontal velocity component U at several X -planes, with good agreement with the computations of Le [202].

Figure 134 shows the pressure coefficient at both, upper and lower walls and the behavior is similar to the one observed in the previous section, and in all the other cases. This effect is completely different from the results presented by Le [202], which is an open channel flow and also different from the results of Kopera [178].

Finally, Figure 135 shows the friction coefficient in the lower wall, showing the same behavior, except between $2 \leq x/h \leq 3$ where becomes constant, due to the small vortex just at the left of the center of the main one.

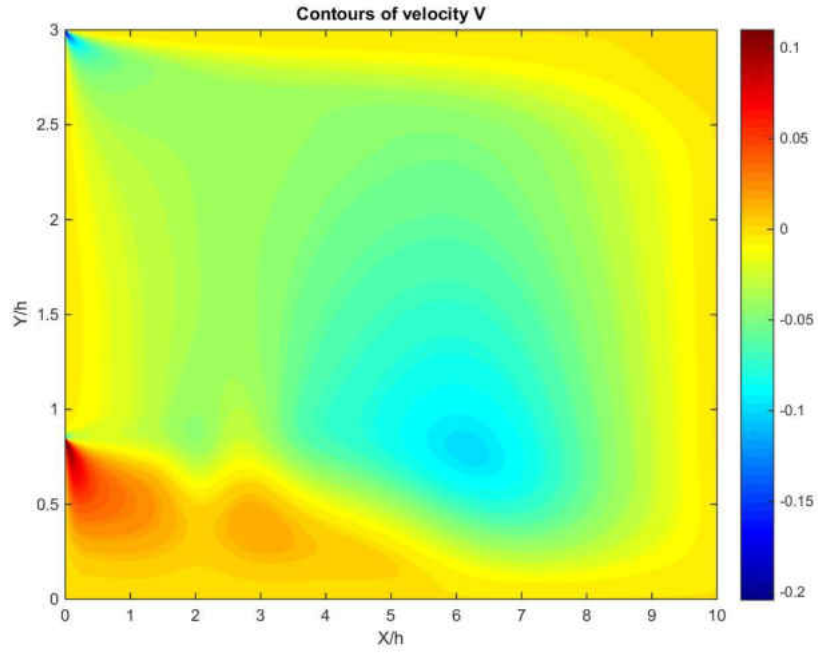


Figure 118: Contours of velocity V/\bar{V} , 2D-DNS BFS, $ER = 1.40$, $Re_{D_h} = 2000$

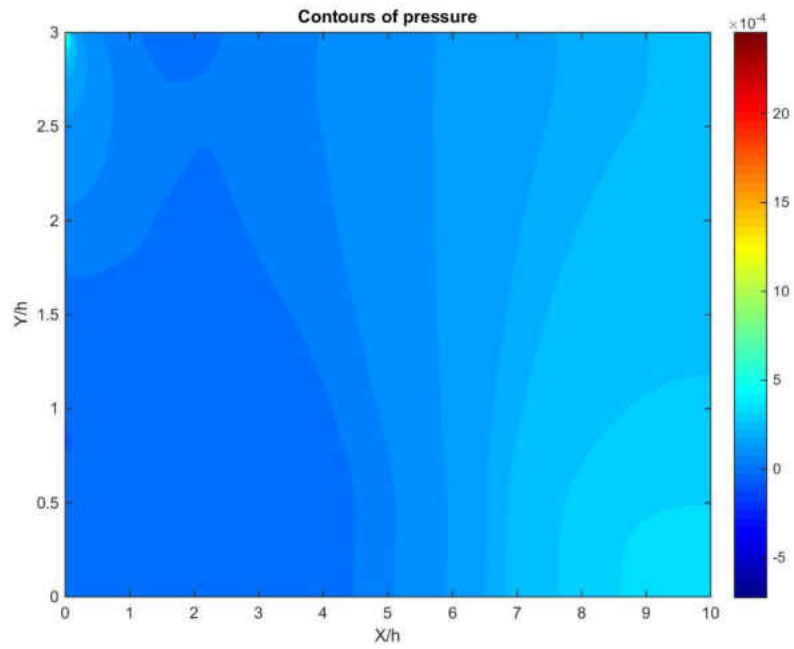


Figure 119: Contours of pressure $p/(0.5 \cdot \rho \cdot \bar{V}^2)$, 2D-DNS BFS, $ER = 1.40$, $Re_{D_h} = 2000$

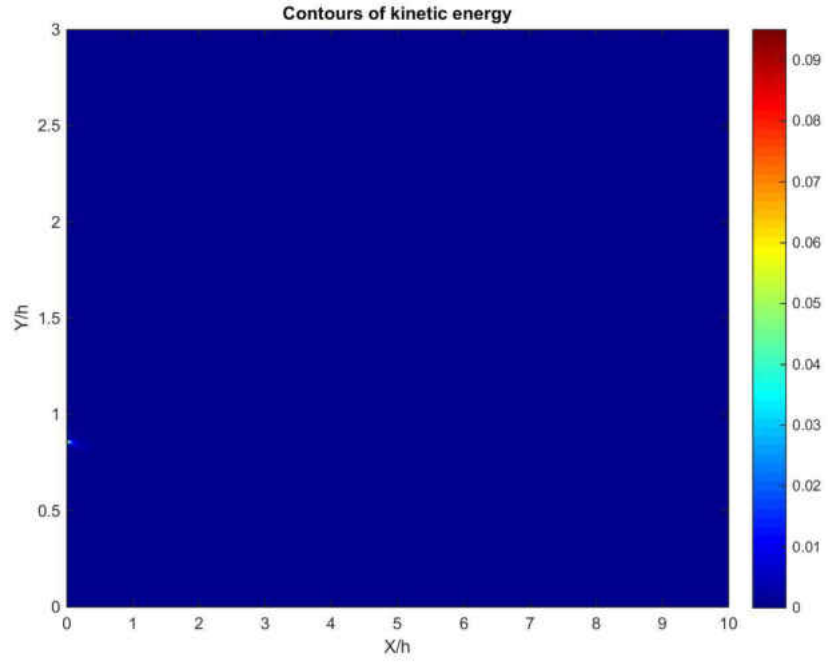


Figure 120: Contours of kinetic energy k/\bar{V}^2 , 2D-DNS BFS, $ER = 1.40$, $Re_{D_h} = 2000$

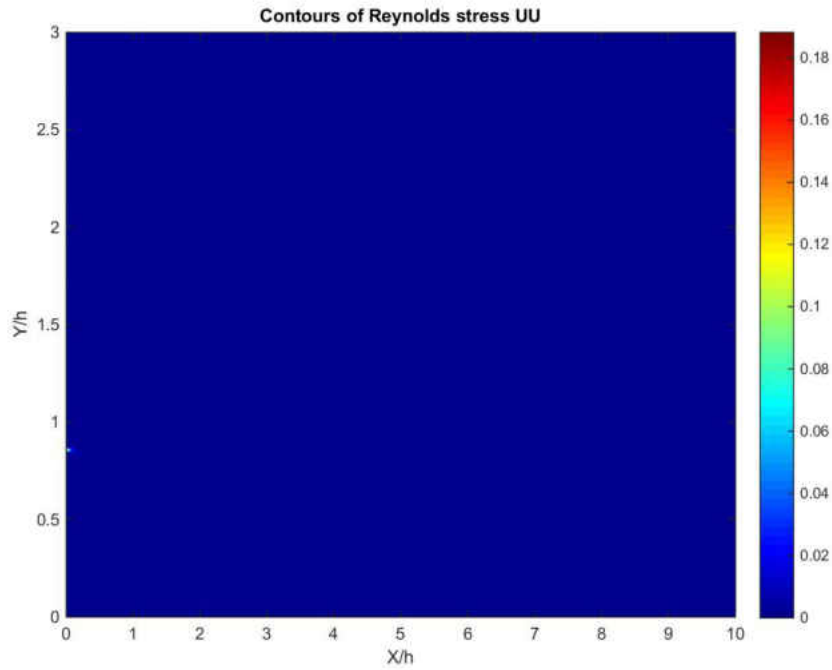


Figure 121: Contours of Reynolds stress $\overline{u'u'}/\bar{V}^2$, 2D-DNS BFS, $ER = 1.40$, $Re_{D_h} = 2000$

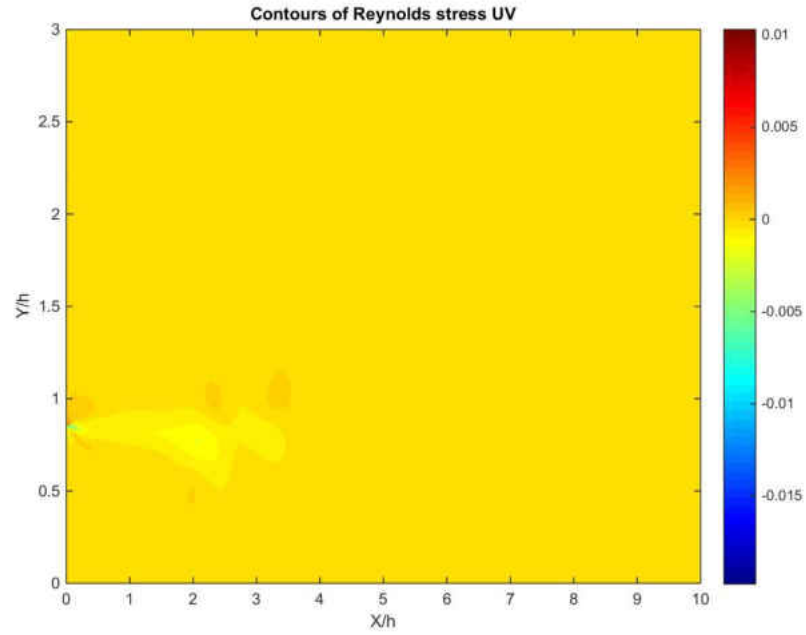


Figure 122: Contours of Reynolds stress $\overline{u'v'}/\overline{V}^2$, 2D-DNS BFS, $ER = 1.40$, $Re_{D_h} = 2000$

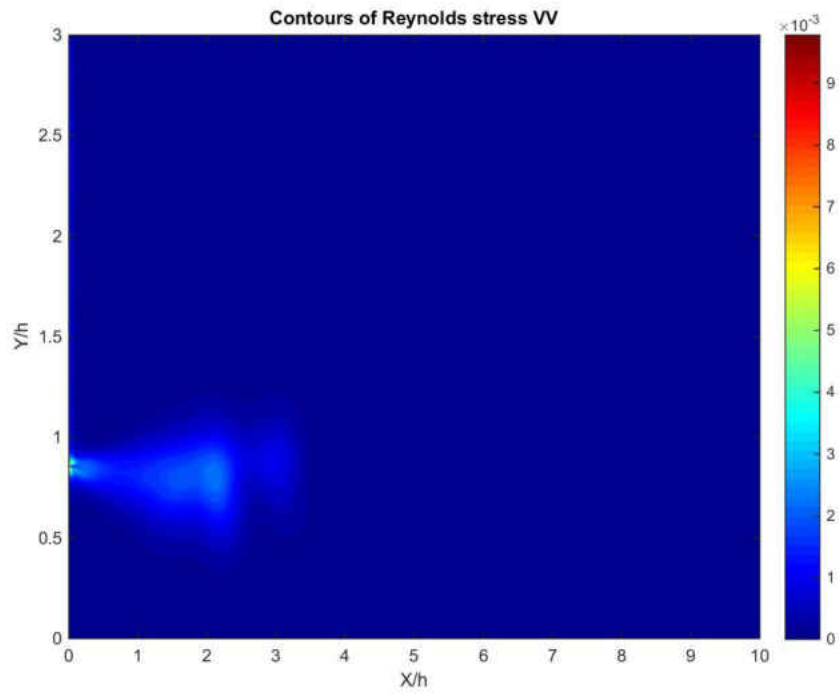


Figure 123: Contours of Reynolds stress $\overline{v'v'}/\overline{V}^2$, 2D-DNS BFS, $ER = 1.40$, $Re_{D_h} = 2000$

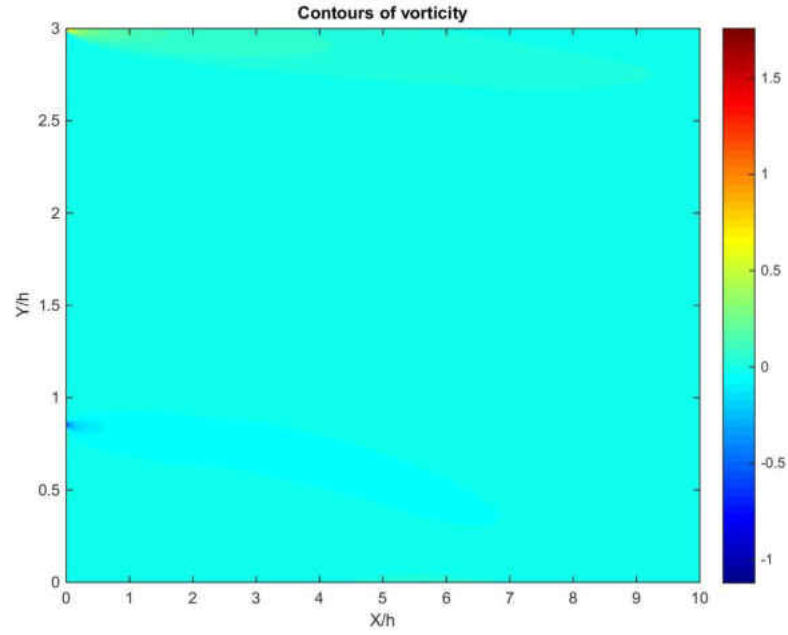


Figure 124: Contours of vorticity $\omega/(0.5 \cdot \rho \cdot \bar{V}^2)$, 2D-DNS BFS, $ER = 1.40$, $Re_{D_h} = 2000$

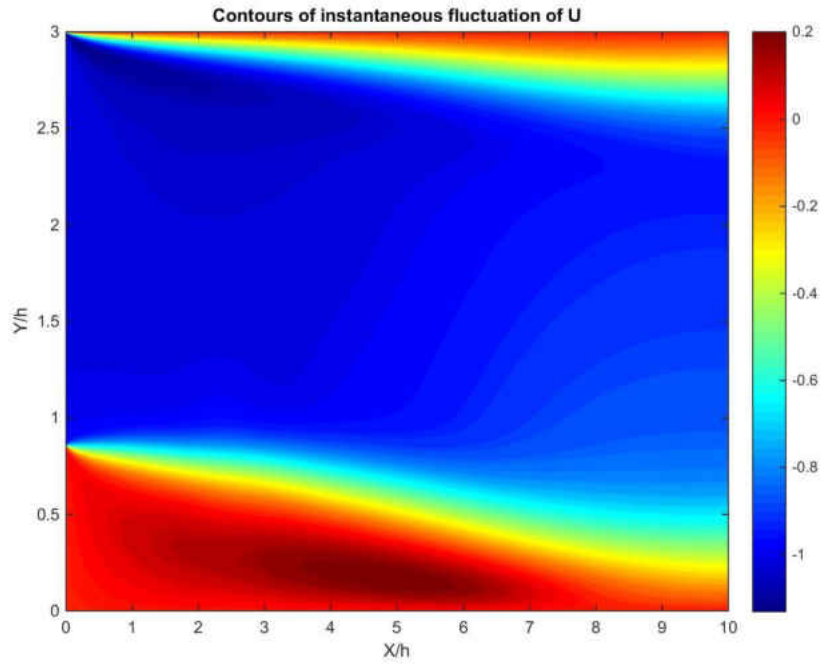


Figure 125: Contours of u'/\bar{V} in the last time step, 2D-DNS BFS, $ER = 1.40$, $Re_{D_h} = 2000$

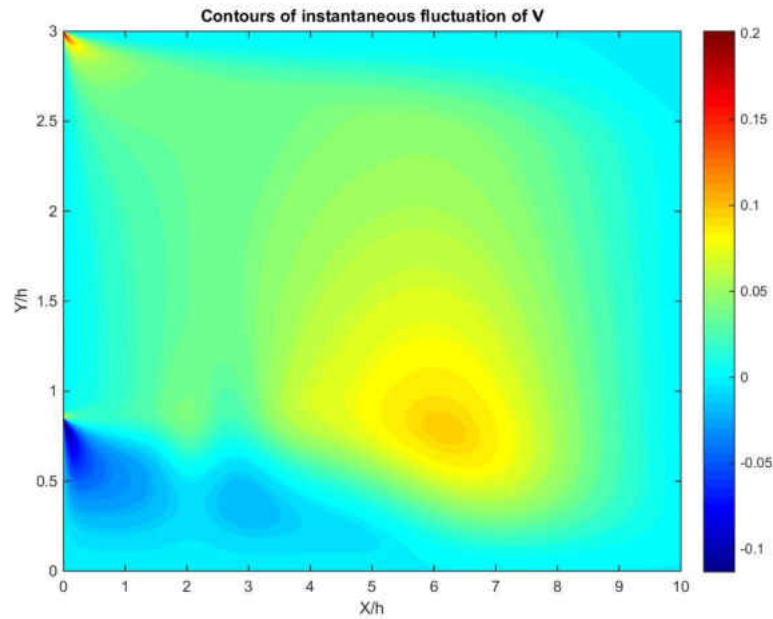


Figure 126: Contours of v'/\bar{V} at last time step, 2D-DNS BFS, $ER = 1.40$, $Re_{D_h} = 2000$

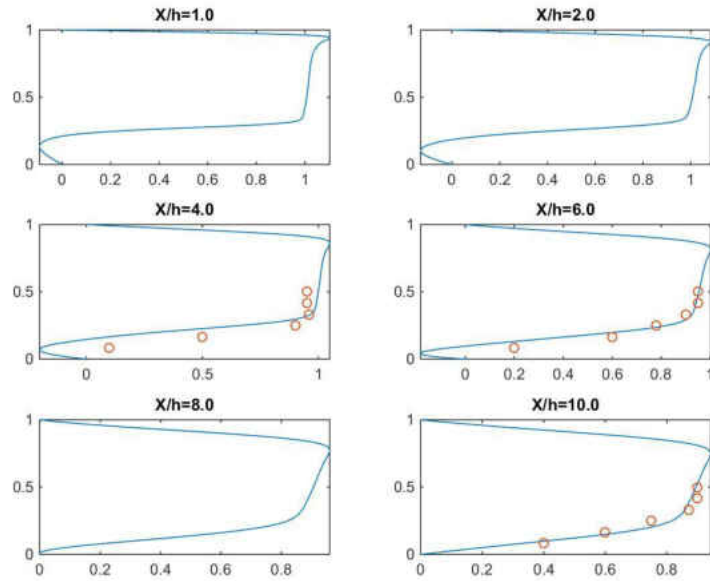


Figure 127: Velocity U/\bar{V} at different X-planes, 2D-DNS BFS, $ER = 1.40$, $Re_{D_h} = 2000$; “o” [202], “-“ this work

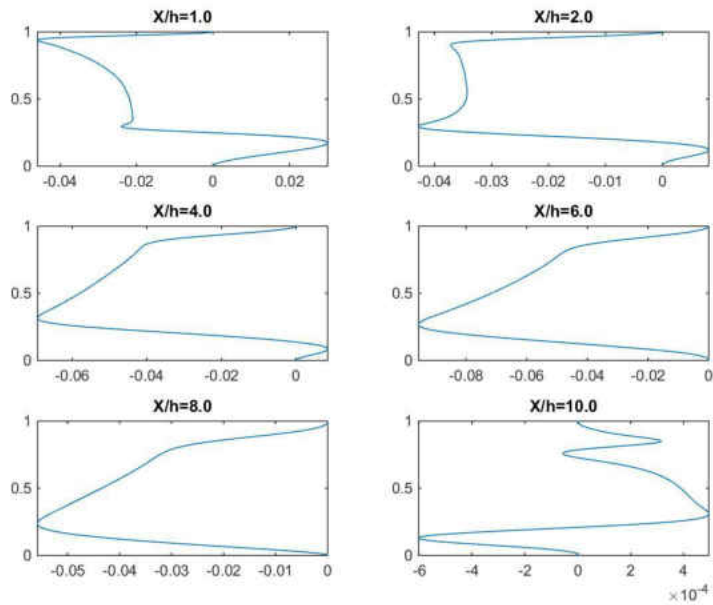


Figure 128: Velocity V/\bar{V} at different X-planes, 2D-DNS BFS, $ER = 1.40$, $Re_{D_h} = 2000$

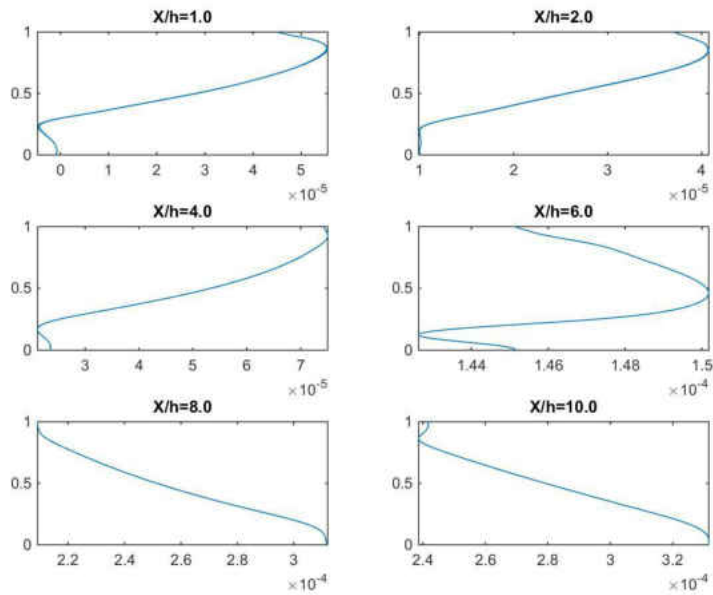


Figure 129: Pressure $p/(0.5 \cdot \rho \cdot \bar{V}^2)$ at different X-planes, 2D-DNS BFS, $ER = 1.40$, $Re_{D_h} = 2000$

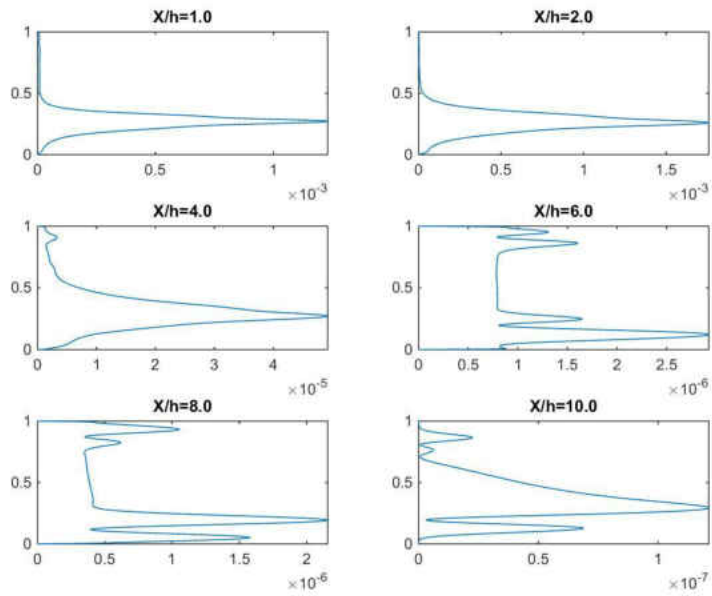


Figure 130: Kinetic energy k/\bar{V}^2 at different X -planes, 2D-DNS BFS, $ER = 1.40$, $Re_{D_h} = 2000$

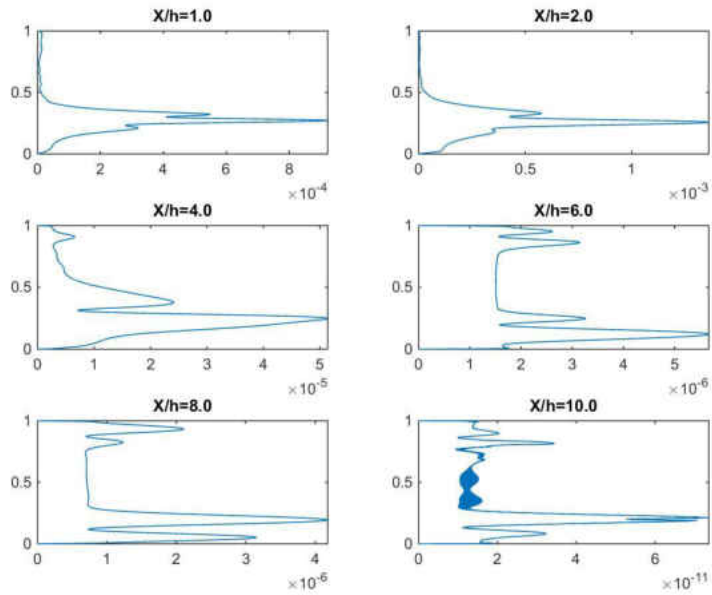


Figure 131: Reynolds stress $\overline{u'u'}/\bar{V}^2$ at different X -planes, 2D-DNS BFS, $ER = 1.40$, $Re_{D_h} = 2000$

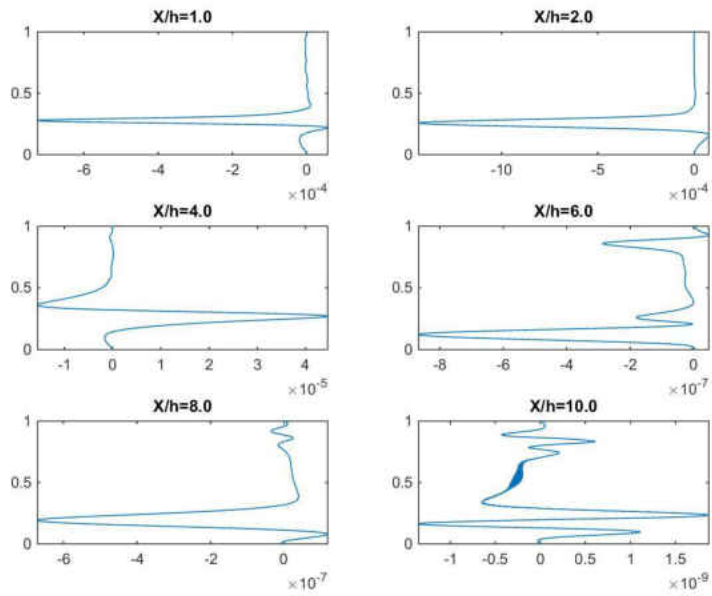


Figure 132: Reynolds stress $\overline{u'v'}/\overline{V}^2$ at different X-planes, 2D-DNS BFS, $ER = 1.40$, $Re_{D_h} = 2000$

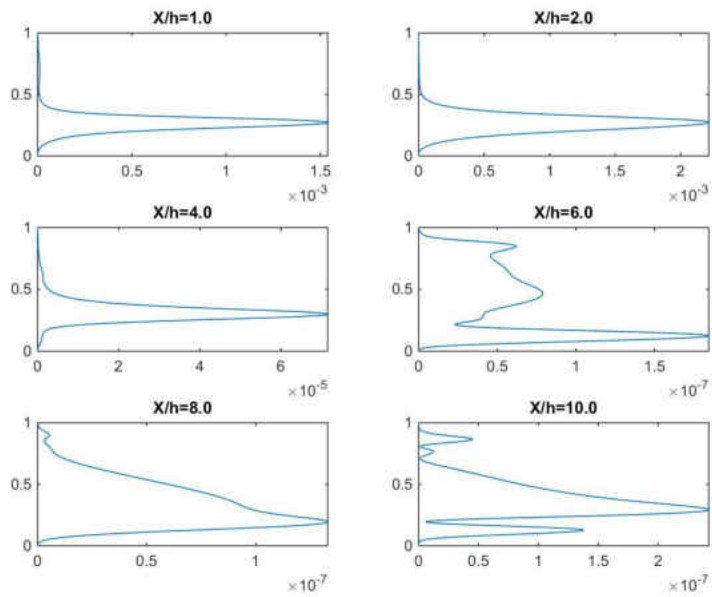


Figure 133: Reynolds stress $\overline{v'v'}/\overline{V}^2$ at different X-planes, 2D-DNS BFS, $ER = 1.40$, $Re_{D_h} = 2000$

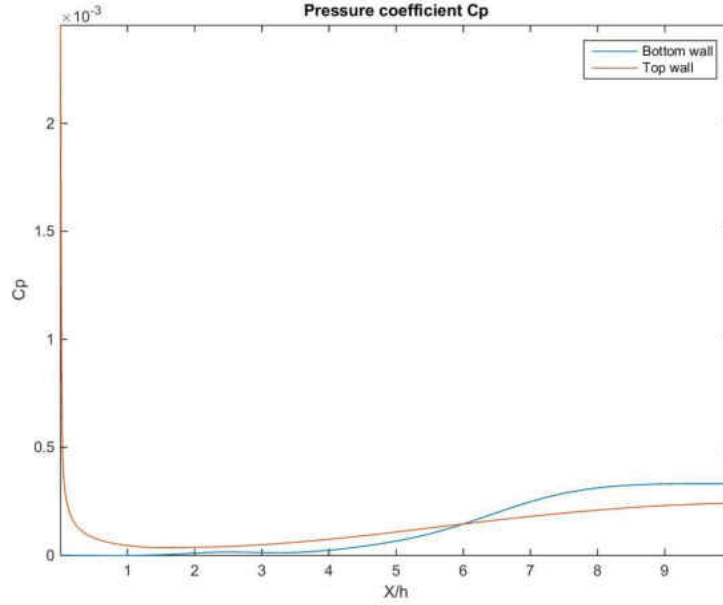


Figure 134: Pressure coefficient C_p as function of position, 2D-DNS BFS, $ER = 1.40$, $Re_{D_h} = 2000$

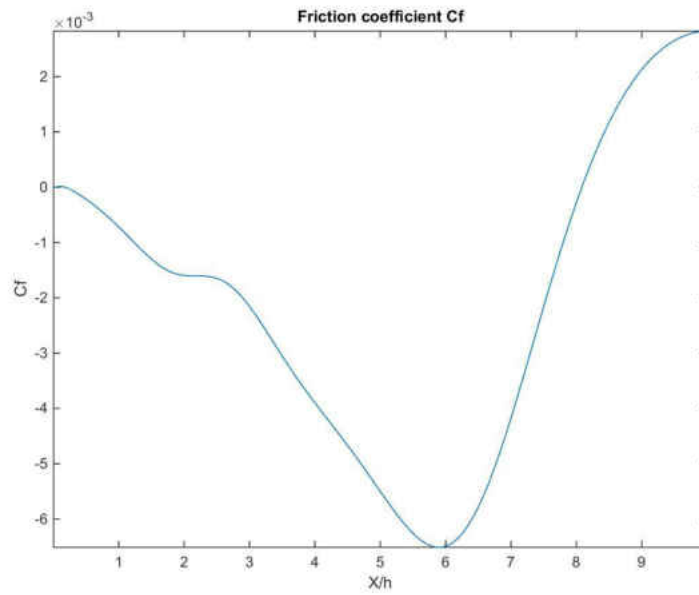


Figure 135: Friction coefficient C_f at different X-planes, 2D-DNS BFS, $ER = 1.40$, $Re_{D_h} = 2000$

CHAPTER NINE CONCLUSIONS

The objective of this work can be divided in several topics, numerical method, implementation, multicore solver, validation and DNS calculations.

With respect to numerical method, the classical segregated velocity-pressure coupling technique was analyzed and a very important inconsistency was found in the mass balance step. The current technique is valid strictly only for parabolic flows and, in order to get good results in elliptic flows, a fine mesh must be used so the first points are in the boundary layer. The technique presented here, with the direct velocity-pressure coupling technique, has robust convergence properties when the convection forces are low or moderate. The validation showed excellent agreement in the limitations already presented.

A very important effort was made to write an efficient code in C++, implementing efficient techniques to reduce the time in the geometric configuration, obtaining an algorithm of order $O(N)$ for problems up to 1 million points and $O(N \log(N))$ from 4 million points and up. In all the iterative calculation all coding techniques were implemented to reduce the allocation time for temporaries and an efficient use of all math calculation units.

A novel multicore flow solver was presented which does not use the traditional MPI communication protocol. The asynchronous concurrent solver allows overlapping some serial operations and excellent speedups are obtained as the Reynolds number increases in the cases evaluated. The implementation of the multicore solver in GPU architectures is straightforward.

Finally, with respect to the DNS calculation procedure, a strong criterion, based on the local Reynolds number was presented, allowing the determination in advance the grid

requirements for any fluid flow calculation. Based on this local Reynolds number criterion, it was found that all reviewed DNS calculations use a grid so stretched that the local Reynolds number is in the unstable region. Direct numerical simulations were performed in parallel plates and backward-facing step with very fine grids and the laminarization phenomena is always present. The results presented here suggest that most current DNS techniques simulate the instability of the flow by the instability of the numerical procedure. Tests performed in this work suggest that the effect of the turbulent inflow conditions is negligible if the system of equations is not unstable.

The specific results obtained in the 2D-DNS on a backward-facing step show good agreement in the velocity profiles, streamlines and pressure, but no important information for the turbulent quantities.

From this work, future directions are the developing of a so-called *dynamic interpolation technique*, which consists in the use of a low order interpolation scheme when the residuals are high and increment the order of the interpolation as the residuals fall. This idea can be expanded to *dynamic discretization*, beginning from second order when the residuals are high and incrementing the order of the scheme as the solution is reached.

Additionally, a new DNS technique can be developed by producing the turbulence from the wall and not from the classical inflow-stretched grid as it is done today. By producing turbulence from the wall the solution of developing turbulent flow will be possible, allowing the study, under controlled conditions, the study of the hypotheses of turbulence and the solution of more realistic problems.

Finally, the 2D DNS/LES technique has been used widely, for example in 2D Taylor flow, as a test for future full DNS/LES implementations, 2D hydromagnetic turbulent flow,

simplified simulation of flow in rivers, interstellar flow, as well as for the study of sea currents in oceans, between others.

Perhaps, the most important question that comes from this dissertation is: *Is it possible to simulate turbulent flow by a simplified 2D DNS or LES simulation?* With the exception to 2D hydromagnetic turbulent flow, the results presented in this work suggest that the 2D DNS/LES as a simplified way to simulate turbulent flow is not possible.

The explanation to this answer comes from an anomaly that happens only in 2D flows. When observing the continuity equation in 2D, $\partial u/\partial x + \partial v/\partial y = 0$, it can be observed that an perturbation to the velocity u will be reflected in a perturbation to the velocity v and viceversa. The mass balance equation in 2D builds a very strong link between both velocity components.

On the other hand, if a look is taken to the continuity equation in 3D, $\partial u/\partial x + \partial v/\partial y + \partial w/\partial z = 0$, any perturbation to the velocity u will be distributed between v and w . The exact fraction of that distribution will be determined by the dynamics of the flow. Even in axisymmetric flows, the inclusion of a third component in the mass balance seems to be fundamental for the link between each pair of velocity components not to be so strong.

On the other hand, the fact that all full DNS/LES simulations reviewed by this author use highly stretched grids, as a way to simulate the physical instabilities by means of numerical instability, suggests that a better way to simulate turbulent flow has to be by a combined effect of inflow conditions and perturbations from the wall, just as experiments show.

APPENDIX A
BACKWARD-FACING STEP WITH $ER=1.14$ AND $Re_{D_h}=1000$

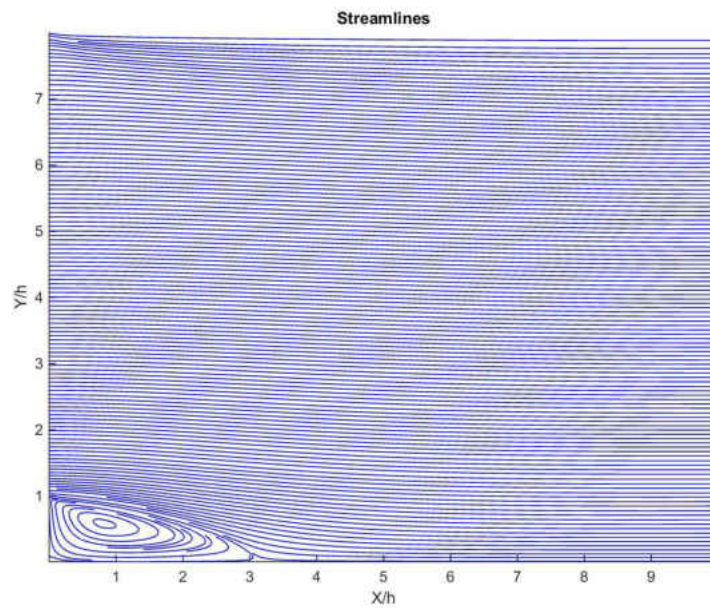


Figure 136: Streamlines, 2D-DNS BFS, $ER = 1.14$, $Re_{D_h} = 1000$

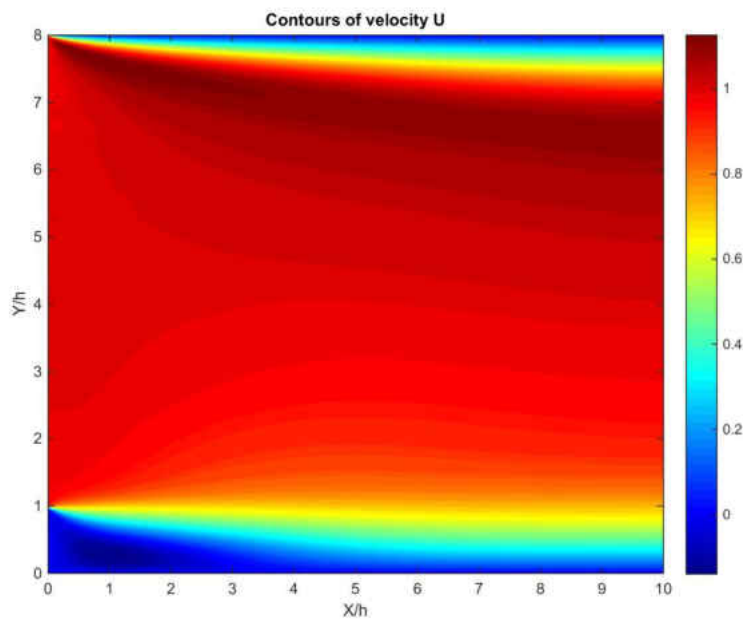


Figure 137: Contours of velocity U/\bar{V} , 2D-DNS BFS, $ER = 1.14$, $Re_{D_h} = 1000$

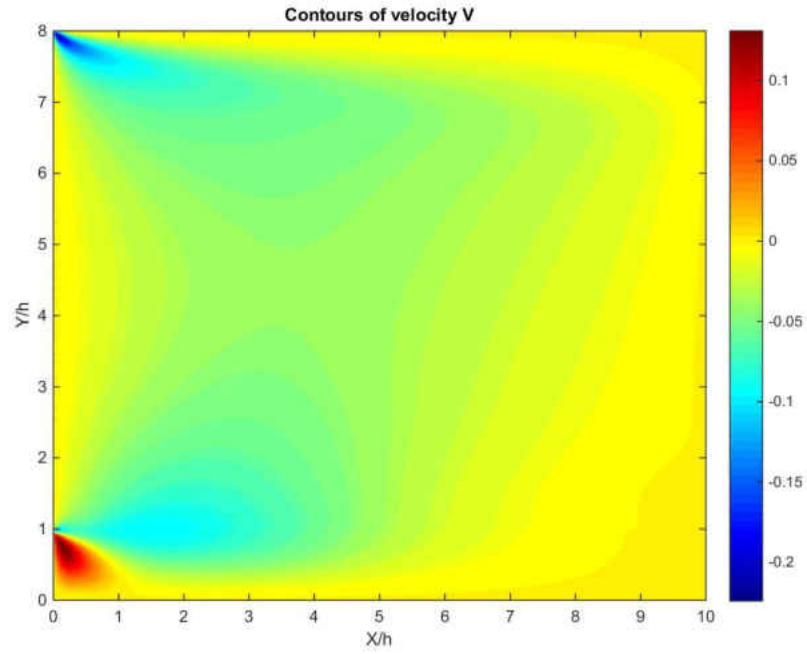


Figure 138: Contours of velocity V/\bar{V} , 2D-DNS BFS, $ER = 1.14$, $Re_{D_h} = 1000$

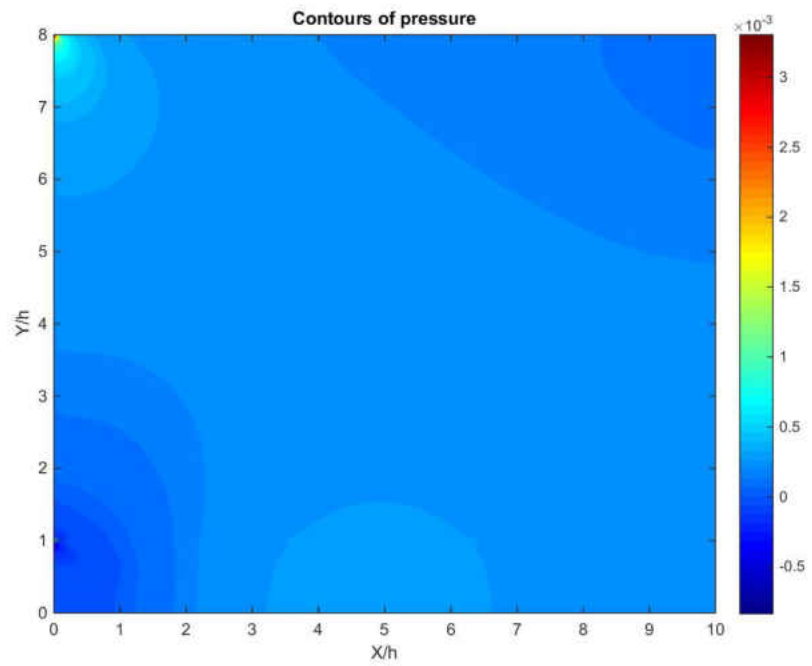


Figure 139: Contours of pressure $p/(0.5 \cdot \rho \cdot \bar{V}^2)$, 2D-DNS BFS, $ER = 1.14$, $Re_{D_h} = 1000$

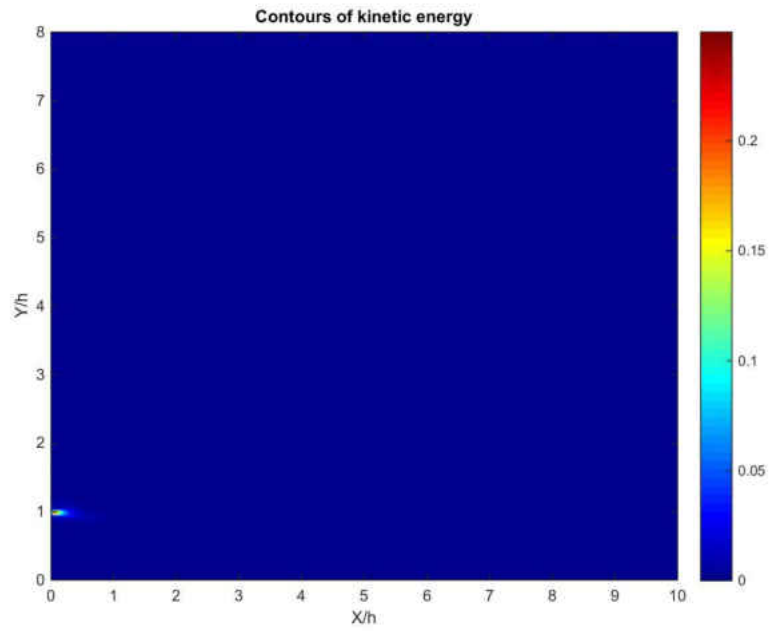


Figure 140: Contours of kinetic energy k/\bar{V}^2 , 2D-DNS BFS, $ER = 1.14$, $Re_{D_h} = 1000$

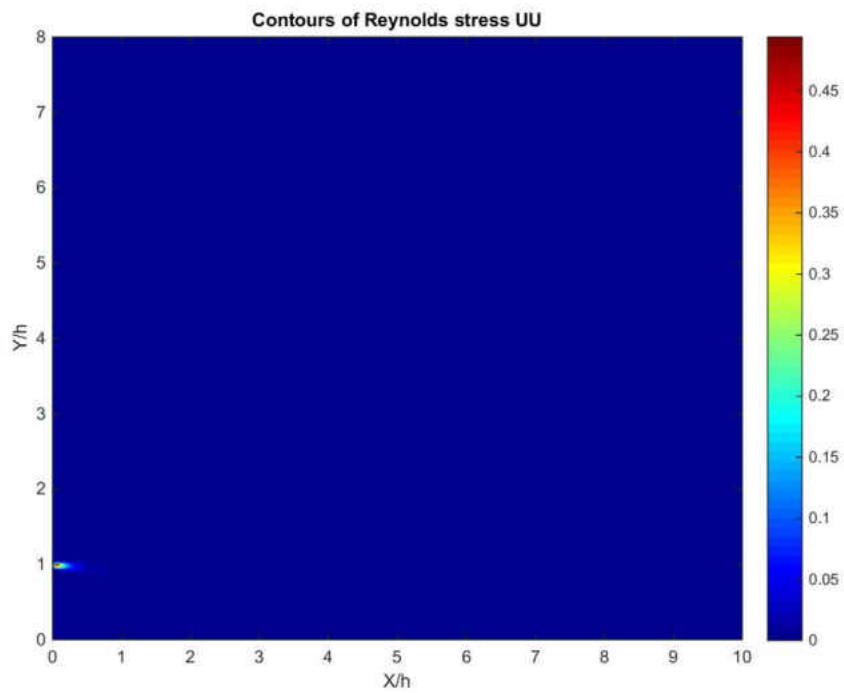


Figure 141: Contours of Reynolds stress $\overline{u'u'}/\bar{V}^2$, 2D-DNS BFS, $ER = 1.14$, $Re_{D_h} = 1000$

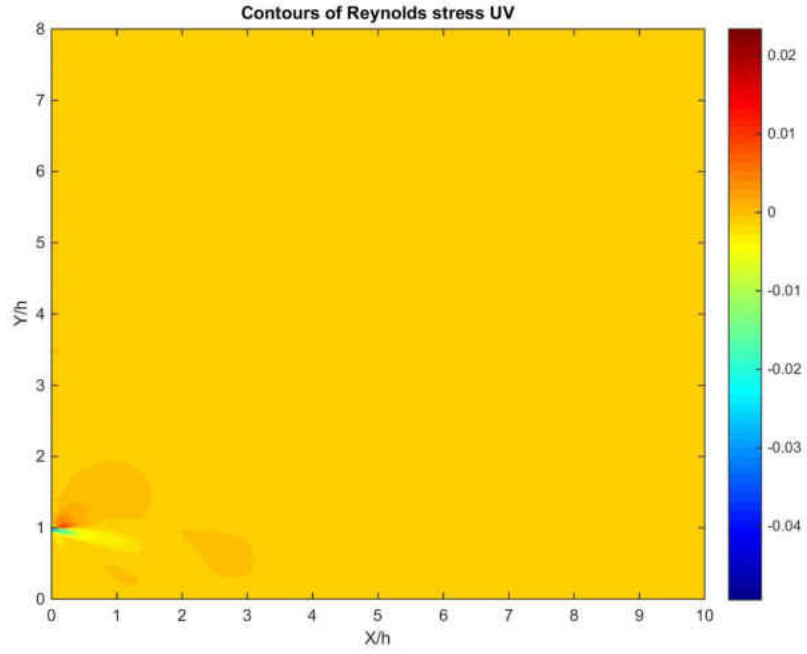


Figure 142: Contours of Reynolds stress $\overline{u'v'}/\overline{V}^2$, 2D-DNS BFS, $ER=1.14$, $Re_{D_h}=1000$

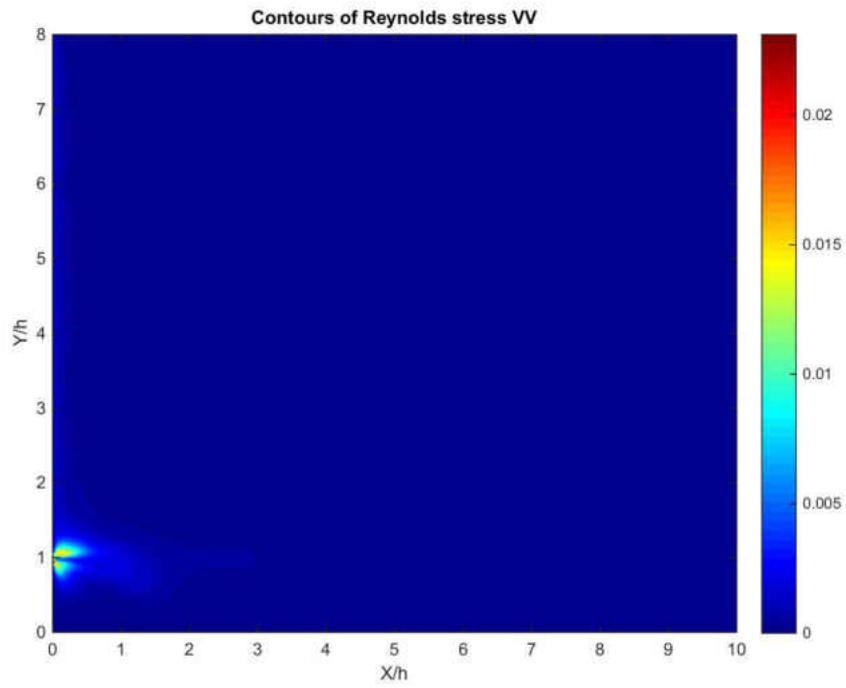


Figure 143: Contours of Reynolds stress $\overline{v'v'}/\overline{V}^2$, 2D-DNS BFS, $ER=1.14$, $Re_{D_h}=1000$

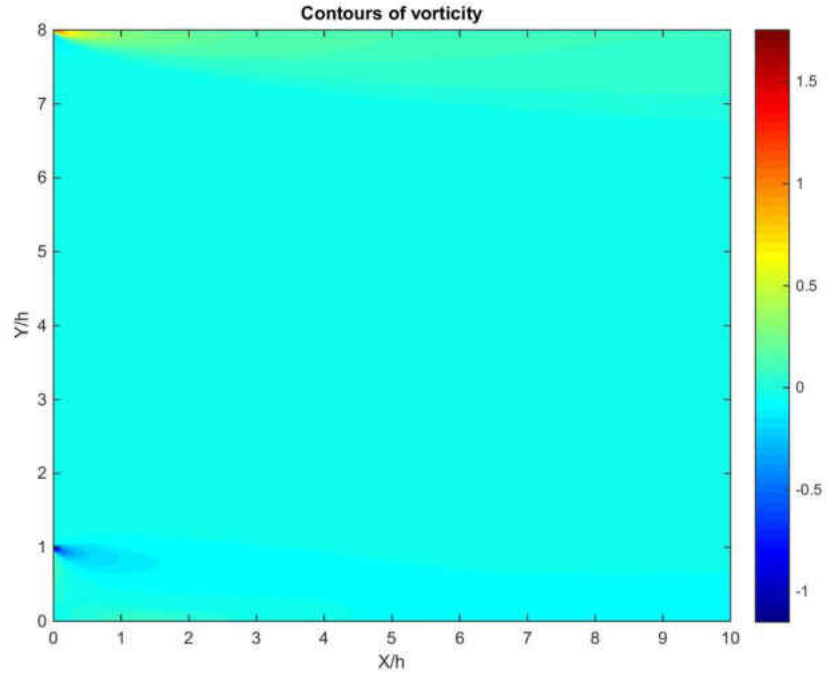


Figure 144: Contours of vorticity $\omega/(0.5 \cdot \rho \cdot \bar{V}^2)$, 2D-DNS BFS, $ER = 1.14$, $Re_{D_h} = 1000$

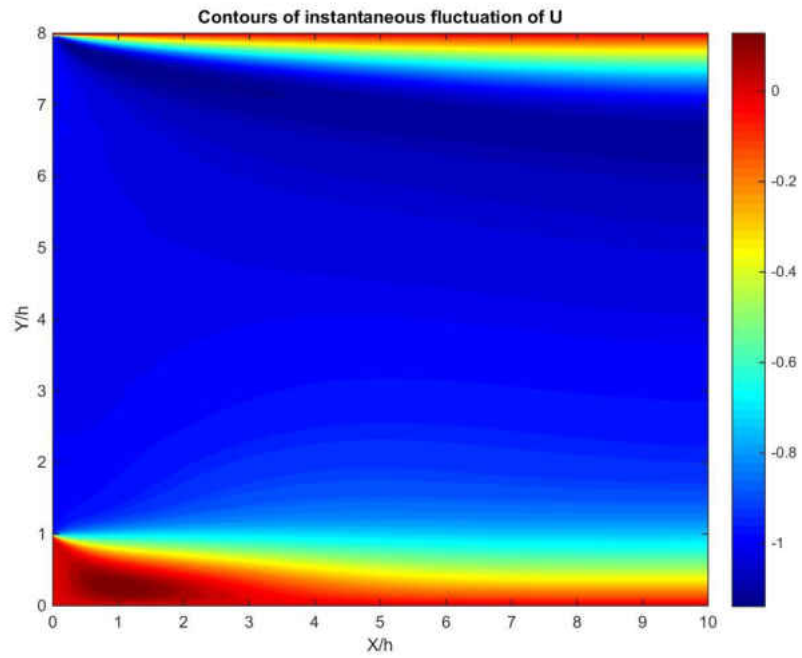


Figure 145: Contours of u'/\bar{V} in the last time step, 2D-DNS BFS, $ER = 1.14$, $Re_{D_h} = 1000$

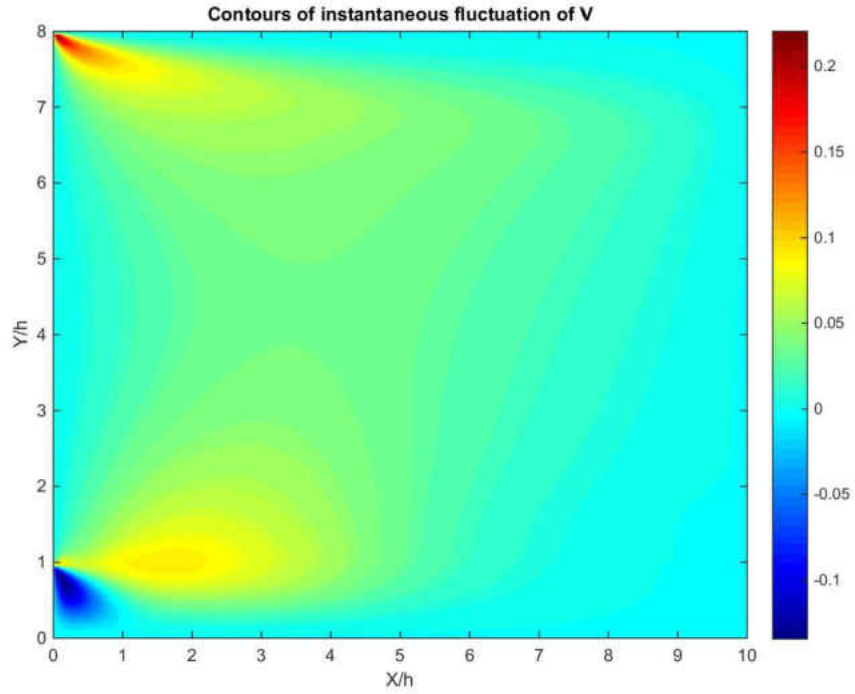


Figure 146: Contours of v'/\bar{V} at last time step, 2D-DNS BFS, $ER=1.14$, $Re_{D_h}=1000$

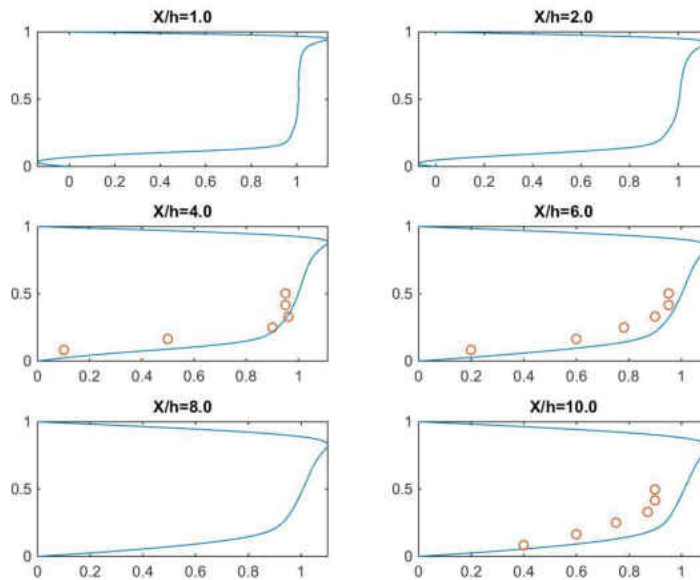


Figure 147: Velocity U/\bar{V} at different X-planes, 2D-DNS BFS, $ER=1.14$, $Re_{D_h}=1000$; “o” [202], “-” this work

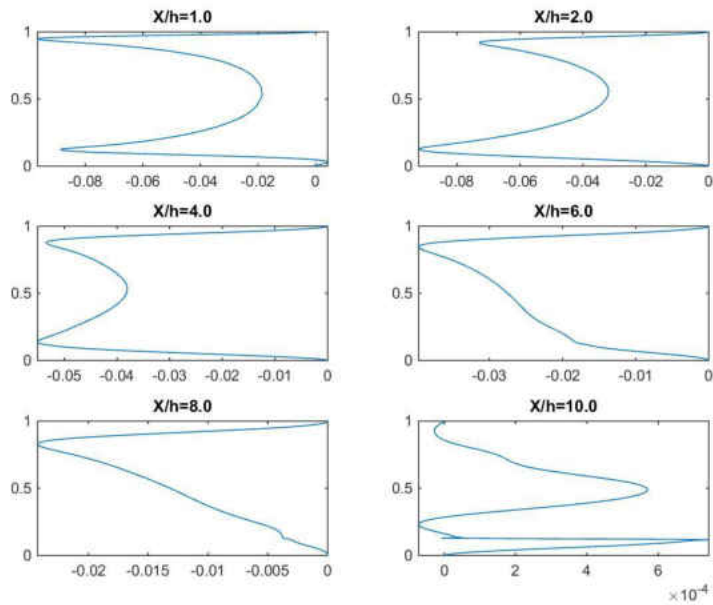


Figure 148: Velocity V/\bar{V} at different X-planes, 2D-DNS BFS, $ER = 1.14$, $Re_{D_h} = 1000$

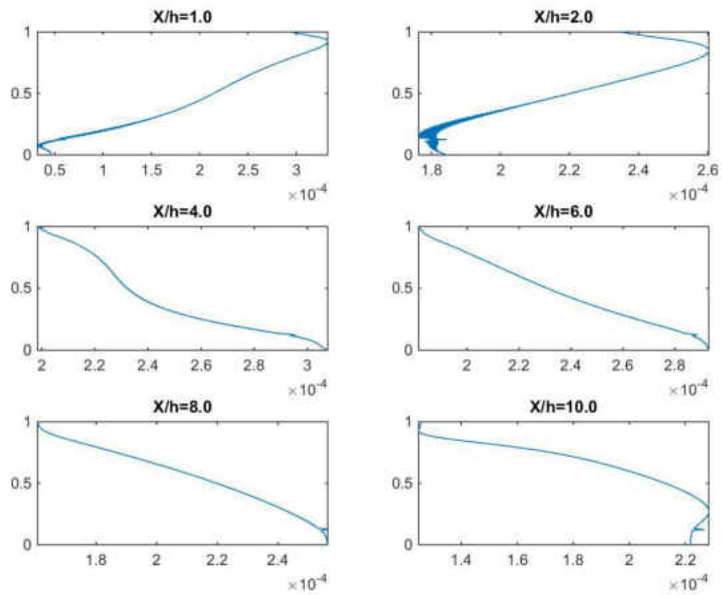


Figure 149: Pressure $p/(0.5 \cdot \rho \cdot \bar{V}^2)$ at different X-planes, 2D-DNS BFS, $ER = 1.14$, $Re_{D_h} = 1000$

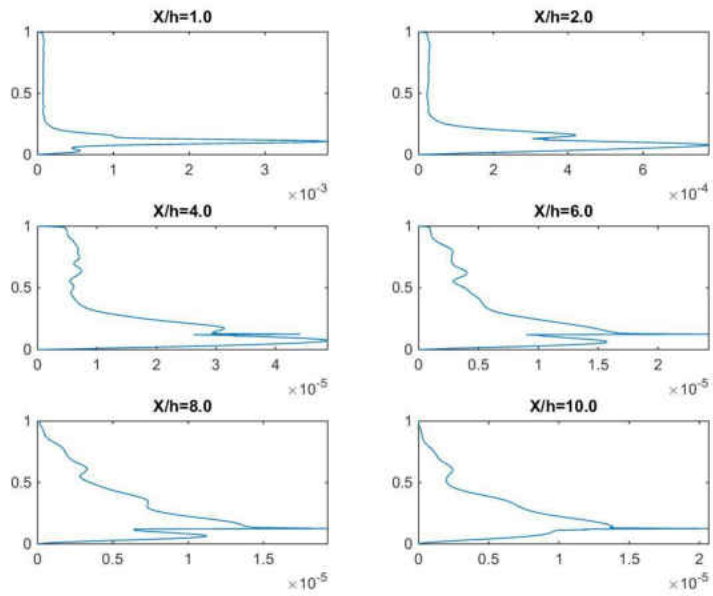


Figure 150: Kinetic energy k/\bar{V}^2 at different X-planes, 2D-DNS BFS, $ER = 1.14$, $Re_{D_h} = 1000$

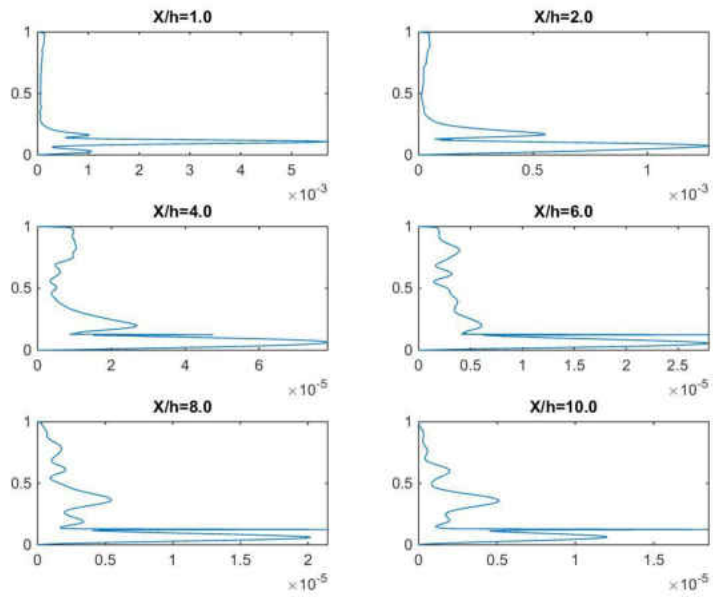


Figure 151: Reynolds stress $\overline{u'u'}/\bar{V}^2$ at different X-planes, 2D-DNS BFS, $ER = 1.14$, $Re_{D_h} = 1000$

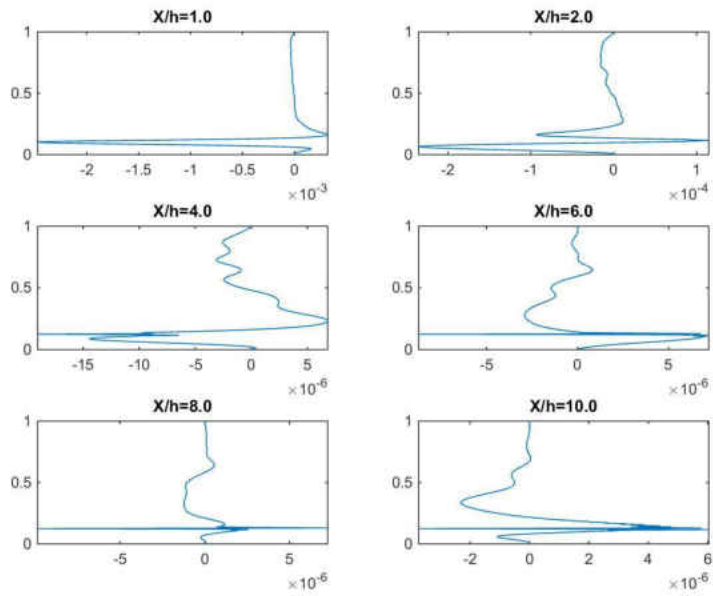


Figure 152: Reynolds stress $\overline{u'v'}/\overline{V}^2$ at different X-planes, 2D-DNS BFS, $ER = 1.14$, $Re_{D_h} = 1000$

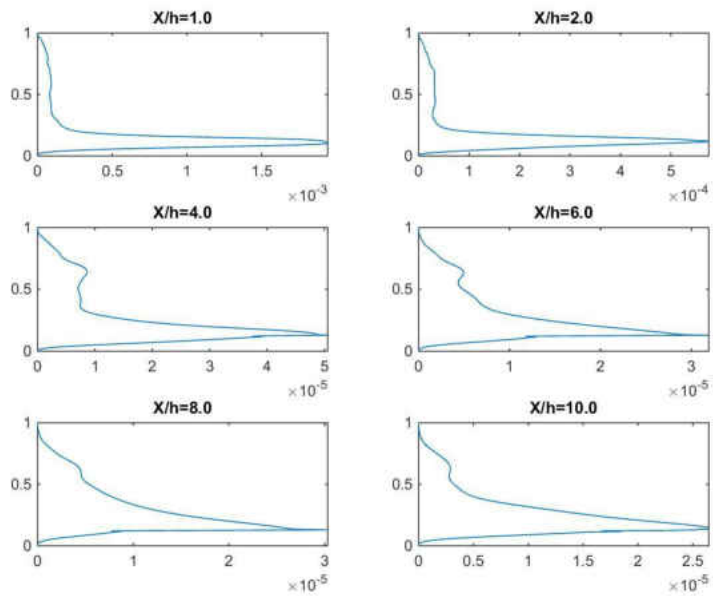


Figure 153: Reynolds stress $\overline{v'v'}/\overline{V}^2$ at different X-planes, 2D-DNS BFS, $ER = 1.14$, $Re_{D_h} = 1000$

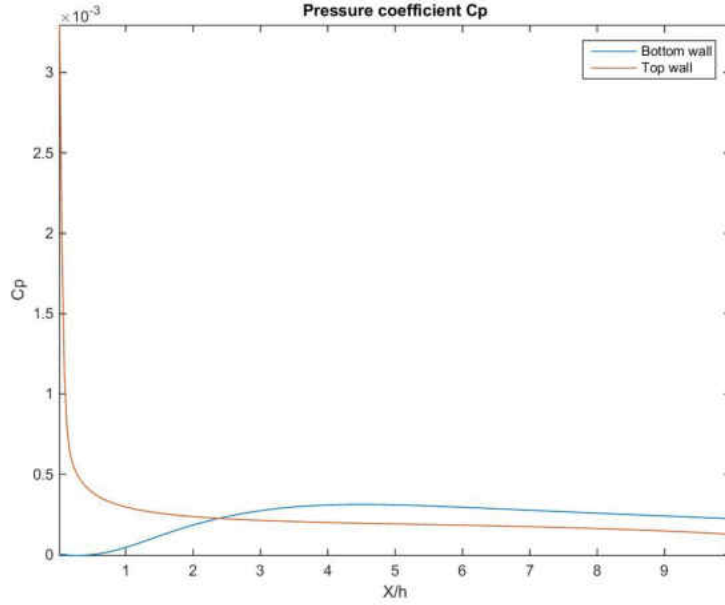


Figure 154: Pressure coefficient C_p as function of position, 2D-DNS BFS, $ER = 1.14$, $Re_{D_h} = 1000$

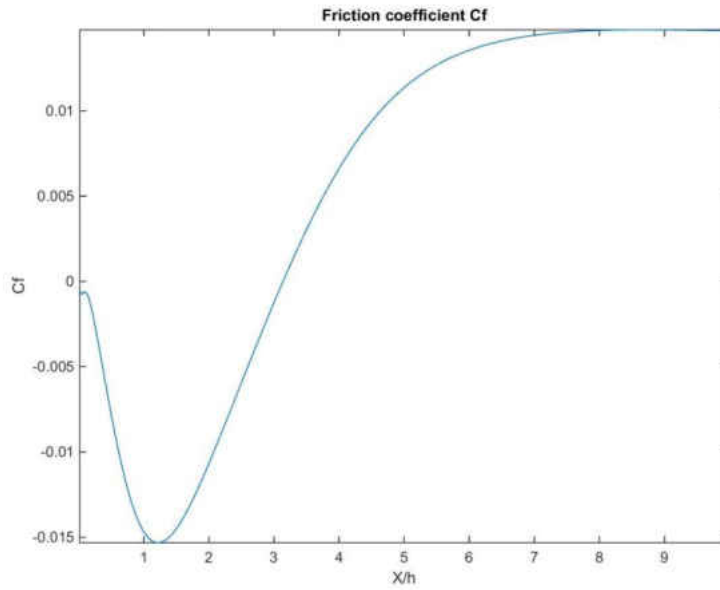


Figure 155: Friction coefficient C_f at different X-planes, 2D-DNS BFS, $ER = 1.14$, $Re_{D_h} = 1000$

APPENDIX B
BACKWARD-FACING STEP WITH $ER=1.14$ AND $Re_{D_h} = 2000$

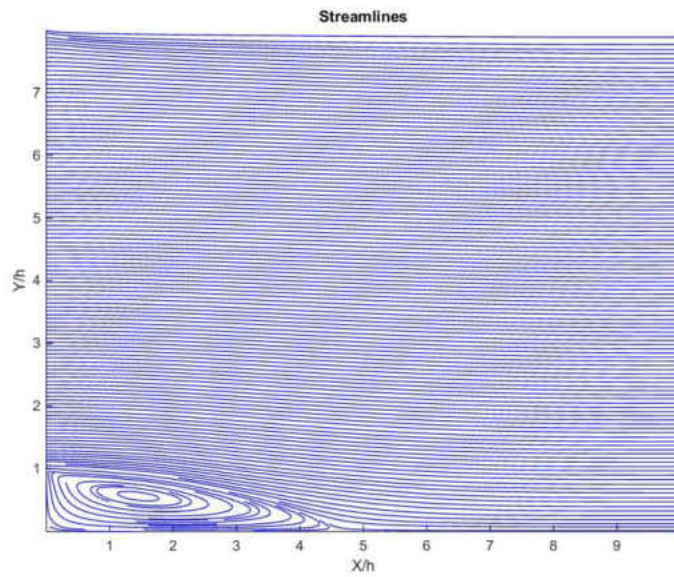


Figure 156: Streamlines, 2D-DNS BFS, $ER = 1.14$, $Re_{D_h} = 2000$

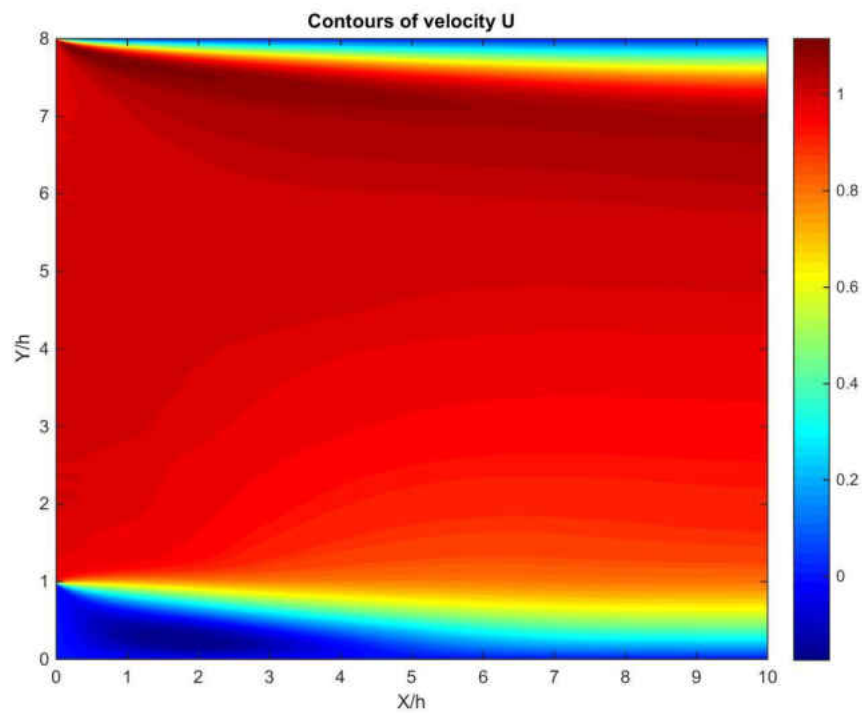


Figure 157: Contours of velocity U/\bar{V} , 2D-DNS BFS, $ER = 1.14$, $Re_{D_h} = 2000$

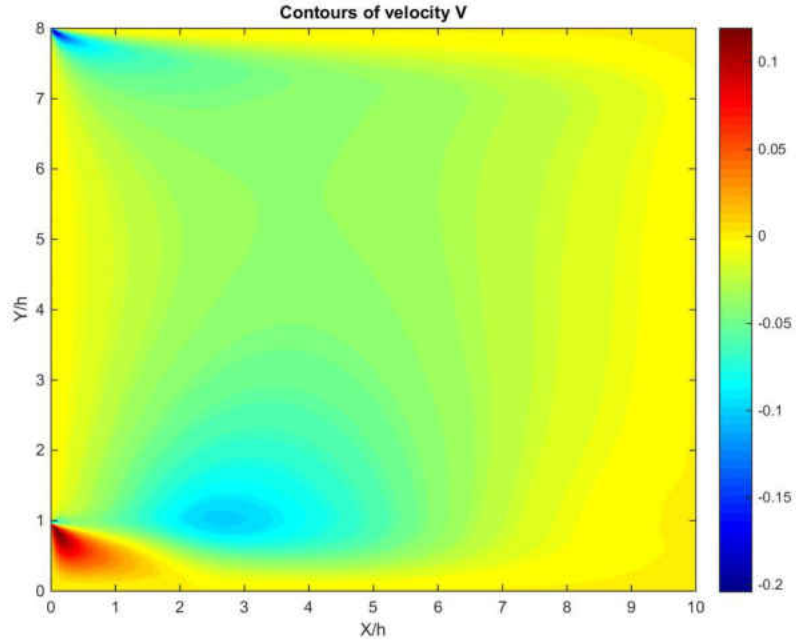


Figure 158: Contours of velocity V/\bar{V} , 2D-DNS BFS, $ER = 1.14$, $Re_{D_h} = 2000$

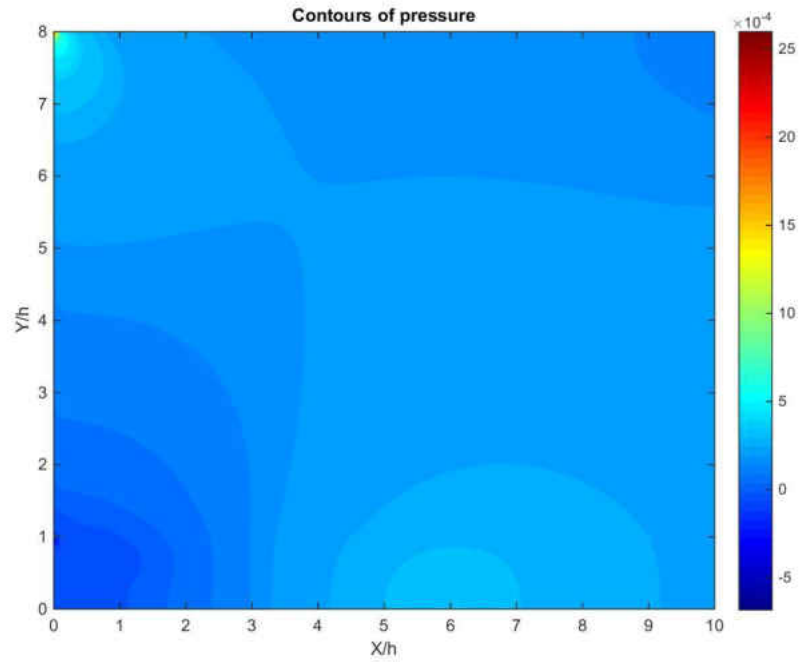


Figure 159: Contours of pressure $p/(0.5 \cdot \rho \cdot \bar{V}^2)$, 2D-DNS BFS, $ER = 1.14$, $Re_{D_h} = 2000$

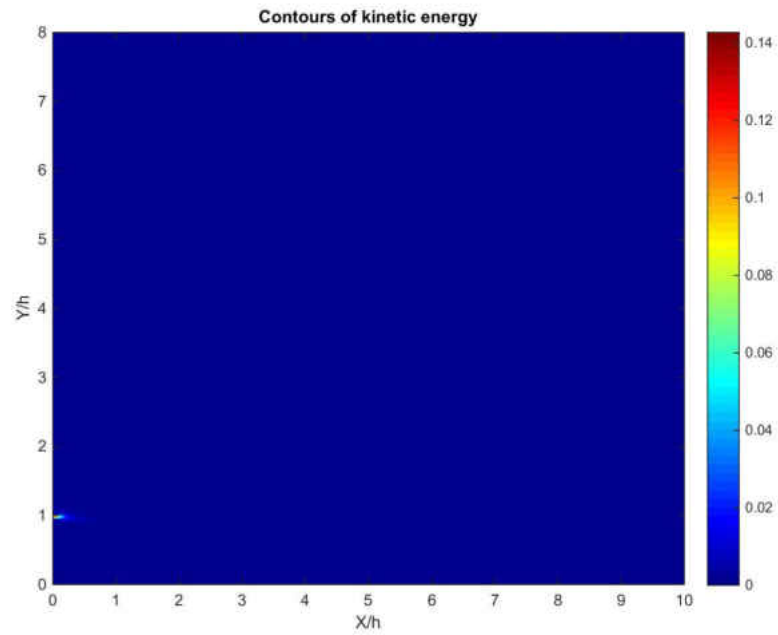


Figure 160: Contours of kinetic energy k/\bar{V}^2 , 2D-DNS BFS, $ER=1.14$, $Re_{D_h} = 2000$

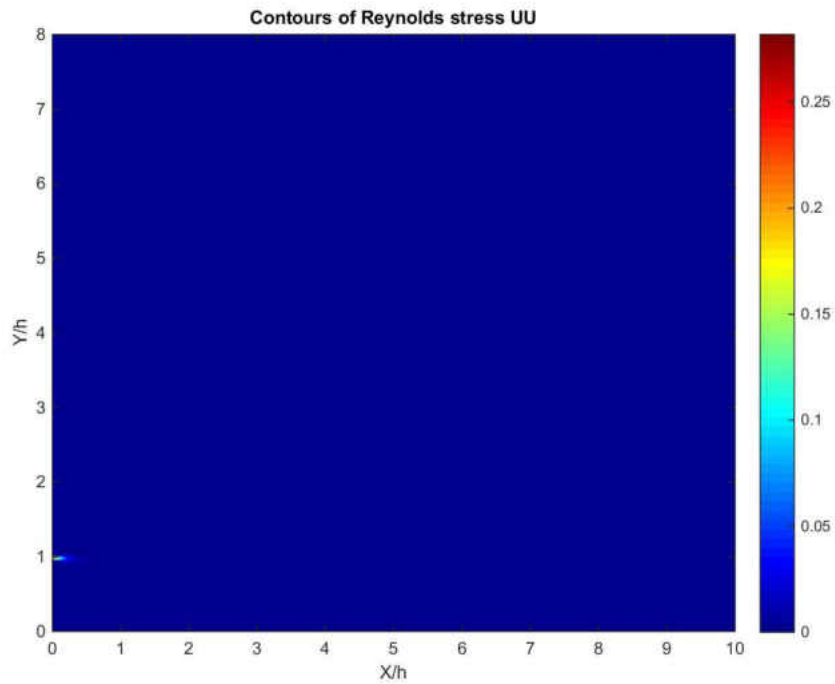


Figure 161: Contours of Reynolds stress $\overline{u'u'}/\bar{V}^2$, 2D-DNS BFS, $ER=1.14$, $Re_{D_h} = 2000$

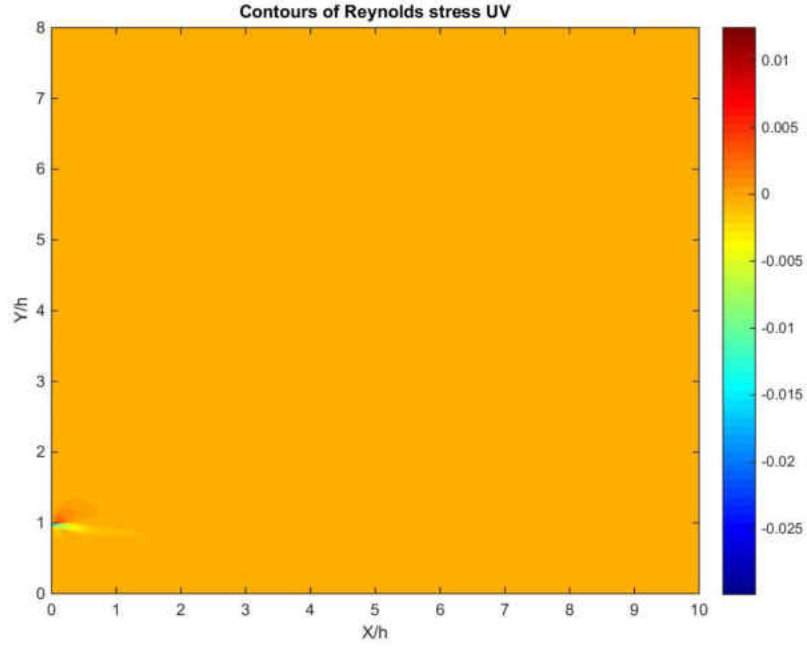


Figure 162: Contours of Reynolds stress $\overline{u'v'}/\overline{V}^2$, 2D-DNS BFS, $ER = 1.14$, $Re_{D_h} = 2000$

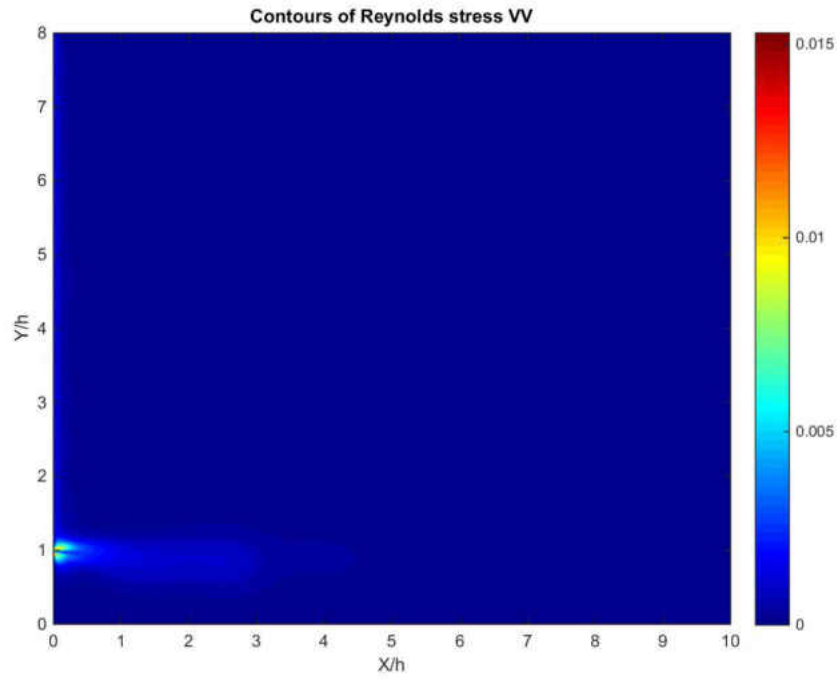


Figure 163: Contours of Reynolds stress $\overline{v'v'}/\overline{V}^2$, 2D-DNS BFS, $ER = 1.14$, $Re_{D_h} = 2000$

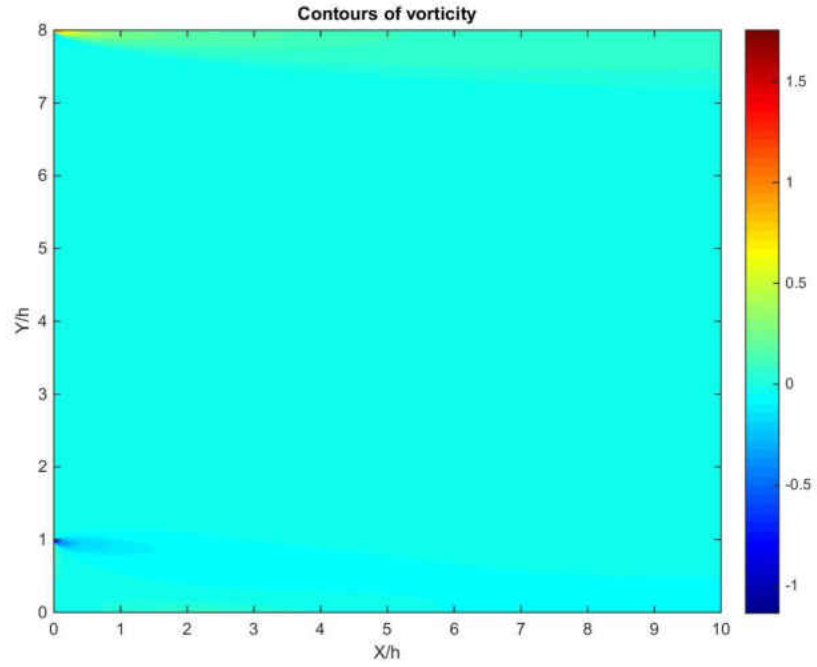


Figure 164: Contours of vorticity $\omega/(0.5 \cdot \rho \cdot \bar{V}^2)$, 2D-DNS BFS, $ER = 1.14$, $Re_{D_h} = 2000$

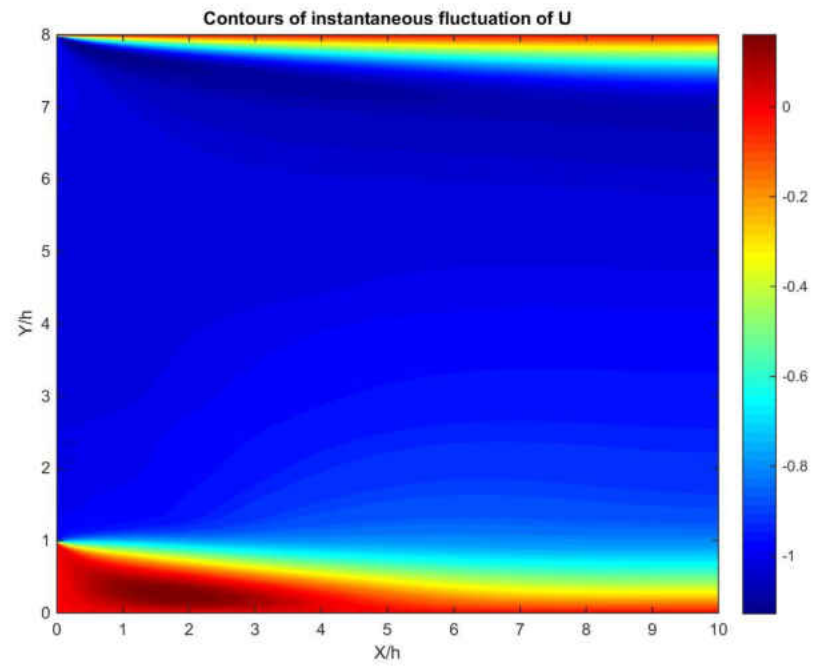


Figure 165: Contours of u'/\bar{V} in the last time step, 2D-DNS BFS, $ER = 1.14$, $Re_{D_h} = 2000$

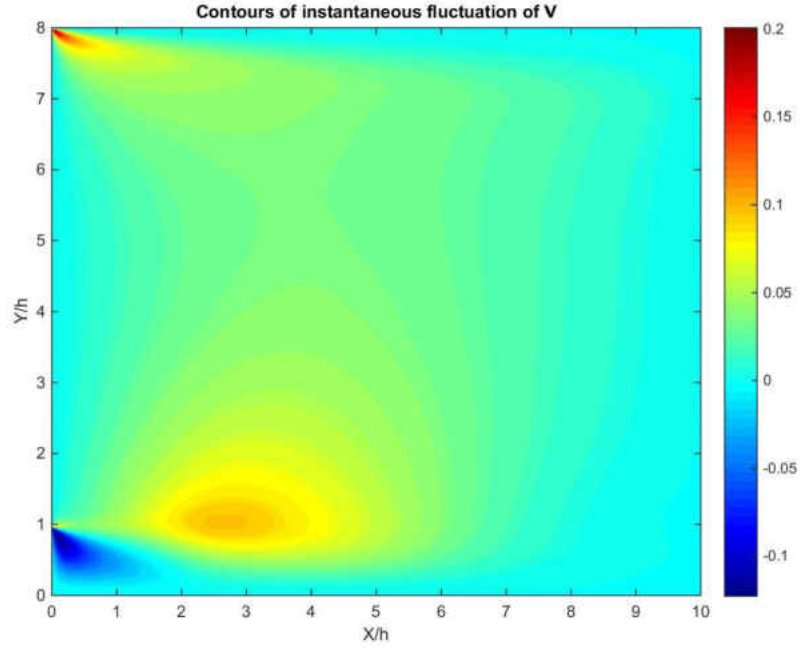


Figure 166: Contours of v'/\bar{V} at last time step, 2D-DNS BFS, $ER = 1.14$, $Re_{D_h} = 2000$

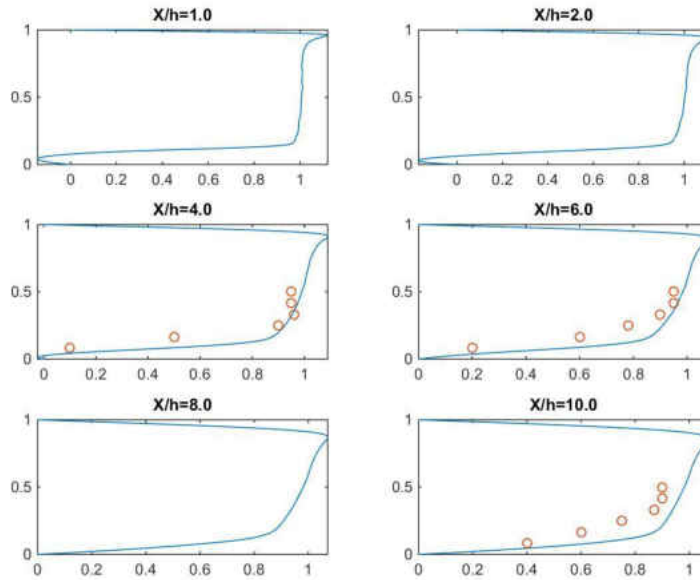


Figure 167: Velocity U/\bar{V} at different X-planes, 2D-DNS BFS, $ER = 1.14$, $Re_{D_h} = 2000$; “o” [202], “-“ this work

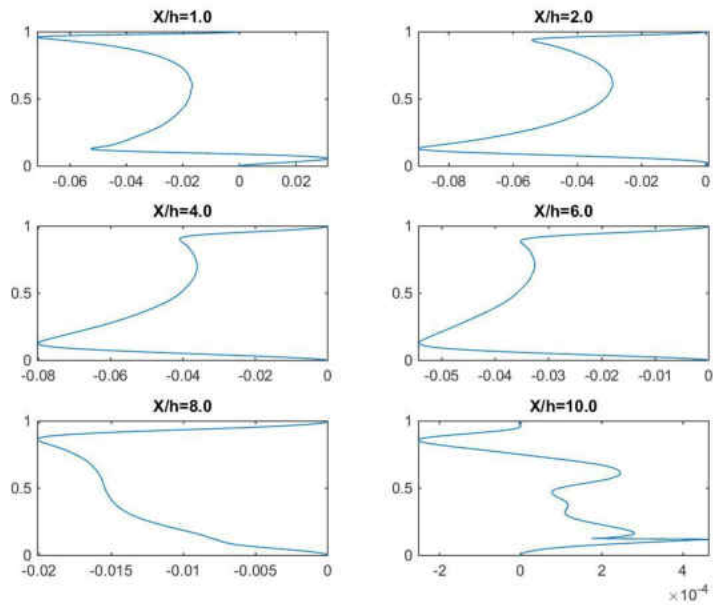


Figure 168: Velocity V/\bar{V} at different X-planes, 2D-DNS BFS, $ER = 1.14$, $Re_{D_h} = 2000$

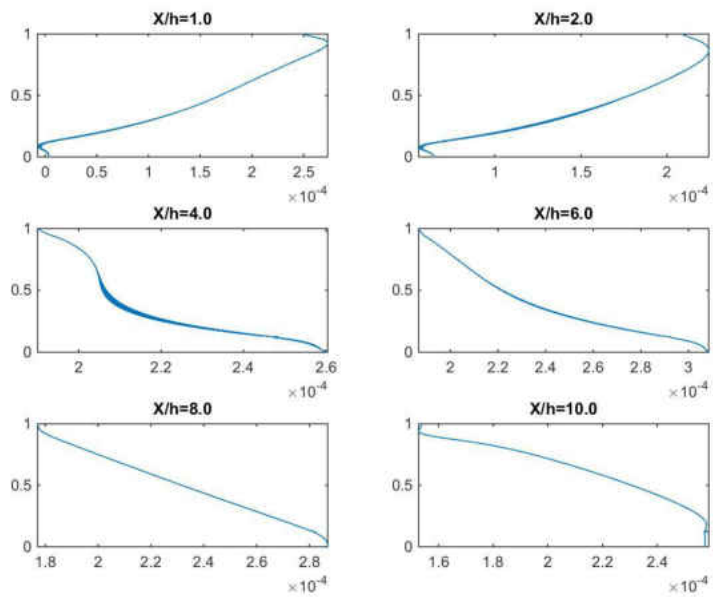


Figure 169: Pressure $p/(0.5 \cdot \rho \cdot \bar{V}^2)$ at different X-planes, 2D-DNS BFS, $ER = 1.14$, $Re_{D_h} = 2000$

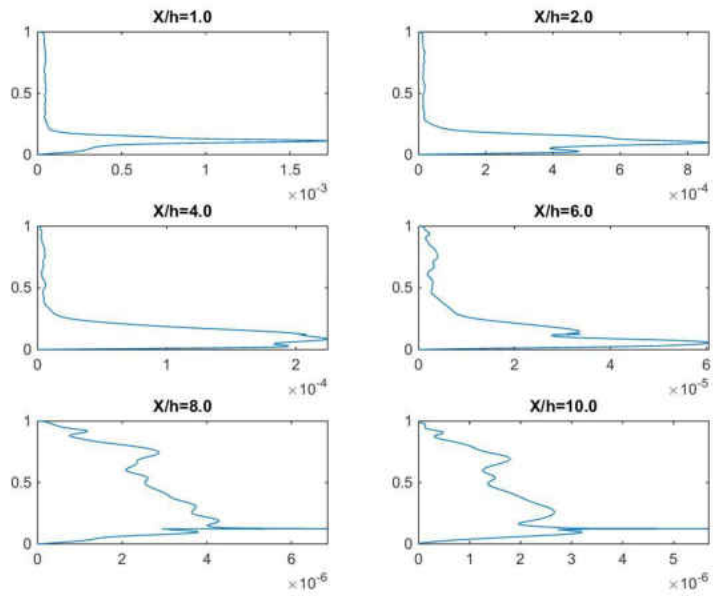


Figure 170: Kinetic energy k/\bar{V}^2 at different X-planes, 2D-DNS BFS, $ER = 1.14$, $Re_{D_h} = 2000$

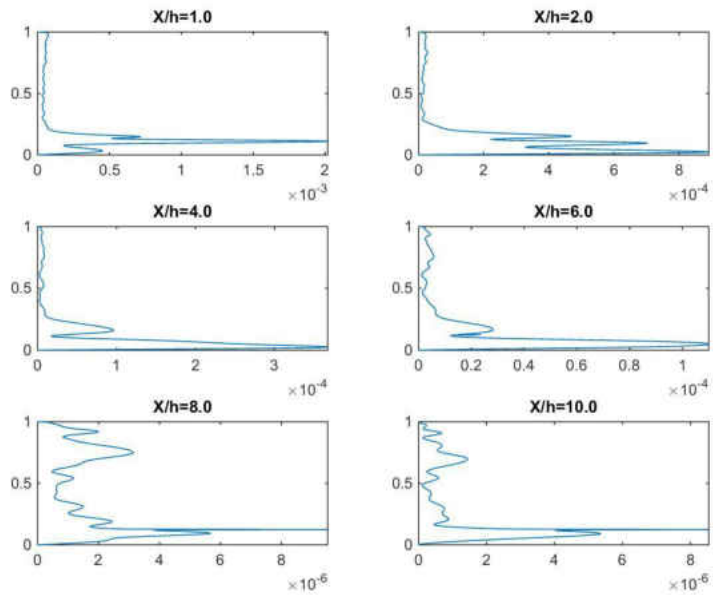


Figure 171: Reynolds stress $\overline{u'u'}/\bar{V}^2$ at different X-planes, 2D-DNS BFS, $ER = 1.14$, $Re_{D_h} = 2000$

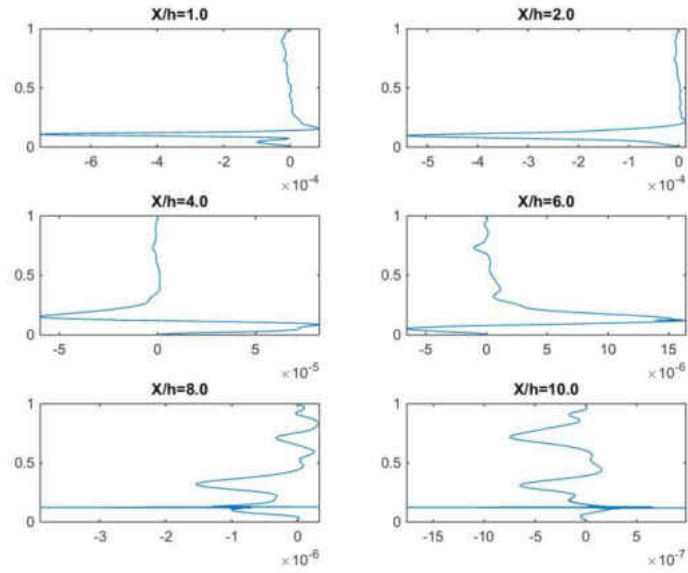


Figure 172: Reynolds stress $\overline{u'v'}/\overline{V}^2$ at different X-planes, 2D-DNS BFS, $ER = 1.14$, $Re_{D_h} = 2000$

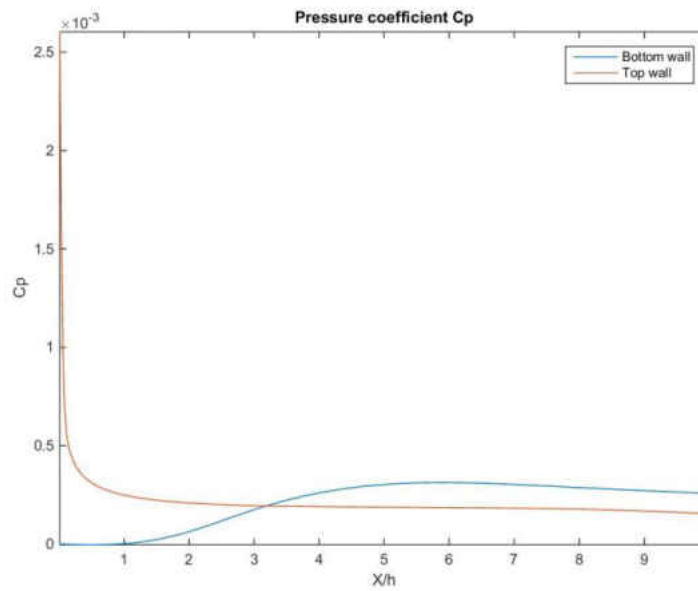


Figure 173: Pressure coefficient C_p as function of position, 2D-DNS BFS, $ER = 1.14$, $Re_{D_h} = 2000$

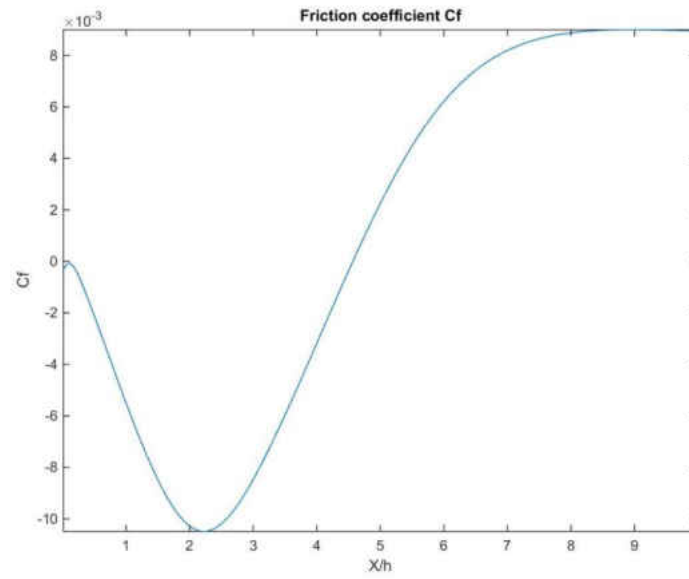


Figure 174: Friction coefficient C_f at different X-planes, 2D-DNS BFS, $ER = 1.14$,
 $Re_{D_h} = 2000$

APPENDIX C
BACKWARD-FACING STEP WITH $ER = 1.40$ AND $Re_{D_h} = 1000$

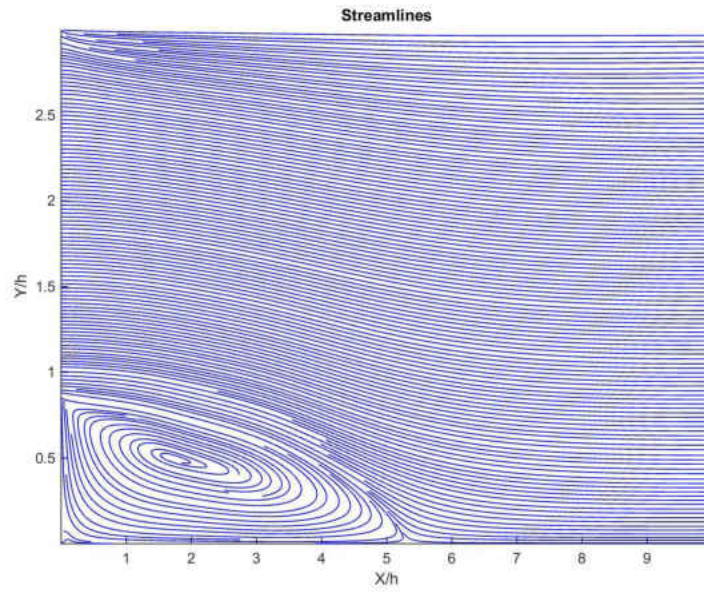


Figure 175: Streamlines, 2D-DNS BFS, $ER = 1.40$, $Re_{D_h} = 1000$

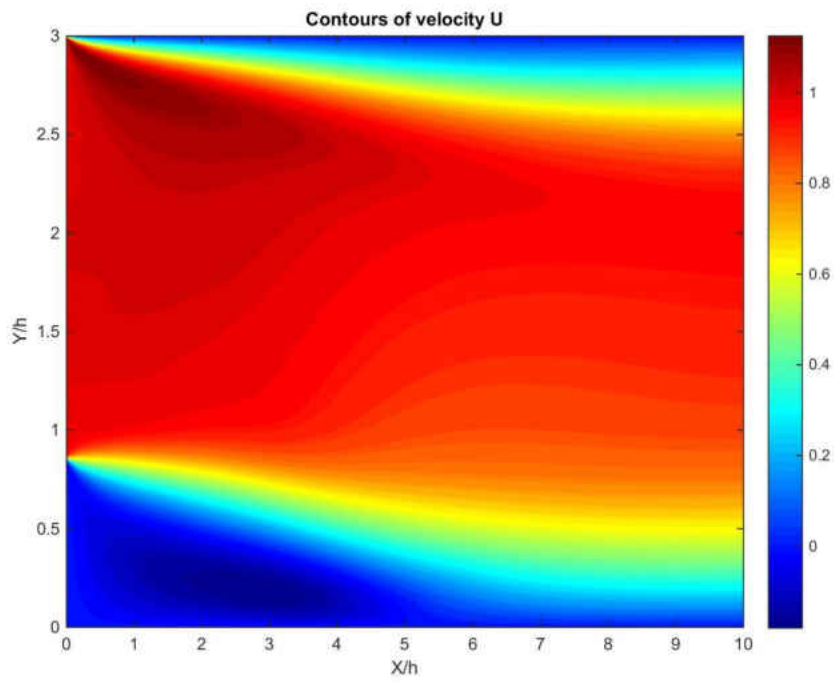


Figure 176: Contours of velocity U/\bar{V} , 2D-DNS BFS, $ER = 1.40$, $Re_{D_h} = 1000$

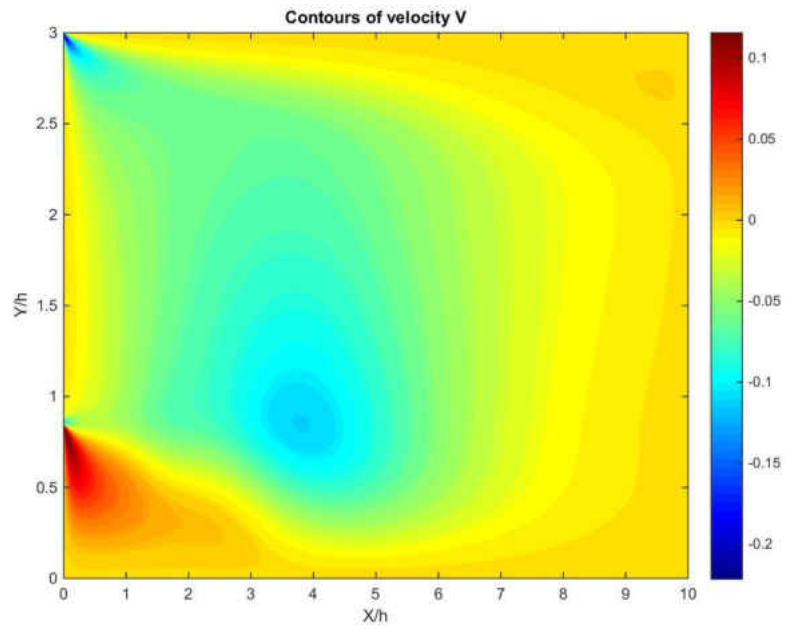


Figure 177: Contours of velocity V/\bar{V} , 2D-DNS BFS, $ER = 1.40$, $Re_{D_h} = 1000$

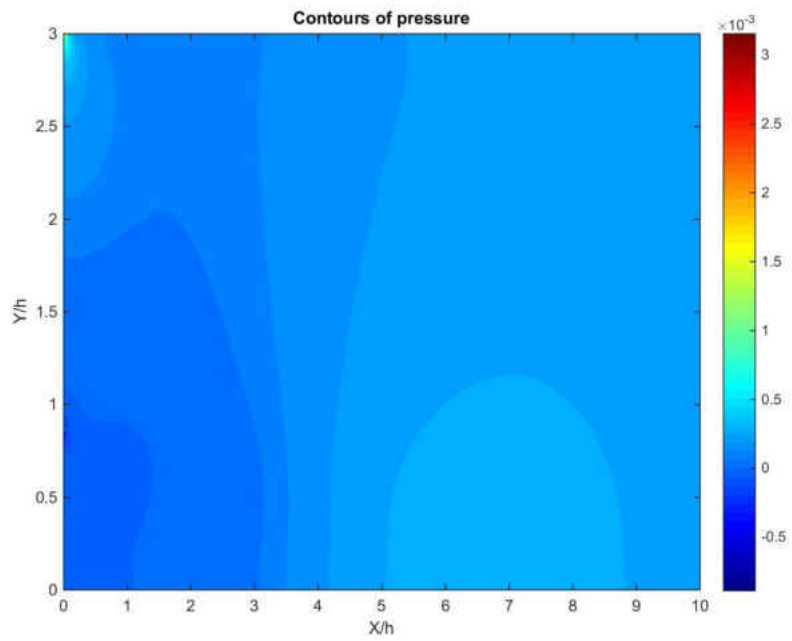


Figure 178: Contours of pressure $p/(0.5 \cdot \rho \cdot \bar{V}^2)$, 2D-DNS BFS, $ER = 1.40$, $Re_{D_h} = 1000$

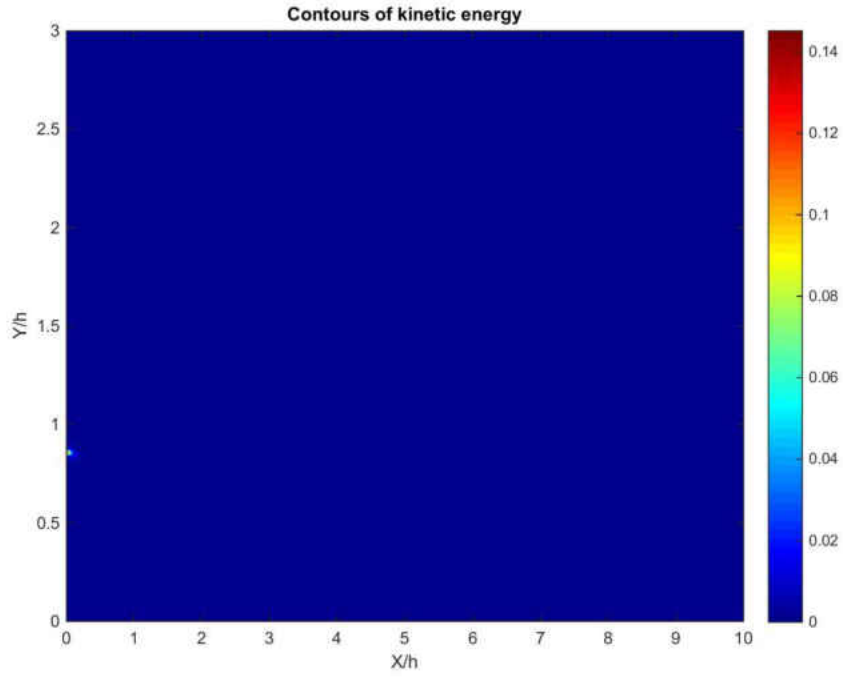


Figure 179: Contours of kinetic energy k/\bar{V}^2 , 2D-DNS BFS, $ER = 1.40$, $Re_{D_h} = 1000$

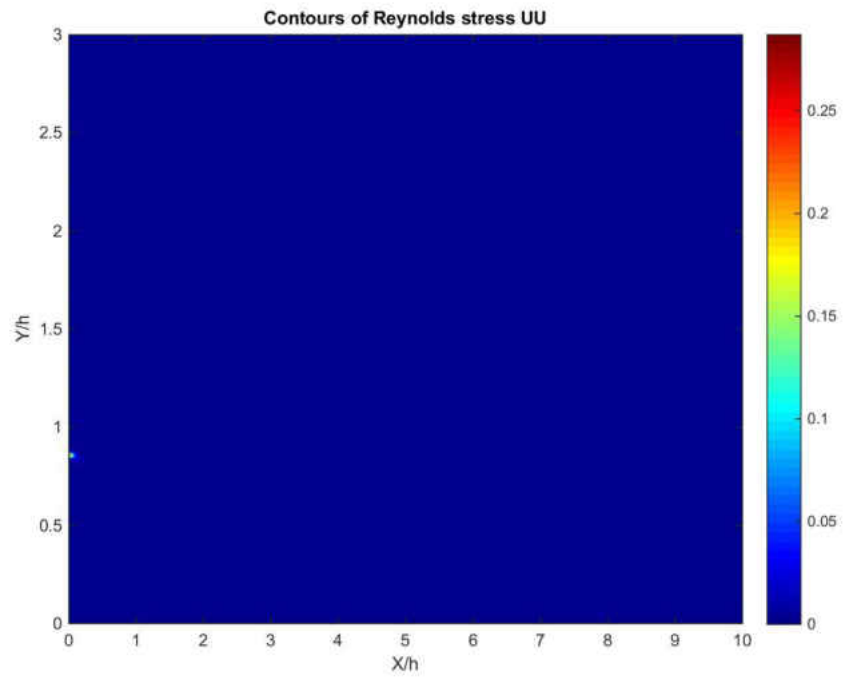


Figure 180: Contours of Reynolds stress $\overline{u'u'}/\bar{V}^2$, 2D-DNS BFS, $ER = 1.40$, $Re_{D_h} = 1000$

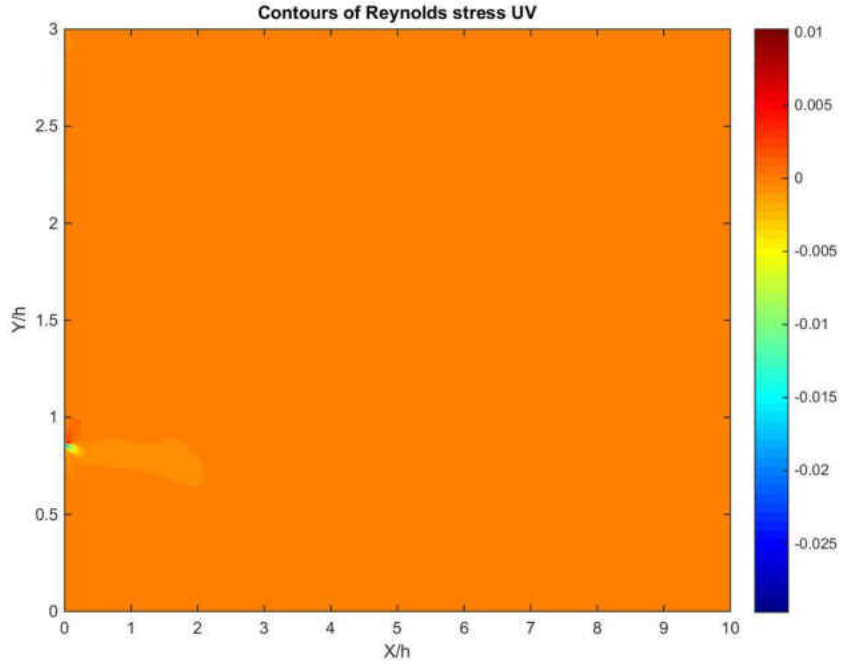


Figure 181: Contours of Reynolds stress $\overline{u'v'}/\overline{V}^2$, 2D-DNS BFS, $ER = 1.40$, $Re_{D_h} = 1000$

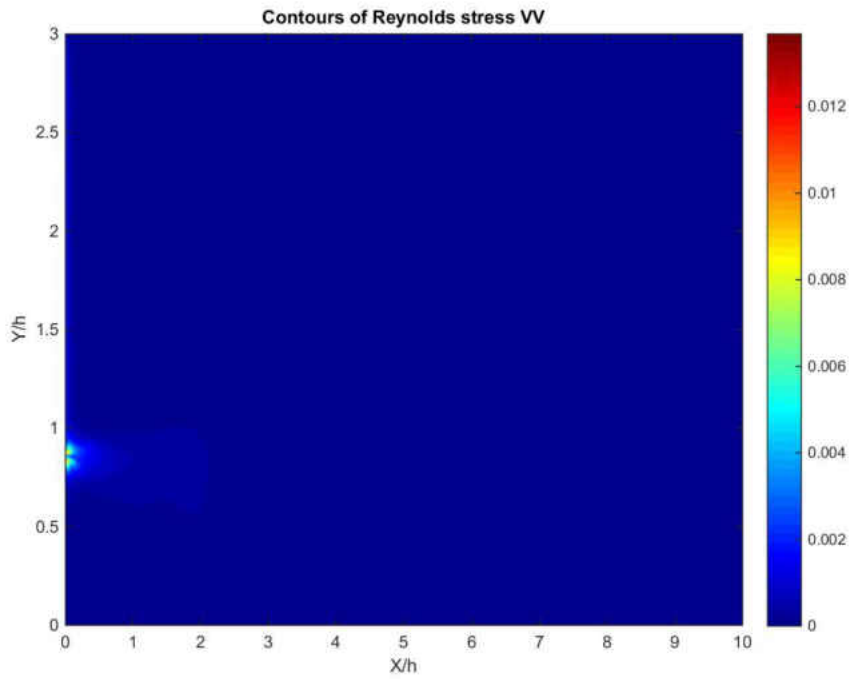


Figure 182: Contours of Reynolds stress $\overline{v'v'}/\overline{V}^2$, 2D-DNS BFS, $ER = 1.40$, $Re_{D_h} = 1000$

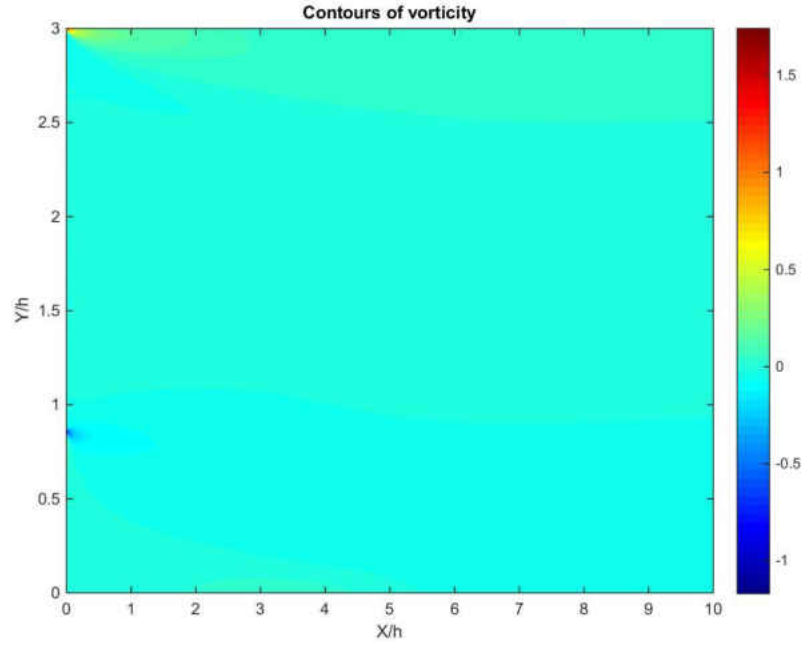


Figure 183: Contours of vorticity $\omega/(0.5 \cdot \rho \cdot \bar{V}^2)$, 2D-DNS BFS, $ER = 1.40$, $Re_{D_h} = 1000$

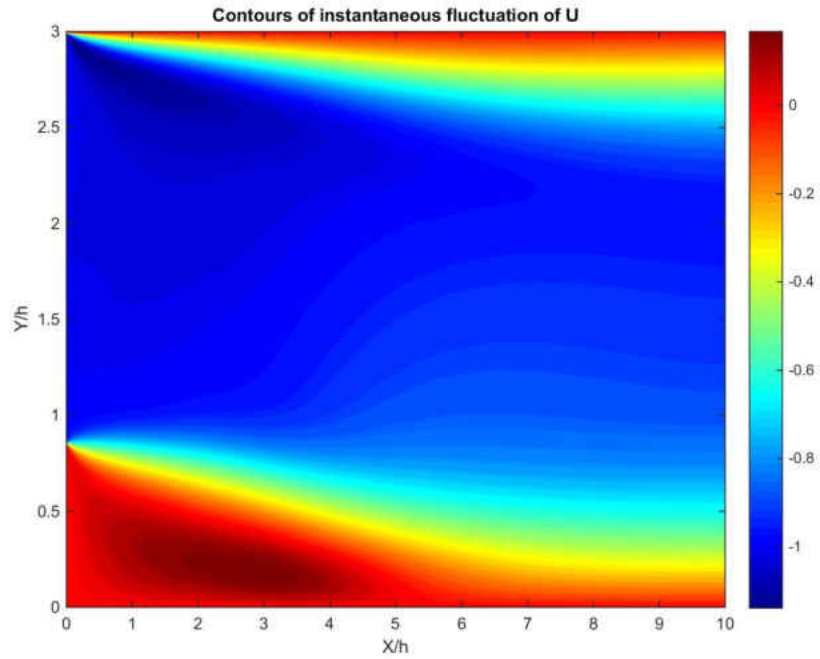


Figure 184: Contours of u'/\bar{V} in the last time step, 2D-DNS BFS, $ER = 1.40$, $Re_{D_h} = 1000$

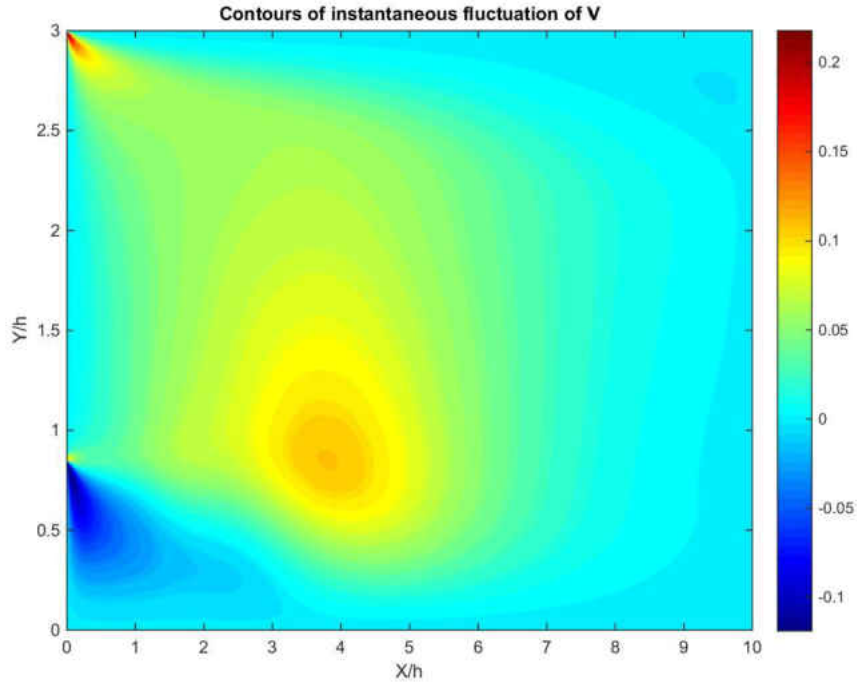


Figure 185: Contours of v'/\bar{V} at last time step, 2D-DNS BFS, $ER = 1.40$, $Re_{D_h} = 1000$

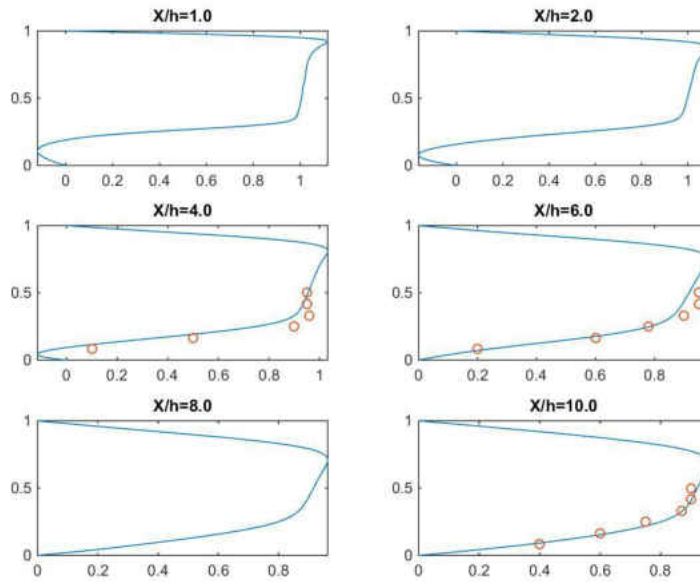


Figure 186: Velocity U/\bar{V} at different X-planes, 2D-DNS BFS, $ER = 1.40$, $Re_{D_h} = 1000$; “o” [1], “-“ this work

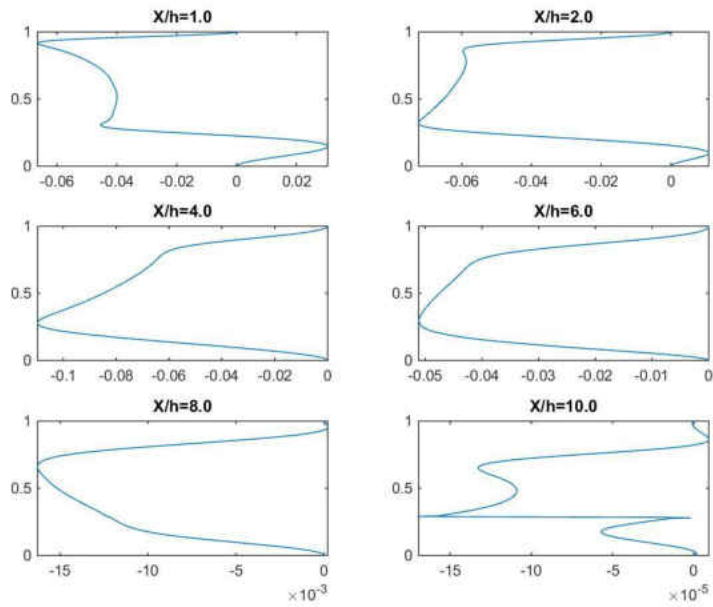


Figure 187: Velocity v/\bar{V} at different X-planes, 2D-DNS BFS, $ER = 1.40$, $Re_{D_h} = 1000$

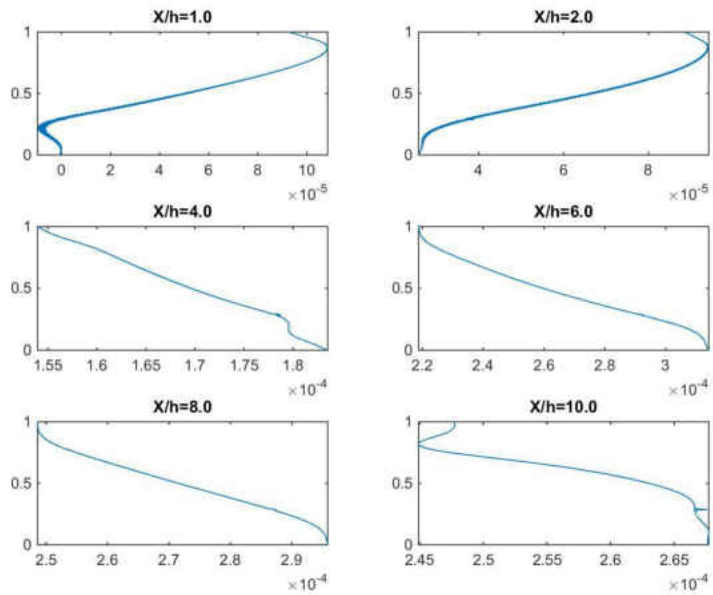


Figure 188: Pressure $p/(0.5 \cdot \rho \cdot \bar{V}^2)$ at different X-planes, 2D-DNS BFS, $ER = 1.40$, $Re_{D_h} = 1000$

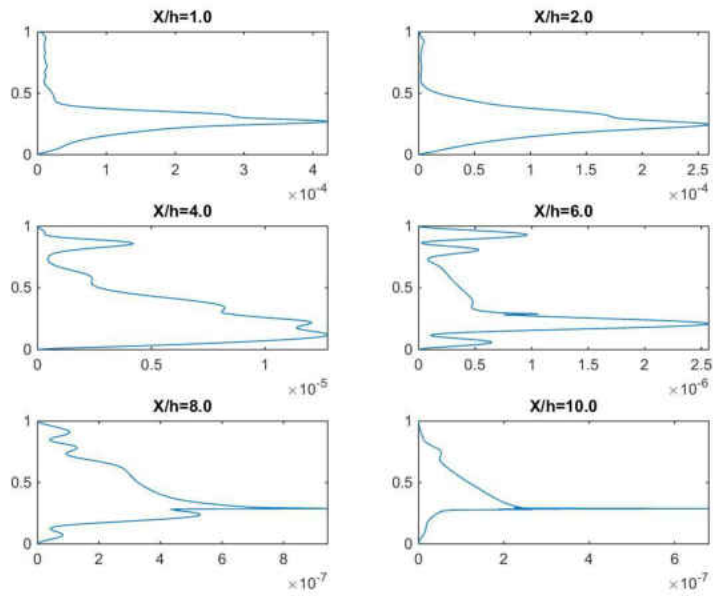


Figure 189: Kinetic energy k/\bar{V}^2 at different X-planes, 2D-DNS BFS, $ER = 1.40$, $Re_{D_h} = 1000$

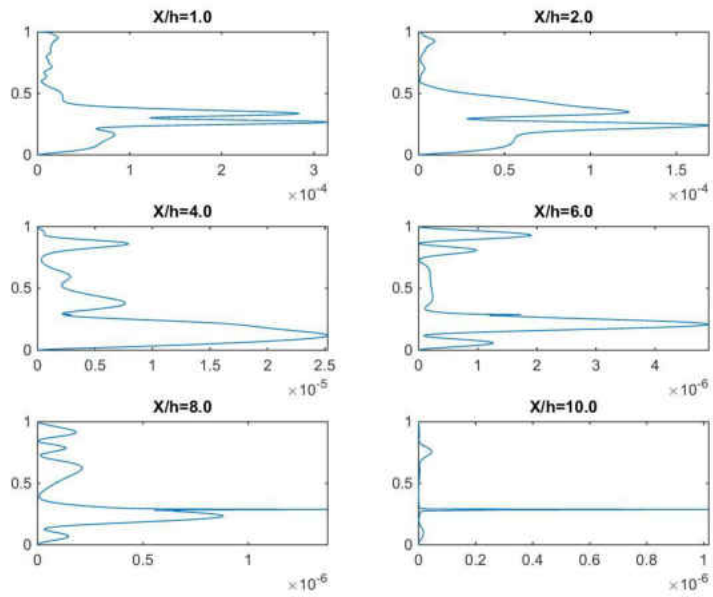


Figure 190: Reynolds stress $\overline{u'u'}/\bar{V}^2$ at different X-planes, 2D-DNS BFS, $ER = 1.40$, $Re_{D_h} = 1000$

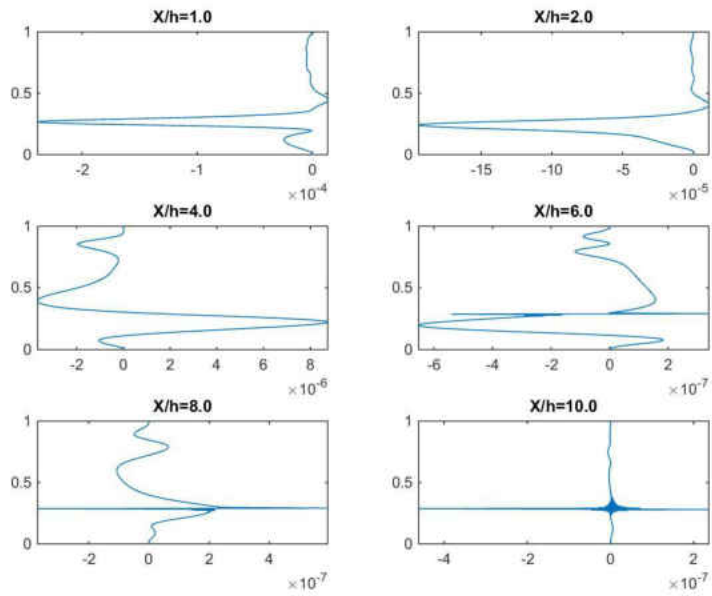


Figure 191: Reynolds stress $\overline{u'v'}/\overline{V}^2$ at different X-planes, 2D-DNS BFS, $ER = 1.40$, $Re_{D_h} = 1000$

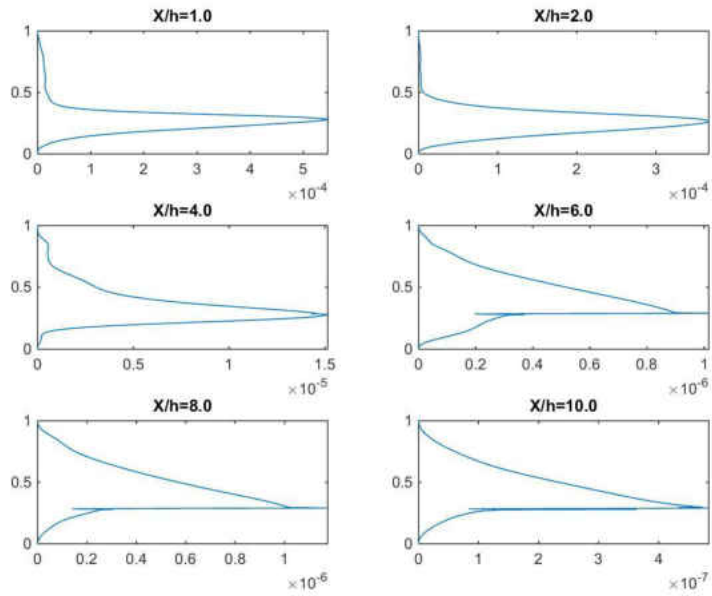


Figure 192: Reynolds stress $\overline{v'v'}/\overline{V}^2$ at different X-planes, 2D-DNS BFS, $ER = 1.40$, $Re_{D_h} = 1000$

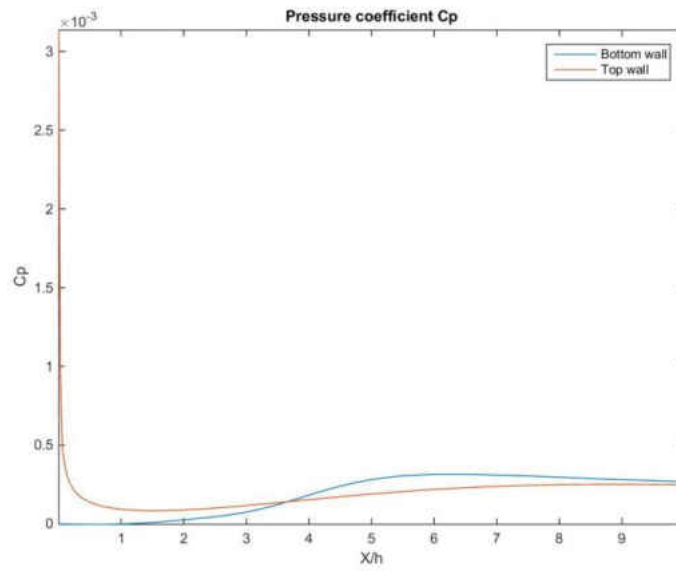


Figure 193: Pressure coefficient C_p as function of position, 2D-DNS BFS, $ER = 1.40$, $Re_{D_h} = 1000$

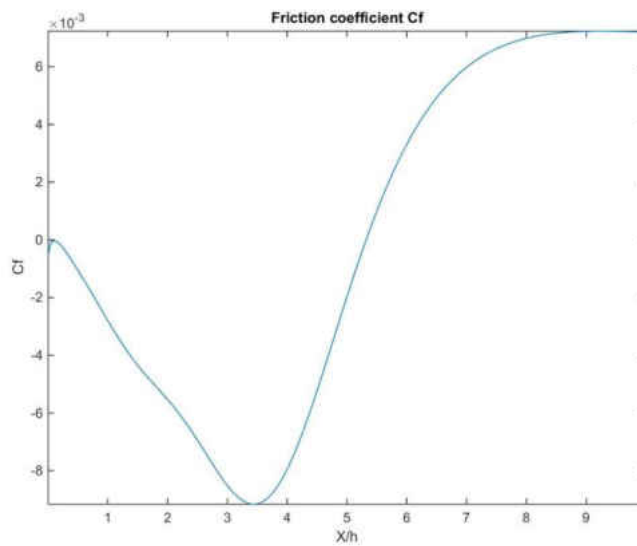


Figure 194: Friction coefficient C_f at different X-planes, 2D-DNS BFS, $ER = 1.40$, $Re_{D_h} = 1000$

APPENDIX D
COMPUTER IMPLEMENTATION

This topic is frequently ignored by the CFD community because, in part, the task of producing an efficient code is left implicitly to the compiler of the corresponding programming language, and also, due to the probably lack of knowledge of how to build efficient code. In other cases, no much attention is paid to how much time can be saved if some basic techniques are used.

This author's experience tells that there are many simple techniques that produce a great improvement in performance, and thus, a considerable reduction in computer time. Obviously, there exist some optimization techniques that depend on the specific programming language and many of them imply some knowledge of computer architecture.

Due to the fact that any DNS/LES simulation usually takes a considerable amount of time, from weeks to months with several tens of processors, one objective of this work is to make some recommendations that can help the production of fast and efficient code. For this kind of simulations, a reduction of 10%-20% in computing time is always convenient and welcome.

In order to accomplish this task, several references have been consulted. First, the fundamental text of software development [237] which presents a global procedure for producing correct code, based mainly in the experience of software engineering. Some recommendations are the use of proper names for all variables; the writing of clear and easy-to-read code as well as the use of unit testing in order to be absolutely sure that any algorithm coded or single piece of code performs correctly.

As expected, all these recommendations imply more programming time but, in the long term, they reduce considerably the time for detection and/or correction of errors. It is important to underline that when a computer code becomes large, from roughly 10,000 to 20,000 lines of

code and up, the detection of any single error is an impossible task. Some errors may not affect the solution significantly, but in many cases the error generated is important.

Since the main objective is performance, the textbook of Goedecker [112] gives good recommendations that can be applied to any programming language. Other optimization techniques are specific to the C++ language [324] (chosen for this research work) [242], [243] and [244] as well as [277] and [343] and they are highly recommended.

Other recommendations are related directly with parallel programming, as for example [79], [273] and [277].

In the next sections, many topics related to procedures implemented in the calculation of all geometric information will be presented. A very important effort was made to reduce the order of the algorithm (respect to problem size) available in previous codes of the group.

Using all the procedures presented here, the order of the algorithm was reduced from quadratic (respect to problem size) to a linear algorithm that needs only one minute to create the geometric information of 1 million points. This calculation time is very competitive with the time needed in the creation of any standard unstructured grid with any commercial package.

D.1 Computation of internal and boundary points

The first thing to do in the geometric calculation is to locate which points are in the region defined by the user. A big grid of points is provided to the code and, one by one, it has to decide if a particular coordinate is inside or outside the region.

A popular technique is a direct application of Green's theorem in which, going along the boundary of the region, performs the summation of angles, with respect to the point whose location is wanted to be determined (called here reference point).

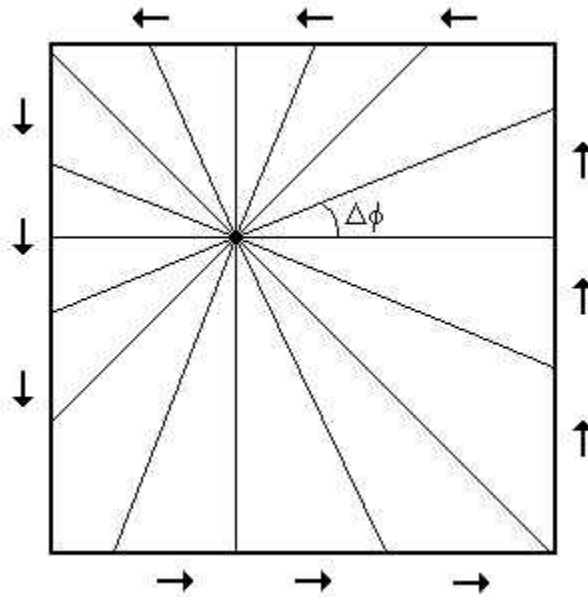


Figure 195: Application of Green's theorem to check if a point is internal

The main drawback of this procedure is that the calculation of arc tangent is necessary. That geometric operation takes usually 220 computer cycles comparing to 1 in the case of addition or product. Additionally, the procedure fails if the reference point is in the boundary.

In order to reduce the time in the determination of an internal point, the Jordan's curve theorem will be used instead. This theorem is widely used in computer graphics.

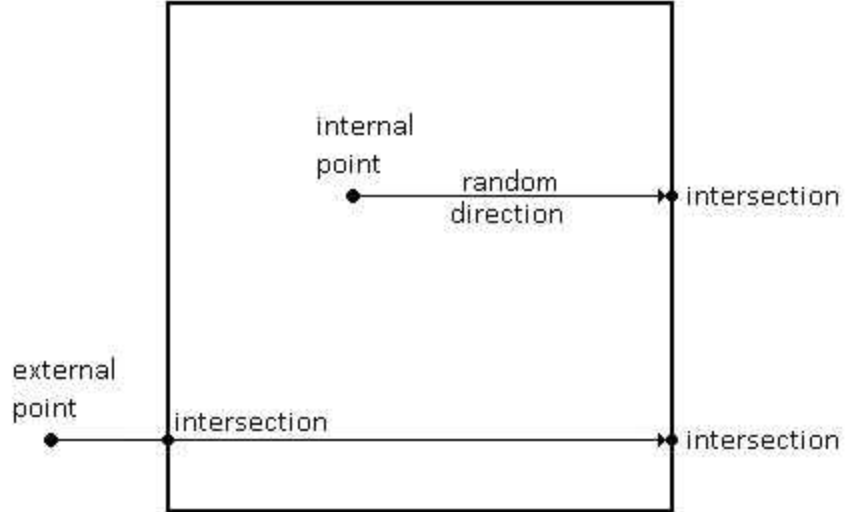


Figure 196: Application of Jordan's curve theorem

The idea behind Jordan's curve theorem is, from the point in question, to draw a straight line in any random direction and count the number of intersections of that line and the boundary. If the number of intersections is even, the point is external; otherwise, the point is internal.

If the boundary is approximated by a sequence of straight lines (very popular in CFD), this operation takes at most the calculation of one square root (50 computer cycles) and some few additions/products. The savings in computer time can be important.

The intersection between the direction vector and a straight boundary can be computed using basic vector operations. The only additional operation is how to determine if a direction will intersect a boundary.

In this procedure, used frequently in computer graphics, it is assumed that the direction will always intersect the boundary. In our case, that is not always true. In Figure 196, the direction chosen for the internal point will never intersect any of the other boundaries.

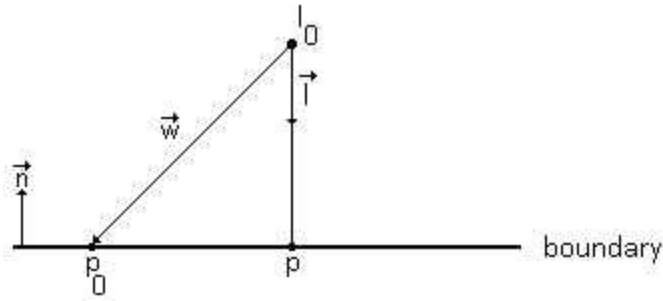


Figure 197: Intersection between a direction and a straight boundary

Figure 197 shows the case of a probable intersection between a boundary and a direction \vec{l} (a unit vector) from a given point l_0 . We can compute the minimum distance h_0 from the point l_0 to the boundary by:

$$\vec{w} = p_0 - l_0 \Rightarrow h_0 = |\vec{w} \cdot \vec{n}| \quad (75)$$

Now, if we move a little bit from l_0 to a new location l_1 we can find the minimum distance to the boundary h_1 :

$$l_1 = l_0 + \delta \cdot \vec{l} \Rightarrow h_1 = |\vec{w}_1 \cdot \vec{n}| \quad (76)$$

Comparing both h_0 and h_1 we can determine if a certain direction intersects a specific boundary. If $h_0 > h_1$, there will be an intersection since the new distance is smaller. But if $h_0 < h_1$, moving in the direction of \vec{l} , the distance will be larger and larger. This method can be efficiently implemented since just basic operations are necessary.

For the calculation of the boundary points, the situation is similar. Starting with the closest internal point to any boundary, just find the intersection using the desired direction (East, West, North or South).

D.2 Search of neighboring points

A key process in the geometric calculation is the location of the neighbors East, West, North and South in order to compute all derivatives (with finite differences). The naïve algorithm, search in all points and store the closest neighbor is too expensive since it is an algorithm of order $O(N^2)$ in time (N ... problem size). For small problems, any technique is suitable but, for DNS/LES simulations with several millions of points, the process could take several weeks/months with today's computers. The proposed algorithm is based on the efficient *binary search* technique, which is of order $O(N \log_2(N))$.

Before proceeding to the search of any neighbor, all points must be sorted with respect to their coordinate. The standard C++ library was used, which uses a combination of Quick-Sort and Heap Sort in order to keep the order of the algorithm in $O(N \log_2(N))$. The sorting procedure was divided into two different sets in order to maximize the efficiency of the later searching procedure.

- 1 Sort all points in XY ($O(N \log_2(N))$)
 - a. Sort all points in increasing X, and for same X, increasing Y (called *SortedXY*)
 - b. Store in an array all different X's present (called *DiffX_XY*)
 - c. Store in an array the position of the first point with the same X in *SortedXY* (called *SameX_XY*)
- 2 Sort all points in YX ($O(N \log_2(N))$)
 - a. Sort all points in increasing Y, and for same Y, increasing X (called *SortedYX*)

- b. Store in an array all different Y's present (called *DiffY_YX*)
- c. Store in an array the position of the first point with the same Y in *SortedYX* (called *SameY_YX*)

With all this sorting information, the search of the neighbors East/West is done with the information of the sorting in YX:

- Search the corresponding Y coordinate in *DiffY_YX* with binary search.
- Get the range of points with same Y from *SameY_YX*
- Perform binary search in *SortedYX* with the range of points provided

Similarly, for the neighbors North/South the procedure is similar:

- Search the corresponding X coordinate in *DiffX_XY* with binary search.
- Get the range of points with same Y from *SameX_XY*
- Perform binary search in *SortedXY* with the range of points provided

What is important here is the analysis of the order of the algorithm. In the sorting step, we have two procedures with order $O(N \log_2(N))$ which is made for XY and YX respectively, but only one time.

In the searching of any neighbor, if a squared grid is used, part (a) takes roughly $O(\sqrt{N} \log_2(\sqrt{N}))$ comparisons with an array that fits in cache memory L1 (inside the CPU and an access time similar to the one of a register). Later, part (b) involves reading two positions (from cache memory) while part (c) takes $O(\sqrt{N} \log_2(\sqrt{N}))$ with all data again completely in cache memory L1. This searching time is basically negligible in comparison with the time spent in sorting all points.

D.3 Search of influence points

The most expensive part of all geometric procedure is the searching of the influence points. Because the flux-limiting scheme used in the convection terms, it is necessary to interpolate both velocity components u and v in the grids of pressure and the intersection of grids u and v .

The number of interpolation vectors is 4 times the number of points. Even with binary search, the procedure takes several weeks if all points are used in the sorting algorithm.

The idea implemented is to use the same sorting technique but limiting the number of points to a vicinity of the interpolation coordinate. The procedure is to build a box of possible coordinates (with the interpolation coordinate) and use the information stored in $DiffX_{XY}$ and $SameX_{XY}$ for the X-coordinate (and $DiffY_{YX}$, $SameY_{YX}$ for the Y-coordinate. By setting the box to cover roughly 200 points, all data fits in cache memory L1 and the sorting process takes a very little time. In general the order of the algorithm here is roughly $O(N)$.

D.4 Calculation of condition number

Finally the calculation of the condition number is a fundamental step to find the optimum shape parameter of each collocation matrix. The usual procedure is to use *singular value decomposition* SVD to find all eigenvalues and then find the condition number by dividing the largest eigenvalue by the smallest eigenvalue. Even that SVD is a very accurate technique is of order $O(N^3)$ and becomes expensive. It is possible to reduce the processing time by eliminating the construction of the matrix U and leaving strictly the calculation of the eigenvalues.

Considering that the range of valid condition numbers (for the shape parameter) is not strict but just a recommendation, it is not restricted only to one specific norm.

The computation of the condition number through eigenvalues is a calculation in norm 2, so by changing the calculation of the condition number to norm infinity, and coding using efficiently the cache memory, the calculation time can be reduced significantly. In this work, all calculations of condition number were implemented using norm infinity.

APPENDIX E
MULTICORE FLOW SOLVER

The parallelization and optimization of any numerical procedure for CFD calculations is becoming a very important step if large problems are desired to be solved in a reasonable amount of time. The most popular parallelization procedure, sub-domain decomposition is still widely used since it is easy to understand and implement for any non-expert programmer. Basically, the problem is decomposed in several sub-domains with their own boundary conditions. The solution procedure on any sub-domain is then a standard serial calculation. The information of the so-called interfaces is transmitted with the aid of a network-based communication protocol, normally MPI.

The development of new computer architectures is imposing a high degree of complexity to any CFD solver that intends to use all resources in an efficient way. In general, there are several inconsistencies in the use of the classical approach on parallel systems where several processors are running on the same machine, and then several machines connected through a network. Additionally, the rise of GPU computing, with hundreds or thousands of processors running on a single card, imposes some limitations due to the fact that the available memory per card is still small for the solution of very large problems.

In recent years, many parallel implementations have been published. For example, in [111], a multi-block structured flow solver is parallelized through sub-domain decomposition, using MPI protocol for communication. The procedure is tested on systems with several processors per machine. Results show good scalability up to 2,048 processors.

One alternative for low-cost clusters can be found in [116], where the main focus is in the solution of the Poisson-like equation in the Fourier domain. The transmission of the common boundary values is performed with MPI. In [134], a predictor-corrector procedure is parallelized, where the flow is solved through the traditional projection method. In this work, good speedups

are obtained up to 500 processors, then, performance deteriorates. In the same type of solvers, in [136], a parallel multigrid level solver is presented for LES simulations. Results show good scalability up to 64 processors.

Following the classical approach, a sequential flow solver is parallelized by means of an algebraic multigrid solver for scalar elliptic PDE's. MPI protocol is used for communication and the results show a constant calculation time as the number of nodes increases (same number of nodes per processor). Another Poisson-like solver is found in [345], where a sparse linear solver is parallelized with GMRES. One more time, communications are done with MPI.

In [346], a parallel flow solver, using the fractional-step method, is presented where the Poisson-like equation is solved with the ADI scheme. With this procedure, good speedup is obtained up to 50 processors.

If the problem size is not large, the GPU computing is a very good low-cost alternative. In [93] for example, the performance of the cyclic reduction algorithm for solving tri-diagonal systems is presented on GPU cards. With this approach, the domain is decomposed in several sub-domains, where each block is solved separately on the GPU card. Speedups up to 20 are obtained in 2D and 3D problems with low-cost cards.

The combined MPI-GPU approach looks as an excellent solution for problems that are too large. In [102], a standard finite-volume procedure is parallelized using a multi-block approach and the MPI-GPU solution is analyzed for large problems. In general, speedups of 30+ are obtained for transonic flow problems.

In the same idea, in [117], a MPI-GPU scheme is presented for the solution of large problems. In the case of meshes of 330 million points, good scalability is obtained up to 5000-6000 processors. Similar solutions MPI-GPU can be observed in [226] and [358].

It is very important to underline that, in computing, parallelization has many different approaches. In all references named here [93], [102], [111], [116], [117], [134], [136], [226], [345], [346] and [358], parallelization is performed through *vectorization* of a global serial algorithm, where the communication between processors is done through the MPI protocol. When the number of processors is increased, the overhead that network communication has will degrade performance sooner than later.

The parallelization through vectorization is the most obvious solution for old architectures, where several serial processors are connected through a network. Most modern processors are *multicore* processors. With these architectures, the solution is to run several copies of the code in the same node and use MPI for communication. Some MPI versions use *interprocess communication* if the communication is in the same machine. In general, if a CFD code is going to be executed on nodes with multicore processors, a procedure without MPI communication looks as a desirable solution.

In [194], a combined MPI-*pthread* model is presented for CFD calculations. Here, in each node (with a multicore processor), the solution procedure is decomposed in several independent problems. Next, threads are organized to solve each sub-problem separately without any communication. The solution presented here is suitable for some specific procedures.

The parallelization through vectorization has important limitations because the top speedup that can be reached is limited by the performance of the serial part. In fact, in order to improve parallelization, the part of the code that must be parallelized is the serial part.

When working with multicore processors on multithreaded environments, a different idea of parallelization arises, *concurrency*. Parallelization through concurrency means that several threads can work together to solve a specific problem without any synchronization at all. This

concurrent way of working can be very attractive for iterative procedures, where the repetitive calculation does not have to be done one by one.

The idea of this chapter is to present a multicore flow solver, using the concurrent ideas developed previously in [341] and [342].

E.1 General multicore procedure

The basic idea of this multicore procedure is to have several independent execution units (*threads*) [269] running and calculating on the same data without any specific synchronization.

The scheme is divided in *main thread* (master) and *execution threads* (slaves). The main thread performs all the setup process and, when everything is ready for iteration, starts the execution threads (slaves). The job of the execution threads is to iterate permanently until the main thread decides that the solution is acceptable. The number of iterations that each execution thread will do is not going to be necessarily the same than the others.

An important observation in any CFD calculation is the fact that more than 80% of the processing time is spent by the floating point unit (FPU). Another important issue to take into consideration is that many multicore processors have more physical threads than FPUs.

In order to achieve an efficient solution, the main thread may launch some additional execution threads to iterate in a portion of the problem. The total number of execution threads does not necessarily have to be equal to the number of FPUs. In this alternative, the main thread can perform the rest of the tasks that are not FPU intensive.

The idea of separating the code into threads that are FPU intensive and threads that are not FPU intensive, all of them running at the same time, will change the way the calculation is

going to converge. It is unlikely that the same flow problem will have the same convergence history in two different runs. Additionally, having threads using the FPU constantly will have all pipelines of the floating point unit full.

Additionally, newer versions of GNU C++ compiler allow the compilation using the standard floating point unit (the math co-processor) and the SSE unit at the same. This option allows any numerical intensive code to run basically as twice as much. With these considerations, the proposed algorithm can be stated as:

- Execute a predefined number of execution threads, and no greater than the number of available floating point units. They will iterate on a portion of the problem, calculating the maximum increment at the end of any iteration.
- Use the main thread to monitor convergence, to update boundary conditions and perform any necessary interpolations.

The basic idea of this solution is that the execution threads will iterate continuously without having to update any boundary condition, waiting for any communication data or doing any other task. The activities of any execution thread can be stated as:

1. Get data of corresponding block.
2. Set initial guess in block.
3. Reset maximum increment and number of iterations.
4. Iterate:

- 4.1. Update solution.
- 4.2. Compute maximum increment.
- 4.3. If *stop condition* is activated, quit.

After some initialization steps, any execution thread will iterate continuously until the stop condition is activated. This separation of tasks will optimize the use of all available FPU's. Because any of the execution threads may not be running at any moment, some execution threads may iterate more than others and/or than the maximum predefined number of iterations (needed if calculation does not converge). On the other hand, the tasks of the main thread are:

1. Perform a general setup.
2. Start execution threads.
3. Wait until all execution threads are running.
4. While *stop condition* is not activated:
 - 4.1 Wait until first solver has done one iteration (just a reference).
 - 4.2 Update boundary conditions and perform interpolations.
 - 4.3 If all execution threads (in all nodes) have converged, activate *stop condition*.
 - 4.4 If all execution threads have reached/exceeded the maximum number of iterations, activate *stop condition*.
5. Write solution.

The idea behind step 4.1 is to avoid the unnecessary recalculation of the boundary conditions as well as the interpolations. On large problems, updating boundary conditions too often (and interpolations) will not improve convergence. Updating the boundary values and recalculating the new ones at the same time, as well as the interpolations, will make convergence completely different than a serial solver. The solution of any flow problem is the same no matter what iterative procedure is used, or what initial values are set or how the points are particularly updated.

The solution presented here, similar to the ones presented in [341] and [342] will execute efficiently if they have almost exclusive use of the entire node. Since at any cluster node, the operating systems needs to perform some maintenance tasks, at least one processor (or physical thread) must be reserved.

E.2 Multicore flow solver for 2D steady flows

For steady state problems, the procedure for the main thread is:

1. Perform a general setup:
 - 1.1 Create geometric configuration
 - 1.2 Create physical configuration
 - 1.2.1 Equations of motion (momentum and continuity)
 - 1.2.2 Flow solver
 - 1.3 Set initial guess

2. Start execution threads.
3. Wait until all threads are running
4. Store current iteration of first thread (just a reference)
5. Iterate:
 - 5.1 Update boundary conditions
 - 5.2 Perform interpolations
 - 5.3 Wait until first thread has done one iteration
 - 5.4 Check *stop condition* and set flag if done:
 - 5.4.1 Check the maximum residual of all execution threads
 - 5.4.2 Check maximum number of iterations
 - 5.5 If *stop condition* is activated, quit iteration
6. Write results

For the execution threads, the procedure is:

1. Get information of block:
 - 1.1 Get points of block
 - 1.2 Create the *scan sequence* for flow equations
2. Iterate:
 - 2.1 Update number of iterations

- 2.2 Store current solution (of block)
- 2.3 Compute momentum equation
- 2.4 Compute flow field (do some sub-iterations)
- 2.5 Compute maximum residual of block
- 2.6 If *stop condition* is activated, quit iteration

E.3 Testing the multicore solver

The first case solved was developing laminar flow in parallel plates of length 5:1. The mesh used in all cases had DNS resolution in order to meet the condition of the local Reynolds number.

The problem was tested in one of the nodes of the cluster of the group with a 16 cores Xeon E5-2690 running at 2.90 GHz and 20 MB of cache memory. In order to leave at least one processor to the operating system, and in order to keep the same work load to all execution threads, the total number of processors used was 11, 1 for the main thread and 10 for the execution threads.

Table 10: Data used in parallel plates (multicore runs)

Re	Nodes X	Nodes Y	Re_{Local}	Δ / Δ_K
1000	500	100	5	1.78
2000	750	150	6.67	1.99
3000	1000	200	7.5	2.03
4000	1250	250	8	2.01
5000	1500	300	8.33	1.98
6000	1750	350	8.57	1.94

Table 10 shows the data used in this case, with a uniform mesh and $\Delta x = \Delta y$, and a delta roughly two times the Kolmogorov delta. Table 11 shows the range of iterations performed by the execution threads. It can be observed that in spite that the variation on the number of iterations is important; the solution meets perfectly the convergence criteria.

The serial code used to compute the speedup was the same original program that was parallelized later. The Reynolds numbers chosen were the entire laminar and transitional region, enough to show the features of the proposed method.

Table 11: Range of iterations, multicore solver, parallel plates

Reynolds	Range of iterations
1000	3507-5178
2000	3888-5663
3000	5336-6565
4000	6663-8694
5000	7302-9901
6000	8781-11494

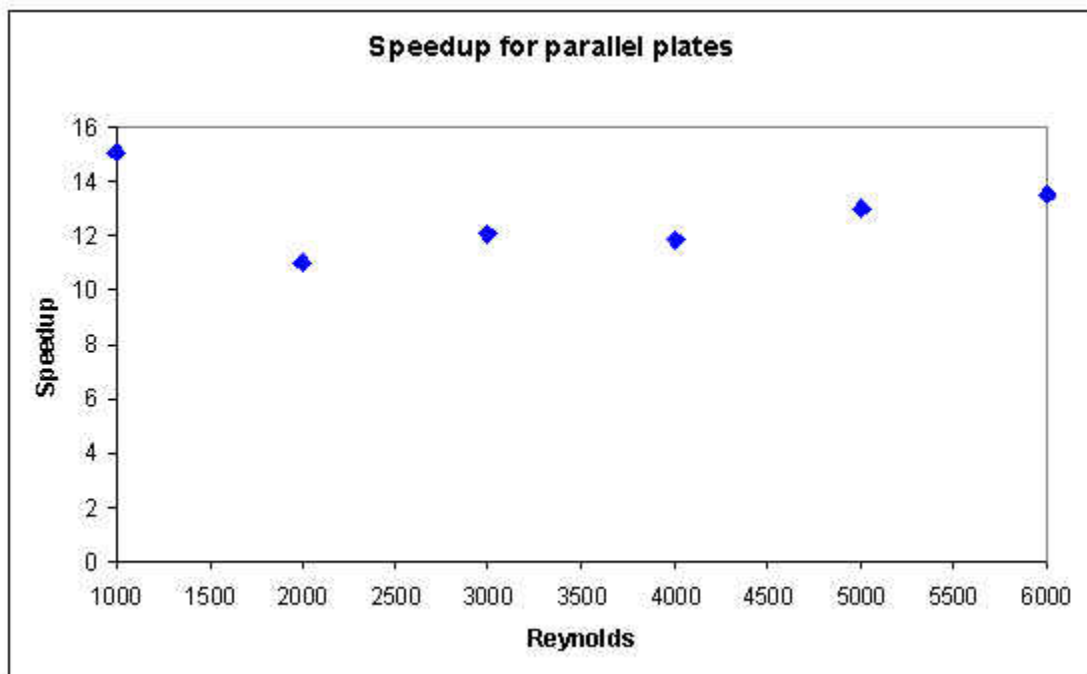


Figure 198: Speedup of multicore solver, parallel plates, 11 cores

Figure 198 shows the speedup obtained, being in all cases equal or larger than the ideal speedup of 11. After a big value of speedup obtained for Reynolds number of 1000, the speedup

decreases a bit and then increases (in average) little by little as the Reynolds number increases. The main reason for this excellent performance is due to that some tasks that are done one by one in the serial solver are overlapped by the multicore solver (boundary conditions and interpolations).

The speedup obtained for the case of Reynolds of 1000 is particularly high and it is not a characteristic of the method. For this case, the size of the mesh (500x100) is small enough that, in the calculation of the flow field, all data fits entirely in cache memory, with an access time way larger than from main memory. This issue is important because is more cores are available, an important part of the data could fit in cache memory, allowing the speedup to increase considerably.

The second case solved was the laminar flow on a backward facing step with an expansion ratio of 1.14. The range of Reynolds number is from 1000 to 6000, enough for the convection terms to be small or moderate. The grid info used is the same as in Table 5.

Table 12: Range of iterations, multicore solver, BFS, $ER = 1.14$

Reynolds	Range of iterations
1000	9665-13255
2000	41029-51349
3000	38652-49800
4000	34088-43319
5000	52618-69186
6000	70562-100043

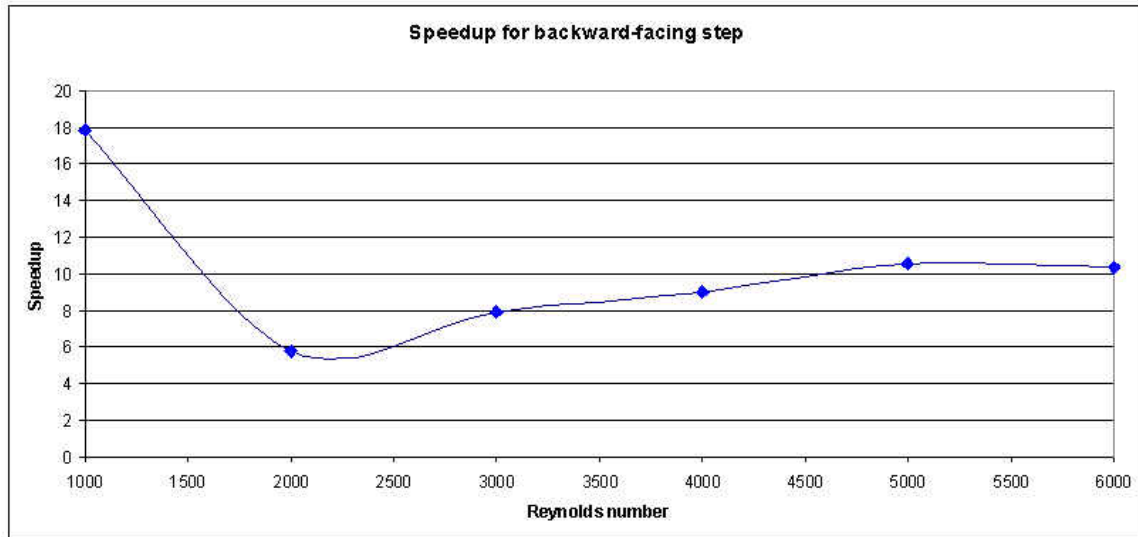


Figure 199: Speedup of multicore solver, BFS, $ER = 1.14$, 11 cores

Table 12 shows the range of iterations performed in all cases solved, with a similar behavior to the previous case. The big variation on the number of iterations is due that not all execution threads are running at the same time. This issue occurs also with all MPI-based solvers.

Figure 199 shows the speedup obtained with the proposed procedure. Here after the big speedup for Reynolds number of 1000, the performance decreases to roughly 6 and then increases to 10 when basically stabilize. This variation in speedup is clearly due to the different convection levels that exist in each case.

This multicore procedure can be easily implemented in GPU architectures and the speedup can be tremendous if the whole problem data fits in the GPU memory.

LIST OF REFERENCES

- [2] Abe, H., Kawamura, H. and Matsuo, Y., *Direct Numerical Simulation of a Fully Developed Turbulent Channel Flow With Respect to the Reynolds Number Dependence*, Journal of Fluids Engineering, Vol. 123, pp. 382-393, 2001.
- [3] Agarwal, R. K., *A third-order-accurate upwind scheme for Navier-Stokes solutions at high Reynolds numbers*, AIAA Paper 81-0112, 1981.
- [4] Aider, J.-L., Danet, A. and Lesieur, M., *Large-eddy simulation applied to study the influence of upstream conditions on the time-dependant and averaged characteristics of a backward-facing step flow*, Journal of Turbulence, Vol. 8, No. 51, 2007.
- [5] Aidun, C. K., Triantafillopoulos, N. G. and Benson, J. D., *Global stability of a lid-driven cavity with throughflow: flow visualization studies*, Physics of Fluids A, Vol. 3, pp. 2081-2091, 1991.
- [6] Alleborn, N., Nandakumar, K., Raszillier, H. and Durst, F., *Further contributions on the two-dimensional flow in a sudden expansion*, Journal of Fluid Mechanics, Vol. 330, pp. 169-188, 1997.
- [7] Anandhanarayanan, K. and Nagarathinam, M., *Parallelisation of a gridfree kinetic upwind solver*, AIAA Paper 2005-4628, AIAA 17th Computational Fluid Dynamics Conference, Toronto, June 2005.
- [8] Armaly, B. F., Durst, F., Pereira, J. C. F. and Schönung, B., *Experimental and theoretical investigation of backward-facing step flow*, Journal of Fluid Mechanics, Vol. 127, pp. 473-496, 1983.

- [9] Armenio, V. and Piomelli, U., *A Lagrangian Mixed Subgrid-Scale Model in Generalized Coordinates*, Flow, Turbulence and Combustion, Vol. 65, pp. 51-81, 2000.
- [10] Atluri, S. N. and Shen, S., *The Meshless Method*, Technical Science Press, Forsyth, Georgia, 2002.
- [11] Atluri, S. N. and Shen, S., *The meshless local Petrov-Galerkin (MLPG) method: a simple & less-costly alternative to the finite element and boundary element methods*, CMES: Computer Modeling in Engineering & Sciences, Vol. 3, pp. 11-52, 2002.
- [12] Aung, W., *Heat Transfer In The Separated Region Beyond A Rearward-Facing Step*, PhD Thesis, University Of Minnesota, 1969.
- [13] Aydin, M. and Fenner, R. T., *Boundary element analysis of driven cavity flow for low and moderate Reynolds numbers*, International Journal for Numerical Methods in Fluids, 37, pp. 45-64, 2001.
- [14] Balasubramanyam, S., *A new grid-free upwind relaxation scheme for compressible flows*, M.Sc. Thesis, Indian Institute of Science, Bangalore, India, 2002.
- [15] Balasubramanyam, S. and Raghurama Rao, S. V., *A new grid-free relaxation scheme for Euler equations*, Fluid Mechanics Report No: 2001 FM 07, Department of Aerospace Engineering, IISc, Bangalore, India.
- [16] Balasubramanyam, S. and Raghurama Rao, S. V., *A new grid-free relaxation scheme for Euler equations*, 4th Annual CFD Symposium, Bangalore, 10-11, August 2001.
- [17] Balasubramanyam, S. and Raghurama Rao, S. V., *A new grid-free relaxation scheme for Euler equations*, Ninth Asian Congress of Fluid Mechanics, Isfahan, Iran, May 27-31, 2002.

- [18] Balasubramanyam, S. and Raghurama Rao, S. V., *A new grid-free relaxation scheme for conservation laws*, Computational Fluid Dynamics 2002, Proceedings of the International Conference on Computational Fluid Dynamics-2. Springer: Berlin, 2003.
- [19] Balasubramanyam, S. and Raghurama Rao, S. V., *A grid-free upwind relaxation scheme for inviscid compressible flows*, International Journal for Numerical Methods in Fluids, Vol. 51, pp. 159-196, 2006.
- [20] Barakos, G., Mitsoulis, E. and Assimacopoulos, D., *Natural convection flow in square cavity revised: laminar and turbulent models with wall functions*, International Journal for Numerical Methods in Fluids, Vol. 18, pp. 695-719, 1994.
- [21] Barkley, D., Gomes, M. G. M. and Henderson, R. D., *Threedimensional instability in flow over a backward-facing step*, Journal of Fluid Mechanics, Vol. 473, pp. 167-190, 2002.
- [22] Barragy, E. and Carey, G. F., *Stream function-vorticity driven cavity solutions using p finite elements*, Computers and Fluids, Vol. 26, pp. 453- 468, 1997.
- [23] Barri, M., El Khoury, G. K., Andersson, H. I. and Pettersen B., *DNS of backward-facing step flow with fully turbulent inflow*, International Journal for Numerical Methods in Fluids, Vol. 64, pp. 777-792, 2010.
- [24] Barton, I. E., *Laminar flow past an enclosed and open backward-facing step*, Physics of Fluids, Vol. 12, pp. 4054-4056, 1994.
- [25] Barton, I. E., *The entrance effect of laminar flow over a backward-facing step geometry*, International Journal for Numerical Methods in Fluids, Vol. 25, pp. 633-644, 1997.
- [26] Barton, I. E., *Improved laminar predictions using a stabilized time dependent simple scheme*, International Journal for Numerical Methods Fluids, Vol. 28, pp. 841-857, 1998.

- [27] Barton, I. E. and Kirby, R., *Finite difference scheme for the solution of fluid flow problems on non-staggered grids*, International Journal for Numerical Methods in Fluids, 33, pp. 939-959, 2000.
- [28] Batina- J. T., *A gridless Euler/Navier-Stokes solution algorithm for complex two-dimensional applications*, NASA-TM-107631, 1992.
- [29] Batina- J. T., *A gridless euler/navier-stokes solution algorithm for complex aircraft applications*, AIAA Paper 1993-0333, AIAA 31st Aerospace Sciences Meeting and Exhibit, Reno, NV, January 1993.
- [30] Belytschko- T., Lu- Y.Y. and Gu- L., *Element-free Galerkin methods*, International Journal for Numerical Methods in Engineering, Vol. 37, pp. 229-256, 1994.
- [31] Belytschko, T., Krongauz, Y., Organ, D., Fleming, M. and Krysl, P., *Meshless methods: An overview and recent developments*, Computer methods in applied mechanics and engineering, Vol. 139, pp. 3-47, 1996.
- [32] Benjamin, A. S. and Denny, V. E., *On the convergence of numerical solutions for 2-D flows in a cavity at large Re*, Journal of Computational Physics, Vol. 33, pp. 340-358, 1979.
- [33] Bhaganagar, K., Kim, J. and Coleman, G., *Effect of Roughness on Wall-Bounded Turbulence*, Flow, Turbulence and Combustion, Vol. 72, pp. 463-492, 2004.
- [34] Bhaganagar, K., *Direct numerical simulation of unsteady flow in channel with rough walls*, Physics of Fluids, Vol. 20, 101508, 2008.

- [35] Biagioli, F., *Calculation of laminar flows with second-order schemes and collocated variable arrangement*, International Journal for Numerical Methods Fluids, Vol. 26, pp. 887-905, 1998.
- [36] Biau, D., Soueid, H. and Bottaro, A., *Transition to turbulence in duct flow*, Journal of Fluid Mechanics, Vol. 596, pp. 133-142, 2008.
- [37] Biswas, G., Breuer, M. and Durst, F., *Backward-Facing Step Flow for Various Expansion Ratios at Low and Moderate Reynolds Numbers*, Journal of Fluid Engineering, Vol. 126, pp. 362-374, 2004.
- [38] Bogatyrev, V. Y. A. and Gorin, A. V., *End effects in rectangular cavities*, Fluid Mechanics-Soviet Research, Vol. 101-106, 1978
- [39] Bose, S. T., Moin, P. and You, D., *Grid-independent large-eddy simulation using explicit filtering*, Center for Turbulent Research, Annual Research Briefs 2008, pp. 173-187, 2008.
- [40] Botella, O. and Peyret, R., *Benchmark spectral results on the lid-driven cavity flow*, Computers and Fluids, 27, pp. 421- 433, 1998.
- [41] Bouris, D. and Bergeles, G., *2D LES of vortex shedding from a square cylinder*, Journal of Wind Engineering, Vol. 80, pp. 31-46, 1999.
- [42] Bozeman, J. D., *Numerical study of viscous flow in a cavity*, Journal of Computational Physics, Vol. 12, pp. 348-363, 1973.
- [43] Brandt, A. and Yavneh, I., *Inadequacy of first-order upwind difference schemes for some recirculating flows*, Journal of Computational Physics, Vol. 93, pp. 128-143, 1991.

- [44] Bruneau, C. H. and Jouron, C., *An efficient scheme for solving steady incompressible Navier Stokes equations*, Journal of Computational Physics, Vol. 89, pp. 389-413, 1990
- [45] Burattini, P., Leonardi, S., Orlandi, P. and Antonia, R. A., *Comparison between experiments and direct numerical simulations in a channel flow with roughness on one wall*, Journal of Fluid Mechanics, Vol. 600, pp. 403-426, 2008.
- [46] Burggraf, O. R., *Analytical and numerical studies of the structure of steady separated flows*, Journal of Fluid Mechanics, Vol. 24, pp. 113-151, 1966.
- [47] Campion-Renson, A. and Crochet, M. J., *On the stream function-vorticity finite element solutions of Navier-Stokes equations*, International Journal of Numerical Methods in Engineering, Vol. 12, pp. 1809-1818, 1978.
- [48] Caruso, S. C., Ferziger, J. H. and Oliger, J., *Adaptive grid techniques for elliptic fluid flow problems*, AIAA Paper 86-0498, 1986.
- [49] Cazemier, W., Verstappen, R. W. C. P. and Veldman, A. E. P., *Proper orthogonal decomposition and low-dimensional models for driven cavity flows*, Physics of Fluids, Vol. 10, pp. 1685-1699, 1998.
- [50] Chen, C. S., Rashed, Y. F. and Golbberg, M. A., *A Mesh-Free Method for Linear Diffusion Equations*, Numerical Heat Transfer, Part B: Fundamentals, Vol. 33, pp. 469-486, 1998.
- [51] Chen, H. Q. and Shu, C., *An efficient implicit mesh-free method to solve two-dimensional compressible Euler equations*, International Journal of Modern Physics, Vol. 16, pp. 439-454, 2005.
- [52] Cheng, M. and Liu, G. R., *A novel finite point method for flow simulation*, International Journal for Numerical Methods in Fluids, Vol. 39, pp. 1161-1178, 2002.

- [53] Cheng, Y. P., Lee, T. S., Sui, Y. and Wang, L. P., *Numerical simulation of 2D lid-driven cavity flow with CLEARER algorithm on extremely highly skewed grids at high Reynolds numbers*, International Journal for Numerical Methods in Fluids, 65, pp. 1201-1216, 2011.
- [54] Chiang, T. P., Sheu, W. H. and Hwang, R. R., *Finite volume analysis of spiral motion in a rectangular lid-driven cavity*, International Journal for Numerical Methods in Fluids, 23, pp. 325-346, 1996.
- [55] Chiang, T. P., Sheu, W. H. and Hwang, R. R., *Effect of Reynolds number on the eddy structure in a lid-driven cavity*, International Journal for Numerical Methods in Fluids, 26, pp. 557-759, 1998.
- [56] Chiang, T. P. and Sheu, T. W. H., *A numerical revisit of backward-facing step flow problem*, Physics of Fluids, Vol. 11, pp. 862-874, 1999.
- [57] Chinchapatnam, P. P., Djidjeli, K., and Nair, P. B., *Meshless rbf collocation for steady incompressible viscous flows*, AIAA Paper 2006-3525, AIAA 36th Fluid Dynamics Conference and Exhibit, San Francisco, CA, June 2006.
- [58] Chinchapatnam, P. P., *Radial Basis Function Based Meshless Methods for Fluid Flow Problems*, PhD Thesis, University of Southampton, 2006.
- [59] Choi, S. K., Nam, H. Y. and Cho, M., *A High Resolution and Bounded Convection Scheme*, KSME Journal, Vol. 9, pp. 240-250, 1995.
- [60] Choi, S. K., Nam, H. Y. and Cho, M., *A comparison of higher-order bounded convection schemes*, Computer Methods in Applied Mechanics and Engineering, Vol. 121, pp. 281-301, 1995.

- [61] Coates, M. J. and Patterson, J. C., *Numerical simulations of the natural convection in a cavity with nonuniform internal sources*, International Journal for Heat and Fluid Flow Vol. 15, pp. 218-225, 1994.
- [62] Comini, G., Manzan, M. and Nonino, C., *Finite element solution of the stream function-vorticity equations for incompressible two-dimensional flows*, International Journal for Numerical Methods in Fluids, Vol. 19, pp. 513-525, 1994.
- [63] Cortes, A. B. and Miller, J. D., *Numerical experiments with the lid driven cavity flow problem*, Computers & Fluids, Vol. 23, pp. 1005-1027, 1994.
- [64] Creusé, E., Giovannini, A. and Mortazavi, I., *Vortex simulation of active control strategies for transitional backward-facing step flows*, Computers & Fluids, Vol. 38, pp. 1348-1360, 2009.
- [65] Cruchaga, M. A., *A study of the backward-facing step problem using a generalized streamline formulation*, Communications in Numerical Methods in Engineering, Vol. 14, pp. 697-708, 1998.
- [66] Cui, G. X., Xu, C. X., Fang, L., Shao, L. and Zhang, Z. S., *A new subgrid eddy-viscosity model for large-eddy simulation of anisotropic turbulence*, Journal of Fluid Mechanics, Vol. 582, pp. 377-397, 2007.
- [67] Demirdzi, I. and Peric, M., *Finite-volume method for prediction of fluid flow in arbitrary shaped domains with moving boundaries*, International Journal for Numerical Methods in Fluids, Vol. 10, pp. 771-790, 1990.
- [68] Deshpande, M. D., *Flow regimes in a three-dimensional driven cavity*, NAL Project Document PD CF 9305, 1993.

[69] Deshpande, M. D. and Milton, S. G., Kolmogorov scales in a driven cavity flow, *Fluid Dynamics Research*, Vol. 22, pp. 359-381, 1998.

[70] Deshpande, M. D., Milton, S. G. and Balaji, S., *A detailed description of transitional and turbulent flow in a three-dimensional cavity*, National Aerospace Laboratory, Document PD CF 9430, Bangalore, India, 1994.

[71] Deshpande, M. D. and Shankar, P. N., *Direct numerical simulation of a complex turbulent flow*, *Current Science*, Vol. 66, pp. 767-770, 1994.

[72] Deshpande, M. D. and Shankar, P. N., *Transitional and turbulent flow in a three-dimensional cavity*, National Aerospace Laboratory, Document PD CF 9411, Bangalore, India, 1994.

[73] di Mare L., Klein M., Jones, W. P. and Janicka, J., *Synthetic turbulence inflow conditions for large-eddy simulation*, *Physics of Fluids*, Vol. 18, 025107, 2006.

[74] Dipankar, A. and Sengupta, T. K., *Symmetrized compact scheme for receptivity study of 2D transitional channel flow*, *Journal of Computational Physics*, Vol. 215, pp. 245-273, 2006.

[75] Divo, E. and Kassab, A. J., *Effective Domain Decomposition Meshless Formulation of Fully-Viscous Incompressible Fluid Flows*, *Boundary Elements XXVII*, pp. 67-77, WIT Press, Southampton, UK, 2005.

[76] Divo, E. and Kassab, A. J., *Efficient localized meshless modeling of natural convective viscous flows*, AIAA Paper AIAA-2006-3089.

[77] Divo, E. and Kassab, A., *An Efficient Localized Radial Basis Function Meshless Method for Fluid Flow and Conjugate Heat Transfer*, *Journal of Heat Transfer*, Vol.129, pp. 124-136, 2007.

[78] Divo, E. and Kassab, A. J., *Localized Meshless Modeling of Natural-Convective Viscous Flows*, Numerical Heat Transfer, Part B: Fundamentals, Vol. 53, pp. 487-509, 2008.

[79] Dongarra, J., Foster, I., Fox, G., Gropp, W., Kennedy, K., Torczon, L. and White, A., *Source Book of Parallel Computing*, Morgan Kaufmann, 2003.

[80] Duarte, C. A., *A review of some meshless methods to solve partial differential equations*, Technical Report 95-06, Texas Institute for Computational and Applied Mathematics, University of Texas at Austin, 1995.

[81] Duarte, C. A. and Oden, J. T., *Hp clouds - a meshless method to solve boundary value problems*, Technical Report 95-05, Texas Institute for Computational and Applied Mathematics, University of Texas at Austin, 1995.

[82] Durst, F. and Pereira, J. C. F., *Time-dependent laminar backward-facing step flow in a two dimensional duct*, Trans. ASME, Journal of Fluids Engineering, Vol. 110, pp. 289-296, 1988.

[83] Durst, F., Peireira, J. C. F. and Tropea, C., *The plane symmetric sudden-expansion flow at low Reynolds numbers*, Journal of Fluid Mechanics, Vol. 248, pp. 567-581, 1993.

[84] El Zahab, Z., Divo, E. and Kassab, A., *A meshless CFD approach for evolutionary shape optimization of bypass grafts anastomoses*, Inverse Problems in Science and Engineering, Vol. 17, pp. 411-435, 2009.

[85] El Zahab, Z., Divo, E. and Kassab, A. J., *A localized collocation meshless method (LCMM) for incompressible flows CFD modeling with applications to transient hemodynamics*, Engineering Analysis with Boundary Elements, Vol. 33, pp. 1045-1061, 2009.

[86] El Zahab, Z., Divo, E. and Kassab, A., *Minimisation of the wall shear stress gradients in bypass grafts anastomoses using meshless CFD and genetic algorithms optimisation*, Computer Methods in Biomechanics and Biomedical Engineering, Vol. 13, pp. 35-47, 2010.

[87] Elhami Amiri, A., Kazemzadeh Hannani S., Mashayek F., *Evaluation of a Fourth-Order Finite-Volume Compact Scheme for LES with Explicit Filtering*, Numerical Heat Transfer, Part B, Vol. 48, pp. 147-163, 2005.

[88] Erhart, K., Divo, E. and Kassab, A., *An evolutionary-based inverse approach for the identification of non-linear heat generation rates in living tissues using a localized meshless method*, International Journal of Numerical Methods for Heat & Fluid Flow, Vol. 18, pp. 401-414, 2008.

[89] Erhart, K., Gerace, S., Divo, E. and Kassab, A., *Turbulent compressible flow analysis with meshless methods*, Proceedings of the International Conference on Computational Methods for Coupled Problems in Science and Engineering (COUPLED PROBLEMS 2009), Ischia Island, Italy, 2009.

[90] Erhart, K., Gerace, S., Divo, E. and Kassab, A., *An RBF interpolated generalized finite difference meshless method for compressible turbulent flows*, Proceedings of the ASME 2009 International Mechanical Engineering Congress & Exposition, ASME, Lake Buena Vista, FL, USA, 2009.

[91] Erturk E., *Numerical solutions of 2-D steady incompressible flow over a backward-facing step, Part I: High Reynolds number solutions*, Computers & Fluids, Vol. 37, pp. 633-655, 2008.

[92] Erturk, E., Corke, T. C. and Gokcol, C., *Numerical solutions of 2-D steady incompressible driven cavity flow at high Reynolds numbers*, International Journal for Numerical Methods in Fluids, 48, pp. 747-774, 2005.

- [93] Esfahanian, V., Baghapour, B., Torabzadeh, M. and Chizari, H., *An efficient GPU implementation of cyclic reduction solver for high-order compressible viscous flow simulations*, Computers & Fluids, Vol.92, pp. 160-171, 2014.
- [94] Farhat, C., Rallu, A., Wang, K. and Belytschko, T., *Robust and provably second-order explicit-explicit and implicit-explicit staggered time-integrators for highly non-linear compressible fluid-structure interaction problems*, International Journal for Numerical Methods in Engineering, Vol. 84, pp. 73-107, 2010.
- [95] Fisher, P. and Bruneau, C.-H., *Wavelet-based analysis of enstrophy transfer in two-dimensional turbulence*, Physics of Fluids, Vol. 21, 065109, 2009.
- [96] Fletcher, C. A. J., *Computational techniques for fluid dynamics*, Springer-Verlag, 1991.
- [97] Fortin, A., Jardak, M., Gervais, J. J. and Pierre, R., *Localization of Hopf bifurcations in fluid flow problems*, International Journal Numerical Methods in Fluids, Vol. 24, pp. 1185-1210, 1997.
- [98] Freitas, C. J., Street, R. L., Findikakis, A. N. and Koseff, J. R., *Numerical simulation of three-dimensional flow in a cavity*, International Journal for Numerical Methods in Fluids, Vol. 5, pp. 561-575, 1985.
- [99] Freitas, C. J. and Street, R. L., *Non-linear transport phenomena in a complex recirculating flow: a numerical investigation*, International Journal for Numerical Methods in Fluids, Vol. 8, pp. 769-802, 1988.
- [100] Friedrich, R. and Arnal, M., *Analysing turbulent backward-facing step flow with the lowpass-filtered Navier-Stokes equations*, Journal of Wind Engineering and Industrial Aerodynamics, Vol. 35, pp. 101-128, 1990.

- [101] Friedrich, R., Hüttl, T. J., Manhart, M. and Wagner, C., *Direct numerical simulation of incompressible flows*, Computers & Fluids, Vol. 30, pp. 555-579, 2001.
- [102] Fu, L., Gao, Z., Xu, G. and xu, F., *A multi-block viscous flow solver based on GPU parallel methodology*, Computers & Fluids, Vol. 95, pp. 19-39, 2014.
- [103] Gartling, D. K., *A test problem for outflow boundary conditions—flow over a backward-facing step*, International Journal for Numerical Methods in Fluids, Vol. 11, pp. 953-967, 1990.
- [104] Gerace, S., *An Interactive Framework for Meshless Methods Analysis in Computational Mechanics and Thermofluids*, M.S. Thesis, University of Central Florida, 2007.
- [105] Gerace, S., Erhart, K., Divo, E. and Kassab, A., *Generalized finite difference meshless method in computational mechanics and thermofluids*, Proceedings of the International Conference on Computational Methods for Coupled Problems in Science and Engineering (COUPLED PROBLEMS 2009), 2009.
- [106] Gerace, S., Erhart, K., Divo, E. and Kassab, A., *Local and virtual RBF meshless method for high-speed flows*, WIT Transactions on Modelling and Simulation, Vol. 49, pp. 83-94, 2009.
- [107] Gerace, S. A., *A Model Integrated Meshless Solver (MIMS) For Fluid Flow And Heat Transfer*, Dissertation, University of Central Florida, 2010
- [108] Gerace, S. , Erhart, K., Divo, E., and Kassab, A., *Adaptively Refined Hybrid FDM/Meshless Scheme with Applications to Laminar and Turbulent Flows*, CMES: Computer Modeling in Engineering and Science, Vol. 81, pp. 35-68, 2011.
- [109] Germano, M., Piomelli, U., Moin, P. and Cabot, W. H., *A dynamic subgrid-scale eddy viscosity model*, Physics of Fluids A, Vol. 3, pp. 1760-1765, 1991.

- [110] Ghia, U., Ghia, K. and Shin C., *High Re solutions for incompressible flow using the Navier-Stokes equations and a multigrid method*, Journal of Computational Physics, Vol. 48, pp. 387-411, 1982.
- [111] Gicquel, L. Y. M., Gourdain, N., Boussuge, J.-F., Deniau, H., Staffelbach, G., Wolf, P. and Poinso, T., *High performance parallel computing of flows in complex geometries*, Comptes Rendus Mecanique, Vol. 339, pp. 104-124, 2011.
- [112] Goedecker, S. and Hoisie, A., *Performance Optimization of Numerically Intensive Codes*, SIAM, 2001.
- [113] Gokarn, A., Battaglia, F., Fox, R. O., Hill, J. C. and Reveillon, J., *Large eddy simulations of incompressible turbulent flows using parallel computing techniques*, International Journal for Numerical Methods in Fluids, Vol. 56, pp. 1819-1843, 2008.
- [114] Goldstein, R. J., Eriksen, V. L., Olson, R. M. and Eckert, E. R. G., *Laminar separation, reattachment, and transition of the flow over a downstream-facing step*, Transactions of ASME D: Journal of Basic Engineering, Vol. 92, pp. 732-739, 1970.
- [115] Goodrich, J., Gustafson, K. and Halasi, K., *Hopf bifurcation in the driven cavity*, Journal of Computational Physics, Vol. 90, pp. 219-261, 1990.
- [116] Gorobets, A. V., Trias, F. X., Soria, M. and Oliva, A., *A scalable parallel Poisson solver for three-dimensional problems with one periodic direction*, Computers & Fluids, Vol. 39, pp. 525-538, 2010.
- [117] Gorobets, A. V., Trias, F. X. and Oliva, A., *A parallel MPI + OpenMPI + OpenCL algorithm for hybrid supercomputations of incompressible flows*, Computers & Fluids, Vol. 88, pp. 764-772, 2013.

- [118] Goyon, O., *High-Reynolds number solutions of Navier-Stokes equations using incremental unknowns*, Computer Methods in Applied Mechanics and Engineering, 130, pp. 319 -335, 1996.
- [119] Gresho, P. M., Gartling, D. K., Torczynski, J. R., Cliffe, K. A., Winters, K. H., Garrat, T. J., Spence, A. and Goodrich, J. W., *Is the steady viscous incompressible two-dimensional flow over a backward-facing step at $Re=800$ stable?*, International Journal for Numerical Methods in Fluids, Vol. 17, pp. 501-541, 1993.
- [120] Grigoriadis, D. G. E., Bartzis, J. G. and Goulas, A., *Efficient treatment of complex geometries for large eddy simulations of turbulent flows*, Computers & Fluids, Vol. 33, pp. 201-222, 2004.
- [121] Grigoriev, M. M. and Dargush, G. F., *A poly-region boundary element method for incompressible viscous fluid flows*, International Journal for Numerical Methods in Engineering, Vol. 46, pp. 1127-1158, 1999.
- [122] Gu, Y. T. and Liu, G. R., *Meshless techniques for convection dominated problems*, Computational Mechanics, Vol. 38, pp. 171-182, 2006.
- [123] Guj, G. and Stella, F., *Numerical solutions of high Re recirculating flow in vorticity-velocity form*, International Journal for Numerical Methods in Fluids, Vol. 8, pp. 405-416, 1988.
- [124] Gustafson, K. and Halasi, K., *Cavity flow dynamics at higher Reynolds numbers and higher aspect ratios*, Journal of Computational Physics, Vol. 70, pp. 271-283, 1987.
- [125] Gullbrand, J., *Grid-independent large-eddy simulation in turbulent channel flow using three-dimensional explicit filtering*, Center for Turbulent Research, Annual Research Briefs 2003, pp. 331-342, 2003.

- [126] Gullbrand, J., Chow, F. K., *The effect of numerical errors and turbulence models in large-eddy simulations of channel flow, with and without explicit filtering*, Journal of Fluid Mechanics, Vol. 495, pp. 323-341, 2003.
- [127] Habisreutinger, M. A., Bouffanais, R., Leriche, E. and Deville, M. O., *A coupled approximate deconvolution and dynamic mixed scale model for large-eddy simulation*, Journal of Computational Physics, Vol. 224, pp. 241-266, 2007.
- [128] Harlow, F. H. and Welch, F. E., *Numerical Calculation of Time-Dependent Viscous Incompressible Flow of Fluid with Free Surface*, The Physics of Fluids, Vol. 3, pp. 2182-2189, 1965.
- [129] Hickel, S. and Adams, N. A., *On implicit subgrid-scale modeling in wall-bounded flows*, Physics of Fluids, Vol. 19, 105106, 2007.
- [130] Higdon, J. J. L., *Stokes flow in arbitrary two-dimensional domains: shear flow over ridges and cavities*, Journal of Fluid Mechanics, Vol. 159, pp. 195-226, 1985.
- [131] Hinterberger, C., Fröhlich, J. and Rodi, W., *2D and 3D Turbulent Fluctuations in Open Channel Flow with $Re\tau = 590$ Studied by Large Eddy Simulation*, Flow, Turbulence and Combustion, Vol. 80, pp. 225-253, 2008.
- [132] Hirsch, C., *Numerical Computation of Internal and External Flows, Vol. 1: Fundamentals of Numerical Discretization*, Wiley, New York, 1989.
- [133] Hou, S., Zou, Q., Chen, S., Doolen, G. and Cogley, A. C., *Simulation of cavity flow by the lattice Boltzmann method*, Journal of Computational Physics, 118, pp. 329-347, 1995.

- [134] Houzeaux, G., Vázquez, M., Aubry, R. and Cela, J. M., *A massively parallel fractional step solver for incompressible flows*, Journal of Computational Physics, Vol. 228, pp. 6316-6332, 2009.
- [135] Howard, J. A. and Sandham, N. D., *Simulation and Modeling of a Skewed Turbulent Channel Flow*, Flow, Turbulence and Combustion, Vol. 65, pp. 83-109, 2000.
- [136] Hsu, H.-W., Hwang, F.-N., Wei, Z.-H., Lai, S.-H. and Lin, C.-A., *A parallel multilevel preconditioned iterative pressure Poisson solver for the large-eddy simulation of turbulent flow inside a duct*, Computers & Fluids, Vol. 45, pp. 138-146, 2011.
- [137] Huang, X. and Durbin, P., *Particulate Dispersion in a Turbulent Serpentine Channel*, Flow, Turbulence and Combustion, Published online May 18th, 2010.
- [138] Huijnen, V., Somers, L. M. T., Baert, R. S. G. and de Goey, L. P. H, *Validation of the LES approach in Kiva-3V on a square duct geometry*, International Journal for Numerical Methods in Engineering, Vol. 64, pp. 907-919, 2005.
- [139] Huser, A. and Biringen, S., *Calculation of two dimensional shear driven cavity flows at high Reynolds numbers*, International Journal of Numerical Methods in Engineering, Vol. 14, pp. 1087-1109, 1992.
- [140] Hutchinson, B. R. and Raithby, G. D., *A multigrid method based on the additive correction strategy*, Numerical Heat Transfer, Vol. 9, pp. 511-537, 1986.
- [141] Iida, O. and Nagano, Y., *The Relaminarization Mechanisms of Turbulent Channel Flow at Low Reynolds Numbers*, Flow, Turbulence and Combustion, Vol. 60, pp. 193-213, 1998.
- [142] Ikeda, T. and Durbin, P. A., *Direct simulations of a rough-wall channel flow*, Journal of Fluid Mechanics, Vol. 571, pp. 235-263, 2007.

- [143] Inagaki, M., Kondoh, T. and Nagano, Y., *A Mixed-Time-Scale SGS Model With Fixed Model-Parameters for Practical LES*, Journal of Fluids Engineering, Vol. 127, pp. 1-13, 2005.
- [144] Ishii, K and Iwatsu, R., *Numerical simulation of the Lagrangian flow structure in a driven cavity*, Topological Fluid Mechanics, 1989.
- [145] Islam, S., Šarler, B., Vertnik, R. and Kosec, G., *Radial basis function collocation method for the numerical solution of the two-dimensional transient nonlinear coupled Burgers' equations*, Applied Mathematical Modeling, Vol. 36, pp. 1148-1160, 2012.
- [146] Iwatsu, R, Hyun, J. M. and Kuwahara, K., *Analyses of three-dimensional flow calculations in a driven cavity*, Fluid Dynamics Research, Vol. 6, pp. 91-102, 1990.
- [147] Iwatsu, R., Ishii, K., Kawamura, T., Kuwahara, K. and Hyun, J. M., *Simulation of transition to turbulence in a cubic cavity*, AIAA Paper 98-0040, 1989.
- [148] Jaisankar, S., Shivashankar, K. and Raghurama Rao, S. V., *A grid-free central scheme for inviscid compressible flows*, AIAA Paper 2007-3946, AIAA 18th Computational Fluid Dynamics Conference, Miami, FL, June 2007.
- [149] Jan, Y. J., Huang, S. J. and Lee, T. Y., *Computational fluid flow in two dimensions using simple T4/C3 element*, International Journal for Numerical Methods in Fluids, Vol. 34, pp. 187-205, 2000.
- [150] Jeffrey, D. J. and Sherwood, J. D., *Streamline patterns and eddies in low-Reynolds-number flow*, Journal of Fluid Mechanics, Vol. 96, pp. 315-334, 1980.
- [151] Jian, X. and Lai, C.-H., *Numerical Techniques for Direct and Large-Eddy Simulations*, Chapman & Hall/RCR, 2009.

- [152] Jiménez, J. and Guegan, A., *Spontaneous generation of vortex crystals from forced two-dimensional homogeneous turbulence*, Physics of Fluids, Vol. 19, 085103, 2007.
- [153] John, V. and Roland, M., *Simulations of the turbulent channel flow at $Re\tau = 180$ with projection-based finite element variational multiscale methods*, International Journal for Numerical Methods in Fluids, Vol. 55, pp. 407-429, 2007.
- [154] Johnstone, R., Coleman, G. N. and Spalart, P. R., *The resilience of the logarithmic law to pressure gradients: evidence from direct numerical simulation*, Journal of Fluid Mechanics, Vol. 643, pp. 163-175, 2009.
- [155] Jordan, S. A. and Ragab, S. A., *On the unsteady and turbulent characteristics of the three-dimensional cavity flow*, Journal of Fluids Engineering, Vol. 116, pp. 439-449, 1992.
- [156] Jovic, S. and Driver, D. M., *Backward-facing step measurement at low Reynolds number, $Re_h = 5000$* , NASA Technical Memorandum 108807, 1994.
- [157] Jovic, S. and Driver, D. M., *Reynolds number effects on the skin friction in separated flows behind a backward facing step*, Experiments in Fluids, Vol. 18, pp. 464-467, 1995.
- [158] Jurvedic, R., *Modeling of two-dimensional laminar flow using finite element method*, International Journal for Numerical Methods in Fluids, Vol. 31, pp. 601-626, 1999.
- [159] Kaiktsis, L., Karniadakis, G. E. and Orszag, S. A., *Onset of threedimensionality, equilibria, and early transition in flow over a backward-facing step*, Journal of Fluid Mechanics, Vol. 231, pp. 501-528, 1991.

- [160] Kaiktsis, L., Karniadakis, G. E., and Orszag, S. A., *Unsteadiness and convective instabilities in a two-dimensional flow over a backward-facing step*, Journal of Fluid Mechanics, Vol. 321, pp. 157-187, 1996.
- [161] Kang, S.-H., Tanahashi M., Miyauchi T., *Dynamics of fine scale eddy clusters in turbulent channel flows*, Journal of Turbulence, Vol. 8, Art. No. N52, 2007.
- [162] Kansa, E. J., *Multiquadrics- A scattered data approximation scheme with applications to computational fluid dynamics: I. Surface approximations and partial derivative estimates*, Computers & Mathematics with Applications, Vol. 19, pp. 127-145, 1990.
- [163] Kansa, E. J., *Multiquadrics- A scattered data approximation scheme with applications to computational fluid dynamics: II. Solutions to parabolic, hyperbolic, and elliptic partial differential equations*, Computers & Mathematics with Applications, Vol. 19, pp. 147-161, 1990.
- [164] Kansa, E. J. and Hon, Y. C., *Circumventing the Ill-Conditioning Problem with Multiquadric Radial Basis Functions: Applications to Elliptic Partial Differential Equations*, Computers & Mathematics with Applications, Vol. 39, pp. 123-137, 2000.
- [165] Kato, Y., Kawai, H. and Tanshashi, T., *Numerical flow analysis in a cubic cavity by the GSMAC finite element method*, JSME International Journal Series II, Vol. 33, pp. 649-658, 1990.
- [166] Katz, A. and Jameson, A., *Edge-based meshless methods for compressible flow simulations*, AIAA Paper 2008-669, AIAA 46th Aerospace Sciences Meeting and Exhibit, Reno, NV, January 2008.
- [167] Katz, A. and Jameson, A., *Edge-based meshless methods for compressible viscous flow with applications to overset grids*, AIAA Paper 2008-3989, AIAA 38th Fluid Dynamics Conference, Seattle, WA, June 2008.

- [168] Katz, A. J., *Meshless Methods for Computational Fluid Dynamics*, Dissertation, Stanford University, 2009.
- [169] Kawaguti, M., *Numerical solution of the Navier-Stokes equations for the flow in a two-dimensional cavity*, Journal of the Physical Society of Japan, Vol. 16, pp. 2307-2315, 1961.
- [170] Keating, A., Piomelli, U., Bremhorst, K. and Nesi, S., *Large-eddy simulation of heat transfer downstream of a backward-facing step*, Journal of Turbulence, Vol. 5, Art. No. N20, 2004.
- [171] Kelmanson, M. A. and Lonsdale, B., *Eddy genesis in the double-lid-driven cavity*, The Quarterly Journal of Mechanics and Applied Mathematics, Vol. 49, pp. 635-655, 1996.
- [172] Keskar, J. and Lyn, D. A., *Computations of a laminar backward-facing step flow at $Re = 800$ with a spectral domain decomposition method*, International Journal Numerical Methods in Fluids, Vol. 29, pp. 411-427, 1999.
- [173] Kim, J. and Moin, P., *Application of a Fractional-Step Method to Incompressible Navier-Stokes Equations*, Journal of Computational Physics, Vol. 59, pp. 308-323, 1985.
- [174] Kirkman, R. D. and Metzger M., *Direct numerical simulation of sensitivity coefficients in low Reynolds number turbulent channel flow*, Journal of Turbulence, Vol. 10, Art. No. 23, 2009.
- [175] Kirshman, D. J. and Liu, F., *Cartesian grid solution of the Euler equations using a gridless boundary treatment*, AIAA Paper 2003-3974, AIAA 16th Computational Fluid Dynamics Conference, Orlando, FL, June 2003.
- [176] Kirshman, D. J. and Liu, F., *A gridless boundary condition method for the solution of the Euler equations on embedded Cartesian meshes with multigrid*, Journal of Computational Physics, Vol. 201, pp. 119-147, 2004.

[177] Kondoh, T., Nagano, Y. and Tsuji, T., *Computational study of laminar heat transfer downstream of a backward-facing step*, International Journal of Heat and Mass Transfer, Vol. 36, pp. 577-591, 1993.

[178] Kopera, M. A., *Direct Numerical Simulation of Turbulent Flow over a Backward-Facing Step*, PhD Thesis, The University of Warwick, 2011.

[179] Kosec, G. and Šarler, B., *Solution of heat transfer and fluid flow problems by the simplified explicit local radial basis function collocation method*, 14th international Conference on FE in Flow Problems. Santa Fe, USA. (2007).

[180] Kosec, G. and Sarler, B., *Local RBF collocation method for Darcy flow*, CMES: Computer Modeling in Engineering & Sciences, Vol. 25, pp. 197-207, 2008.

[181] Kosec, G. and Šarler, B., *Solution of thermo-fluid problems by collocation with local pressure correction*, International Journal of Numerical Methods for Heat & Fluid Flow, Vol. 18., pp. 868-882, 2008.

[182] Kosec, G. and Šarler, B., *Adaptive mesh-free method for thermo-fluid problems with phase change*, Eighth International Conference on Advances in Fluid Mechanics, 2010.

[183] Kosec, G. and Šarler, B., *Meshless approach to solving freezing with natural convection*, Materials Science Forum, Vol. 22, pp. 205-210, 2010.

[184] Kosec, G., Založnik, M., Šarler, B. and Combeau H., *A Meshless Approach Towards Solution of Macro-segregation Phenomena*, CMC, Vol. 580, pp. 1-27, 2011.

[185] Kosec, G., *Local Meshless Method for Multi-Phase Thermo-Fluid Problems*, Dissertation, University of Nova Gorica, 2011

- [186] Koseff, J. R. and Street, R. L., *Visualization studies of a shear driven three-dimensional recirculating flow*, Journal of Fluids Engineering, Vol. 106, pp. 21-29, 1984.
- [187] Koseff, J. R. and Street, R. L., *On the end wall effects in a lid-driven cavity flow*, Journal of Fluids Engineering, Vol. 106, pp. 385-389, 1984.
- [188] Koseff, J. R. and Street, R. L., *The lid-driven cavity flow: a synthesis of qualitative and quantitative observations*, Journal of Fluids Engineering, Vol. 106, pp. 390-398, 1984.
- [189] Koseff, J. R. and Street, R. L., *Visualization studies of a shear driven three-dimensional recirculating flow*, Three Dimensional Turbulent Shear Driven Flow, ASME, New York, pp. 23-31, 1982.
- [190] Koseff, J. R., Street, R. L., Gresho, P. M., Upson, C. D., Humphrey, J. A. C. and To, W. M., *A three-dimensional lid-driven cavity flow: experiment and simulation*, Proceedings 3rd International Conference On Numerical Methods in Laminar and Turbulent Flow, Seattle, WA, pp. 564-581, August 1983.
- [191] Kramer, W., Clercx, J. H. and van Heijst, G. J. F., *On the large-scale structure and spectral dynamics of two-dimensional turbulence in a periodic channel*, Physics of Fluids, Vol. 20, 056602, 2008.
- [192] Ku, H. C., Hirsh, R. S. and Taylor T. D., *A pseudospectral method for solution of the threedimensional incompressible Navier-Stokes equations*, Journal of Computational Physics, Vol. 70, pp. 439-462, 1987.
- [193] Kuhlmann, H. C., Wanschura, M. and Rath, H. J., *Flow in two-sided lid-driven cavities: nonuniqueness, instabilities and cellular structures*, Journal of Fluid Mechanics, Vol. 336, pp. 267-299, 1997.

[194] Kvarving, A. M. and Ronquist, E. M., *A fast tensor-product solver for incompressible fluid flow in partially deformed three-dimensional domains: Parallel implementation*, Computers & Fluids, Vol. 52, pp. 22-32, 2011.

[195] Ladevéze, J. and Peyret, R., *Calcul numérique d'une solution avec singularité des équations de Navier-Stokes: écoulement dans un canal avec variation brusque de section*, Journal de Mécanique, Vol. 13, pp. 367-396, 1974.

[196] Laskowski, G. M., Durbin, P. A., *Direct numerical simulations of turbulent flow through a stationary and rotating infinite serpentine passage*, Physics of Fluids, Vol. 19, 015101, 2007.

[197] Launder, B. and Sandham, N., *Closure Strategies for Turbulent and Transitional Flows*, Cambridge University Press, 2002.

[198] Laval, J.-P., Dubrulle, B. and Nazarenko, S. V., *Fast numerical simulations of 2D turbulence using a dynamic model for subfilter motions*, Journal of Computational Physics, Vol. 196, pp. 184-207, 2004.

[199] Le, P, Mai-Duy, N., Tran-Cong, T. and Baker, G., *A meshless IRBFN-based numerical simulation of adiabatic shear band formulation in one dimension*, International Conference on Non-linear Analysis & Engineering Mechanics Today, Ho Chi Minh city, Vietnam, 11-14 December 2006. CD, Paper No 28.

[200] Le, P., Mai-Duy, N., Tran-Cong, T. and Baker, G., *A meshless modeling of dynamic strain localization in quasi-brittle materials using radial basic function networks*, CMES: Computer Modeling in Engineering & Sciences, Vol. 25, pp. 43-66, 2008.

[201] Le-Cao, K., Mai-Duy, N. and Tran-Cong, T., *An Effective Integrated-RBFN Cartesian-Grid Discretization for the Stream Function-Vorticity-Temperature Formulation in*

Nonrectangular Domains, Numerical Heat Transfer, Part B: Fundamentals, Vol. 55, pp. 480-502, 2009.

[202] Le, H., Moin, P. and Kim, J., *Direct numerical simulation of turbulent flow over a backward-facing step*, Journal of Fluid Mechanics, Vol. 330, pp. 349-374, 1997.

[203] Lee, D. and Tsuei, Y. M., *A modified adaptive grid method for recirculating flows*, International Journal for Numerical Methods in Fluids, Vol. 14, pp. 775-791, 1992.

[204] Lee, T. and Mateescu, D., *Experimental and numerical investigation of 2D backward-facing step flow*, Journal of Fluids and Structures, Vol. 12, pp. 703-716, 1998.

[205] Leonard, B. P., *The ULTIMATE conservative difference scheme applied to unsteady one-dimensional advection*, Computer Methods in Applied Mechanics and Engineering, Vol. 88, pp. 17-74, 1991.

[206] Leonard, B. P. and Mokhtari, S., *ULTRA-SHARP Nonoscillatory Convection Schemes for High-Speed Steady Multidimensional Flow*, NASA Technical Memorandum 102568, ICOMP-90-12, 1990.

[207] Leonardi, S. and Castro, I. P., *Channel flow over large cube roughness: a direct numerical simulation study*, Journal of Fluid Mechanics, Vol. 651, pp. 519-539, 2010.

[208] Leonardi, S., Orlandi, P., Djenidi, L. and Antonia, R. A., *Guidelines for Modeling a 2D Rough Wall Channel Flow*, Flow, Turbulence and Combustion, Vol. 77, pp. 45-57, 2006.

[209] Leonardi, S., Orlandi, P., Smalley, R. J., Djenidi, L. and Antonia, R. A., *Direct numerical simulations of turbulent channel flow with transverse square bars on one wall*, Journal of Fluid Mechanics, Vol. 491, pp. 229-238, 2003.

- [210] Leone Jr., J. M., *Open boundary condition symposium benchmark solution: stratified flow over a backward-facing step*, International Journal for Numerical Methods in Fluids, Vol. 11, pp. 969-984, 1990.
- [211] Lévêque, E., Toschi, F. and Shao, L., *Shear-improved Smagorinsky model for large-eddy simulation of wall-bounded turbulent flows*, Journal of Fluid Mechanics, Vol. 570, pp. 491-502, 2007.
- [212] Li, Z. Y. and Tao, W. Q., *A new stability-guaranteed second-order difference scheme*, Numerical Heat Transfer, Part B, Vol. 42, pp. 349-365, 2002.
- [213] Liao, S.-J. and Zhu, J.-M., *A short note on higher-order streamfunction-vorticity formulation of 2-D steady state Navier-Stokes equations*, International Journal for Numerical Methods in Fluids, Vol. 22, pp. 1-9, 1996.
- [214] Lin, J. T., Armaly, B. F. and Chen, T. S., *Mixed convection heat transfer in inclined backward-facing step flows*, International Journal of Heat Transfer, Vol. 34, pp. 1568-1571, 1991.
- [215] Lin, H. and Atluri, S. N., *The meshless local Petrov-Galerkin (MLPG) method for solving incompressible Navier-Stokes equations*, CMES: Computer Modeling in Engineering and Sciences, Vol. 2, pp. 117-142, 2001.
- [216] Liu, C.-H., *Turbulent Plane Couette Flow and Scalar transport at Low Reynolds Number*, Journal of Heat Transfer, Vol. 125, pp. 988-998, 2003.
- [217] Liu, G. R., *Mesh Free Methods: Moving beyond the Finite Element Method*, CRC Press, Boca Raton, FL, 2002.

- [218] Liu, G. R., Liu, M. B. and Lam, K. Y., *A general approach for constructing smoothing functions for meshfree methods*, Proceedings of the Ninth International Conference on Computing in civil and Building Engineering, pp. 431-436, Taipei, Taiwan, 2002.
- [219] Liu, G. R., Wu, Y. L. and Ding, H., *Meshfree weak-strong (MWS) form method and its application to incompressible flow problems*, International Journal for Numerical Methods in Fluids, Vol.46, pp. 1025-1047, 2004.
- [220] Liu, J. and Su, S., *A potentially gridless solution method for the compressible Euler/Navier-Stokes equations*, AIAA Paper 1996-0526, AIAA 34th Aerospace Sciences Meeting and Exhibit, Reno, NV, January 1996.
- [221] Liu, K. and Pletcher, R. H., *Inflow conditions for the large eddy simulation of turbulent boundary layers: A dynamic recycling procedure*, Short note, Journal of Computational physics, Vol. 219, pp. 1-6, 2006.
- [222] Liu, M. B. and Liu, G. R., *Meshfree particle simulation of micro channel flows with surface tension*, Computational Mechanics, Vol. 35, pp. 332-341, 2005.
- [223] Liu, N.-S. and Lu, X.-Y., *Large eddy simulation of turbulent concentric annular channel flows*, International Journal for Numerical Methods in Fluids, Vol. 45, pp. 1317-1338, 2004.
- [224] Lu, Y. Y., Belytschko, T. and Gu, L., *A new implementation of the element free Galerkin method*, Computer Methods in Applied Mechanics and Engineering, Vol. 113, pp. 397-414, 1994.
- [225] Luo, H., Baum, J. D. and Löhner, R., *A hybrid cartesian grid and gridless method for compressible flows*, AIAA Paper 2005-0492, AIAA 43rd Aerospace Sciences Meeting and Exhibit, Reno, NV, January 2005.

- [226] Ma, Z. H., Wang, H. and Pu, S. H., *A parallel meshless dynamic cloud method on graphic processing units for unsteady compressible flows past moving boundaries*, Computer methods in applied mechanics and engineering, Vol. 285, pp. 146-165, 2015.
- [227] Madabhushi, R. K. and Vanka, S. P., *Large eddy simulation of turbulence-driven secondary flow in a square duct*, Physics of Fluids A, Vol. 3, pp. 2734-2745, 1991.
- [228] Matsunaga, K. N., *A Three-dimensional particle-tracking measurement of turbulence statistics and energy budget in a backward-facing step flow*, International Journal of Heat and Fluid Flow, Vol. 16, pp. 477-485, 1995.
- [229] Mai-Cao, L., *Meshless Radial Basis Function Method For Unsteady Incompressible Viscous Flows*, Dissertation, University of Southern Queensland, 2008.
- [230] Mai-Cao, L. and Tran-Cong, T., *A meshless IRBFN-based method for transient problems*, CMES: Computer Modeling in Engineering and Sciences, Vol. 7, pp. 149-171, 2005.
- [231] Mai-Cao, L. and Tran-Cong, T., *A meshless level-set scheme for interfacial flows*, International Conference on Non-linear Analysis & Engineering Mechanics Today, Ho Chi Minh City, Vietnam, 11-14 December 2006, CD paper No 26.
- [232] Mai-Cao, L. and Tran-Cong, T., *A meshless approach to capturing moving interfaces in passive transport problems*, CMES: Computer Modeling in Engineering & Sciences, Vol. 31, pp. 157-188, 2008.
- [233] Mai-Duy, N. and Tran-Cong, T., *Mesh-free radial basis function network methods with domain decomposition for approximation of functions and numerical solution of Poisson's equations*, Engineering Analysis with Boundary Elements, Vol. 26, pp. 133-156, 2002.

- [234] Mai-Duy, N., Mai-Cao, L. and Tran-Cong, T., *Computation of transient viscous flows using indirect radial basis function networks*, CMES: Computer Modeling in Engineering & Sciences, Vol. 18, pp. 59-77, 2007.
- [235] Marquillie, M., Laval, J.-P. and Dolganov, R., *Direct numerical simulation of a separated channel flow with a smooth profile*, Journal of Turbulence, Vol. 9, No. 1, 2008.
- [236] Matsumoto, M., <http://www.math.sci.hiroshima-u.ac.jp/~m-mat/MT/emt.html>, 2010.
- [237] McConnell, S., *Code Complete*, 2nd Edition, Microsoft Press, 2004.
- [238] McMullan, W. A., Gao, S. and Coats, C. M., *A comparative study of inflow conditions for two- and three-dimensional spatially developing mixing layers using large eddy simulation*, International Journal for Numerical Methods in Fluids, Vol. 55, pp. 589-610, 2007.
- [239] Meleshko, V. V., *Steady Stokes flow in a rectangular cavity*, Proceedings of the Royal Society, London, Series A, Vol. 452, pp. 1999-2022, 1996.
- [240] Meurant, G., *Computer Solution of Large Linear Systems*, Elsevier, 1999.
- [241] Meyers, J. and Sagaut, P., *Evaluation of Smagorinsky variants in large-eddy simulations of wall-resolved plane channel flows*, Physics of Fluids, Vol. 19, 095105, 2007.
- [242] Meyers, S., *More Effective C++*, 2009.
- [243] Meyers, S., *Effective STL*, Addison-Wesley, 2008.
- [244] Meyers, S., *Effective C++*, Addison-Wesley, 2005.

- [245] Monin, A. S. and Yaglom, A. M., *Statistical Fluid Mechanics - Mechanics of Turbulence*, Volumes I and II, Dover Publications Inc., 2007.
- [246] Morgan, K., Periaux, J. and Thomasset, F., *Analysis of Laminar Flow over a Backward-Facing Step*, Vieweg, Braunschweig, 1984.
- [247] Morrison, J. H. and Napolitano, M., *Efficient solutions of two-dimensional incompressible steady viscous flows*, Computers & Fluids, Vol. 16, pp. 119-132, 1988.
- [248] Moser, R. and Kim, J., *Direct numerical simulation of turbulent channel flow up to $Re_\tau = 559$* , Physics of Fluids, Vol. 11, pp. 943-945, 1999.
- [249] Nagamani, K. and Pepper, D. W., *A Meshless Radial Basis Function Method for Fluid Flow with Heat Transfer*, ICCES, Vol.6, pp.13-18, 2008.
- [250] Nallasamay, M. and Prasad, K. K., *On cavity flow at high Reynolds numbers*, Journal of Fluid Mechanics, Vol. 79, pp. 391-414, 1977.
- [251] Neumann, J. and Wengle, H., *DNS and LES of Passively Controlled Turbulent Backward-Facing Step Flow*, Flow, Turbulence and Combustion, Vol. 71, pp. 297-310, 2003.
- [252] Nie, J. H. and Armaly, B. F., *Three-dimensional convective flow adjacent to backward-facing step—effects of step height*, International Journal of Heat and Mass Transfer, Vol. 45, pp. 2431-2438, 2002.
- [253] Nikitin, N. and Yakhot, A., *Direct numerical simulation of turbulent flow in elliptical ducts*, Journal of Fluid Mechanics, Vol. 532, pp. 141-164, 2005.

- [254] Nishida, H. and Satofuka, N., *Higher order solutions of square driven cavity flow using a variable order multigrid method*, International Journal of Numerical Methods in Engineering, Vol. 34, pp. 637-653, 1992.
- [255] Nobile, E., *Simulation of the time-dependent flow in cavities with the additive-correction multigrid method. Part II: Applications*, Numerical Heat Transfer, Part B, Vol. 30, pp. 351-370, 1996.
- [256] Oñate, E. and Idelsohn, S., *A mesh-free finite point method for advective-diffusive transport and fluid flow problems*, Computational Mechanics Vol. 21, pp. 283-292, 1998.
- [257] Oñate, E. and Idelshon, S., *Meshless analysis of incompressible flows using the finite point method*, Innovative tools for scientific computation in aeronautical engineering, Barcelona, CIMNE, 2002.
- [258] Orlandi, P., *Vorticity-velocity formulation for high Re flows*, Computers & Fluids, Vol. 15, pp. 137-149, 1987.
- [259] Orlandi, P., Leonardi, S., Tuzi, R. and Antonia, R. A., *Direct numerical simulation of turbulent channel flow with wall velocity disturbances*, Physics of Fluids, Vol. 15, pp. 3587-3601, 2003.
- [260] Orlandi, P. and Leonardi, S., *Passive Scalar in a Turbulent Channel Flow with Wall Velocity Disturbances*, Flow, Turbulence and Combustion, Vol. 72, pp. 181-197, 2004.
- [261] Orlandi, P. and Leonardi, S., *Direct numerical simulation of three-dimensional turbulent rough channels: parameterization and flow physics*, Journal of Fluid Mechanics, Vol. 606, pp. 399-415, 2008.

- [262] Pan, F. and Acrivos, A., *Steady flows in rectangular cavities*, Journal of Fluid Mechanics, Vol. 28, pp. 643-655, 1967.
- [263] Papageorgakopoulos, J., Arampatzis, G., Assimacopoulos, D. and Markatos, N. C., *Enhancement of the momentum interpolation method on non-staggered grids*, International Journal for Numerical Methods in Fluids, Vol. 33, pp. 1-22, 2000.
- [264] Patankar, S. V., *Numerical Heat Transfer and Fluid Flow*, Hemisphere, 1980.
- [265] Peng, Y.-F., Shiau, Y.-H. and Hwang, R. R., *Transition in a 2-D lid-driven cavity flow*, Computers and Fluids, Vol. 32, pp. 337-352, 2003.
- [266] Peric, M., Kessler, R. and Scheuerer, G., *Comparison of finite-volume numerical methods with staggered and collocated grids*, Computers & Fluids, Vol. 16, pp. 389-403, 1988.
- [267] Perko, J., Chen, C. and Šarler, B., *A polygon-free numerical solution of steady natural convection in solid-liquid systems*, Moving Boundaries VI: Computational Modelling of Free and Moving Boundary Problems, (Computational and Experimental Methods, Vol. 4), WIT Press, Boston, pp. 111-122, 2001.
- [268] Perng, C.-Y. and Street, R. L., *Three-dimensional unsteady flow simulations: alternative strategies for a volume averaged calculation*, International Journal for Numerical Methods in Fluids, Vol. 9, pp. 341-362, 1989.
- [269] POSIX, <http://standards.ieee.org/regauth/posix/>, 2011.
- [270] Prasad, A. K. and Koseff, J. R., *Reynolds number and end-wall effects on a lid-driven cavity flow*, Physics of Fluids A, Vol. 1, pp. 208-218, 1989.

- [271] Priymak, V. G. and Miyazaki, T., *Accurate Navier-Stokes Investigation of Transitional and Turbulent Flow in a Circular Pipe*, Journal of Computational Physics, Vol. 142, pp. 370-411, 1998.
- [272] Priymak, V. G. and Miyazaki, T., *Direct numerical simulation of equilibrium spatially localized structures in pipe flow*, Physics of Fluids, Vol. 16, pp. 4221-4234, 2004.
- [273] Quinn, M. J., *Parallel Programming in C with MPI and OpenMP*, McGraw-Hill, 2003.
- [274] Ramanan, N. and Homsy, G. M., *Linear stability of lid-driven cavity flow*, Physics of Fluids, Vol. 6, pp. 2690-2701, 1994.
- [275] Ramsak, M. and Skerget, L., *A subdomain boundary element method for high-Reynolds laminar flow using stream function-vorticity formulation*, International Journal for Numerical Methods in Fluids, Vol. 46, pp. 815-847, 2004.
- [276] Rani, H. P. and Sheu, T. W. H., *Eddy structures in a transitional backward-facing step flow*, Journal of Fluid Mechanics, Vol. 588, pp. 43-58, 2007.
- [277] Rauber, T. and Runger, G., *Parallel Programming for Multicore and Cluster Systems*, Springer, 2010.
- [278] Redjem-Saad, L., Ould-Rouiss, M. and Lauriat, G., *Direct numerical simulation of turbulent heat transfer in pipe flows: Effect of Prandtl number*, International Journal of heat and Fluid Flow, Vol. 28, pp. 847-861, 2007.
- [279] Rhie, C. M. and Chow, W. L., *Numerical Study of the Turbulent Flow Past an Airfoil with Trailing Edge Separation*, AIAA Journal, Vol. 21, pp. 1525 -1532, 1983.

- [280] Rizzetta, D. P., Visbal, M. R. and Blaisdell, G. A., *A time-implicit high-order compact differencing and filtering scheme for large-eddy simulation*, International Journal for Numerical Methods in Fluids, Vol. 42, pp. 665-693, 2003.
- [281] Roache, P. J., *Computational Fluid Dynamics*, Hermosa, New Mexico, pp. 139-173, 1972.
- [282] Roe, P. L., *Characteristic-based schemes for the Euler equations*, Annual Review of Fluid Mechanics, Vol. 18, pp. 337-365, 1986.
- [283] Sadat, H. and Couturier, S., *Performance and Accuracy of a Meshless Method for Laminar Natural Convection*, Numerical Heat Transfer, Part B: Fundamentals, Vol. 37, pp. 455-467, 2000.
- [284] Sagaut, P., *Large Eddy Simulation for Incompressible Flows*, Second Edition, Springer, 2002.
- [285] Šarler, B., *Towards a mesh-free computation of transport phenomena*, Engineering Analysis with Boundary Elements, Vol. 26, pp. 731-738, 2002.
- [286] Šarler, B., *From global to local radial basis function collocation method for transport phenomena*, Advances in Meshfree Techniques, Springer, Berlin, 2003.
- [287] Šarler, B., *A radial basis function collocation approach in computational fluid dynamics*, CMES: Computer Modeling in Engineering and Sciences, Vol. 7, pp. 185-194, 2005.
- [288] Šarler, B. and Kuhn, G., *Primitive variable dual reciprocity boundary element method solution of incompressible Navier-Stokes equations*, Engineering Analysis with Boundary Elements, Vol. 23, pp. 443-455, 1999.

- [289] Šarler, B., Perko, J. and Chen, C. S., *Radial basis function collocation method solution of natural convection in porous Media*, International Journal of Numerical Methods for Heat & Fluid Flow, Vol. 14, pp. 187-212, 2004.
- [290] Šarler, B., Perko, J., Chen, C. S. and Kuhn, G., *A meshless approach to natural convection*, International Conference on Computational Engineering and Sciences, CD proceedings, 2001.
- [291] Šarler, B., Perko, J., Gobin, D., Goyeau, B. and Power, H., *Dual reciprocity boundary element method solution of natural convection in Darcy-Brinkman porous media*, Engineering Analysis with Boundary Elements. Vol. 28, pp. 23-41, 2004
- [292] Šarler, B., Tran-Cong, T., and Chen, C. S., *Meshfree Direct and Indirect Local Radial Basis Function Collocation Formulations for Transport Phenomena*, Boundary Elements XXVII, pp. 417-428, WIT Press, Southampton, UK, 2005.
- [293] Šarler, B. and Vertnik, R., *Meshfree Explicit Local Radial Basis Function Collocation Method for Diffusion Problems*, Computers and Mathematics with Applications, Vol. 51, pp. 1269-1282, 2006.
- [294] Šarler, B. and Atluri, S. N., *Recent Studies in Meshless & Other Novel Computational Methods*, Tech Science Press, Duluth, 2010.
- [295] Sashi Kumar, G. N., Mahendra, A. K., and Raghurama Rao, S. V., *Shape optimization using hybrid GA-ACO method and grid-free CFD solver*, AIAA Paper 2007-3830, AIAA 18th Computational Fluid Dynamics Conference, Miami, FL, June 2007.
- [296] Schreiber, R. and Keller, H. B., *Spurious solutions in driven cavity calculations*, Journal of Computational Physics, Vol. 49, pp. 165-172, 1983.

[297] Schreiber, R. and Keller, H. B., *Driven cavity flows by efficient numerical techniques*, Journal of Computational Physics, Vol. 49, pp. 310-333, 1983.

[298] Schlichting, H., *Boundary-layer theory*, McGraw-Hill, 1955.

[299] Shah, K. B., Ferziger, J. H., *A new non-eddy viscosity subgrid-scale model and its application to channel flow*, Center for Turbulent Research, Annual Briefs 1995, pp. 73-90, 1995.

[300] Shan, H., Zhang, Z. and Nieuwstadt, F. T. M., *Direct numerical simulation of transition in pipe flow under the influence of wall disturbances*, International Journal of Heat and Fluid Flow, Vol. 19, pp. 320-325, 1998.

[301] Shankar, P. N., *The eddy structure in Stokes flow in a cavity*, Journal of Fluid Mechanics, Vol. 250, pp. 371-383, 1993.

[302] Shankar, P. N., *Three-dimensional eddy structure in a cylindrical container*, Journal of Fluid Mechanics, Vol. 342, pp. 97-118, 1997.

[303] Shankar, P. N., *Three-dimensional Stokes flow in a cylindrical container*, Physics of Fluids, Vol. 10, pp. 540-549, 1998.

[304] Shankar, P. N., *On a class of three-dimensional corner eddies*, Pramana - Journal of Physics, Vol. 51, pp. 489-503, 1998.

[305] Shankar, P. N. and Deshpande, M. D., *Fluid mechanics in the driven cavity*, Annual Review of Fluid Mechanics, Vol. 32, pp. 93-136, 2000.

- [306] Shen, J., *Numerical simulation of the regularized driven cavity flows at high Reynolds numbers*, Computer Methods in Applied Mechanics and Engineering, Vol. 80, pp. 273-280, 1990.
- [307] Shen, J., *Hopf bifurcation of the unsteady regularized driven cavity flow*, Journal of Computational Physics, Vol. 95, pp. 228-245, 1991.
- [308] Sheu, T. W. H. and Tsai, S. F., *Consistent Petrov Galerkin finite element simulation of channel flows*, International Journal for Numerical Methods in Fluids, Vol. 31, pp. 1297-1310, 1999.
- [309] Shu, C., Ding, H. and Yeo, K. S., *Local radial basis function-based differential quadrature method and its application to solve two dimensional incompressible Navier-Stokes equations*, Computer Methods in Applied Mechanics and Engineering, Vol. 192, pp. 941-954, 2003.
- [310] Shu, C., Ding, H., Chen, H. Q. and Wang, T. G., *An upwind local RBF-DQ method for simulation of inviscid compressible flows*, Computer methods in applied Mechanics and engineering, Vol. 194, pp. 2001-2017, 2005.
- [311] Shyy, W., *A study of finite difference approximations to steady-state, convection-dominated flow problems*, Journal of Computational Physics, Vol. 57, pp. 415-438, 1985.
- [312] Sivaloganathan, S. and Shawl, G. J., *A multigrid method for recirculating flows*, International Journal for Numerical Methods in Fluids, Vol. 8, pp. 417-440, 1988.
- [313] Smagorinsky, J., *General circulation experiments with the primitive equations. I: The basic experiment*, Monthly Weather Review, Vol. 91, pp. 99-164, 1963.
- [314] Smolentsev, S. and Moreau, R., *One-equation model for quasi-two-dimensional turbulent magnetohydrodynamic flows*, Physics of Fluids, Vol. 19, 078101, 2007.

- [315] Sohn, J. L., *Evaluation of FIDAP on some classical laminar and turbulent benchmarks*, International Journal for Numerical Methods in Fluids, Vol. 8, pp. 1469-1490, 1988.
- [316] Sophy, T., Sadat, H. and Prax, C., *A Meshless Formulation for Three-Dimensional Laminar Natural Convection*, Numerical Heat Transfer, Part B: Fundamentals, Vol. 41, pp. 433-445, 2002.
- [317] Sparrow, E. M. and Chuck, W., *PC solutions for heat transfer and fluid flow downstream of an abrupt, asymmetric enlargement in a channel*, Numerical Heat Transfer, Vol. 12, pp. 19-40, 1987
- [318] Spatz, W. F., *Accuracy and performance of numerical wall boundary conditions for steady 2D incompressible streamfunction vorticity*, International Journal for Numerical Methods in Fluids, Vol. 28, pp. 737-757, 1998.
- [319] Sridar, D. and Balakrishnan, N., *An upwind finite difference scheme for meshless solvers*, Journal of Computational Physics, Vol. 189, pp. 1-29, 2003.
- [320] Sridar, D. and Balakrishnan, N., *Convergence acceleration of an upwind least squares finite difference based meshless solver*, AIAA Journal, Vol. 44, pp. 2189-2196, 2006.
- [321] Srinivasan, R., *Accurate solutions for steady plane flow in the driven cavity. I. Stokes flow*, Zeitschrift für angewandte Mathematik und Physik, Vol. 46, pp. 524-545, 1995.
- [322] Stalio, E. and Nobile, E., *Direct numerical simulation of heat transfer over riblets*, International Journal of Heat and Fluid Flow, Vol. 24, pp. 356-371, 2003.
- [323] Stolz, S., Schlatter, P. and Kleiser, L., *High-pass filtered eddy-viscosity models for large-eddy simulations of transitional and turbulent flow*, Physics of Fluids, Vol. 17, 065103, 2005.

- [324] Stroustrup, B., *The C++ Programming Language*, Special Edition, Addison-Wesley, 2008.
- [325] Su, M. D., Friedrich R., *Investigation of Fully Developed Turbulent Flow in a Straight Duct With Large Eddy Simulation*, Journal of Fluids Engineering, Vol. 116, pp. 677-684, 1994.
- [326] Sweby, P. K., *High resolution schemes using flux limiters for hyperbolic conservation laws*, SIAM Journal on Numerical Analysis, Vol. 21, pp. 995-1011, 1984.
- [327] Tadjfar, M. and Smith, F. T., *Direct simulations and modeling of basic three-dimensional bifurcating tube flows*, Journal of Fluid Mechanics, Vol. 519, pp. 1-32, 2004.
- [328] Thangam, S. and Knight, D. D., *Effect of stepheight on the separated flow past a backward facing step*, Physics of Fluids A, Vol. 1, pp. 604-606, 1989.
- [329] Thangam, S. and Knight, D. D., *A computational scheme in generalized coordinates for viscous incompressible flows*, Computers & Fluids, Vol. 18, pp. 317-327, 1990.
- [330] Templeton, J. A., Medic, G. and Kalitzin, G., *An eddy-viscosity based near-wall treatment for coarse grid large-eddy simulation*, Physics of Fluids, Vol. 17, 105101, 2005.
- [331] Tiselj, I., Bergant, R., Mavko, B., Bajsić, I. and Hetsroni, G., *DNS of Turbulent Heat Transfer in Channel Flow With Heat Conduction in the Solid Wall*, Journal of heat Transfer, Vol. 123, pp. 849-857, 2001.
- [332] Trobec, R., Kosec, G., Šterk, M. and Šarler, B., *Comparison of local weak and strong form meshless methods for 2-D diffusion equation*, Engineering Analysis with Boundary Elements, Vol. 36, pp. 310-321, 2012.

- [333] Trofimova, A. V., Tejada-Martínez, A. E., Jansen, K. E. and Lahey Jr., R. T., *Direct numerical simulation of turbulent channel flows using a stabilized finite element method*, Computers & Fluids, Vol. 38, pp. 924-938, 2009.
- [334] Tropea, C. D., *Die turbulence Stufenströmung in Flachkanälen und offenen Gerinnen*, Ph.D. Thesis, University of Karlsruhe, Federal Republic of Germany, Rept. SFB 80/E-21.
- [335] Tsukahara, T., Kawamura, H. and Shingai, K., *DNS of turbulent Couette flow with emphasis on the large-scale structure in the core region*, Journal of Turbulence, Vol. 7, No. 19, 2006.
- [336] Veloudis, I., Yang, Z., McGuirk, J. J., Page, G. J. and Spencer, A., *Novel Implementation and Assessment of a Digital Filter Based Approach for the Generation of LES Inlet Conditions*, Flow, Turbulence and Combustion, Vol. 79, pp. 1-24, 2007.
- [337] Vertnik, R. and Šarler, B., *Meshless local radial basis function collocation method for convective-diffusive solid-liquid phase change problems*, International Journal of Numerical Methods for Heat & Fluid Flow, Vol. 16, pp. 617-640, 2006.
- [338] Vertnik, R. and Sarler, B., *Solution of Incompressible Turbulent Flow by a Mesh-Free Method*, CMES: Computer Modeling in Engineering and Sciences, Vol. 44, pp. 65-95, 2009.
- [339] Vidal, A., *Cálculo de Flujo Turbulento por Diferencias Finitas*, Trabajo de Ascenso Profesor Asociado, Universidad Simón Bolívar, 2005.
- [340] Vidal, A., Rodríguez J., *A Direct Pressure-Linking Method for Turbulent Flow Computations*, Numerical Heat Transfer, Part B, Vol. 52, pp. 531-549, 2007.

- [341] Vidal, A., Kassab, A., Mota, D. and Dechev, D., *A Multithreaded Solver for the 2D Poisson Equation*, 20th High Performance Computing Symposium, Orlando, Florida, March 26 - 29, 2012.
- [342] Vidal, A., Kassab, A. and Dechev, D., *Evaluation of two acceleration techniques in a multithreaded 2D Poisson equation solver*, International Conference on Computational Science, Omaha, Nebraska, June 4 - 6, 2012.
- [343] Wadleigh, K. R. and Crawford, I. L., *Software Optimization for High Performance Computing*, Hewlett-Packard Professional Books, 2000.
- [344] Wagner, C., Hüttl, T.J. and Friedrich, R., *Low-Reynolds number effects from direct numerical simulations of turbulent pipe flow*, Computers & Fluids, Vol. 30, pp. 581-590, 2001.
- [345] Wakam, D. N. and Pacull, F., *Memory efficient hybrid algebraic solvers for linear systems arising from compressible flows*, Computers & Fluids, Vol. 80, pp. 158-167, 2013.
- [346] Wang, Y., Baboulin, M., Dongarra, J., Falcou, J., Fraigneau, Y. and Le Maître, O., *A parallel solver for incompressible flows*, Procedia Computer Science, Vol. 18, pp. 439-448, 2013.
- [347] Weinan, E. and Liu, J.-G., *Vorticity boundary condition and related issues for finite difference schemes*, Journal of Computational Physics, Vol. 124, pp. 368-382, 1996.
- [348] Williams, P. T. and Baker, A. J., *Numerical simulations of laminar flow over a 3D backward-facing step*, International Journal for Numerical Methods in Fluids Vol. 24, pp. 1159-1183, 1997.
- [349] Wissink, J. G., *DNS of 2D Turbulent Flow Around a Square Cylinder*, International Journal for Numerical Methods in Fluids, Vol. 25, pp. 51-62, 1997.

- [350] Wright, N. G. and Gaskell, P. H., *An efficient multigrid approach to solving highly recirculating flows*, Computers and Fluids, Vol. 24, pp. 63-79, 1995.
- [351] Wu, Y. L. and Liu, G. R., *A meshfree formulation of local radial point interpolation method (LRPIM) for incompressible flow simulation*, Computational Mechanics, Vol. 30, pp. 355-365, 2003.
- [352] Wu, Y. L., Liu, G. R. and Gu, Y. T., *Application of Meshless Local Petrov-Galerkin (MLPG) Approach to Simulation of Incompressible Flow*, Numerical Heat Transfer, Part B: Fundamentals, Vol. 48, pp. 459-475, 2005.
- [353] Wu, X. and Moin, P., *A direct numerical simulation study on the mean velocity characteristics in turbulent pipe flow*, Journal of Fluid Mechanics, Vol. 608, pp. 81-112, 2008.
- [354] Xiao, J. R. and McCarthy, M. A., *On the use of radial basis functions in a local weighted meshless method*, Second M.I.T. Conference on Computational Fluid and Solid Mechanics. June 17-20, 2003.
- [355] Xie, Z.-T. and Castro, I. P., *Efficient Generation of Inflow Conditions for Large Eddy Simulation of Street-Scale Flows*, Flow, Turbulence and Combustion, Vol. 81, pp. 449-470, 2008.
- [356] Xu, H. and Pollard, A., *Large eddy simulation of turbulent flow in a square annular duct*, Physics of Fluids, Vol. 13, pp. 3321-3337, 2001.
- [357] Xu, H., *Direct numerical simulation of turbulence in a square annular duct*, Journal of Fluid Mechanics, Vol. 621, pp. 23-57, 2009.

- [358] Xu, C., Deng, X., Zhang, L., Fang, J., Wang, G., Jiang, Y., Cao, W., Che, Y., Wang, Y., Wang, Z., Liu, W. and Cheng, X., *Collaborating CPU and GPU for large-scale high-order CFD simulations with complex grids on the TianHe-1A supercomputer*, Journal of Computational Physics, Vol. 278, pp. 275-297, 2014.
- [359] Yagawa, G. and Furukawa, T., Recent developments of free mesh method, International Journal for Numerical Methods in Engineering, Vol. 47, pp. 1419-1443, 2000.
- [360] Yanaoka, H., Yoshikawa, H. and Ota, T., *Direct Numerical Simulation of Turbulent Separated Flow and Heat Transfer over a Blunt Flat Plate*, Journal of heat Transfer, Vol. 125, pp. 779-787, 2003.
- [361] Yao, G., Islam, S. and Šarler, B., *Assessment of global and local meshless methods based on collocation with radial basis functions for parabolic partial differential equations in three dimensions*, Engineering Analysis with Boundary Elements, Vol. 36, pp. 1640-1648, 2012.
- [362] Yee, H. C., Torczynski, J. R., Morton, S. A., Visbal, M. R. and Sweby, P. K., *On spurious behavior of CFD simulations*, International Journal for Numerical Methods in Fluids, Vol. 30, pp. 675-711, 1999.
- [363] You, D., Wang, M. and Mittal, R., *A methodology for high performance computation of fully inhomogeneous turbulent flows*, International Journal for Numerical Methods in Fluids, Vol. 53, pp. 947-968, 2007.
- [364] Yu, B., Tao, W. Q., Wei, J. J., Kawaguchi, Y., Tagawa, T. and Ozoe, H., *Discussion on momentum interpolation method for collocated grids of incompressible flow*, Numerical Heat Transfer, Part B, Vol. 42, pp. 141-166, 2002.
- [365] Zang, Y., Street, R. L. and Koseff, J. R., *A dynamic mixed subgrid-scale model and its application to turbulent recirculating flows*, Physics of Fluids A, Vol. 5, pp. 3186-3196, 1993.

[366] Zang, Y., Street, R. L. and Koseff, J. R., Grid A Non-staggered Fractional step method for time-dependent incompressible Navier-Stokes equations in curvilinear coordinates, *Journal of Computational Physics*, Vol. 114, pp. 18-33, 1994.

[367] Zhang, L. T., Wagner, G. J. and Liu, W. K., *A Parallelized Meshfree Method with Boundary Enrichment for Large-Scale CFD*, *Journal of Computational Physics*, Vol. 176, pp. 483-506, 2002.

[368] Zhang, X. K., Kwon, K.-C. and Youn, S.-K., *The least-squares meshfree method for the steady incompressible viscous flow*, *Journal of Computational Physics*, Vol. 206, pp. 182-207, 2005.

[369] http://en.wikipedia.org/wiki/Flux_limiter, 2012.